

**DEVELOPMENT AND  
CHARACTERISTICS OF ULTRAFINE  
GRAINED Mg-Zn/Al MULTILAYER  
COMPOSITES BY ACCUMULATIVE ROLL  
BONDING PROCESS**

Thesis

Submitted in partial fulfillment of the requirements for the degree of

**DOCTOR OF PHILOSOPHY**

by

**GAJANAN ANNE**



**DEPARTMENT OF MECHANICAL ENGINEERING  
NATIONAL INSTITUTE OF TECHNOLOGY KARNATAKA  
SURATHKAL, MANGALORE – 575025  
NOVEMBER, 2017**

## DECLARATION

I hereby declare that the Research Thesis entitled “**DEVELOPMENT AND CHARACTERISTICS OF ULTRAFINE GRAINED Mg-Zn/Al MULTILAYER COMPOSITES BY ACCUMULATIVE ROLL BONDING PROCESS**” which is being submitted to the **National Institute of Technology Karnataka, Surathkal** in partial fulfillment of the requirements for the award of the Degree of **Doctor of Philosophy in Mechanical Engineering** is a *bonafide report of the research work carried out by me*. The material contained in this Research Thesis has not been submitted to any other Universities or Institutes for the award of any degree.

Register Number: **ME13F03**

Name of the Research Scholar: **GAJANAN ANNE**

Signature of the Research Scholar:

Department of Mechanical Engineering

Place: NITK-Surathkal

Date:

## **CERTIFICATE**

This is to certify that the Research Thesis entitled “**DEVELOPMENT AND CHARACTERISTICS OF ULTRAFINE GRAINED Mg-Zn/Al MULTILAYER COMPOSITES BY ACCUMULATIVE ROLL BONDING PROCESS**” submitted by **Mr. GAJANAN ANNE (Register Number: 135054ME13F03)** as the record of the research work carried out by him, *is accepted as the Research Thesis submission* in partial fulfillment of the requirements for the award of the Degree of **Doctor of Philosophy.**

**Dr. RAMESH. M. R**

Research Guide

Date:

**Dr. H. SHIVANANDA NAYAKA**

Research Co-Guide

**Chairman-DRPC**

Date:

## ACKNOWLEDGEMENTS

The author has great privilege and pride to express his immense sense of gratitude to **Dr. Ramesh M R** and **Dr. H Shivananda Nayaka**, Assistant Professor, Department of Mechanical Engineering, National Institute of Technology Karnataka, Surathkal for their valuable guidance, inspiration, unwavering moral support, constructive criticism, and painstaking efforts during the course of this work. They provide me much more than just an education.

Author wishes to record his deep sense of gratitude to **Prof. Narendranath S**, The Head, Department of Mechanical Engineering and all the faculty members, technical and administrative staffs of the Mechanical Engineering, National Institute of Technology Karnataka, Surathkal for their help, as and when needed.

The author is highly thankful to **Prof. Prasad Krishna**, **Prof. Gangadharan K V**, Department of Mechanical Engineering, **Prof. K Rajendra Udupa**, **Dr. Udaya Bhat K**, The Head, Department of Metallurgical, and Materials Engineering. The author wishes to record his deep sense of gratitude to **Dr. Shashibhushan Arya**, Department of Metallurgical and Materials Engineering for his support and interaction in extending corrosion facility. **Prof. N K Udayashankar** and **Mr. Ramana Reddy**, Department of Physics, for his support helps to carry out the anodization test facility.

The author is highly thankful to RPAC members **Dr. Suresha S N**, Dept. of Civil Engineering and **Dr. D Chakradhar**, Dept. of Mechanical Engineering and DRPC members Dr. Sathyabhama A, Dr. Gnanasekaran and Dr. Sharnappa Joladarashi, Dept. of Mechanical Engineering.

The author wishes to record his deep sense of gratitude to **Prof. Satyam Suwas**, Department of Materials Engineering, Indian Institute of Science, Bangalore, for his support and interaction in extending Accumulative Roll Bonding facility. **Dr. Shashank Shekhar** and **Mr. Sandeep Sahu**, Materials Science and Engineering, Indian Institute of Technology, Kanpur, for his support and interaction in extending Electron backscattered diffraction (EBSD) facility. The Author wishes to register his sincere thanks to **Exclusive Magnesium Private limited**, Hyderabad, India, providing Magnesium alloy casting facility.

The author is highly obliged to **Prof. Katta Venkataramana**, Dean Academic, National Institute of Technology Karnataka, Surathkal. Deep sense of gratitude is acknowledged to **Dr. G S Shivashankar**, Siddaganga Institute of Technology Tumkur, **Dr. Anil Kumar**, M S Ramaiah Institute of Technology Bangalore, **Shri. M V Hegde**, Director R N S Group of educations, **Mr. Nagaraj P**, Head of the department Automobile Engineering, **Mr. Dinesh Acharya**, who were kind enough to encourage pursuing Ph.D.

I would like to express my sincere thanks to Ms. Rashmi, Mr. Dhanush Department of Metallurgical and Materials Engineering NITK, Mr. Ravi Kumar, Mr. Pradeep, Materials Science and Engineering, IIT Kanpur for their help in carrying out SEM/EBSD/TEM analysis.

Author wishes to thank his seniors Dr. Manjaiah M, Dr. Muralidhar Avvari, Dr. Arun Kumar Shettigar, Dr. Raghavendra, Dr. Gagadhar, Dr. Nivish Gorge, Mr. Vignesh, Mr.Prashanth, for their constant help and encouragement during the entire process of this research work. Author also wishes to thank to his friends especially to Mr.Gopi K R, Mr.Nithin H S, Mr.Veeresh Nayak, Mr. Mahantayya Matapathi, Mr. Thippeswamy, Mr.Venkataesh Lambani, Mr. Ramesh Babu, Mr. Girish Kumar, Dr. Priyaranjan Sharma, Mr. Ashrith H. S, Mr. Pradeep B, Mr. Hargovind Soni, Dr. Hemanth K, Mr.Vasu, Mr.Suhas, Mr.Anil Kadam, Mr.Rakesh R, Mr. Jayavardhana, Mr.Karthik Rao, Mr. Madagonda B, Mr.Nuthan Prasad, Mr. Parashuram C, Mr.Pinakesh, Mr.Mallikarjun, Mr.Prashantha B, Dr.Rajesh M, Mr. Shrikanth B, Mr.Venkatesh G, Mr.Vinod Bhagat, Mr.Vinnyas, Mr.Praveen, Mr.Ramesh, Mr.Madhusudhan, Mr.Shivram. M, Mr.Baskaran, Dr.Bharath K, Mr.Durgaprasad, and all the research scholars of Dept. of Mechanical and Metallurgical and Materials Engineering for their everlasting support.

Finally, I thank my parents, my grandmother, wife, and Mr. Ganesh Hedge & Family, Late Mr. Manjunath Hedge & Family, Mr. Ramesh R Shastri & Family and Late Ganapa Hedge & Family, Mr. Narayan Bhat & Family, for their inspiration and love that accompanies me all the time.

(GAJANAN ANNE)

## ABSTRACT

Considerable demands for weight reduction in engineering applications led to an interest in light weight composites. A multilayered laminate composite fabricated via accumulative roll bonding (ARB) with two different alloys has been reported, which combine the advantage of both the alloys. Magnesium based alloys have been attracting much attention as light weight materials due to their high specific strength, good castability, good machinability, high damping capacity, and its availability as a natural mineral. However, major limiting factors in using magnesium include its low ductility, poor creep and corrosion resistance. The primary focus of this work is to develop ultra fine grained multilayered composite materials capable of exhibiting good combination of mechanical and corrosion properties. This is necessary in order to fulfill the requirements in applications such as in aerospace, automobile and electronics sectors. In this work, Mg-Zn/Al based multilayered composites were developed to address these issues. In this study, accumulative roll bonding was chosen as the SPD method to develop Mg-Zn/Al based multilayered composites in order to study the relationship between the resultant microstructure and mechanical and corrosion properties. A thorough microstructural characterization was performed on the composites by scanning electron microscope (SEM), electron backscatter diffraction (EBSD), transmission electron microscope (TEM) and phase analysis by x-ray diffraction. In addition, mechanical properties were evaluated by microhardness and tensile tests. Corrosion behavior of the multilayered composite was examined using electrochemical polarization and immersion test.

Mg-(2-6%)Zn/Al and Mg-(2-6%)Zn/anodized Al multilayered composite were developed by accumulative roll bonding process at 300 °C up to five passes. Electron back scattered diffraction and transmission electron microscopy results revealed ultra-fine grain with fraction of high angle grain boundaries. Grain size of ARB processed composite is in the range of 0.6  $\mu\text{m}$  to 1.9  $\mu\text{m}$ . Enhancement of microhardness, yield strength and ultimate tensile strength of the multilayered composites as compared to rolled Mg-(2-6%)Zn alloy was attributed to strain hardening and grain refinement (grain boundary strengthening mechanism) and presence of  $\text{Al}_{12}\text{Mg}_{17}$ ,  $\text{AlMg}_4\text{Zn}_{11}$  and

$\text{Al}_2\text{O}_3$ . Mg-4%Zn/Al and Mg-4%Zn/anodized Al composites exhibited better strength as compared to other two systems of multilayered composites. Potentiodynamic polarisation and immersion corrosion test results revealed that Mg-6%Zn/Al and Mg-6%Zn/anodized Al multilayered composite exhibited better corrosion resistance as compared to lower Zn alloying composites of Mg-(2-4%)Zn/Al and Mg-(2-4%)Zn/anodized Al. Presence of higher content of Zn in the composites results in the formation of large amount of ZnO, which can enhance the protectiveness of the passive film and kinetics of passivation there by inhibiting the corrosion.

Mg-(2-6%)Zn/Al-7075 and Mg-(2-6%)Zn/anodized Al-7075 multilayered composite were developed by accumulative roll bonding using Mg-(2-6%)Zn with Al and anodized Al at 350 °C up to four passes successfully. EBSD and TEM results revealed ultra-fine grain with fraction of high angle grain boundaries. Grain size of the ARB processed composite is in the range of 0.6  $\mu\text{m}$  to 1.3  $\mu\text{m}$ . Microhardness, yield strength and ultimate tensile strength of the multilayered composites increase with increase in number of ARB passes. Mg-4%Zn/Al-7075 and Mg-4%Zn/anodized Al-7075 composite gives better mechanical properties as compared to Mg-2%Zn/Al-7075 and Mg-2%Zn/anodized Al-7075 and Mg-6%Zn/Al-7075 and Mg-6%Zn/anodized Al-7075. Higher corrosion resistance has been observed in Mg-6%Zn/Al-7075 and Mg-6%Zn/anodized Al-7075 as compared to composites containing lower Zn content. Higher content of Zn in the multilayered composites results in the formation of large amount of ZnO, which can enhance the protectiveness of the passive film there by inhibiting the corrosion.

Mg-(2-6%)Zn/Ce/Al multilayered hybrid composites were developed by reinforcing Ce powder between Mg-(2-6%) and Al subjected to ARB process at 300 °C up to five passes successfully. EBSD and TEM analysis showed the UFG with high angle misorientation in the microstructure. Hybrid composite exhibits 1.2 times lighter weight as compared to Al. The intermetallics of  $\text{Al}_{17}\text{Mg}_{12}$ ,  $\text{AlMg}_4\text{Zn}_{11}$  and  $\text{Al}_{11}\text{Ce}_3$  were identified through the XRD analysis. It is observed that, tensile strength and microhardness of the composites increases with in ARB passes. Increase in strength was due to strain hardening, grain refinement and cerium particle reinforcement. Mg-4%Zn/Ce/Al hybrid composite exhibited higher strength as compared to Mg-2%Zn/Ce/Al and Mg-6%Zn/Ce/Al hybrid composites. The percentage elongation

decreases with increases in the number of ARB passes. Potentiodynamic polarization and immersion study revealed that Mg-6%Zn/Ce/Al hybrid composites exhibited better corrosion resistance as compared to lower Zn alloying composites of Mg-2%Zn/Ce/Al and Mg-4%Zn/Ce/Al. The developed composites with UFG structure exhibited lower density, good mechanical properties and higher corrosion resistance and can find potential applications in automobile, aerospace and electronic sectors.



# CONTENTS

<i>DECLARATION</i>	
<i>CERTIFICATE</i>	
<i>ACKNOWLEDGEMENT</i>	<i>i-ii</i>
<i>ABSTRACT</i>	<i>iii-v</i>
<i>CONTENTS</i>	<i>vi-xiv</i>
<i>LIST OF FIGURES</i>	<i>xvi-xxvi</i>
<i>LIST OF TABLES</i>	<i>xxvii-xxiii</i>
<i>ABBREVIATIONS</i>	<i>xxix-xxx</i>
<i>SYMBOLS</i>	<i>xxxi</i>
<b>CHAPTER 1</b>	<b>1- 5</b>
<b>INTRODUCTION</b>	<b>1</b>
<b>CHAPTER 2</b>	<b>6-36</b>
<b>LITERATURE SURVEY</b>	<b>6</b>
2.1 Introduction	6
2.2 Severe plastic deformation	6
2.2.1 Strengthening mechanisms	7
2.2.1.1 Strain hardening	7
2.2.1.2 Grain boundary strengthening	8
2.2.1.3 Precipitation hardening	8
2.3 Accumulative roll bonding	8
2.3.1 Phenomena of interfacial bonding	11
2.3.2 Microstructural evolution during ARB	11

2.3.3 Solid state bonding of metals	13
2.3.4 Experimental factors influencing ARB	13
2.3.4.1 Rolling temperature and speed	14
2.3.4.2 Degree of reduction	14
2.3.4.3 Roll diameter	15
2.3.4.4 Lubrication	15
2.3.4.5 Surface roughening	16
2.4 ARB of dissimilar material combinations	17
2.5 Advantages and disadvantages of ARB	17
2.6 Characteristics of magnesium	18
2.6.1 Mg-Zn alloys	19
2.6.2 Mechanical properties of magnesium alloys	20
2.6.2.1 Effects of texture on mechanical properties	20
2.6.2.2 Mechanical twinning	22
2.6.2.3 Recrystallization and grain growth	23
2.6.3 Corrosion of magnesium alloys	24
2.6.3.1 Mg/Al alloys	25
2.6.4 Factors affecting the corrosion resistance of magnesium alloys	26
2.6.4.1 Alloying elements and secondary particles	26
2.6.4.2 Dislocation density, twins and internal stress	27
2.6.4.3 Grain size	27
2.7 Aluminium and aluminium alloys	27
2.7.1 Aluminium-7075 alloy	28
2.7.2 Mechanical properties of Al alloys	29
2.7.3 Corrosion in aluminum	29

2.8	Effect of intermetallics formation during ARB on mechanical properties	30
2.9	Effect of grain refinement by ARB on mechanical and corrosion properties of multilayered composites	31
2.10	Effect of combined anodization and ARB on mechanical and corrosion properties multilayered composite	33
2.11	Effect of cerium (rare earth element) on mechanical and corrosion properties ARB processed multilayered composite	34
2.12	Research gap from literature survey	35
2.13	Objectives of the present study	36
<b>CHAPTER 3</b>		<b>37-51</b>
<b>EXPERIMENTAL PROCEDURE</b>		<b>37</b>
3.1	Material preparation	38
3.1.1	Casting of Mg-(2-6%)Zn binary alloys	38
3.2	Rolling	38
3.3	Anodization treatment	40
3.4	Preparation of Mg/Al sandwich composite	40
3.5	Accumulative roll bonding	41
3.6	Microstructural characterization	42
3.6.1	Optical microscope	43
3.6.2	Scanning electron microscope	44
3.6.3	Field emission scanning electron microscope	44
3.6.4	Transmission electron microscope	45
3.7	X-ray diffraction	46
3.8	Density	47
3.9	Mechanical properties	47
3.9.1	Microhardness	47
3.9.2	Tensile strength test	48

3.10 Corrosion behavior	49
3.10.1 Electrochemical measurements	49
3.10.2 Immersion corrosion	50
<b>CHAPTER 4</b>	<b>52-183</b>
<b>RESULTS AND DISCUSSION</b>	<b>52</b>
4.1 Microstructural analysis of as cast alloys	52
4.1.1 Optical microstructure of Mg-Zn alloy	52
4.1.1.2 SEM and EDS analysis of Mg-Zn alloys	53
4.1.1.3 Optical microstructure of Al-1100	54
4.1.1.4 Property evolution of as cast alloy	54
4.1.2. Microstructural analysis of the homogenized alloys	55
4.1.2.1 Optical microstructure	55
4.1.2.2 SEM observation	56
4.1.2.3 Property evolution of cast alloy after homogenization	56
4.1.3. Microstructural analysis of as rolled alloys	57
4.1.3.1 Optical microstructure Mg-Zn alloys	57
4.1.3.2 Optical microstructure of as rolled Al-1100	58
4.1.3.3 Optical microstructure of as rolled Al-7075 alloy	58
4.1.3.4 SEM observation	59
4.1.3.5 Anodized Al sample	60
4.1.3.6 Property evolution of rolled alloys	60
<b>4.2 Mg-Zn/Al and Mg-Zn/anodized Al multilayered composites</b>	<b>61</b>
<b>4.2.1 Mg-2%Zn/Al and Mg-2%Zn/anodized Al multilayered composites</b>	<b>61</b>
4.2.1.1 Microstructural observations	61
4.2.1.2. EBSD analysis	63

4.2.1.3 TEM analysis	66
4.2.1.4 X-ray diffraction analysis	67
4.2.1.5 Density test	68
4.2.1.6. Microhardness	69
4.2.1.7 Tensile strength	70
4.2.1.8 Fractography	72
4.2.1.9 Potentiodynamic polarisation	73
4.2.1.10 Immersion study	75
<b>4.2.2 Mg-4%Zn/Al and Mg-4%Zn/anodized Al multilayered composites</b>	76
4.2.2.1 Microstructural observations	76
4.2.2.2. EBSD analysis	78
4.2.2.3 TEM analysis	81
4.2.2.4 X-ray diffraction analysis	82
4.2.2.5 Density test	83
4.2.2.6 Microhardness test	83
4.2.2.7 Tensile test	84
4.2.2.8 Fractography	86
4.2.2.9 Potentiodynamic polarization	87
4.2.2.10 Immersion test	89
<b>4.2.3 Mg-6%Zn/Al and Mg-6%Zn/anodized Al multilayered composites</b>	90
4.2.3.1 Microstructural Analysis	90
4.2.3.2. EBSD analysis	92
4.2.3.3 TEM analysis	95
4.2.3.4 X-ray diffraction analysis	96
4.2.3.5 Density	96

4.2.3.6 Microhardness	97
4.2.3.7 Tensile strength	98
4.2.3.8 Fractography	100
4.2.3.9 Potentiodynamic polarization	101
4.2.3.10 Immersion test	103
4.2.4 Summary	103
<b>4.3 Mg-Zn/Al-7075 and Mg-Zn/anodized Al-7075 multilayered composites</b>	106
<b>4.3.1 Mg-2%Zn/Al-7075 and Mg-2%Zn/anodized Al-7075 multilayered composite</b>	106
4.3.1.1 Microstructural analysis	106
4.3.1.2 EBSD analysis	107
4.3.1.3 TEM analysis	111
4.3.1.4 XRD analysis	112
4.3.1.5 Density test	113
4.3.1.6 Microhardness test	113
4.3.1.7 Tensile test	114
4.3.1.8 Fractography	116
4.3.1.9 Potentiodynamic polarisation	117
4.3.1.10 Immersion test	119
<b>4.3.2 Mg-4%Zn/Al-7075 and Mg-4%Zn/anodized Al-7075 multilayered composites</b>	120
4.3.2.1 Microstructural analysis	120
4.3.2.2 EBSD analysis	122
4.3.2.3 TEM analysis	125
4.3.2.4 X-ray diffraction analysis	126
4.3.2.5 Density	127

4.3.2.6	Microhardness	127
4.3.2.7	Tensile strength	128
4.3.2.8	Fractography	129
4.3.2.9	Potentiodynamic polarization	130
4.3.2.10	Immersion test	133
<b>4.3.3</b>	<b>Mg-6%Zn/Al-7075 and Mg-6%Zn/anodized Al-7075 multilayered composites</b>	133
4.3.3.1	Microstructural analysis	134
4.3.3.2	EBSD analysis	135
4.3.3.3	TEM analysis	138
4.3.3.4	X-ray diffraction analysis	138
4.3.3.5	Density test	139
4.3.3.6	Microhardness	140
4.3.3.7	Tensile strength	141
4.3.3.8	Fractography	142
4.3.3.9	Potentiodynamic polarization	143
4.3.3.10	Immersion test	146
4.3.4	Summary	146
<b>4.4</b>	<b>Mg-Zn/Ce/Al hybrid composite</b>	149
<b>4.4.1</b>	<b>Mg-2%Zn/Ce/Al hybrid composite</b>	149
4.4.1.1	Microstructural observations	149
4.4.1.2	EBSD analysis	150
4.4.1.3	TEM analysis	153
4.4.1.4	X-ray diffraction analysis	154
4.4.1.5	Density	154

4.4.1.6	Microhardness	155
4.4.1.7	Tensile test	156
4.4.1.8	Fractography	157
4.4.1.10	Immersion test	160
<b>4.4.2</b>	<b>Mg-4%Zn/Ce/Al Hybrid composite</b>	160
4.4.2.1	Microstructure analysis	161
4.4.2.2	EBSD analysis	162
4.4.2.3	TEM analysis	164
4.4.2.4	X-ray diffraction analysis	164
4.4.2.5	Density test	165
4.4.2.6	Microhardness	166
4.4.2.7	Tensile test	167
4.4.2.8	Fractography	168
4.4.2.9	Potentiodynamic polarization	169
4.4.2.10	Immersion test	170
<b>4.4.3</b>	<b>Mg-6%Zn/Ce/Al hybrid composite</b>	171
4.4.3.1	Microstructure evaluation	171
4.4.3.2	EBSD analysis	172
4.4.3.3	TEM analysis	174
4.4.3.4	X-ray diffraction analysis	175
4.4.3.5	Density	176
4.4.3.6	Microhardness	176
4.4.3.7	Tensile test	177
4.4.3.8	Fractography	179



4.4.3.9 Potentiodynamic polarization	180
4.4.3.10 Immersion test	182
4.4.4 Summary	182
<b>CHAPTER 5</b>	<b>184-187</b>
<b>CONCLUSIONS</b>	184
<b>REFERENCES</b>	188-200
List of publications	201-202
Bio-data	

## LIST OF FIGURES

<b>Figure No</b>	<b>Particulars</b>	<b>Page No</b>
Figure 2.1	Accumulative roll bonding process	9
Figure 2.2	Relationships between total reduction and strain produced by ARB	10
Figure 2.3	Theoretical shear strain distribution within ARB processed Al alloy sheet for different cycles	12
Figure 2.4	Variation of shear strain	15
Figure 2.5	Surface roughness after different surface treatments	16
Figure 2.6	Mg-Zn binary phase diagram	19
Figure 2.7	Slip plane and slip direction	21
Figure 2.8	Schematic diagram of twinning mechanism	22
Figure 2.9	Pourbaix diagram of Mg in water	25
Figure 2.10	Schematic diagram of main factors affecting corrosion of the magnesium alloys.	26
Figure 2.11	Pourbaix diagram of Al in water	29
Figure 3.1	Over view of the research program of present thesis	37
Figure 3.2	Rolling machine	39

Figure 3.3	Anodization equipment	40
Figure 3.4	(a) Rolling mill (b&c) Multilayered composite sample	41
Figure 3.5	Optical microscope	43
Figure 3.6	Scanning electron microscope	44
Figure 3.7	Field emission scanning electron microscope	45
Figure 3.8	Transmission electron microscope	45
Figure 3.9	X-ray diffraction	46
Figure 3.10	Microhardness testing machine	47
Figure 3.11	(a) Tensometer (b) ASTM-E8 standard tensile specimen dimensions (c) Tensile samples	48
Figure 3.12	Electrochemical workstation	49
Figure 3.13	Immersion study equipment	50
Figure 4.1	Optical microstructure of cast Mg-Zn alloys (a) Mg-2%Zn (b) Mg-4%Zn and (c) Mg-6%Zn	52
Figure 4.2	SEM images of as cast Mg-Zn alloys (a) Mg-2%Zn (b) Mg-4%Zn and (c) Mg-6%Zn and EDS area analysis (I) Mg-2%Zn (II) Mg-4%Zn and (III) Mg-6%Zn alloys	53
Figure 4.3	Optical microstructure of the as cast Al-1100	54
Figure 4.4	Optical microstructure of cast Mg-Zn alloys after homogenization (a) Mg-2%Zn (b) Mg-4%Zn and (c) Mg-6%Zn	55
Figure 4.5	SEM of cast Mg-Zn alloys after homogenization (a) Mg-2%Zn (b) Mg-4%Zn and (c) Mg-6%Zn	56

Figure 4.6	Optical microstructure of rolled (a) Mg-2%Zn (b) Mg-4%Zn and (c) Mg-6%Zn alloy	57
Figure 4.7	Optical microstructure of the as rolled Al-1100	58
Figure 4.8	Optical microstructure of the as rolled Al-7075 alloy	58
Figure 4.9	Scanning electron microscope (SEM) of rolled (a) Mg-2%Zn (b) Mg-4%Zn and (c) Mg-6%Zn alloy	59
Figure 4.10	SEM micrographs of (a) Anodized Al sheet and (b) magnified image showing thickness of the alumina layer	60
Figure 4.11	SEM micrographs of the ARB processed Mg-2%Zn/Al multilayered composite (a) five pass multilayered composite (b) magnified image of the different layers and grain structure (c) Mg-2%Zn layer (d) Al layer (e) anodized Al layer and EDS area analysis (I) Al layer (II) Mg-2%Zn layer (III) Interface region	62
Figure 4.12	OIM images of Al layer in the 5-pass ARB processed Mg-2%Zn/Al multilayered composite (a) IPF map (b) Grain boundary map with twins (c) Misorientation angle distribution profile (d) Grain size distribution.	63
Figure 4.13	OIM images analysis of anodized Al layer in the 5-pass ARB processed Mg-2%Zn/Al multilayered composite (a) IPF map (b) Grain boundary map with twins (c) Misorientation angle distribution profile (d) Grain size distribution.	64
Figure 4.14	EBSD based analysis of Mg-2%Zn layer in the 5-pass ARB processed Mg-2%Zn/Al multilayered composite (a) IPF map (b) Grain boundary map with twins (c) Misorientation angle distribution profile (d) Grain size distribution	65
Figure 4.15	TEM micrographs and corresponding SAED patterns (a & b) Mg-2%Zn/Al (c & d) Mg-2%Zn/anodized Al multilayered composite	67
Figure 4.16	XRD patterns along the cross section of accumulative roll bonded multilayered composite	68
Figure 4.17	Microhardness variation in different layers of the Mg-2%Zn/Al and Mg-2%Zn/anodized Al composite with ARB passes	69

Figure 4.18	Variation of UTS, YS and percentage elongation of the multilayered composite with different ARB passes (a) Mg-2%Zn/Al composite (b) Mg-2%Zn/anodized Al composite	71
Figure 4.19	SEM micrographs of the fractured surface of 5-pass ARB processed (a) Mg-2%Zn/Al (b) Mg-2%Zn/anodized Al multilayered composite.	72
Figure 4.20	Potentiodynamic polarization curves of the as rolled Mg-2%Zn, Mg-2%Zn/Al and Mg-2%Zn/anodized Al multilayered composites	74
Figure 4.21	SEM micrographs of corroded (a) as rolled Mg-2%Zn (b) Mg-2%Zn/Al and (c) Mg 2%Zn/anodized Al composites after electrochemical test in a 0.1M NaCl solution	75
Figure 4.22	SEM micrographs of the Mg-4%Zn/Al multilayered composite (a) five pass multilayered composite (b) magnified image of different layers (c) Al layer (d) anodized Al layer (e) Mg-4%Zn layer	77
Figure 4.23	EBSD based analysis of Al layer in the Mg-4%Zn/Al multilayered composite (a) IPF map (b) Grain boundary map with twins (c) Misorientation angle distribution profile (d) Grain size distribution	78
Figure 4.24	EBSD based analysis of anodized Al layer in the Mg-4%Zn/anodized Al multilayered composite (a) IPF map (b) Grain boundary map with twins (c) misorientation angle distribution profile (d) Grain size distribution	79
Figure 4.25	EBSD based analysis of Mg-4%Zn layer in the multilayered composite (a) IPF map (b) Grain boundary map with twins (c) misorientation angle distribution profile (d) Grain size distribution	80
Figure 4.26	TEM micrographs and SAED patterns of the ARB processed Mg-4%Zn/Al (a & b) and Mg-4%Zn/anodized Al (c & d)	81
Figure 4.27	XRD patterns along the cross section of accumulative roll bonded multilayered composite	82
Figure 4.28	Microhardness variation in different layers of the Mg-4%Zn/Al and Mg-4%Zn/anodized Al composite with number of ARB passes	83

- Figure 4.29 Variation of UTS, YS and percentage elongation of the 85  
multilayered composite with different ARB passes (a) Mg-  
4%Zn/Al composite (b) Mg-4%Zn/anodized Al composite
- Figure 4.30 SEM micrographs of the fractured ARB processed (a) Mg- 86  
4%Zn/Al and (b) Mg-4%Zn/anodized Al multilayered  
composite
- Figure 4.31 Potentiodynamic polarization curves of the Mg-4%Zn, Mg- 87  
4%Zn/Al and Mg-4% Zn/anodized Al
- Figure 4.32 SEM micrographs of corroded (a) rolled Mg-4%Zn (b) Mg- 89  
4%Zn/Al and (c) Mg 4%Zn/anodized Al after electrochemical  
test in a 0.1 M NaCl solution
- Figure 4.33 SEM micrographs of (a) 5-pass ARB processed Mg- 91  
6%Zn/anodized Al multilayered composite (b) Magnified  
image (c) Micrographs revealing the grains in Al layer (d)  
Anodized Al layer (e) Mg-6%Zn layer and (I) EDS of the Mg-  
6%Zn layer (II) anodized Al layer (III) Interphase between Mg-  
6%Zn/anodized Al layer
- Figure 4.34 EBSD based analysis of Al layer in the Mg-6%Zn/Al 92  
multilayered composite (a) IPF map (b) Misorientation angle  
distribution profile (c) Grain boundary map with twins (d)  
Grain size distribution
- Figure 4.35 EBSD based analysis of anodized Al layer in the Mg- 93  
6%Zn/anodized Al multilayered composite (a) IPF map (b)  
Misorientation angle distribution profile (c) IPF map overlaid  
with grain boundaries and twins (d) Grain size distribution
- Figure 4.36 EBSD based analysis of Mg-6%Zn layer in the multilayered 94  
composite (a) IPF map (b) Grain boundary map overlaid with  
twins (c) misorientation angle distribution profile (d) Grain size  
distribution
- Figure 4.37 TEM micrographs and SAED patterns of the 5-pass ARB 95  
processed (a) Mg-6%Zn/Al (b) Mg-6%Zn/anodized Al  
multilayered composite
- Figure 4.38 XRD analysis along the cross section of ARB processed 96  
multilayered composite

Figure 4.39	Microhardness variation of composite layers of the Mg-6%Zn, Al and anodized Al at different ARB passes	97
Figure 4.40	UTS, YS and percentage elongation for various ARB passes of multilayered composite (a) Mg-6%Zn/Al (b) Mg-6%Zn/anodized Al	99
Figure 4.41	Fracture profile of the 5-pass ARB processed multilayered composite layers (a) Al (b) Anodized Al and (c) Mg-6%Zn	100
Figure 4.42	Potentiodynamic polarization curves of the Mg-6%Zn, Mg-6%Zn/Al and Mg-6% Zn/anodized Al	101
Figure 4.43	SEM micrographs of corroded (a) rolled Mg-6%Zn (b) Mg-6%Zn/Al and (c) Mg-6%Zn/anodized Al after electrochemical test in a 0.1 M NaCl solution	102
Figure 4.44	SEM micrographs of (a) 4-pass accumulative roll bonded Mg-2%Zn/Al-7075 multilayered composite (b) Enlarged image of multilayered composite (c) Al-7075 layer (c) Mg-2%Zn layer showing ultrafine grains (e) EDS of the Mg-2%Zn layer (f) EDS of the Al-7075 layer	107
Figure 4.45	EBSD based analysis of Al-7075 layer in the 4-pass ARB processed Mg-2%Zn/Al-7075 multilayered composite (a) IPF map (b) Grain boundary map with twins (c) Misorientation angle distribution profile (d) Grain size distribution	108
Figure 4.46	EBSD based analysis of anodized Al-7075 layer in the 4-pass ARB processed Mg-2%Zn/anodized Al-7075 multilayered composite (a) IPF map (b) Grain boundary map with twins (c) Misorientation angle distribution profile (d) Grain size distribution	109
Figure 4.47	EBSD based analysis of Mg-2%Zn layer in the 4-pass ARB processed Mg-2%Zn/Al-7075 multilayered composite (a) IPF map (b) Grain boundary map with twins (c) Misorientation angle distribution profile (d) Grain size distribution	110
Figure 4.48	TEM micrographs and SAED patterns of the ARB processed Mg-2%Zn/Al-7075 (a & b) and Mg-2%Zn/anodized Al-7075 (c & d)	111
Figure 4.49	XRD patterns along the cross section of accumulative roll bonded Mg-2%Zn/Al-7075 multilayered composites	112

Figure 4.50	Microhardness variation in Mg-2%Zn, Al-7075 and anodized Al-7075 layers during different passes of the ARB process	114
Figure 4.51	Variations of UTS, YS and percentage elongation of the multilayered composite with different ARB passes (a) Mg-2%Zn/Al-7075 (b) Mg-2%Zn/anodized Al-7075 composite	115
Figure 4.52	SEM micrographs of the fractured surface of 4-pass ARB processed (a) Mg-2%Zn/Al-7075 (b) Mg-2%Zn/anodized Al-7075 multilayered composite	116
Figure 4.53	Potentiodynamic polarization curves of the Mg-2%Zn, Mg-2%Zn/Al-7075 and Mg-4% Zn/anodized Al-7075 multilayered composite	117
Figure 4.54	SEM micrographs of corroded (a) Mg-2%Zn alloy (b) Mg-2%Zn/Al-7075 (c) Mg-2%Zn/anodized Al-7075 multilayered composites after electrochemical test in a 0.1M NaCl solution	119
Figure 4.55	SEM micrographs of the ARB processed Mg-4%Zn/anodized Al multilayered composite (a) five pass multilayered composite (b) magnified image of the different layers (c) Al layer (d) anodized Al layer (e) Mg-2%Zn layer and EDS (I) anodized Al layer (II) Mg-2%Zn layer	121
Figure 4.56	EBSD based analysis of Al-7075 layer in the 4-pass ARB processed Mg-4%Zn/Al-7075 multilayered composite (a) IPF map (b) Grain boundary map with twins (c) Misorientation angle distribution profile (d) Grain size distribution	122
Figure 4.57	EBSD based analysis of anodized Al-7075 layer in the Mg-4%Zn/anodized Al-7075 multilayered composite (a) IPF map (b) Grain boundary map with twins (c) Misorientation angle distribution profile (d) Grain size distribution	123
Figure 4.58	EBSD based analysis of Mg-4%Zn layer in the 4-pass ARB processed Mg-4%Zn/Al-7075 multilayered composite (a) IPF map (b) Grain boundary map with twins (c) Misorientation angle distribution profile (d) Grain size distribution	124
Figure 4.59	TEM micrographs and SAED patterns of the 4-pass ARB processed (a & b) Mg-4%Zn/Al-7075, (c & d) Mg-4%Zn/anodized Al-7075 multilayered composite	125



Figure 4.60	XRD patterns along the cross section of the 4-pass ARB processed multilayered composite	126
Figure 4.61	Microhardness variation of the rolled and Mg-4%Zn/anodized Al-7075 multilayered composite after different numbers of ARB passes	127
Figure 4.62	Variations of UTS, YS and percentage elongation of the multilayered composite with different ARB passes (a) Mg-4%Zn/Al-7075 (b) Mg-4%Zn/anodized Al-7075 composite	129
Figure 4.63	SEM micrographs of the fractured surface of the multilayered composites layers (a) Al-7075 (b) anodized Al-7075 (c) Mg-4%Zn layer	130
Figure 4.64	Potentiodynamic polarization curves of the Mg-4%Zn and 4-pass ARB processed multilayered composites	131
Figure 4.65	Surface morphologies of the corroded (a) Mg-4%Zn alloy (b) Mg-4%Zn/Al-7075 (c) Mg-4%Zn/Al-7075 multilayered composites	132
Figure 4.66	SEM micrographs of the ARB processed Mg-6%Zn/Al-7075 multilayered composite (a) five pass multilayered composite (b) magnified image of the different layers and grain structure (c) Mg-6%Zn layer (d) Al layer (e) anodized Al layer	134
Figure 4.67	EBSD based analysis of Al-7075 layer in the 4-pass ARB processed Mg-6%Zn/Al-7075 multilayered composite (a) IPF map (b) Grain boundary map with twins (c) Misorientation angle distribution profile (d) Grain size distribution	135
Figure 4.68	EBSD based analysis of anodized Al-7075 layer in the Mg-6%Zn/anodized Al-7075 multilayered composite (a) IPF map (b) Grain boundary map with twins (c) Misorientation angle distribution profile (d) Grain size distribution.	136
Figure 4.69	EBSD based analysis of Mg-6%Zn layer in the 4-pass ARB processed Mg-6%Zn/Al-7075 multilayered composite (a) IPF map (b) Grain boundary map with twins (c) Misorientation angle distribution profile (d) Grain size distribution	137
Figure 4.70	TEM micrographs and SAED patterns of the ARB processed (a) Mg-6%Zn/Al-7075 and (b) Mg-6%Zn/anodized Al-7075	138

Figure 4.71	XRD patterns along the cross section of accumulative roll bonded multilayered composite	139
Figure 4.72	Microhardness variation of Mg-6%Zn, Al-7075 and anodized Al-7075 layers during different passes of the ARB process	140
Figure 4.73	Variation of UTS, YS and percentage elongation of the multilayered composite with different ARB passes (a) Mg-6%Zn/Al-7075 composite (b) Mg-6%Zn/anodized Al-7075 composite	142
Figure 4.74	SEM micrographs of the fractured surface of 5-pass ARB processed (a) Mg-4%Zn/Al (b) anodized Al multilayered composite	143
Figure 4.75	Pentidynamic polarization curves of the Mg-6%Zn, Mg-6%Zn/Al-7075 and Mg-2% Zn/anodizedAl-7075 multilayered composite	144
Figure 4.76	SEM micrographs of corroded (a) rolled Mg-6%Zn (b) Mg-6%Zn/Al-7075 and (c) Mg-6%Zn/anodized Al-7075 after electrochemical test in a 0.1 M NaCl solution	145
Figure 4.77	SEM micrographs of 5-pass ARB processed (a) Mg-2%Zn/Ce/Al hybrid composite (b) Magnified image (c & d ) EDS of cerium particle (e) Microstructure of the Mg-2%Zn layer(f) Microstructure of the Al layer	150
Figure 4.78	EBSD based analysis of Al layer in the Mg-2%Zn/Ce/Al hybrid composite (a) IPF map (b) Misorientation angle distribution profile (c) IPF map, grain boundary map with twins (d) Grain size distribution	151
Figure 4.79	EBSD based analysis of Mg-2%Zn layer in the 5-pass ARB processed Mg-2%Zn/Ce/Al hybrid composite (a) IPF map (b) Grain boundary map with twins (c) Misorientation angle distribution profile (d) Grain size distribution	152
Figure 4.80	TEM micrographs and SAED patterns of the 5-pass ARB processed Mg2%Zn/Ce/Al hybrid composite	153
Figure 4.81	XRD patterns along the cross section of the Mg-2%Zn/Ce/Al hybrid composite	154

Figure 4.82	Microhardness variation of the rolled and Mg-2%Zn/Ce/Al hybrid composite after different numbers of ARB passes	155
Figure 4.83	Variation of UTS, YS and percentage elongation of the Mg-2%Zn/Ce/Al hybrid composite with different ARB passes	156
Figure 4.84	SEM micrographs of the fractured surface of the (a) 5-pass ARB processed Mg-2%Zn/Ce/Al hybrid composite (b) Al layer (c) Mg-2%Zn layer	157
Figure 4.85	Potentiodynamic polarization curves of the Mg-2%Zn and 5-pass ARB processed Mg-2%Zn/Ce/Al hybrid composite	158
Figure 4.86	SEM micrographs of corroded (a) Mg-2%Zn (b) Mg-2%Zn/Ce/Al hybrid composite after electrochemical test in a 0.1 M NaCl solution	159
Figure 4.87	SEM micrographs of 5-pass ARB processed (a) Mg-4%Zn/Ce/Al Hybrid composite (b) Magnified image (c) Microstructure of the Mg-4%Zn layer (d) Microstructure of the Al layer (e) EDS of cerium particle	161
Figure 4.88	EBSD based analysis of Al layer in the Mg-4%Zn/Ce/Al hybrid composite (a) IPF map (b) Misorientation angle distribution profile (c) IPF map, grain boundary map with twins (d) Grain size distribution	162
Figure 4.89	EBSD based analysis of Mg-2%Zn layer in the 5-pass ARB processed Mg-4%Zn/Ce/Al hybrid composite (a) IPF map (b) Grain boundary map with twins (c) Misorientation angle distribution profile (d) Grain size distribution	163
Figure 4.90	TEM micrographs and SAED patterns of the 5-pass ARB processed Mg-4%Zn/Ce/Al hybrid composite	164
Figure 4.91	XRD patterns along the cross section of the Mg-4%Zn/Ce/Al hybrid composite	165
Figure 4.92	Microhardness variation of the rolled and Mg-4%Zn/Ce/Al hybrid composite after different numbers of ARB passes	166
Figure 4.93	Variation of UTS, YS and percentage elongation of the Mg-4%Zn/Ce/Al hybrid composite with different ARB passes	167

Figure 4.94	SEM micrographs of the fractured surface of the (a) 5-pass ARB processed Mg-4%Zn/Ce/Al hybrid composite (b) Al layer (c) Mg-4%Zn layer	168
Figure 4.95	Potentiodynamic polarization curves of the Mg-4%Zn and 5-pass ARB processed Mg-4%Zn/Ce/Al hybrid composite	169
Figure 4.96	SEM micrographs of corroded (a) Mg-4%Zn (b) Mg-4%Zn/Ce/Al hybrid composite	170
Figure 4.97	SEM micrographs of 5-pass ARB processed (a) Mg-6%Zn/Ce/Al hybrid composite (b) Magnified image (c) Microstructure of the Mg-6%Zn layer (d) Microstructure of the Al layer. (d) EDS of cerium particle	172
Figure 4.98	EBSD based analysis of Al layer in the Mg-6%Zn/Ce/Al hybrid composite (a) IPF map (b) Misorientation angle distribution profile (c) IPF map, grain boundary map with twins (d) Grain size distribution	173
Figure 4.99	EBSD based analysis of Mg-6%Zn layer in the 5-pass ARB processed Mg-6%Zn/Ce/Al hybrid composite (a) IPF map (b) Grain boundary map with twins (c) Misorientation angle distribution profile (d) Grain size distribution	174
Figure 4.100	TEM micrographs and SAED patterns of the 5-pass ARB processed Mg-6%Zn/Ce/Al hybrid composite	175
Figure 4.101	XRD patterns along the cross section of the Mg-6%Zn/Ce/Al hybrid composite	176
Figure 4.102	Microhardness variation of the rolled and Mg-6%Zn/Ce/Al hybrid composite after different numbers of ARB passes	177
Figure 4.103	Variation of UTS, YS and percentage elongation of the Mg-6%Zn/Ce/Al hybrid composite with different ARB passes	178
Figure 4.104	SEM micrographs of the fractured surface of the (a) 5-pass ARB processed Mg-6%Zn/Ce/Al hybrid composite (b) Al layer (c) Mg-6%Zn layer	179
Figure 4.105	Potentiodynamic polarization curves of the Mg-6%Zn and 5-pass ARB processed Mg-6%Zn/Ce/Al hybrid composite	180

Figure 4.106 SEM micrographs of corroded (a) Mg-6%Zn (b) Mg- 181  
6%Zn/Ce/Al hybrid composite after electrochemical test in a  
0.1 M NaCl solution

## LIST OF TABLES

<b>Table No</b>	<b>Particulars</b>	<b>Page No</b>
Table 2.1	List of common alloying elements and their effect in Mg alloy system	18
Table 2.2	Possible slip system in magnesium	22
Table 3.1	Chemical composition of the alloys	38
Table 4.1	Mechanical properties of the Mg-(2-6)%Zn alloys and Al-1100	54
Table 4.2	Mechanical properties of the homogenized Mg-(2-6)%Zn alloys and Al-1100	57
Table 4.3	Mechanical properties of rolled alloys	60
Table 4.4	Density test results	69
Table 4.5	Electrochemical kinetic parameters	74
Table 4.6	Immersion test results	76
Table 4.7	Density test results	83
Table 4.8	Potentiodynamic polarization curves data of the Mg-4%Zn, Mg-4%Zn/Al and Mg-4% Zn/anodized Al	88
Table 4.9	Immersion test results	89
Table 4.10	Density test results	97
Table 4.11	Potentiodynamic polarization results	102
Table 4.12	Immersion test results	103
Table 4.13	Density test results	113
Table 4.14	Electrochemical kinetic parameters of the rolled Mg-2%Zn alloy and multilayered composites	118
Table 4.15	Immersion test results	120
Table 4.16	Density test results	127

Table 4.17	Potentiodynamic polarization test results	131
Table 4.18	Immersion test results	133
Table 4.19	Density test results	140
Table 4.20	Potentiodynamic polarization results	144
Table 4.21	Immersion test results	146
Table 4.22	Density test results	154
Table 4.23	Potentiodynamic polarization test results	159
Table 4.24	Immersion test results.	160
Table 4.25	Density test results	165
Table 4.26	Potentiodynamic polarization test results	169
Table 4.27	Immersion test results	170
Table 4.28	Density test results	176
Table 4.29	Potentiodynamic polarization test results	180
Table 4.30	Immersion test results	182

## ABBREVIATIONS

SPD	: Severe Plastic Deformation
UFG	: Ultrafine Grain
ARB	: Accumulative Roll Bonding
HCP	: Hexagonal Closed Packed
Mg	: Magnesium
Al	: Aluminum
Zn	: Zinc
Ce	: Cerium
OM	: Optical Microscopy
SEM	: Scanning Electron Microscopy
EDS	: Energy Dispersive Spectiscopy
EBSD	: Electron Back Scattered Diffraction
OIM	: Orientation Image Mapping
TEM	: Transmission Electron Microscopy
XRD	: X-ray Diffraction
JCPDS	: Joint Committee on Powder Diffraction Standards
HV	: Vickers Microhardness
% E	: Percentage of Elongation
YS	: Yield Strength
UTS	: Ultimate Tensile Strength
Al <sub>2</sub> O <sub>3</sub>	: Aluminum Oxide
DRX	: Dynamic Recrystallization
ND	: Normal Direction



RD	: Rolling Direction
TD	: Transverse Direction
HAGBs	: High Angle Boundaries
LAGBs	: Low Angle Boundaries
IPF	: Inverse Pole Figure
SAED	: Selected Area Diffraction
$E_{\text{corr}}$	: Corrosion Potential
$i_{\text{corr}}$	: Corrosion Current Density
NaCl	: Sodium Chloride

## SYMBOLS

$\sigma_y$	Yield strength
$\sigma_o$	Frictional stress
$k$	Factors associated with the hardening contribution of the grain boundaries
$d$	Average grain size
$t_i$	Initial thickness
$t_o$	Final thickness of the strip
$r_t$	Total reduction
$\epsilon_T$	Total equivalent strain
$n$	Number of ARB passes
$m$	Schmid factor
$\chi$	Angle between the direction of applied force and slip plane
$\lambda$	Angle between applied force and slip direction
$\epsilon_i$	Strain accumulated during rolling
$\epsilon_{cum}$	Cumulative strain
$P_H$	Corrosion rate through hydrogen evolution
$\rho$	Density
$\Delta w$	Weight loss rate
$V_H$	Hydrogen evolution rate

# CHAPTER 1

## INTRODUCTION

Microstructures with ultra fine grains in bulk materials have gained popularity because the grain refinement is one of the method that improves the strength of the material without compromising the ductility and flow properties (Bhowmik et al. 2009). Ultra-fine grained metals and alloys showed outstanding mechanical properties such as high strength, high toughness, superplasticity and good corrosion resistance (Saito et al. 1999). It is necessary to impose a high strain in order to introduce a high density of dislocation which in turn rearranges grain boundaries to convert a material with coarse grain in to material with ultrafine grain. Severe plastic deformation (SPD) process is one of the techniques, where in very high strain is imposing on the materials at relatively low temperature and without any significant change in the overall dimensions of the materials. SPD is known for producing ultrafine-grained (UFG) materials, thereby improving properties of the materials (Iwahashi et al. 1997; Valiev et al. 2000; Yeh et al. 1998). Various SPD techniques are high pressure torsion (Smirnova et al. 1986; Zhilyaev et al. 2003) equal-channel angular pressing (Valiev et al. 1991; Segal et al. 1981), accumulative roll bonding process (ARB) (Saito et al. 1998), multi axial forging (Salishchev et al. 1993; Sitdikov et al. 2004) and repetitive corrugation and straightening (Huang et al. 2001; Zhu et al. 2001) Among all SPD techniques, accumulative roll bonding is emerging as a most attractive and easily implementable technique to produce bulk materials in the form of sheets with ultrafine grains with large misorientations. ARB is an intense plastic straining process introducing high strain in the materials and is a function of the rolling step is to achieve simultaneous deformation and bonding of the adjacent metallic layers being rolled. It involves roll bonding of sheet, cutting the bonded materials into two equal halves, stacking them one on another and followed by rolling process. Major advantages of ARB technique is low cost, high productivity and defects-free microstructure. ARB can be performed in conventional rolling mill without any

special equipment and hence it has more potential for commercialization (Chang et al. 2012).

In addition, ARB has been reported to be capable of producing multilayer composites using dissimilar materials. This method of combining dissimilar materials is another prospective way of improving the mechanical property and widespread the application of light metals. These multilayered composites developed from dissimilar metal combinations have superior properties as compared to individual metals and exhibit unique physical, mechanical and corrosion properties when the grain size reaches the micro or nanometer regime (Eizadjou et al. 2008; Matsumoto et al., 2005).

Aluminium alloys are most widely used in the automotive industry because of its excellent strength to weight ratio and finds applications in wings, fuselage and the supporting structures (Starke et al. 1996). For further weight reduction, recently magnesium has proved a key material for light weight composites. Magnesium and its alloys have superior physical and mechanical properties which make them extremely attractive for applications in field which have requirement of lightweight materials (Song, 2011; Kojima et al. 2000). Magnesium exhibited density of only 60% that of aluminium and 25% that of steel and it is lightest metallic material. Utilization of magnesium and its alloys in the light weight application have been significantly increased in the past few years. Consequently, magnesium alloys are considered as the most promising green-engineering material as a result of aforementioned advantages compared to other structural materials. Such replacement of automotive heavy components made of steel and Al alloys with Mg alloy components offers an opportunity to increase efficiency and decrease emission (Aghion et al. 2001; Kulekci, 2008). In that aspect, considerable demands for weight reduction in engineering applications led to an interest in light weight composites.

On the other hand, Mg alloys have conspicuous disadvantages which include poor formability at ambient temperatures, poor strength, and large propensity for corrosion (Ghali et al. 2004). These limitations can be overcome by adding alloying elements (Baker, 1999; Cai et al. 2012), refining its microstructure (Zeng et al. 2011; Ralston

and Birbilis 2010; Argade et al. 2012; Saha et al. 2015), surface treatment (Jamaati and Toroghinejad, 2010; Toroghinejad et al. 2014) and bonding with high strength, good corrosion resistance alloys. Alloying magnesium is a necessary step to improve both mechanical and corrosion properties. The choice of alloying elements is important and it determines the microstructure and therefore influences the properties of alloys. It was reported that the addition of Zn element can effectively increase the strength, improve the plasticity and corrosion resistance (Gao et al. 2009; Liu et al 2008; Ha et al. 2013).

A multilayered composite developed by ARB with two different alloys having the advantage of both the alloys is of recent interest in industry (Wu et al. 2010; Liu et al.2011). Multilayered composite composed of Mg and Al alloys have received an immense consideration because of their exceptional combination of high strength to weight ratio from the Mg alloy and good corrosion resistance from the Al alloy (Matsumoto et al 2005; Liu et al.2011). More specifically, AZ31/Al-1060 (Liu et al. 2016), AZ31/Al-5052 (Zhang et al. 2015), pure Mg/Al-1050 (Chang et al. 2013), AZ31/Al-1100 (Chen et al. 2007), AZ31/Al-7075 (Zhang et al. 2011) and AZ31/Al-6082 (Xin et al. 2015) etc, has been reported in literature.

In this study, zinc and Al are alloyed with magnesium. Alloying with Zn improves the hardness and corrosion of magnesium alloys. Aluminium alloys possess good specific strength and corrosion resistance. Addition of rare earth element such as Ce can enhance ductility by means of operating non-basal slip at ambient temperatures and recrystallization nucleation at shear bands at elevated temperatures associated with texture development (Laser et al. 2008; Stanford et al. 2008; Mackenzie and Pegguleryuz, 2008) Furthermore, rare earth element also has a positive influence on the corrosion behavior of Mg alloys (Mishra et al. 2008). Generally, metal matrix composites are developed by squeeze casting, spray forming and powder metallurgy methods. Some of the defects incurred in these techniques are agglomeration and non-uniform distribution of reinforcement particles (Lee et al. 2004) and also higher manufacturing cost due to costly equipment and complex processing routes, resulting in limited applications in engineering industries. In order to overcome the problems of

agglomeration and non-uniform distribution of reinforcement particles in composite materials, Jamaati et al. (2010) reported that combination of anodizing and ARB processes as a novel approach has been used to produce high strength good corrosion resistance composites. During ARB process, alumina layer was reported to be broken, followed by dispersion into the matrix (Liu et al. 2011). Efforts have been made to develop light weight, high strength and corrosion resistant Mg-Zn/Al multilayered composite produced by ARB process. The process involved the alloy development (Mg-(2-6%)Zn binary alloy), surface treatment (anodization on Al and Al-7075) and roll bonding. Microstructural evolution, mechanical properties and corrosion behaviour of ARB processed multilayered composite were investigated.

### **Organization of the thesis**

The present work consists of five chapters and is summarized as follows:

**Chapter 1**, Contains introductory remarks on severe plastic deformation, accumulative roll bonding process, multilayered composites, application and advantages magnesium alloys. The broad objectives of the present research work are prescribed through the literature review gap.

**Chapter 2**, Presents critical review of the published literature relevant to the present study. Literature review is discussed with the severe plastic deformation, accumulative roll bonding process, factors influencing ARB and advantages of ARB over other SPD process, characteristics of magnesium and mechanical and corrosion properties of magnesium alloys, aluminium and aluminium alloys, mechanical and corrosion of aluminum alloys.

**Chapter 3**, Description of equipment and the various characterization techniques used for analysis of microstructural features, mechanical properties and corrosion behavior of the multilayered composites used in the present work.

**Chapter 4**, Explain the results and discussion of the multilayered composite systems used in this research work.

Composite system 1: Mg-(2-6%)Zn/Al and Mg-(2-6%)Zn/anodized Al multilayered composites.

Composite system 2: Mg-(2-6%)Zn/Al-7075 and Mg-(2-6%)Zn/anodized Al-7075 multilayered composites.

Composite system 3: Mg-(2-6%)Zn/Ce/Al multilayered hybrid composites.

**Chapter 5**, Conclusions and future work.

## CHAPTER 2

### LITERATURE REVIEW

#### 2.1 Introduction

Modern trends of ultrafine-grained materials forming are classified into two approaches which are bottom up approach and top-down approach (Zhu and Liao, 2004). In the bottom-up approach, nanoparticles or individual atoms are used as the building blocks to produce complex structures. These are the techniques, like inert gas condensation (Sanders et al. 1997), and high energy ball milling (Eckert et al. 1992). However, these techniques are restricted to produce small samples that are generally not suitable for structural applications. Products obtained from bottom up approach have some limitations like residual porosity and also contamination which is introduced during the fabrication. Top-down approach is an example for solid-state processing in which, coarse grained materials are refined into micro or nanostructured materials through high straining or severe plastic deformation. This approach overcome the limitations of bottom-up approach and can be applied to a wide range of metals and alloys and can produce fairly homogeneous and equiaxed microstructures (Valiev et al. 1990; Valiev et al. 1991).

#### 2.2 Severe plastic deformation

Severe plastic deformation is a metal working process imposes very large strain in to the material to get UFG microstructure. The term severe plastic deformation was introduced by Valiev in 1992. Many different SPD techniques have been designed to impose large plastic strain to the materials

- Accumulative roll-bonding (ARB) (Saito et al. 1998)
- Equal-channel angular pressing (ECAP) (Valiev et al. 1991; Segal et al. 1981)
- High-pressure torsion (HPT) (Smirnova et al. 1986; Zhilyaev et al. 2003)
- Multi-directional forging (Salishchev et al. 1993; Sitdikov et al. 2004)



- Repetitive corrugation and straightening (RCS) (Huang et al. 2001; Zhu et al. 2001)
- Cyclic-extrusion/compression (Richert and Ritchert, 1986; Richert et al. 1999)
- Friction stir processing (FSP) (Rhodes et al. 1997; Mishra and Ma, 2005)

All these techniques are capable of introducing large plastic strain in to the bulk crystalline materials to get significant microstructural refinement. Among various SPD techniques, accumulative roll bonding (ARB) is a metal forming process for producing ultrafine grained (UFG) materials. The process has attracted considerable interest in recent years because of its inherent advantages over other SPD techniques like it can be performed in conventional rolling mill without any special equipment, continuous process and the ability to produce bulk materials on an industrial scale.

### **2.2.1 Strengthening mechanisms**

In order to produce materials with desirable properties and considerable strength, various strengthening mechanisms such as solid solution hardening, grain refinement, dislocation hardening (strain or work hardening) and precipitation hardening can be employed. The main mechanisms responsible for material strengthening during SPD processes are precipitation hardening, dislocation hardening and grain refinement.

#### **2.2.1.1 Strain hardening**

Strain or work hardening is an important technique to strengthen the metallic materials using metal forming processes. During forming processes, the materials are plastically deformed into a desired shape, hence strengthened. The principle of strain hardening is based on dislocation multiplication, dislocation motion and mutual dislocation interaction. During strain hardening, the dislocations become activated and the number of dislocations increases. Since the dislocations incorporate strain fields due to lattice distortion, the dislocation strain fields can interact with each other within proximity limit. Therefore, by increasing the amount of plastic deformation, the number of dislocations rises, leading to a significant increase of the yield strength. On the other hand, one of the disadvantages of this strengthening mechanism is that it leads to reduction in ductility of the materials.

### 2.2.1.2 Grain boundary strengthening

It is well known that the mechanical properties of metallic materials are strongly affected by the grain size. Increase in yield strength with a decrease in grain size was found to be applicable to a wide variety of metals and obeys the Hall-Petch relationship (Hall, 1951; Petch, 1953).

$$\sigma_y = \sigma_o + \frac{k}{\sqrt{d}} \dots\dots\dots(2.1)$$

where,

$\sigma_y$  = yield strength,

$\sigma_o$  = frictional stress,

k = factors associated with the hardening contribution of the grain boundaries

d = grain size

If a dislocation source within one grain produces dislocations which pile-up at the next grain boundary, the stress at the tip of the pile-up must exceed some critical stress in order for the slip to continue into the neighbouring grain. Therefore, grain boundaries act as efficient barriers to dislocation movement. Because of this, it is desirable to produce materials with small grain size, as a result more number of grain boundaries acting as obstacles to dislocation glide.

### 2.2.1.3 Precipitation hardening

Perez-Prado and Ruano, 2004; Slamova et al. 2007 investigated the influence of precipitates in the accumulative roll bonded magnesium alloy and reported that the small particles exert substantial pinning on grain boundaries, stabilize the deformed structure and contribute to material strengthening.

## 2.3 Accumulative roll bonding

ARB technique involves the following steps; preparing the surfaces, stacking and roll bonding of two strips followed by cutting the roll bonded sheet into two halves. The process sequence of cutting – surface preparation – stacking – roll bonding constitutes one cycle of ARB and the sequence is repeated a number of times to achieve desired

levels of micro or nano-structuring. Schematic diagram of ARB process is shown in figure 2.1.

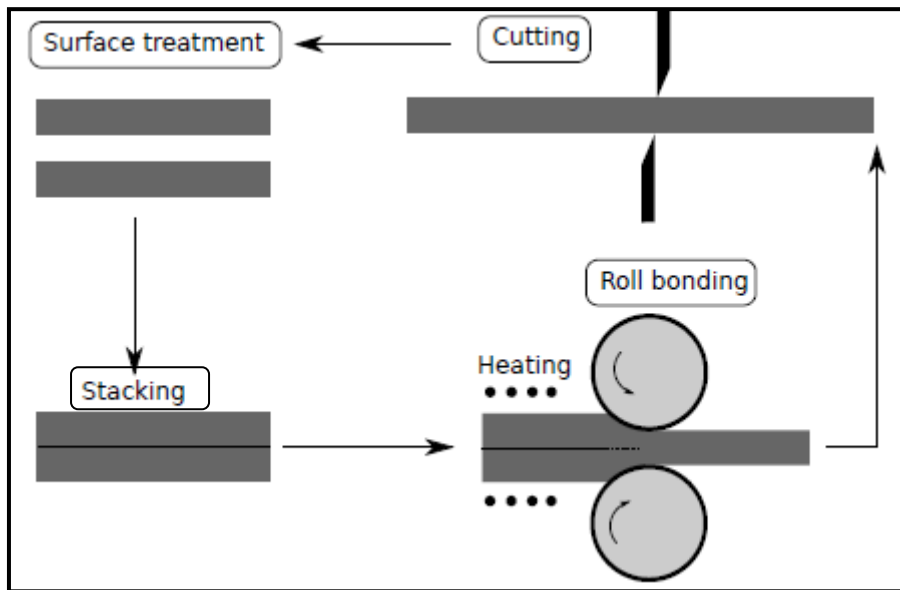


Figure 2.1. Accumulative roll bonding process (Saito et al. 1999).

Process involves continuous production of bulk materials with ultra-fine grains with large misorientations and without any geometrical shape change in the final product. The number of strengthening mechanisms involved during ARB process includes grain refinement, strain hardening, severe shear deformation at the sub-surface, redundant shear strain due to introduction of severely deformed material in the interior (Lee et al. 2002), introduction of new interfaces, and uniform distribution of oxides and inclusions at the interface. There are two possible mechanisms in the ARB process, which differ from the other SPD process. First possible mechanism has been reported that, severe stress is introduced by friction between the work piece and the roll under dry conditions. This shear deformation significantly increases the equivalent strain and promotes grain refinement (Li et al. 2006). The second mechanism is the formation of new interfaces. A large number of interfaces are introduced by several ARB cycles. These second phase particles contribute to strengthening and may act as obstacle for grain growth (Lee et al. 2002). Generally, in ARB process, the extent to which the material can be strained is unlimited because ARB is a repetitive and continuous process. However, consideration of practical factors like strain hardening, pressure requirements and edge cracking limits ARB

process. Pre-heating of the samples and rolls may be adopted prior to rolling for some materials. A reduction of 50% is usually applied in each cycle of ARB.

The thickness of the strip ‘ $t_o$ ’ after ‘ $n$ ’ cycles is given by

$$t_o = t_i/2^n \dots\dots\dots(2.2)$$

After ‘ $n$ ’ cycles, the total reduction  $r_t$  is given by

$$r_t = 1 - 1/2^n \dots\dots\dots(2.3)$$

Equation 2.4 illustrates the relation between the equivalent strain ( $\epsilon_T$ ) and number of ARB cycles ( $n$ ), where the von Mises yield criterion, 50% thickness reduction and plane strain condition are assumed (Saito et al. 1999).

$$\epsilon_T = [2/\sqrt{3}\ln(1 - 50\%)]n \dots\dots\dots(2.4)$$

Where

$t_o$  = initial thickness

$t$  = final thickness of the strip

$r_t$  = total reduction

$\epsilon_T$  = total equivalent strain

$n$  = number of ARB passes

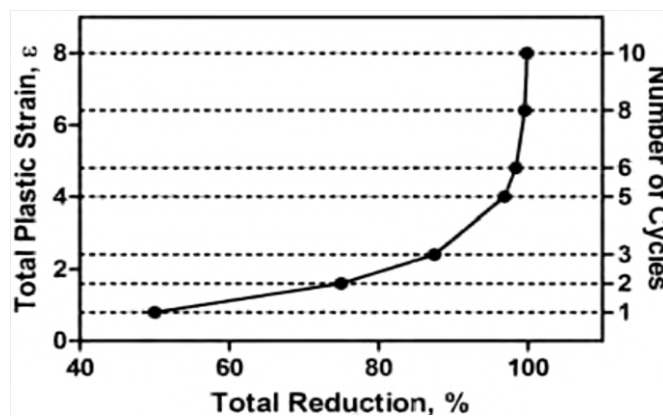


Figure 2.2. Relationships between total reduction and strain produced by ARB (Kamikawa et al. 2007).

The relationship between total reduction and strain produced by ARB process is shown in figure 2.2. The unprepared sheet material is usually not suitable for ARB processing due to their inadequate surface condition (Lee et al. 2002). Uneven sheet surfaces or pre existing contamination can weaken interfacial bonding. Surface treatments are usually carried out by grinding, wire brushing and cleaning for removing contamination such as oxides and grease.

### **2.3.1 Phenomena of interfacial bonding**

Accumulative roll bonding process is a cold welding process in metallic sheet samples are bonded together. The strength of bonds depends on various metallurgical and mechanical factors and the bond quality reflects its mechanical properties. Therefore, good bonding between layers becomes of more important and the quality of the bond depends on the following process parameters (Krallics and Lenard, 2004).

- Ductility of the materials
- Roughness of the joining faces
- Roll pressure
- Duration of the contact
- Rolling temperature
- Oxide formation on the joining surface

### **2.3.2 Microstructural evolution during ARB**

Surface and interface shearing is a key factor responsible for microstructure development during ARB. Degree of deformation decreased toward the centre of the sheet and almost no rolling strain was measured at the core. Shear strain distribution across the thickness was uneven during rolling with a large amount of resultant shear strain concentrated near the surface of the sheet. The rolling strain increase with the increase in number of ARB cycles as shown in figure 2.3. The rolling and stacking sequence associated with ARB strongly affects the distribution of the shear strain within the sheet. Heterogeneous microstructures and textures across the sheet

thickness would be expected in the material processed with less than four ARB cycles. However, as the number of ARB cycles increases, eventually the rate of strain hardening slows down near the ends of the surface, but not in the centre. Ultrafine-grained microstructure develops after repeated rolling, irrespective of the type of material being rolled; grain size reaches submicron scale, ranging from 100 nm to 1000 nm. ARB processed materials consists of UFG with a high fraction of high angle grain boundaries. Hughes and Hansen, 1997 suggested a possible mechanism for high angle boundary formation involving grain subdivision. Initially, at low strains, the dislocations may be freely standing and may form tangles or cells.

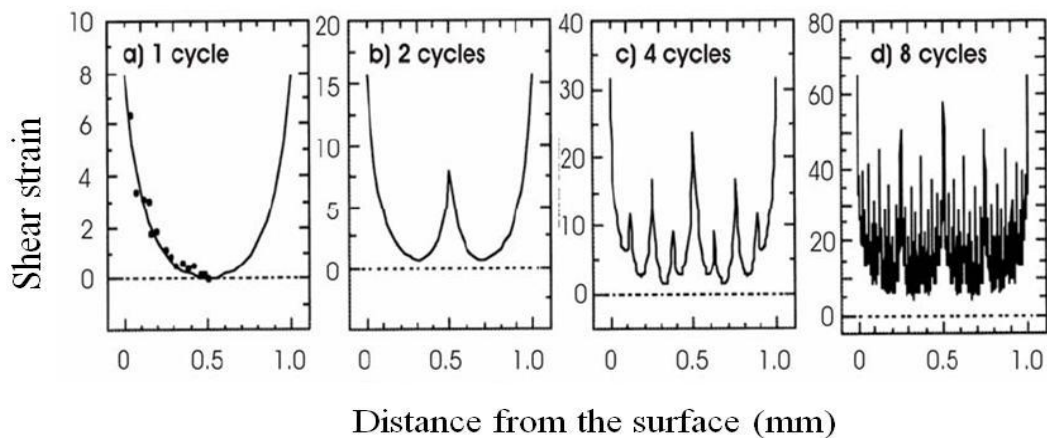


Figure 2.3. Theoretical shear strain distribution within ARB processed Al alloy sheet for different cycles (Lee et al. 2002).

These cells can be separated by dislocation boundaries such as dense dislocation walls and lamellar boundaries. By increasing the strain level, distance between the HAGBs decreases in the normal direction, i.e. they are pushed together and they are separated by fewer cells/subgrains. There is an increasing tendency for the dislocations to be stored within the subgrains, thus subdividing the microstructure. Subgrain size decreases to submicrometer range and the dislocation boundary misorientation is widely distributed. Microstructure evolves small dislocation boundaries i.e. subgrains are divided into high and low angle grain boundaries. Grain misorientation increases and as a consequence, the number of HAGBs increases; indicating reduction in grain size during severe plastic deformation (Hughes and Hansen, 1997). Another theory regarding the development of ultrafine-grained HAGBs is based on recrystallisation processes (Humphreys and Hatherly, 2004), which suggests that the ultrafine-grained

HAGBs microstructure forms by the continuous recrystallization. If the metal undergoes large strain at intermediate or high temperatures, high angle grain boundaries are evolved. At large strains HAGBs are pushed together and they are separated by subgrains. Once the separation of HAGB equals the subgrain size, HAGB impinge upon one another and a microstructure of small and equiaxed grains are formed. Continuous recrystallisation usually occurs after annealing of heavily deformed materials or in case where the grain boundary migration is strongly pinned and impeded by the secondary phase particles. This leads to strongly recovered microstructure of low angle grain boundaries (LAGB), as well as, high angle grain boundaries (HAGB) (Hughes and Hansen, 1997).

### **2.3.3 Solid state bonding of metals**

Solid state bonding of metals can be divided in two types, namely diffusion bonding and mechanical bonding. Diffusion bonding is a joining process where the principal mechanism is the interdiffusion of atoms across the interface. Diffusion requires substantial amount of time, temperature and pressure. Mechanical bonding, occurs instantaneously or over a very short period of time and depends on the forces of attraction between the atoms (Wu et al. 1998). Roll bonding is a mechanical solid state bonding process, based on cold welding. Bowden and Tabor, 1950 suggested that cold welding process depends on adhesion caused by intermolecular forces between the interfaces of materials. Main requirement for good adhesion is the contamination free surfaces and some of the factors affecting the mechanical properties are process temperature, surface roughness, and normal pressure, percentage reduction, annealing temperature and rolling speed.

### **2.3.4 Experimental factors influencing ARB**

Several processing parameters that have significant influence on the properties of the ARB processed metal, which are discussed here are rolling temperature and speed, degree of reduction, roll diameter, lubrication, surface contamination and surface roughness.

#### **2.3.4.1 Rolling temperature and speed**

Temperature is one of the most important factors, which influences the microstructure, thermal stability, mechanical properties as well as the quality of the metal bonding. An optimal process temperature has to be determined for every material. Conventionally, rolling can be performed at either a low homologous temperature (cold rolling) or elevated temperature (hot rolling). In general, hot rolling tends to provide a more flexible rolling environment by reducing the occurrence of cracking. At the same time, it promotes interfacial diffusion and dynamic recovery, (Quadir et al. 2008) thereby allowing for better bonding. Materials with high hardness and high tensile strength but low ductility materials, are more suitable for hot rolling. Conventional hot rolling generally carried out at a temperature above the material's recrystallization temperature. ARB is carried out below this critical temperature to retain the accumulated strain (Saito et al. 1999). However, higher temperatures may also be used deliberately to activate dynamic recrystallization for increasing the bond strength between sheet layers (Quadir et al. 2008). Ductile metals are capable of ARB at low homologous temperature.

A high rolling speed may significantly reduce the time for bond formation and may result in a weakened interfacial bond (Quadir et al. 2008). Rolling speed should therefore not be neglected and weak bonding has been observed as the rolling temperature is reduced with increasing rolling speed.

#### **2.3.4.2 Degree of reduction**

The quality of the bonding is important because, it affects the microstructural development of the material, thereby influencing its mechanical properties. Bonding mechanism is similar to traditional solid-phase welding or cold pressure welding (Messler, 2004). As a non-fusion technique, compression is the primary force required to initiate SPD between the contact areas and forming a weld. For a sound bonding to be produced, considerable plastic deformation is necessary. In ARB, this is measured in terms of the degree of reduction. For a high degree of reduction, more pressure is applied onto the sample causing more plastic deformation. It is proved that a minimum of 50% reduction at ambient temperature is required to generate a



reasonable strength bond in roll-bonded aluminium alloys (Saito et al. 1999). However, low ductility materials with higher degree of reduction leads to the formation of cracks.

### 2.3.4.3 Roll diameter

Roll diameter determines the amount of contact area between the sample and the rolls during rolling. A large contact area generates high amount of friction and introduces more redundant shear strain to the surface (Lee et al. 2002). Moreover, the surface texture of the specimen may also be altered depending on the amount of redundant shear strain. It has been shown that roll diameter indirectly affects the homogeneity of the texture within the sheets (Truszkowski et al. 1980).

### 2.3.4.4 Lubrication

In conventional rolling, lubrication reduces the friction between the rolls and the work piece. Subsequently, the amount of redundant shear strain is reduced and plane strain compression conditions are expected throughout the sheet thickness. In ARB, the generation of redundant shear strain is encouraged because it aids the formation of UFG structures.

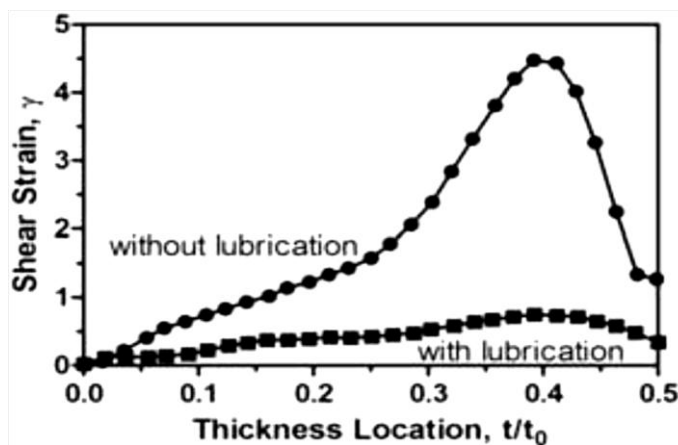


Figure 2.4. Variation of shear strain

As a result, lubrication is not necessary in ARB as compared to conventional rolling. Without lubrication, a shear texture concentrating near the surface area is developed

due to the introduction of redundant shear strain (Truskowski et al. 1980). These simultaneous shear and rolling textures result in complicated microstructures and deformation textures. The effect of lubrication on ARB has been studied by Kamikawa et al. 2007. The difference in shear strain between the lubricated and non lubricated conditions is shown in figure 2.4. In conventional ARB processing, surface contamination is always removed prior to rolling to improve the bond strength between sheets (Quadir et al. 2008).

### 2.3.4.5 Surface roughening

Surface roughening is another important parameter influencing the strength of the bonds. Generally, materials are roughened by using wire brushing before rolling. Surface roughness after different surface treatment is shown in figure 2.5.

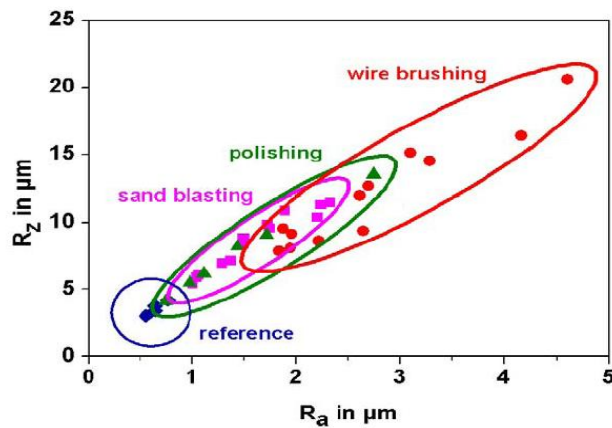


Figure 2.5. Surface roughness after different surface treatments (Klosterters et al. 2006).

Klosterters, 2006 compared the surface roughness values of the as-received aluminium sheets with the one which have been treated using different surface treatments, including wire brushing, polishing and sand blasting. The as-received material has the smoothest and the wire brushed sheets has the roughest surfaces. It was shown that the highest surface roughness achieved by wire brushing provided the strongest interlamellar bonding between the metal sheets.

## **2.4 ARB of dissimilar material combinations**

ARB has also been reported to be capable of producing multilayered composites by using dissimilar materials (Kuo and Lin, 2007). Development of multilayered composites by ARB process using dissimilar materials is another prospective way of improving the mechanical property and widespread the applications of light metals. These multilayer composites developed from dissimilar metal combinations combine the unique advantages of the different metals involved to make composites that have exhibits better properties than the individual metals. ARB process has the potential of exploiting severe plastic deformation for producing multilayer composites and exhibit unique mechanical, electrical, magnetic and corrosion properties when the layer thickness reaches the micro or nanometer regime. However, when two metals with difference in flow properties undergo co-deformation, plastic instabilities are prone to occur and the hard phase usually necks and ruptures leaving behind a dispersion of the hard phase in the matrix. This type of composite may be suitable for certain applications where layer continuity is not important like mechanical alloying.

## **2.5 Advantages and disadvantages of ARB**

The major advantages of ARB against other SBD processes are:

- i. It has the capability of high productivity and the feasibility of bulk material production.
- ii. It does not require any special equipment; conventional rolling mills can be used for bonding process.
- iii. The materials processed by this technique have almost homogeneous microstructure.
- iv. It can be applied to all type of ferrous and nonferrous alloys and can develop metal matrix composites.
- v. Formation of edge cracks reduces the ductility

## 2.6 Characteristics of magnesium

Magnesium is the eighth most abundant element in earth. It is estimated that approximately about 1.93 wt% of earth crust and 0.13 mass percentage of the ocean contains magnesium (Emley, 1966). Magnesium is the lightest structural metal with a specific density of  $1.74 \text{ g/cm}^3$  which is about two third of density of aluminum ( $2.7 \text{ g/cm}^3$ ) and one quarter of that of iron ( $7.874 \text{ g/cm}^3$ ). Magnesium exhibits a hexagonal close-packed crystal structure. Pure Mg has poor physical properties at room temperature and alloying is necessary to tailor these properties to the specific requirements of a lightweight alloys. Magnesium alloys are also ductile, easily castable and have good damping characteristics (Eliezer et al. 1998). Mg is alloyed with many other elements to improve the characteristics and the common alloying elements are tabulated in Table 2.1

Table 2.1. List of common alloying elements and their effect in Mg alloy systems

Elements	Properties	Reference
Al	Improve castability, precipitation hardening , corrosion protection	Polmear, 2006
Ca	Grain refinement, improves creep resistance, improve high temperature properties	Luo, 2004
Si	Improves creep resistance	Pekguleryuz and Kaya, 2003
Mn	Purification	Song, 2005
Zn	Ductility and castability	Pekguleryuz and Kaya, 2003
Zr	Grain refiner, purification	Polmear, 2006
Rare Earths (Ce, La,Nd)	Improve creep resistance, castability, grain refining, age hardening	Atrens et al. 2011
Ag	Improve elevated temperature properties and creep when present with rare earths	Polmear, 2006

### 2.6.1 Mg-Zn alloys

Zinc is an important alloying element for Mg but rarely serves as the major element (ZK, ZH, ZM, ZC and ZE series of alloys). There is 6.2 wt.% solubility of zinc in magnesium at the eutectic temperature. It is considered as the second important alloying addition after aluminum. Zn can effectively strengthen Mg matrix through solid solution strengthening effect (Clark, 1968), as well as secondary-phase-particles strengthening effect, when the solute atoms content exceeds its solubility in Mg matrix. The Mg-Zn binary phase diagram is shown in figure 2.6. The commercial ZK60 alloy (Mg–6Zn–0.6Zr) has been reported to be a good combination of strength and ductility, and is one of the strongest and cost-effective wrought magnesium alloys (Mendis et al. 2009).

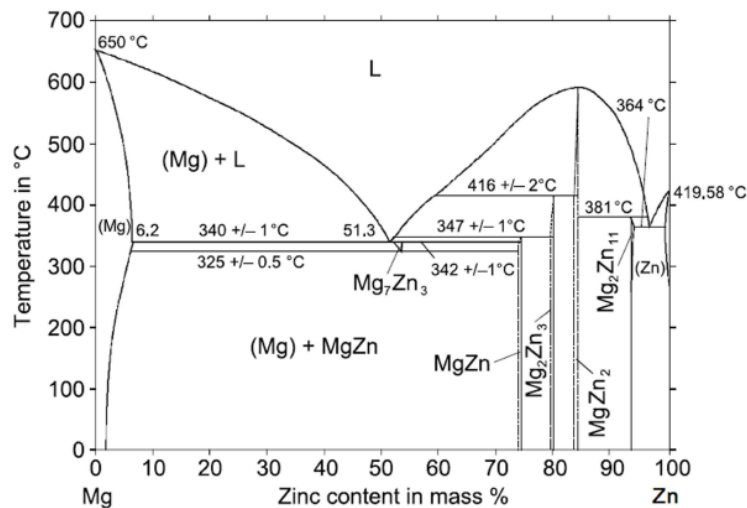


Figure 2.6. Mg-Zn binary phase diagram.

However, enhancement in strength through these secondary-phase constituents is normally accompanied by a reduction in ductility. Therefore, wrought Mg alloys necessitating large values of uniform elongation usually contain low levels of Zn in the range of 1-4 wt.%. In addition, a number of commercial magnesium alloys are based on the Mg–Zn binary alloy system with small additions of RE elements used to enhance creep resistance and tensile strength at elevated temperature.

## **2.6.2 Mechanical properties of magnesium alloys**

Mechanical properties of any alloys depend on the microstructure of the material. Microstructure is significantly affected by alloying elements (formation of secondary intermetallic particles and solute solution strengthening), casting conditions and thermomechanical processing. During thermomechanical process, one could control properties such as grain size, texture and total amount of strain energy stored in the material. Several researchers have reported that mechanical property of magnesium alloys could be significantly improved by achieving an ultra-fine grain structure through severe plastic deformation. Mechanical strength of metallic materials at the room temperature depends on the movement of the dislocations. Propagation of dislocations is restricted by pinning points that obstruct the dislocation movement, and therefore, higher force is required to overcome the barrier. The most usual pinning points are point defects, alloying elements, second phase precipitates and grain boundaries. In polycrystalline metals, grain boundaries take significant part in strengthening the material. Grain boundaries limit the motion of dislocations due to the fact that the dislocations have to change direction when entering adjacent grains and also because grain boundaries are much more disordered than grains interiors. When metal is deformed, existing dislocations and new dislocations start to move until they reach grain boundary. The dislocations pile-up at the grain boundary and it is forced to cross into the next grain by external stress. When grain structure refines, fewer dislocations occur in grains, and therefore, a greater amount of external stress needs to be applied to compensate stress field. In the polycrystalline material, the mechanical strength is depends on the grain size, describe by the Hall-Petch.

### **2.6.2.1 Effects of texture on mechanical properties**

Crystallographic slip is the most important deformation mechanism in metallic materials. Magnesium has a variety of potential deformation mechanisms, such as basal slip, prismatic slip, pyramidal slip and twinning. The motion of dislocations is activated along the most densely packed planes and is driven by a critical resolved shear stress. The activation of a particular slip system is given by the Schmid's law.

$$\sigma_{0.2} = \left(\frac{1}{M}\right)\tau_{CRS} \dots \dots \dots (2.5)$$

$$M = \cos(\chi) \cos \lambda \dots \dots \dots (2.6)$$

Schmid factor (m) represents the angle between the directions of applied force and slip plane and ( $\lambda$ ) represents the angle between applied force and slip direction. It is well known that if materials undergo homogeneous deformation, five independent slip systems are necessary (Honeycombe, 1984). Magnesium is HCP crystal structure exhibits poor formability at room temperature due to its limited number of active slip systems. In both FCC and HCP metals, slip occurs preferentially in the close-packed planes along the close-packed directions

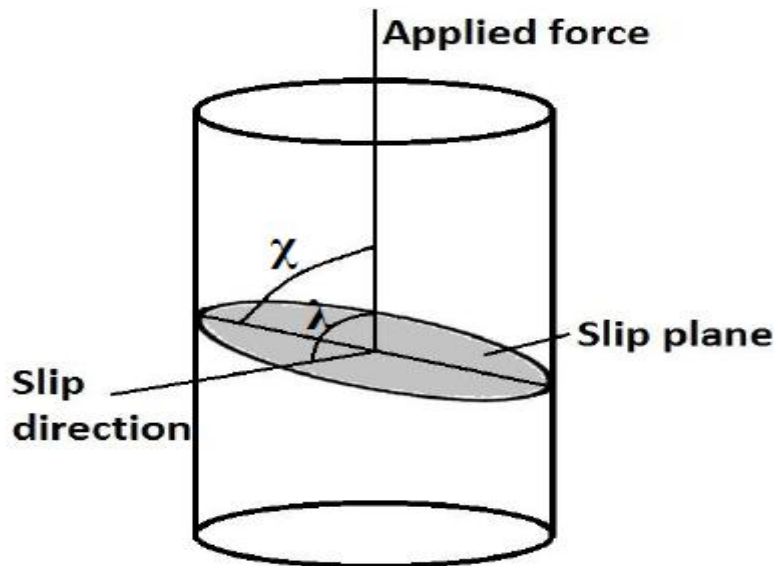


Figure 2.7. Slip plane and slip direction (Honeycombe et al. 1984).

Thus at room temperature, the FCC structure contains 12 slip systems of which five are independent, while the HCP structure has only three slip systems, out of which, two are independent. It was reported that, possible independent slip systems in hcp are: (1) the basal slip system (0001)  $[1\bar{1}20]$ ; (2) the prismatic slip systems  $\{1\bar{0}10\}[1120]$ ,  $\{1010\}[0001]$  and  $\{1\bar{1}20\}[0001]$  (3) the pyramidal slip systems  $\{1\bar{0}11\}[1\bar{1}20]$  and  $\{1\bar{1}22\}[1\bar{1}23]$ . The possible slip system in Magnesium is tabulated in the table 2.2.

Table 2.2. Possible slip system in magnesium

Burgers Vector	Slip plane	Slip direction	Number of slip system	
			Total	Independent
(a)	Basal (0001)	(1 $\bar{1}$ 20)	3	2
(a)	Prismatic (1010)	(1 $\bar{1}$ 20)	3	2
(c)	Prismatic(1010)	(0001)	3	2
(c)	Prismatic (1120)	(0001)	3	2
(a)	Pyramidal (1011)	(1 $\bar{1}$ 20)	6	4
(c+a)	Pyramidal (1122)	(1 $\bar{1}$ 23)	6	5

### 2.6.2.2 Mechanical twinning

Metallic materials, in addition to crystallographic slip, plastic deformation can also occur by the formation of twins. Mechanical twinning is defined as a homogeneous shear, evenly distributed over a three-dimensional region.

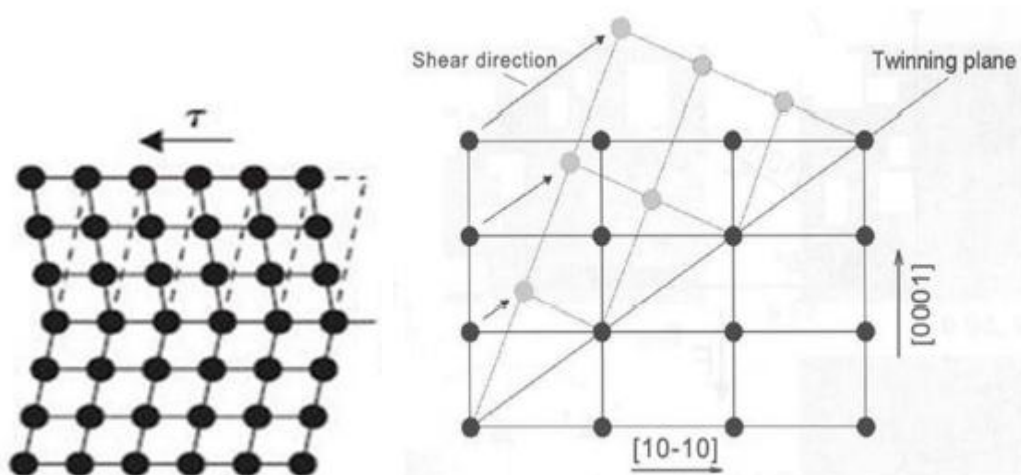


Figure 2.8. Schematic diagram of twinning mechanism.

Not only the strain is produced by the twinning process, but also the orientation changes, resulting from twinning may place new slip systems in a favorable orientation with respect to the stress axis so that additional slip can take place. It can produce atomic displacements such that on one side of a plane (twin boundary), atoms



are located in mirror-image positions of atoms on the other side as shown in figure 2.8. Displacement magnitude with the twin region is proportional to the distance from the twin plane. Twinning occurs on definite crystallographic planes and the direction that depends on the crystal structure. Nucleation and growth of twins are affected by initial and deformation conditions such as, temperature, strain rates, grain size, pre-strain and precipitates (Christian and Mahajan, 1995).

### **2.6.2.3 Recrystallization and grain growth**

Recrystallization (RX) is a process by which deformed grains are replaced by a new set of undeformed grains that nucleate and grow until the original grains have been entirely consumed. Recrystallization is usually accompanied by a reduction in the strength and hardness of a material and a simultaneous increase in the ductility (Doherty et al. 1997). When the recrystallization process takes place during the deformation, recrystallization is referred to as dynamic recrystallization (DRX). Static recrystallization (SRX) refers to the evolution of the new grains after the hot or cold working deformation. The most important uses are the softening of metals previously hardened by cold work, which have lost their ductility, and the control of the grain structure in the final product. Static recrystallization may occur when a hot deformed material is subsequently annealed. In addition, static recrystallization of cold-worked metals may be used to refine the grain structure and release the stored energy in order to be imposed to high deformation strains. Stacking fault energy (SFE) can significantly affect microstructure evolution during both deformation and annealing. During recrystallization, the mechanical properties that resulted from cold working are restored to their precold-worked values and the metal becomes softer, weaker, yet more ductile. Annealing releases the stored strain energy and restores the ductility of deformed materials. Some heat treatments are designed to allow recrystallization to occur to modify texture, microstructure and mechanical properties (Cram et al. 2009). Dynamic recrystallization is depending upon the microstructure evolution during hot deformation. DRX can be classified as continuous or discontinuous. A continuous DRX process is a recovery process and proceeds by continuous absorption of dislocations in subgrain boundaries which result in the formation of high angle grain

boundaries (HAGBs) and thus formation of new grains (Ion et al. 1982). Recovery process is controlled by the thermally activated dislocation motions, which result in rearrangement and annihilation of dislocations. In discontinuous DRX process, the new strain free grains with HAGBs evolve in the place of pre-existing grains whereas in continuous DRX low angle grain boundaries (LAGBs) convert into HAGBs during deformation. The driven force is attributed to the difference of dislocation density between new and deformed structure. In discontinuous DRX process, the subgrain boundaries formed at low strains which evolve to HAGBs at higher strains (Bhattacharya et al. 2011).

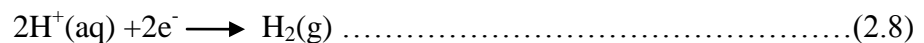
### 2.6.3 Corrosion of magnesium alloys

Nowadays, the use of magnesium in the automotive industry is creating a huge demand because it is the lightest structural metal. However, the use of magnesium alloys is limited due to the poor corrosion resistance compared to aluminum, the most widespread light metals. The magnesium standard potential (-2.375 V) is the lowest of all structural metals. Use of magnesium in a conductive contact with other metals exhibits galvanic corrosion on the interface accelerates the degradation process in an aggressive media. Magnesium forms a surface oxide in dry air (Valiev, 1997) and form MgO film on the surface that protects the metal from further oxidation, called as passive film. In the presence of water MgO is converted to Mg(OH)<sub>2</sub> and it is thermodynamically more stable in water (Nordlien et al. 1996). Mg and its alloys are reported to corrode electrochemically in aqueous media.

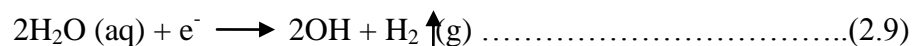
Anodic dissolution of Mg according to:



Corresponding cathodic reaction is the evolution of hydrogen



In alkaline solutions hydrogen evolution occurs according to



The electrochemical corrosion of Mg in water corresponds to the sum of the two reactions (2.7) and (2.9):

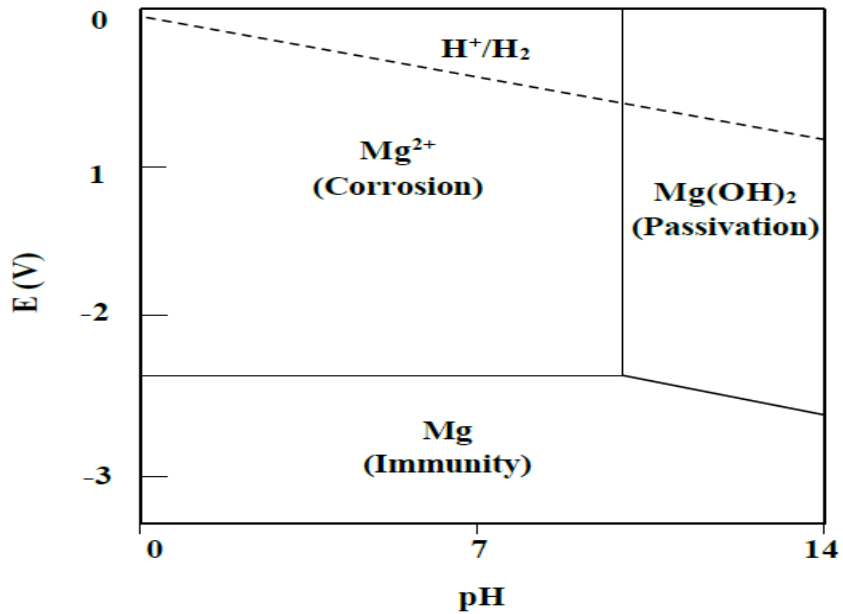
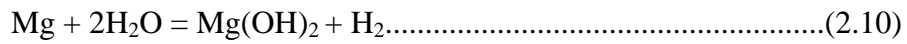


Figure 2.9. Pourbaix diagram of Mg in water (Ryoo et al. 2005).

Thermodynamic stability of different phases in aqueous corrosion are shown in pourbaix diagrams (Figure 2.9). The Mg(OH)<sub>2</sub> is insoluble in an alkaline environment and in contrast, it dissolves in neutral and acidic solutions where Mg<sup>2+</sup> is produced. Both MgO and Mg(OH)<sub>2</sub> are electronically insulating and therefore cannot act as cathodes.

### 2.6.3.1 Mg/Al alloys

Aluminum is used to improve the castability and mechanical properties of Mg and reported that aluminium addition increases the corrosion resistance of MgAl alloys (Lunder et al. 1993; Ambat et al. 2000). High aluminum content of Mg<sub>17</sub>Al<sub>12</sub> precipitates (β-phase) is believed to give rise a more protective passive film compared to that formed on the matrix material (i.e. solid solution of Al in α-Mg)( Song et al. 1998). It has been suggested that the β-phase has a dual role in the corrosion of MgAl alloys, it can serve both as a cathode and a corrosion barrier (Song and Atrens 1999).

A continuous distribution and large fraction of  $\beta$ -phase has been shown to contribute significantly to reduce corrosion (Jonsson and Persson, 2010).

#### 2.6.4 Factors affecting the corrosion resistance of magnesium alloys

Figure 2.10 represents the main attributes that affect the corrosion of the magnesium alloys.

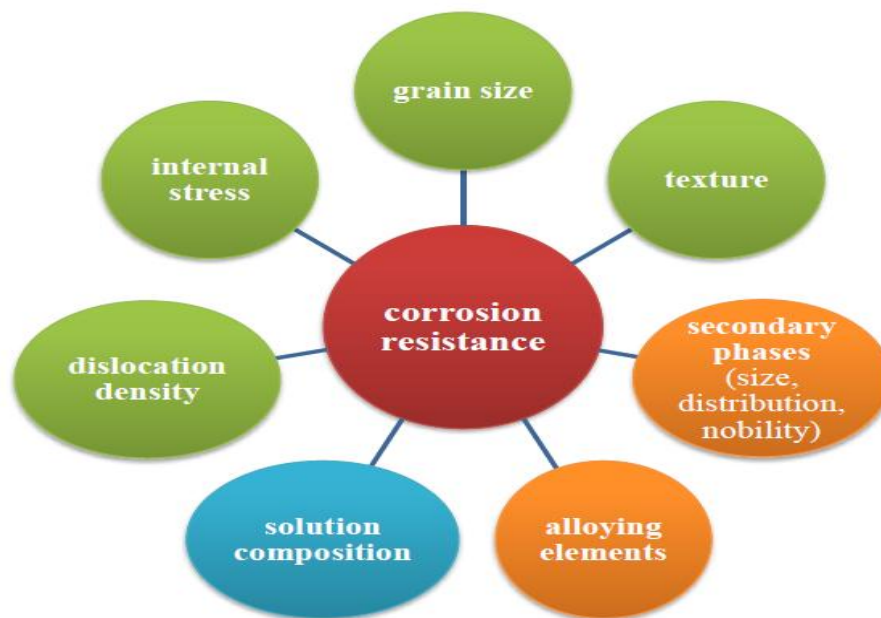


Figure 2.10. Schematic diagram of main factors affecting corrosion of the magnesium alloys (Song et al. 1999).

##### 2.6.4.1 Alloying elements and secondary particles

Pure magnesium exhibits several undesirable properties that are partially suppressed by alloying elements in magnesium alloys. After exceeding the solubility limit, secondary phases, in the magnesium matrix, helps to improve strength and creep resistance. Alloying elements of Fe, Ni, Co and Cu are typical examples because of their low solid-solubility limits in the matrix and creating such cathodic sites (Merino et al. 2010). On the other hand, a beneficial effect of increased aluminum concentration on corrosion resistance was reported in Mg-Al alloys (Cao et al. 2013). Dissolution during the corrosion attack, favors aluminum enrichment on the metallic

surface and allows the formation of semi-protective Al-rich oxide layer which improves the corrosion resistance of the alloy.

#### **2.6.4.2 Dislocation density, twins and internal stress**

Dislocation density, twins and residual internal stress are direct consequences of thermomechanical processing. While the crystal defects are a potential initiation location for the corrosion process, dislocation density and twins directly affect the severity of the initial corrosion attack. Severe plastic deformation resulted in a complete dynamic recrystallization connected with a decrease of the internal residual stress and the intragranular dislocation density. This lowered the localized corrosion and corrosion layer cracking and therefore contributed to the decrease of the overall corrosion rate (Heintzenberg, 1989).

#### **2.6.4.3 Grain size**

Altering the microstructure can have a direct effect, not only on the physical and mechanical properties of the alloy, but also on its corrosion performance. Grain refinement in materials is often performed by thermomechanical processing that alters the microstructure and it is reported with a positive effect on corrosion resistance. The size of the grains in Mg alloys has been reported to affect the corrosion behaviour, with a decrease in grain size causing a decrease in corrosion rate (Ralston and Birbilis, 2010). This has been shown to be the trend in many Mg alloys such as AZ31, AZ91, ZK60 and rare earth containing systems (Argade et al. 2012). It has been suggested that the beneficial effect of reducing grain size arises from the formation of a better passive layer (Liao et al. 2012), an improvement in the protection capabilities of the  $\beta$ -phase network (Song et al. 1999). Conflictingly, there are reports that a decrease in grain size leads to an increase in corrosion rate (Kutniy et al. 2009).

### **2.7 Aluminium and aluminium alloys**

Aluminium is the world's most abundant metal and is the third most common element, comprising 8% of the earth's crust. The versatility of aluminium makes it the

most widely used metal after steel. Pure aluminium is soft, ductile and corrosion resistant and has a high electrical conductivity. It is widely used for foil and conductor cables, but alloying with other elements is necessary to provide the higher strengths needed for other applications like transport, food preparation, energy generation, packaging, architecture, and electrical transmission (Sverdlin, 2003). Typical alloying elements are copper, magnesium, manganese, silicon, tin and zinc. There are two principal classifications, namely cast alloys and wrought alloys, both of which are further subdivided into the categories heat-treatable and non-heat-treatable. About 85% of aluminium is used for wrought products, for example rolled plate, foils and extrusions. Cast aluminium alloys are generally has lower tensile strengths than wrought alloys. Aluminium alloys are widely used in engineering structures and components where light weight and corrosion resistance is required. For wrought Al alloys, in these designation systems the first series are written in the form of 1xxx and has no major alloying elements. Other system like 2xxx, 3xxx, 4xxx, 5xxx, 6xxx and 7xxx, each of them has major alloying elements like copper, manganese, magnesium and silicon and Zinc respectively. For 7xxx series of Al alloy, Zinc is the main alloying element. Addition of Zinc with magnesium has improved the strength through precipitation of  $\eta$  phase and improve corrosion resistance.

### **2.7.1 Aluminium-7075 alloy**

Aluminium 7075 is an aluminium alloy, with zinc as the primary alloying element. This is one of the highest strength aluminum alloys and its strength-to weight ratio is excellent and it is ideally used for highly stressed parts (Hidalgo et al. 2012). It may be formed in the annealed condition and subsequently heat treated. Al-7075 was developed by Japanese company Sumitomo Metal in 1936. 7xxx series Al alloys based on the ternary Al-Zn-Mg or the quaternary Al-Zn-Mg-Cu alloying systems have long been regarded as some of the best candidates for the demanding structural applications in the aerospace and automotive industries due to their high strength-to-density ratio with moderate toughness and corrosion resistance (Starke et al 1996).

### 2.7.2 Mechanical properties of Al alloys

Generally mechanical properties of the aluminium alloys can be improved through a process of solid solution hardening, grain boundary hardening, strain or work hardening and precipitation hardening (Katgerman et al. 2003). Solid solution strengthening is due to different atomic sizes of solute and solvent atoms. It causes mismatch and induce elastic interaction between strain fields of the solute atoms and dislocations present in the lattice. The solute atoms hinder dislocation motion thereby attributed to solid solution strengthening. In grain boundary strengthening mechanism, grain boundaries acts as barrier to dislocation. Hall and Petch have shown that grain size plays a major role in the deformation and strengthening the alloys. In strain hardening strengthening mechanism, dislocation density increases due to dislocation interaction (Hertzberg, 1996). The common way to achieve the strain hardening is by applying plastic deformation to the alloys. In the precipitation hardening process, solute concentration in the alloys exceeds the limit of solubility. The strength of the alloys improved by precipitation hardening process, which depends on several factors such as time, alloying element, temperature of the precipitation heat treatment (Maurice and Courtney, 1990).

### 2.7.3 Corrosion in aluminum

Aluminum generally has excellent resistance to corrosion in natural atmospheres, fresh water, seawater, many soils and chemicals.

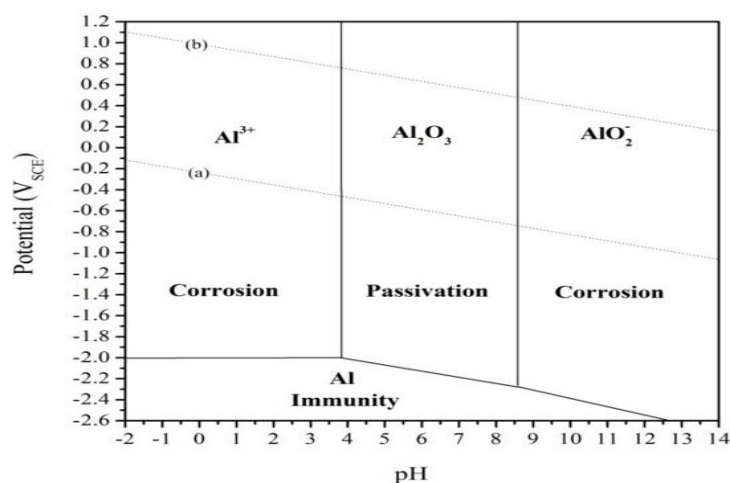


Figure 2.11. Pourbaix diagram of Al in water.

Aluminum has its excellent corrosion resistance to the barrier, oxide film that is bonded strongly to its surface. The conditions for thermodynamic stability of the oxide film are expressed by the Pourbaix diagram as shown in figure 2.11. Aluminum is passive in the pH range of about 4 to 8.5. Electrode potential of aluminum with respect to other metals becomes particularly important when considering galvanic effects arising from dissimilar metal contact. Electrode potentials of Al ranges from - 0.69 V to - 0.99 V and Mg has an electrode potential of - 1.73 V.

## **2.8 Effect of intermetallics formation during ARB on mechanical properties**

Liu et al. (2006) investigated microstructure and phase constituents in the interface zone of Mg/Al diffusion bonding. Diffusion zone of the Mg/Al diffusion-bonded joint consists of three intermetallic compounds MgAl, Mg<sub>3</sub>Al<sub>2</sub>, and Mg<sub>2</sub>Al<sub>3</sub> were found in the X-ray diffraction analysis. Fracture morphology of the Mg/Al diffusion-bonded joint mainly consists of coarse and gray fracture, and the fracture is mainly the mixed fracture of cleavage and intergranular. Microhardness of the diffusion zone is higher than that of the Mg and Al substrate found to be 260 HV to 350 HV depending on the location in the diffusion zone and also exhibited good strength and toughness.

Chen et al. (2007) fabricated Al/Mg composite by accumulative roll-bonding process up to five pass, successfully and investigated diffusion and formation of intermetallic compounds. Two intermetallic phases Al<sub>3</sub>Mg<sub>2</sub> and Al<sub>12</sub>Mg<sub>17</sub> were found after four ARB cycle. Thickness of the diffusion zone after four cycles of the ARB process without annealing and after annealing found to be 4.5 μm and 25 μm respectively.

Zhang et al. (2011) developed hot-rolled Al-7075 /AZ31B/Al-7075 laminated composite and investigated microstructure, bonding strength of the composite and found equiaxed grains due to dynamic recrystallization. Grain size depends on rolling temperature and reduction ratio. Diffusion layer existed in the interface, and the diffusion layer width increased with rolling temperature and reduction ratio. Composites rolled at 400 °C with 60% reduction exhibited maximal bonding strength of 66 MPa.

Chang et al. (2012) studied microstructure and mechanical properties of accumulative roll bonded Mg/Al multilayered composite at ambient temperature. During ARB



process, due to high strain,  $Mg_{17}Al_{12}$  intermetallic layer with the thickness of 150 nm, is formed at the Mg/Al interface due to the inter-diffusion between the Mg and Al layers. The layer thickness of the multilayered composite decreases with increase in the number of ARB passes, consequently the grain size also decreased. Yield strength and ultimate tensile strength, along both rolling and transverse direction, increased, but elongation, along both directions, decreased with increasing of the ARB cycles.

Liu et al. (2012) fabricated Al/ $Al_3Mg_2$  laminated composites by roll-bonding using Al-1060 and AZ31 foils. Developed laminated composites were annealed in vacuum at 400 °C for 6 h. Uniform distribution of  $Al_3Mg_2$  phase in the Al matrix was observed after six cycle of the warm roll bonding process. Strength and ductility of the composite was increases with increase in the number of ARB cycles. Tensile strength was found to be 168 MPa which was significantly higher than that of the annealed and ARB monolithic Al-1060 alloy.

## **2.9 Effect of grain refinement by ARB on mechanical and corrosion properties of multilayered composites**

Chen et al. (2006) fabricated composite by accumulative roll bonding process using pure aluminum (A1100) and magnesium alloy (AZ31) and investigated microstructures and mechanical properties. Bonding condition gradually improved from one to three ARB cycles. Multilayered composite exhibited ultra fine grain structure with a grain size of 875 nm and 656 nm after three cycles in the Al and Mg alloys respectively. Hardness of the both Al and Mg layers of the multilayered composite layer is increases with increase in the strain and reached up to HV42 and HV90 respectively.

Ralston and Birbilis, (2010) reviewed the effect of grain sizes on corrosion resistance. Processing or grain refinement that alters the reactivity of a surface will impact the corrosion response. Grain refinement appears to increase the corrosion resistance of Mg alloys. This effect is not consistent, cause both increased and decreased corrosion susceptibility, depending on processing conditions and environment. Primary reason for improvements in corrosion resistance for UFG materials is attributed to an

improvement in passive film formation and adhesion due to increased grain boundary density.

Orlov et al. (2011) investigated corrosion behavior of ZK60 alloy after processing by integrated extrusion and equal channel angular pressing. Processed ZK60 alloy exhibited refined microstructure consequently enhanced strength and a reduced corrosion rate. With regard to the role of grain refinement, it appears that grain refinement had the greatest effect upon anodic reaction kinetics, while chemical effects had a greater impact on cathodic reaction kinetics. Combination of grain refinement and solute redistribution produced the material with superior mechanical and corrosion properties relative to the initial material.

Argade et al. (2012) investigated the effect of grain size on the corrosion resistance of wrought magnesium alloys containing neodymium. Friction stir processing is used to refine grains of the Mg–Y–RE alloy and it lead to good corrosion resistance. UFG microstructure showed highest polarization resistance, repassivation potentials and the most positive pitting potentials as compared to coarse grain microstructure. During constant immersion testing, a clear relationship between grain size and corrosion rate is obtained and reported that UFG samples exhibits lowest corrosion rate and coarse grain samples exhibits highest corrosion rates.

Liao et al. (2012) compared the corrosion behavior of fine-grained AZ31B alloys, coarse grained hot-extruded AZ31B and AM60 alloys. Corrosion behaviors of the samples were investigated using cyclic neutral-salt spray test and electrochemical analysis in a 0.1 M NaCl solution. Passive oxide film was formed on the surface of these magnesium alloys and the passivity depended on chemical compositions and grain size. Corrosion rate of AZ31B alloy obtained from immersion test had a linear relationship with reciprocal square root of average grain size ( $d^{-1/2}$ ). The corrosion resistance of AZ31B alloy tends to increase, as grain size is reduced and is attributed to the enhanced passivity of surface oxide film.

Roy et al. (2012) carried out accumulate roll bonding of AA5086 alloy up to 8 passes and investigated the mechanical properties and also correlated with the corresponding microstructure and texture. Average grain size was found to be 200-300 nm and strength of the material improved due to grain refinement and strain hardening

process during ARB. Mechanical behavior is highly anisotropic in nature because of strong texture after ARB.

Kadkhodae et al. (2013) developed nanocomposite using Al1050 and nanosilica by ARB process and evaluated corrosion properties. Corrosion properties of the produced sheets with and without the nanoparticles were investigated and compared to the aluminum sheet. In UFG microstructures, the grain boundaries were not the active sites than the grains, it causes to the formation of more uniform and denser passive oxide layers on the specimens.

### **2.10 Effect of combined anodization and ARB on mechanical and corrosion properties multilayered composite**

Jamaati, and Toroghinejad, (2010) developed high strength composite by anodizing and accumulative roll bonding process. Alumina particle size reduces and the distribution of alumina particles in aluminum matrix become uniform with the increase in ARB cycles. Developed Al/3.55 vol.%  $Al_2O_3$  composites exhibited 3.5 times higher tensile strength, as compared annealed aluminum. If the quantity of the alumina particle increased in the composite, tensile strength increased and elongation decreased.

Ahmadi et al. (2014) developed Al/ $Al_2O_3$ /SiC hybrid composites fabricated by accumulative roll bonding process and evaluate the microstructure and mechanical properties. Uniformity of particles in the aluminum matrix and bonding quality between reinforcement particles and aluminum matrix were improved with the increase in ARB cycles. Tensile strength of Al/1.6 vol.%  $Al_2O_3$ /1 vol.% SiC composite was 3.1 times higher than that of the as-received, annealed aluminum.

Toroghinejad et al. (2014 a) investigated the effect of alumina content on the mechanical properties of hybrid composites fabricated by ARB process. Hybrid composite has homogeneous distribution and a good bonding between the particles and the matrix without any porosity after tenth ARB cycle. Tensile strength of the ARB-processed hybrid composites with 0.3, 1.0, and 1.6 vol%  $Al_2O_3$  was about 200 MPa, 242 MPa and 281 MPa which is 2.2 times, 2.7 times and 3.1 times, respectively higher than that of the annealed sample. ARB-processed hybrid composites exhibited

a higher hardness than the annealed sample and with increasing the alumina content in the aluminum matrix, the hardness of hybrid composites was increased.

Toroghinejad et al. (2014 b) fabricated hybrid composites using commercial aluminum sheets and 1.5% vol B<sub>4</sub>C particles by anodizing and accumulative roll bonding process. With increasing the number of ARB cycles, better distribution of Al<sub>2</sub>O<sub>3</sub> and B<sub>4</sub>C particles was obtained in the aluminum matrix. ARB processed hybrid composite showed 3.07 times higher strength and hardness values 2.55 times higher than those of the annealed sample. Hybrid composite exhibited a shear ductile fracture and had dimples and shear zones.

### **2.11 Effect of cerium (rare earth element) on mechanical and corrosion properties ARB processed multilayered composite**

Ma et al. (2003) investigated the tensile properties of extruded ZK60/RE alloys, found that UTS and YS strength and yield strength improved by the addition of cerium-rich misch metal. Also, UTS and YS decreased with increasing extrusion temperature. Improvement of tensile properties of ZK60/RE alloys is due to the extrusion texture and the fine microstructure induced by cerium-rich misch metal additions.

Chino et al. (2008) investigated compressive properties of Mg–0.2 mass% (0.035 at.%) Ce alloy at room temperature and understood the effects of Ce on deformation mechanisms at 773 K. Addition of 0.035 at.% Ce strongly affected the mechanical properties of Mg. Unique behavior of the Mg-Ce alloy was related to homogeneous deformation due to non-basal slips and addition of Ce responsible for the improvement of ductility at room temperature. On the other hand, Mg-Ce alloy exhibited higher flow stress and poorer ductility at 573 K, due to the suppression of dynamic recrystallization and the low diffusion due to Ce addition.

Mishra et al. (2008) investigated the effect of cerium on the texture and ductility of magnesium extrusions and found significantly enhanced the ductility of Mg. 0.2 % Ce addition favors the formation of recrystallized grains with their basal planes, oriented at 40-50° to the extrusion axis compared to extruded Mg where a majority of the grains were oriented with their basal planes parallel to the extrusion axis. Twinning and slip activities occurred in the Mg-Ce sample, but twinning dominates Mg

deformation. Addition of Ce helps to reduce the yield strength, refines the grain size and leads to a substantial increase in work hardening rate. Mg-0.2 Ce alloy exhibits a dimple structure as a result of slip accumulation and ductile tear.

Yan et al. (2016) investigated the microstructures and electrochemical corrosion properties of Mg-Al-Pb and Mg-Al-Pb-Ce anode materials. Addition of Ce to Mg-Al-Pb alloy refines the grain structure and promotes the formation of  $\text{Al}_{11}\text{Ce}_3$  phase, which leads to reduced grains size and uniform distribution of  $\text{Mg}_{17}\text{Al}_{12}$  phase. Corrosion current density and hydrogen evolution rate of Mg-Al-Pb-Ce alloy are larger than Mg-Al-Pb alloy and the discharge activity of Mg-Al-Pb-Ce alloy at  $180 \text{ mA/cm}^2$  is improved because of the refined grain and the increasing amount of cathodic secondary phases.

## **2.12 Research gap from literature survey**

A very meagre information is available in the literature about the ARB processed Mg/Al multilayered composites. Only few studies have also dedicated to the microstructure and mechanical properties of composite produced by accumulative roll bonding process. It is at most important to develop ultrafine grained Mg based composites having high strength along with good corrosion resistance for structural applications.

In that aspect, present research work focuses on the development of Mg-Zn/Al multilayered composite produced by ARB process. The process involved the development of Mg-(2-6%)Zn alloys, anodization of Al-1100 and Al-7075 alloys, uniform distribution of Ce powder in between the bonding materials and finally accumulative roll bonding of different combination of multilayered hybrid composites having ultrafine grain structure. Composites are characterized with respect to microstructural, mechanical properties and corrosion behaviour.

## **2.13 Objectives of the present study**

Looking at the ongoing developments in the area of wrought magnesium alloys, and improving mechanical properties and corrosion resistance, the following broad objectives have been derived.

1. To develop ultrafine grained multilayered composite material system by accumulative roll bonding of Mg-Zn binary alloy (2, 4, 6% Zn) with following materials.
  - i. Al-1100
  - ii. Anodized Al-1100
  - iii. Al-7075 alloy
  - iv. Anodized Al-7075 alloy
  - v. Al-1100 and reinforcement of Cerium powder
2. To characterize roll bonded composites with respect to microstructure, physical and mechanical properties.
3. To elucidate corrosion behavior of accumulative roll bonded Mg-Zn/Al multilayered composite.
4. To understand the relation between microstructure, mechanical properties and corrosion resistance.

## CHAPTER 3

### EXPERIMENTAL PROCEDURE

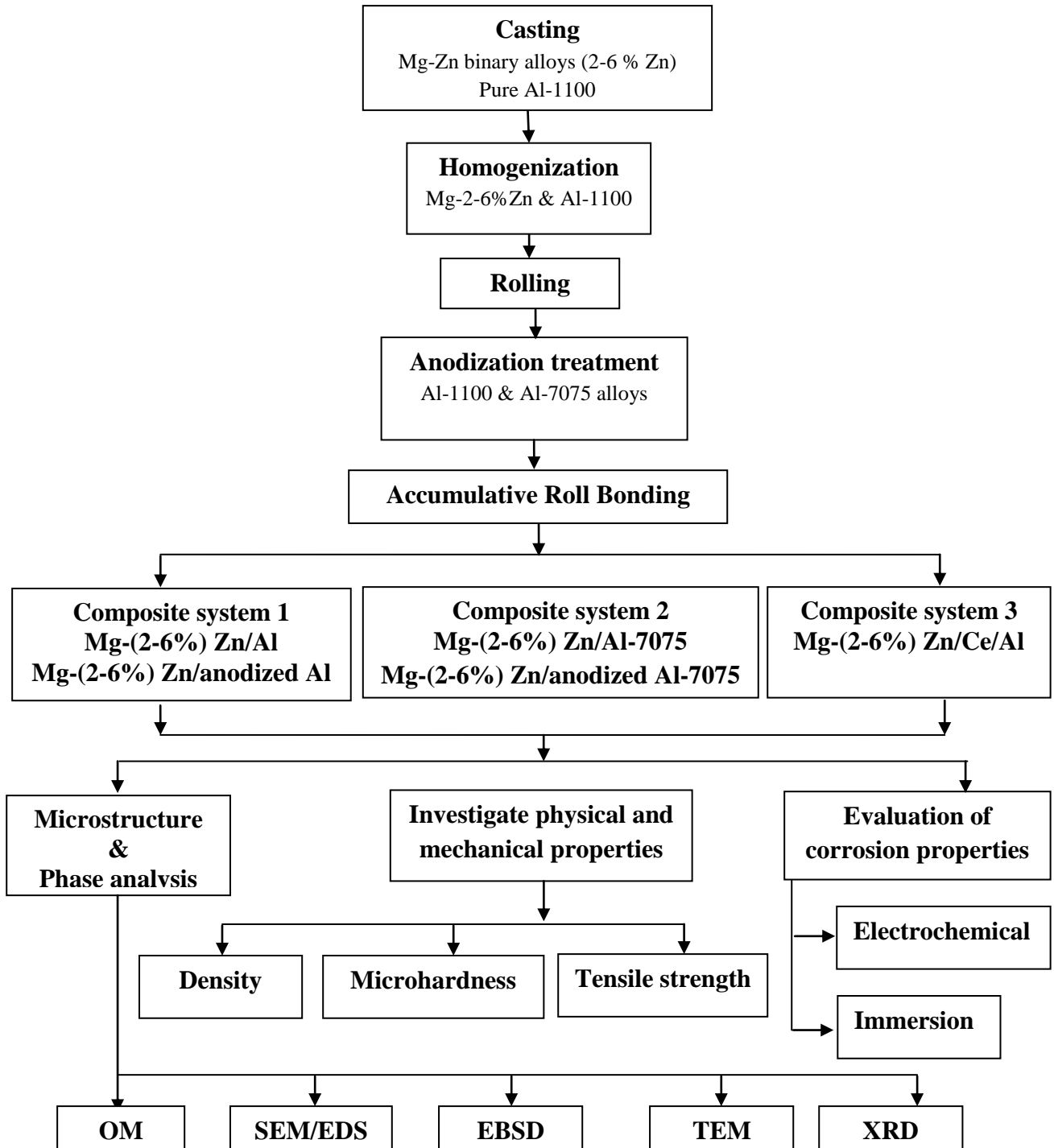


Figure 3.1. Over view of the research program of present thesis

Procedure adopted for preparing different multilayered composite system, description of equipment and the various characterization techniques used for analysis of microstructure, mechanical properties, and corrosion behavior are presented in this chapter.

### 3.1 Material preparation

#### 3.1.1 Casting of Mg-(2-6%)Zn binary alloys

Mg–Zn binary alloys with varying percentages of Zn (2, 4 and 6 wt.%) were cast using high purity magnesium ( $\geq 99.9$  wt.%) ingots and zinc ( $\geq 99.9$  wt.%). Initially Mg is melted at 750–800 °C under control of 99% CO<sub>2</sub> in an electrical resistance furnace. Zinc was added in to the molten Mg and mechanical agitation was carried out throughout the process to minimize the impurities in molten alloy. The alloy ingot was produced using steel mould. The cast Mg-Zn binary alloy were homogenized at about 400 °C for 24 h in the tubular furnace. During the homogenization treatment, intermetallic phases present in the alloys gets dissolved and the alloy is compositionally homogenized. Al-1100, Al-7075 alloy, and cerium power (purity 99.9%, size 40 mesh) were procured. Chemical compositions of cast alloys were determined using chemical spectroscopy and obtained results are indicated in Table 3.1.

Table 3.1. Chemical composition of the alloys

Alloys	Composition (Wt %)							
	Mg	Zn	Al	Cu	Cr	Fe	Si	Mn
Mg-2%Zn alloy	Bal	2.08	-	-	-	-	-	-
Mg-4%Zn alloy	Bal	4.23	-	-	-	-	-	-
Mg-6%Zn alloy	Bal	6.18	-	-	-	-	-	-
Al-1100 alloy	-	0.05	Bal	0.12	-	0.38	0.45	0.02
Al-7075 alloy	2.0	4.98	Bal	1.27	0.128	0.27	0.06	0.02

### 3.2 Rolling

Homogenized Mg-(2-6%) Zn alloys and Al-1100 slabs with the dimensions of 40 mm × 30 mm × 10 mm thick were cut from the cast ingot. The samples were heated in the



tubular furnace at 300 °C for 10 min. The schematic illustration of the rolling machine is shown in figure 3.2.



Figure 3.2. Rolling machine.

During conventional rolling, percentage reduction, temperature and heating time is very important, in order to avoid cracks during rolling due to accumulative strain in the material. The heated samples were rolled with a reduction of 0.25mm per pass in a laboratory rolling mill of diameter 65 mm at 30 rpm in order to reduce the sample size to 1 mm thick, suitable for ARB. Strain ( $\epsilon_i$ ) accumulated during rolling from a thickness of 10 mm to a thickness of 1 mm is given by the equation

$$\epsilon_i = \ln \left( \frac{t_i}{t_o} \right) \dots \dots \dots (3.1)$$

Where,

$t_i$  = Initial thickness of the sample.

$t_o$  = Final thickness of the sample.

The cumulative strain after rolling process (reduction of the sample thickness from 10 mm to 1 mm) found to be 2.3.

### 3.3 Anodization treatment

Al-1100 and Al-7075 alloys were anodized before ARB process. Cleaning was carried out before anodization treatment using NaOH solution and followed by immersion in HNO<sub>3</sub> solution. Anodization equipment is shown in figure 3.3.

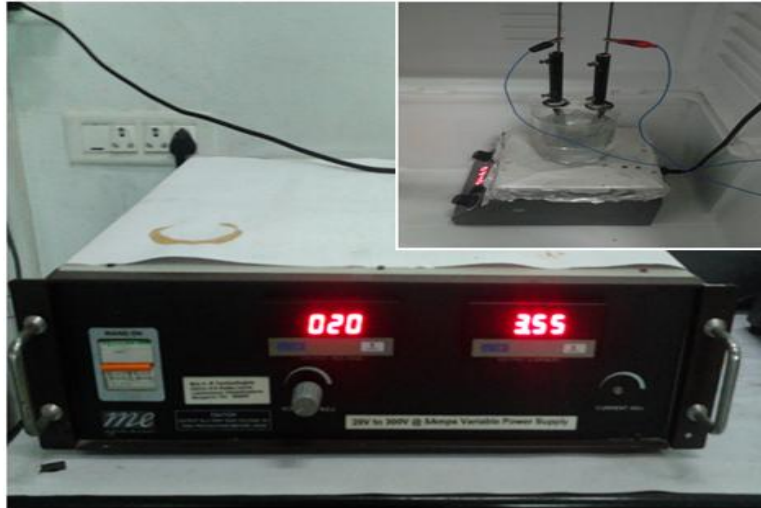


Figure 3.3. Anodization equipment.

Anodizing treatment was done in electrolyte bath containing 15 % H<sub>2</sub>SO<sub>4</sub> solution with operating potential of 16 V at 3.5 A for 60 min at 18 °C under forced circulation for the period of one hour, in order to obtain uniform aluminium oxide film. Anodized samples were rinsed in deionized water and dried in air. Thickness of the alumina layer was measured using scanning electron microscopy (SEM) and found to be  $10 \pm 0.2 \mu\text{m}$ .

### 3.4 Preparation of Mg/Al sandwich composite

Rolled Mg-(2-6%) Zn binary alloys, Al-1100 and Al-7075 alloy with the dimension of 40 mm × 30 mm × 1 mm sheets were cleaned using steel wire-brush followed by acetone cleaning to remove the dirt grease, oils etc. Mg-Zn alloy and Al sheets were stacked by the sequence of Mg-Al alternatively to produce a sandwich multilayered composite. Stacked samples were heated at 300 °C for 10 min before being subjected to ARB process.

### 3.5 Accumulative roll bonding

ARB is a type of severe plastic deformation technique to develop ultra-fine grains. It involves rolling of sheets repeatedly. Two sheets that are rolled are wire brushed to provide rough surface and cleaned by acetone to make dust free surfaces. Samples that are prepared are stacked together heated, and rolled to form a single sheet of thickness equal to the thickness of sample before rolling. The obtained sheet is ARB - 1 pass sheet. The amount of reduction given is 50%. The ARB 1 pass sample is cut in to 2 half, are cleaned, stacked together heated and rolled to obtain ARB 2 pass sample. This process is continued to obtain as many layers as required. The number of layers in the multilayered samples is given by  $2^n$ , where n is the number of ARB passes. The schematic representation of ARB process is shown in figure 3.4.

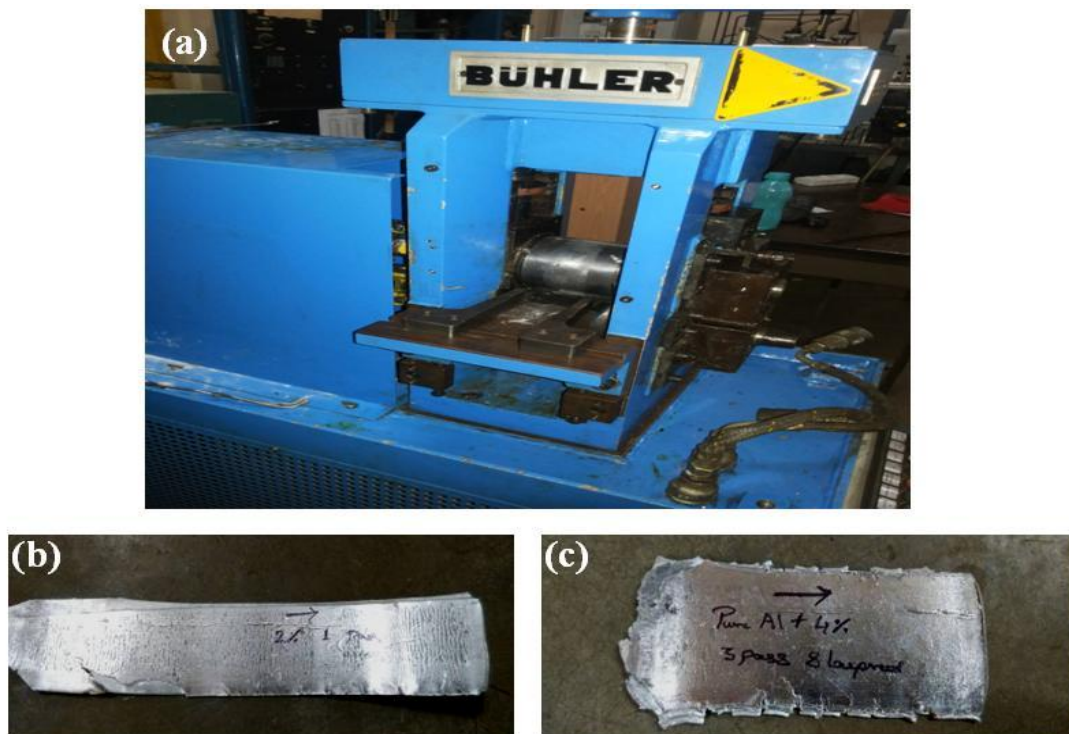


Figure 3.4. (a) Rolling mill (b&c) Multilayered composite sample.

Two high rolling mills (Buhler's Germany) having the diameter of the rolls being 110 mm was used for ARB process. Before ARB process, rolls are cleaned and the thickness of the samples before and after the rolling operations is measured using a digital micrometer. A steel wire brush is used for roughening and cleaning the surface of the samples. The electric tubular furnace is used for heating the samples to the

temperature below recrystallization. Stacked samples are rolled with 50% reduction. The resulting sample is termed as one pass ARB sample and make in to two equal halves and heated further for 10 min for second ARB pass and procedure repeated till the materials sustain the applied load.

The total cumulative strain of the ARB processed multilayered composite was calculated according to the following equations (for 50% reduction per pass)

$$\varepsilon = 2 / \sqrt{3} \ln \left\{ \frac{1}{2^n} \right\} \dots\dots\dots(3.2)$$

Cumulative strain accumulated in the roll bonded sample can be given by

$$\varepsilon_{cum} = \varepsilon_i + \varepsilon = 2.3 + 2 / \sqrt{3} \ln \left\{ \frac{1}{2^n} \right\} \dots\dots\dots(3.3)$$

In the present work, following procedure and parameters was adopted for different composite systems, are illustrated in table 3.2.

Table 3.2. Composite systems and ARB parameters.

Sl. No	Composite systems	Temp	Heating Time	Number of pass	% reduction
1	Mg-(2-6%)Zn/Al Mg-(2-6%)Zn/anodized Al	300 °C	10 min	5	50 %
2	Mg-(2-6%)Zn/Al-7075 Mg-(2-6%)Zn/anodized Al-7075	350 °C	10 min	4	50 %
3	Mg-(2-6%)Zn/Ce/Al	300 °C	10 min	5	50 %

### 3.6 Microstructural characterization

Study of the material behavior is very much essential in metallurgical and material science because the crystallographic structure defines the properties of the material. Microstructural analysis was done for cast, rolled and ARB processed samples to study the dimensional changes, bonding quality and grain refinement. All the samples

were sectioned along the normal to the rolling direction. Metallographic specimens were cold mounted with the help of acrylic powder and resins. The specimens were polished up to 2000 grit SiC paper and final polishing was done with the help of cloth using 0.25  $\mu\text{m}$  diamond paste. For microstructure analysis, chemical etching was performed in order to visualize grain boundaries. Polished samples were etched with acetic-picral solution (4.2 gm picric acid, 70 ml ethanol, 20 ml glacial acetic acid and 20 ml distilled water) solution and then dried in hot air. The following characterization techniques were used for observing the microstructures and evaluate the size of the grains and its orientation.

- Optical Microscope (OM)
- Scanning Electron Microscopy (SEM)
- Electron Backscattered Diffraction (EBSD)
- Transmission Electron Microscopy (TEM)

### 3.6.1 Optical microscope (OM)

Microstructure of the as cast, rolled and ARB processed composite samples were characterized by using image analyzer inbuilt with a software (BIOVIS materials plus) designed mainly for physical and metallographic applications. The optical microscope is as shown in figure 3.5. Grain size measurements are done using liner intercept method.

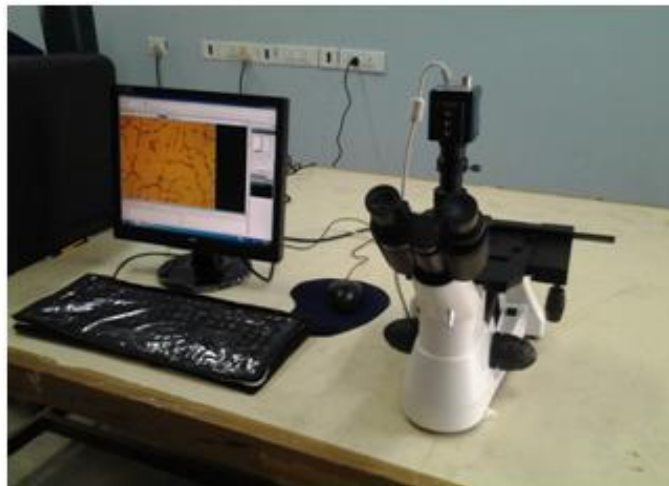


Figure 3.5. Optical microscope.

### 3.6.2 Scanning electron microscope (SEM)

Scanning electron microscope makes use of interactions between a high energy electron beam and a specimen to obtain topographic and microstructural information from the specimen. When an accelerated beam of electrons is impinged upon the prepared surface of the specimen, a variety of signals are produced. Secondary electrons are generally used for imaging and observation of topographical features on the surface.



Figure 3.6. Scanning electron microscope.

In the present study, microstructural characterization was done using scanning electron microscope (SEM) (JEOL JSM- 6380LA; USA) (Figure 3.6) with energy dispersive spectrometer (EDS), can provide to gives the additional quantitative and qualitative elemental composition. It is mainly used for microstructural characterization.

### 3.6.3 Field emission scanning electron microscope (FESEM)

Diffraction of the backscattered electrons can be used for investigating the local misorientations by using the EBSD (Electron Back-Scatter Diffraction) technique. Oxford Instruments ‘Nordlys’ detector, attached to field emission scanning electron microscope (JEOL JSM-7100F; USA), has been used in this work to investigate

misorientations and to obtain grain boundary maps on ARB processed multilayered composites as shown in figure 3.7.



Figure 3.7. Field emission scanning electron microscope.

For EBSD analysis, samples were cut along the RD-ND plane and electro-polished in Struers' AC2 electrolyte at 16 V for 60 sec at -25 °C. Obtained EBSD results were analyzed using HKL Channel 5 software.

### 3.6.4 Transmission electron microscope (TEM)

TEM basically uses a focused beam of electrons accelerated to a high potential to probe an electron transparent specimen i.e a sample that is thin enough to transmit electrons through it.



Figure 3.8. Transmission electron microscope (TEM).

Transmitted and diffracted electrons contain information about the crystal structure of the region being analyzed. Since precipitates have preferred orientations in the matrix, the sample may be tilted so that the electron beam impinges at specific angles, thus enabling better observation in different orientations. Transmission electron microscope (JEOL JEM-2100; USA) has been used in this work to observe microstructural features in the final pass of the ARB processed multilayered composites as shown in figure 3.8. ARB processed samples were cut along the RD-ND plane and samples were mechanically polished. Final thinning was performed by dimpling machine followed by ion beam milling.

### 3.7 X-ray diffraction (XRD)



Figure 3.9. X-ray diffraction.

X-ray Diffraction (XRD) has been used to find the crystal structures and phase analysis of the five pass ARB processed multilayered composites. In the present work, XRD analysis was carried out in rolling direction (RD) - transverse direction (TD) plane, so that all the layers of the multilayered composites are exposed to the X-ray analysis. XRD analysis (JEOL, JDX-@P-XRD; USA) (Figure 3.9) was carried out using the target of Cu  $k_{\alpha}$  with the angle range of  $30^{\circ} \leq 2\theta \leq 95^{\circ}$  in steps of  $2^{\circ}$ /minute.



### 3.8 Density

Density test was performed according to Archimedes principle on rolled alloys and accumulative roll bonded multilayered composite. Density tests works on the Archimedes principle, initially samples were weighed in air and the same samples weighed under water using physical weighing balance. Density of the samples was calculated by using equation 3.4.

$$Density = \frac{Mass\ in\ air}{(Mass\ in\ air - Mass\ in\ water)} * Specific\ gravity\ of\ water$$

.....(3.4)

### 3.9 Mechanical properties

In the present study, mechanical properties were evaluated for as rolled alloys and composites with different of ARB passes. Following tests were carried out for evaluating the mechanical properties.

- Vicker's microhardness
- Tensile test

#### 3.9.1 Microhardness

Hardness is defined as the ability of a material to resist permanent indentation when in contact with an indenter under load.

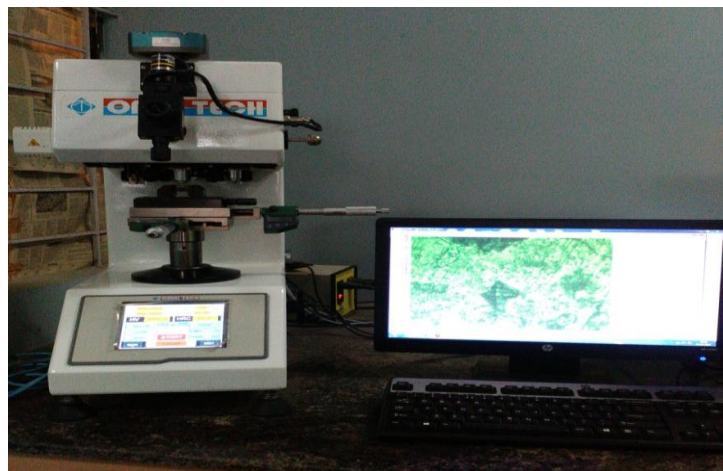


Figure 3.10. Microhardness testing machine.

Microhardness of the material determines to characterize the sample's hardness for as rolled alloys and composites with different passes of ARB. Layer-wise hardness in the ARB-processed composites was measured by micro-indentation up to the final pass and indentations were made on the transverse surfaces (RD–ND plane) using the Vickers's microhardness testing machine (Omni-tech, Maharashtra, India) is as shown in figure 3.10 Initially samples were polished and micro hardness of the samples was measured by imposing a load of 10 gm for dwell time 11 sec. A minimum of 10 indentations were taken throughout the surface to meet statistical reliability. The average microhardness was calculated and the error is expressed as the standard deviation of the total data set.

### 3.9.2 Tensile strength test

Tensile test was carried out using Tinius Olsen Tensometer (Noida, India) according to ASTM E8 M standard at room temperature (Figure 3.11).

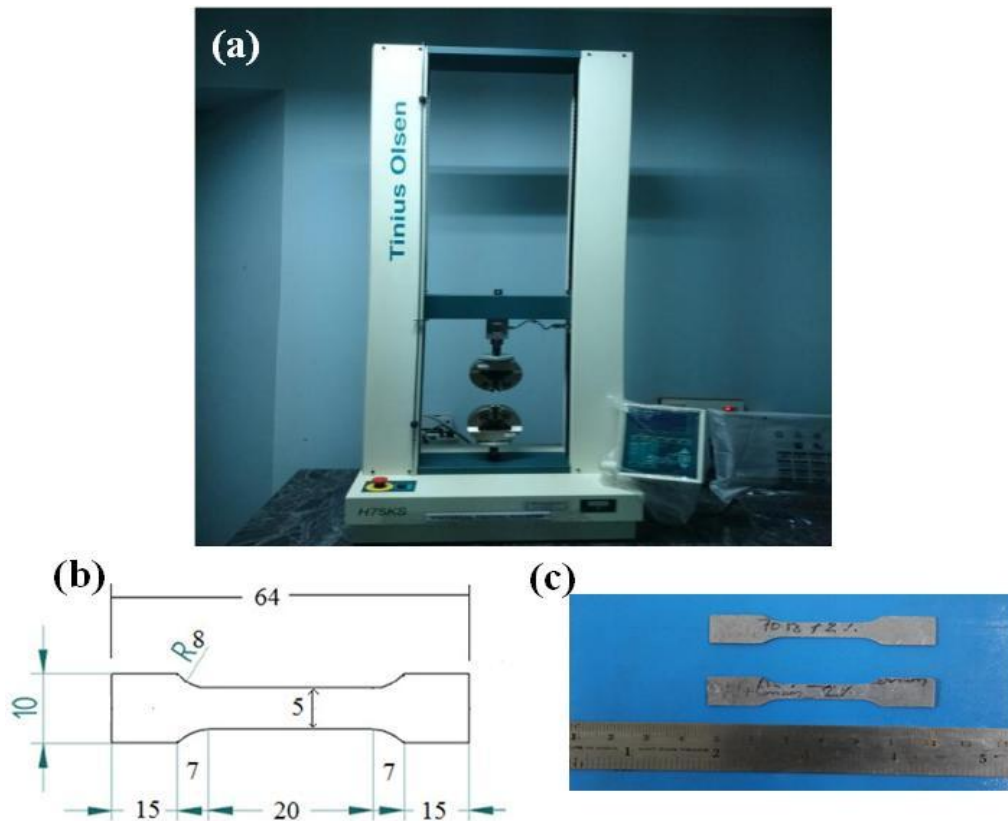


Figure 3.11.(a) Tensometer (b) ASTM-E8 standard tensile specimen dimensions (c) Tensile samples.

All the specimens were taken from middle of the sheet along the rolling direction. Following the standard, gage length, radius of fillet, length and width of the specimens were equal to 20, 7, 64 and 10 mm respectively. The thickness, width and gauge length of the each specimens were measured before and after the tensile test. Fractured surface was analyzed to investigate the type of fracture.

### 3.10 Corrosion behavior

#### 3.10.1 Electrochemical measurements

All the specimens used for electrochemical corrosion studies were mirror finished and properly cleaned. Electrochemical measurements were carried out using an electrochemical workstation as shown in figure 3.12 (EC lab-Biologic SP-150, France) with a standard three-electrode system containing a saturated calomel electrode (SCE) as reference electrode, a platinum wire as counter electrode, and the sample with 10 mm x 1 mm surface area, exposed to solution was used as working electrode. The aqueous solution of 0.1 M NaCl was prepared using NaCl in distilled water and the pH of solution was kept 7.5.



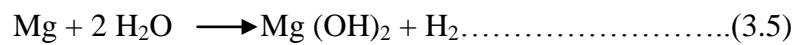
Figure 3.12. Electrochemical workstation.

Potentiodynamic polarization experiments were carried out at a scan rate of 1 mV/s. Cathodic and anodic portions of the generated Tafel plots were accordingly extrapolated to calculate the corrosion potential ( $E_{\text{corr}}$ ), corrosion current density ( $i_{\text{corr}}$ ) and corrosion rate. Surface morphology of composite were examined after

electrochemical corrosion tests with the help of SEM. Corrosion product was removed using 200 g/L of chromic acid and 10 g/L of AgNO<sub>3</sub> solutions.

### 3.10.2 Immersion corrosion

Immersion corrosion test was carried out according to ASTM G31-72. The weight loss or hydrogen evolution during immersion test is proportional to the corrosion rate of the materials. Based on the overall corrosion reaction (Eq. 3.5), 1 mol of magnesium corroded corresponds to 1 mol of hydrogen gas evolved. Hence, the measurement of hydrogen evolved is equivalent to measurement of the weight loss of the metal.



For the immersion study, multilayered composites were cut normal to the rolling direction and were fine polished. The samples were immersed in 0.1 M NaCl solution of pH 7.5 at room temperature for 120 h. Immersion study set up is shown in figure 3.13. Hydrogen evolution and pH of the solutions was recorded during immersion study. The corrosion rate was calculated using the following equations (Shi et al. 2010)

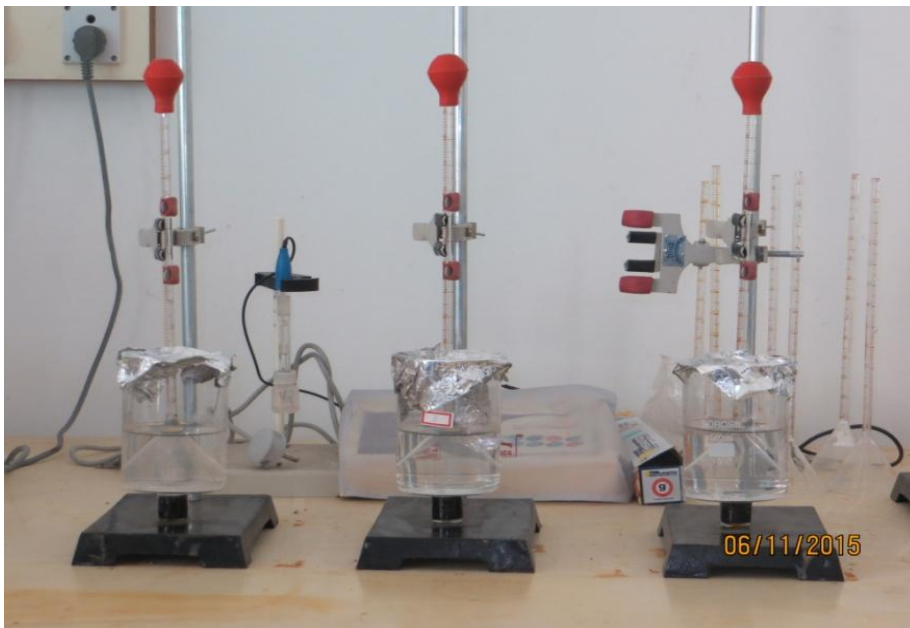


Figure 3.13. Immersion study equipment.

$$P_H = 3.65 \frac{\Delta w}{\rho} \dots\dots\dots(3.6)$$

where  $P_H$  = Corrosion rate through hydrogen evolution (mm/y)

$\rho$  = Metal density (g/cm<sup>3</sup>)

$\Delta w$  = Weight loss rate (mg/cm<sup>2</sup>/d)

One mol (24.31 g) of Mg metal corroded for each mol (22.4 L) of hydrogen gas produced. Therefore, the hydrogen evolution rate,  $V_H$  (ml/cm<sup>2</sup>/d), is related to the metallic weight loss rate is given by

$$\Delta w = 1.085V_H \dots\dots\dots(3.7)$$

where  $V_H$  = Hydrogen evolution rate (ml/cm<sup>2</sup>/d)

## CHAPTER 4

### RESULTS AND DISCUSSION

Results obtained from different multilayered composite systems are presented and discussed in this chapter. As the main objective of the present work is to establish a qualitative relationship between the microstructural evolution of ARB process and their effect on mechanical and corrosion properties.

#### 4.1 Microstructural analysis of as cast alloys

##### 4.1.1 Optical microstructure of Mg-Zn alloy

Microstructure analysis of the Mg-Zn binary alloys with varying percentage of Zn (2-6 wt.%) were carried out using optical microscope.

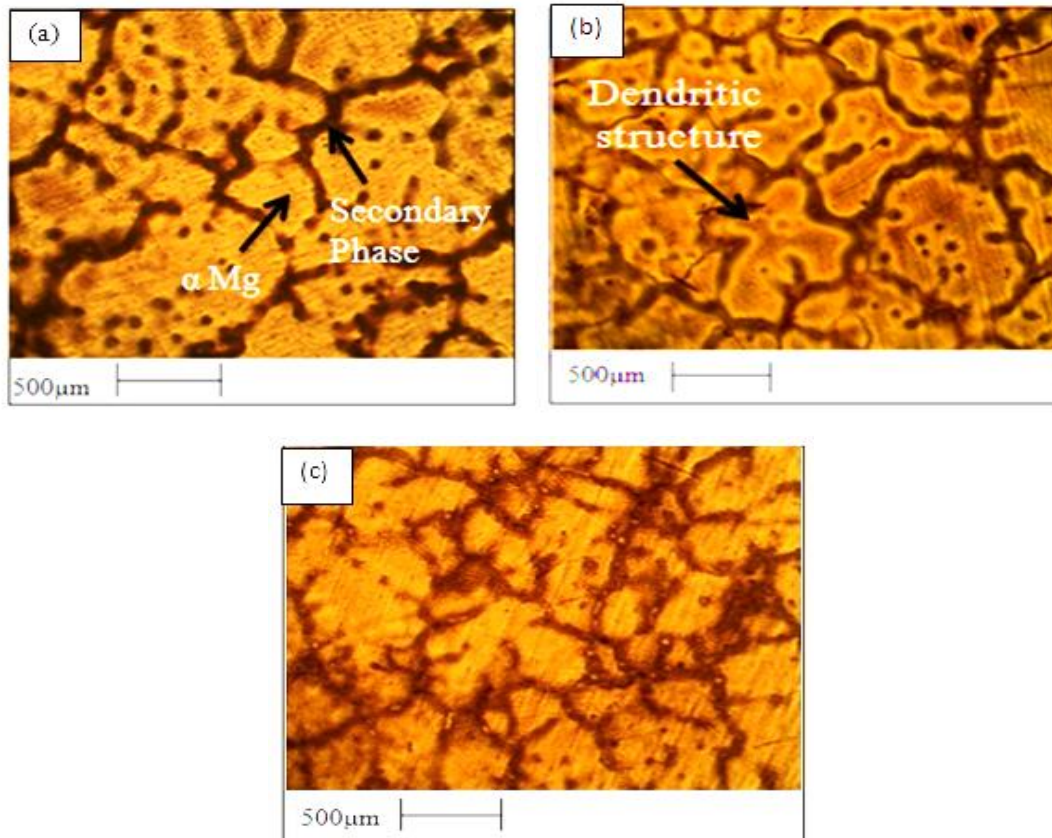


Figure 4.1. Optical microstructure of cast Mg-Zn alloys (a) Mg-2%Zn (b) Mg-4%Zn and (c) Mg-6%Zn.

As-cast Mg-Zn alloys consist of primary  $\alpha$ -Mg phase and secondary phase ( $\beta$  phases), mainly distributed along grain boundaries (Cai et al. 2012). Microstructures revealed that, presence of Zn increases the dendritic regions, as well as network of secondary phases ( $\beta$  phase) along the grain boundary of the alloy. Grain size of Mg-2%Zn, Mg-4%Zn and Mg-6%Zn alloys was calculated using linear intercept method and is found to be 630  $\mu\text{m}$ , 580  $\mu\text{m}$  and 510  $\mu\text{m}$  respectively. It is clearly showed that the grain size decreased with increasing Zn content in alloy. Similar results are discussed by Cai et al. 2012; Koc et al. 2015 for Mg-Zn alloys.

#### 4.1.1.2 SEM and EDS analysis of Mg-Zn alloys

Figure 4.2 shows the SEM images of ascast Mg-Zn alloys of varying percentages of Zn with corresponding EDS graph and elemental composition.

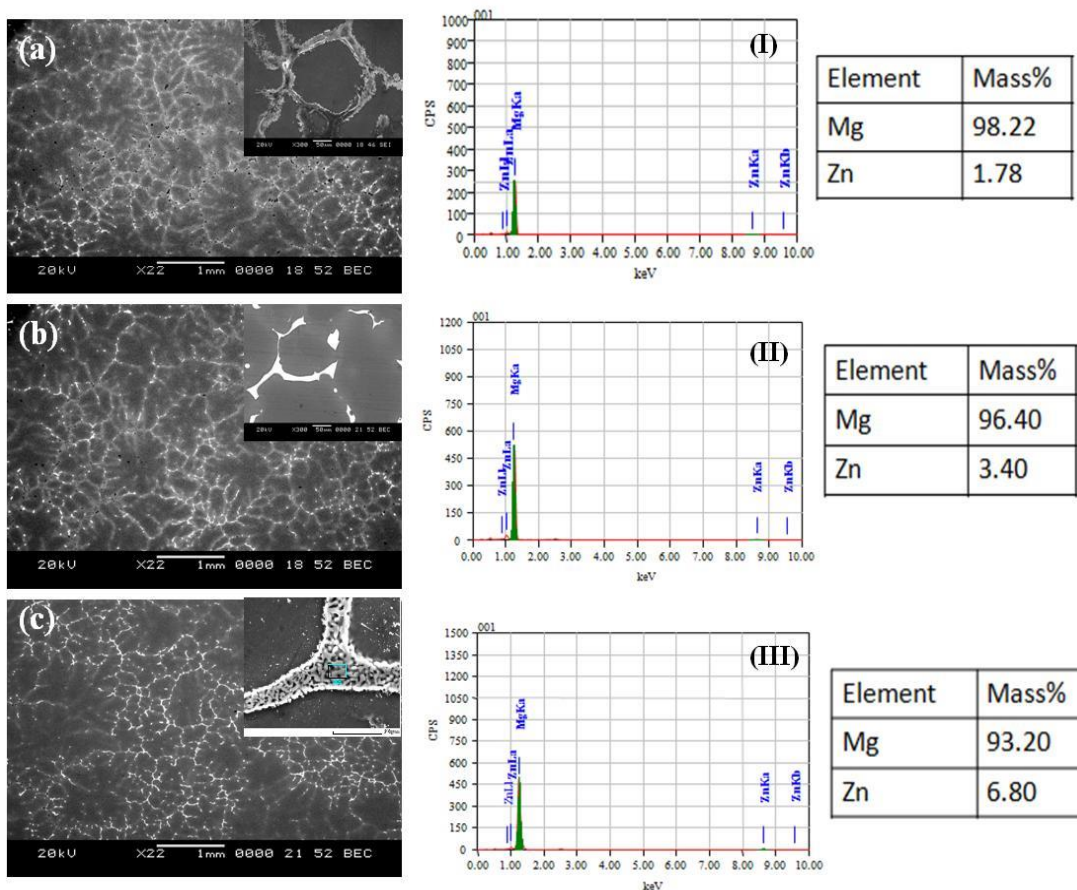


Figure 4.2. SEM images of as cast Mg-Zn alloys (a) Mg-2%Zn (b) Mg-4%Zn and (c) Mg-6%Zn and EDS area analysis (I) Mg-2%Zn (II) Mg-4%Zn and (III) Mg-6%Zn alloys.

Because of the large difference in atomic number between Mg and Zn, such images clearly reveal that pure Mg contains only  $\alpha$ -Mg phase and Zn-rich second phase mainly distributed along grain boundary (magnified image of the 4.2 a-c). The chemical composition of the different Mg-Zn alloys was identified by EDS area analysis and results are tabulated as shown in figure 4.2 (I-III). The grains are bimodal in nature with the combination of course grains and few fine grains

#### 4.1.1.3 Optical microstructure of Al-1100

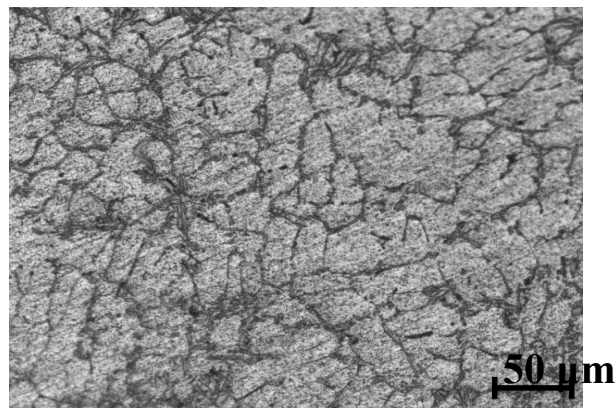


Figure 4.3. Optical microstructure of the as cast Al-1100.

Figure 4.3 shows the optical microstructure of as-cast Al-1100, and it is observed that the average grain size is about 38  $\mu\text{m}$  and the grain structure is dendritic in nature.

#### 4.1.1.4 Property evolution of as cast alloy

Mechanical properties of the cast Mg-(2-6)%Zn and Al-1100 used in this study have been summarized in tables 4.1.

Table 4.1. Mechanical properties of the Mg-(2-6)%Zn alloys and Al-1100.

Alloys	Mg-2%Zn	Mg-4%Zn	Mg-6%Zn	Aluminium
Microhardness (HV)	54.9	61.1	58.6	30.1
Tensile strength (MPa)	128	140	134	92
Percentage Elongation (%)	11	12.5	8.5	36



Microhardness and tensile strength of the Mg-Zn alloys increase with increase in the Zn content. Since Zn acts as a grain refiners, increase in Zinc content reduces the grain size of the alloys (Nam et al. 2014). Mechanical properties of Mg-6%Zn decreases due to solubility of Zn in Magnesium (Koc et al. 2015). Excess Zn will react with Mg and form large amount of (Mg-Zn) containing phases in the matrix and grain boundary resulting in residual defects and increase the number of crack sources, thus strength and elongation of the alloy decreases.

#### 4.1.2. Microstructural analysis of the homogenized alloys

##### 4.1.2.1 Optical microstructure

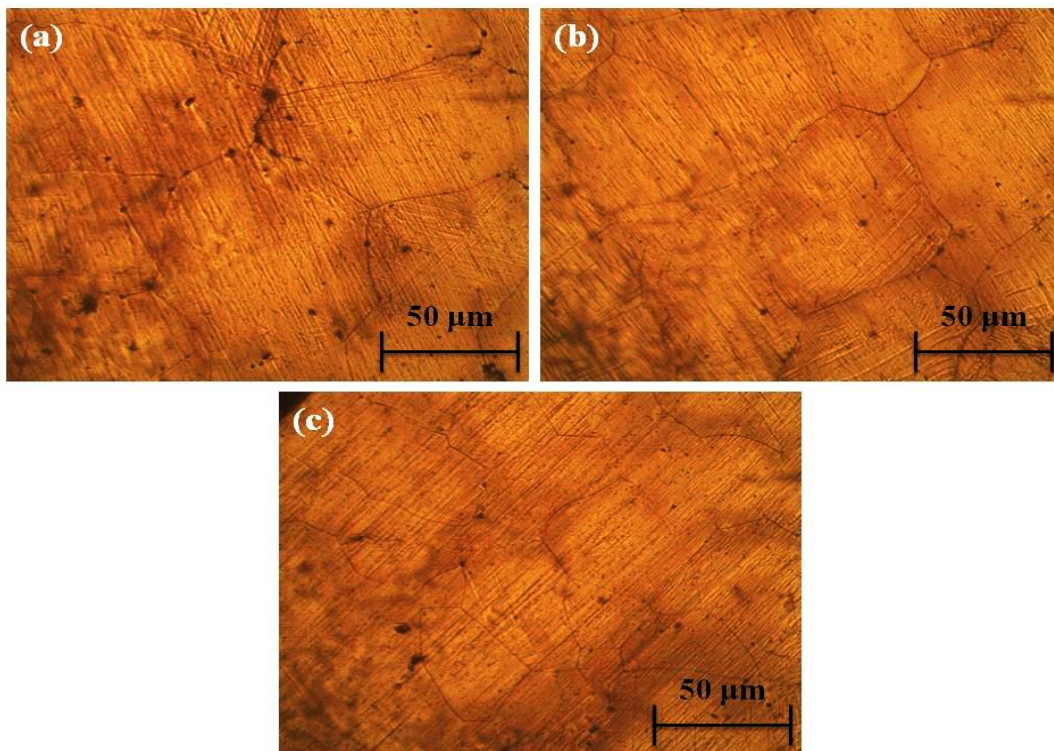


Figure 4.4. Optical microstructure (OM) of cast Mg-Zn alloys after homogenization (a) Mg-2%Zn (b) Mg-4%Zn and (c) Mg-6%Zn.

Homogenization treatment was carried out at 400 °C for 24 h, in order to obtain to homogeneous (uniform) microstructure in the alloys by dissolving micro irregularities during alloying. The OM (Figure. 4.4) shows the homogenized Mg-2%Zn, Mg-4%Zn and Mg-6%Zn.

#### 4.1.2.2 SEM observation

SEM images of the homogenized Mg-2%Zn, Mg-4%Zn and Mg-6%Zn alloy are shown in Figure. 4.5. Grain boundaries are clearly visible; thus, each grain can be distinguished.

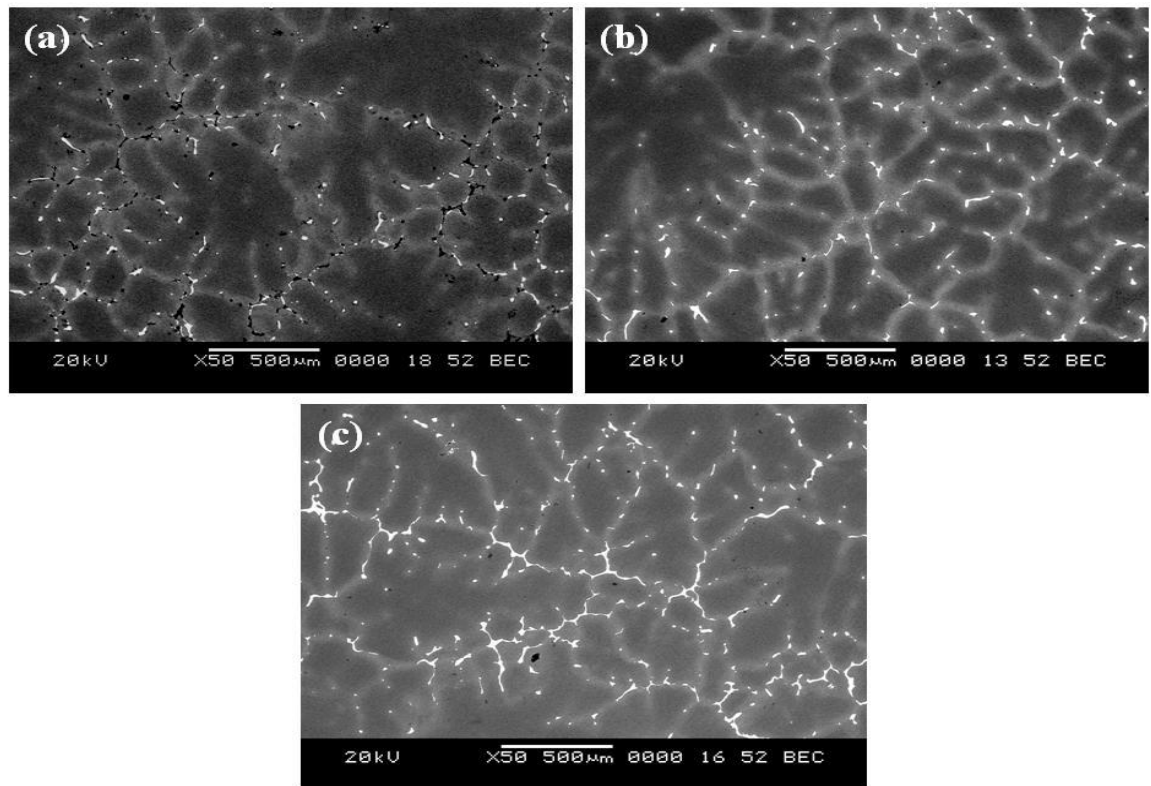


Figure 4.5. SEM of cast Mg-Zn alloys after homogenization (a) Mg-2%Zn (b) Mg-4%Zn and (c) Mg-6%Zn.

Secondary phases that were present on the grain boundaries dissolved in the matrix and grain boundaries are clearly visible and are shown in figure 4.4 and 4.5. Since the alloys are heated to a high temperature of 400 ° C, the samples are annealed, which results in increased grain size. Hence the grain size of the homogenized sample increased.

#### 4.1.2.3 Property evolution of cast alloy after homogenization

Mechanical properties of the homogenized Mg-(2-6)%Zn and Al-1100 used in this study have been summarized in tables 4.2.

Table 4.2. Mechanical properties of the homogenized Mg-(2-6)%Zn alloys and Al-1100.

Alloys	Mg-2%Zn	Mg-4%Zn	Mg-6%Zn	Aluminium
Properties				
Microhardness (HV)	49.7	52.8	52.2	26.2
Tensile strength (MPa)	115	120	119	86
Percentage Elongation (%)	12.6	14	11.2	44.2

### 4.1.3. Microstructural analysis of as rolled alloys

#### 4.1.3.1 Optical microstructure Mg-Zn alloys

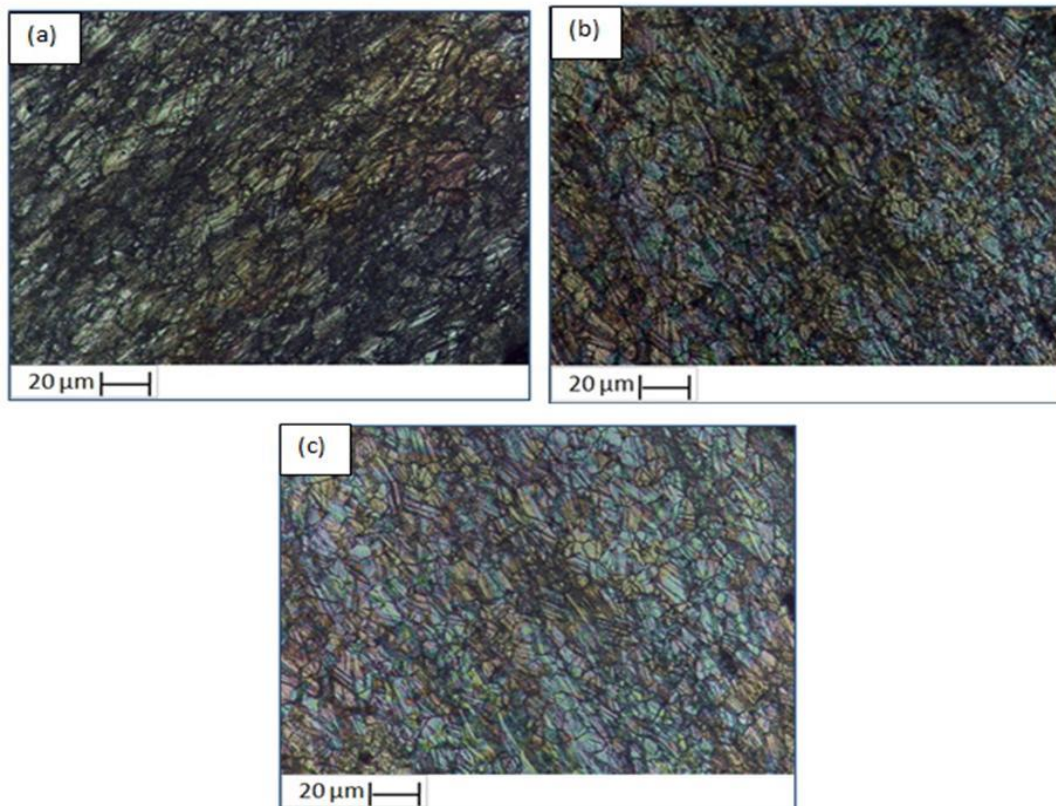


Figure 4.6. Optical microstructure (OM) of rolled (a) Mg-2%Zn (b) Mg-4%Zn and (c) Mg-6%Zn alloy.

Homogenized samples (10 mm thick) were heated in the tubular furnace at 300 °C for 10 min, and then rolled to a thickness of 1 mm with a reduction of 0.25 mm per pass. Significant grain refinement took place after rolling. OM images of the rolled Mg-

2%Zn, Mg-4%Zn, and Mg-6%Zn alloy are shown in Figure 4.6. It shows homogenized and uniaxial grains with significant grain refinement in all 3 systems. The average grain size for the three systems are measured by linear intersect method, is 6.4  $\mu\text{m}$  5.8  $\mu\text{m}$  and 5.4  $\mu\text{m}$  respectively.

#### 4.1.3.2 Optical microstructure of as rolled Al-1100

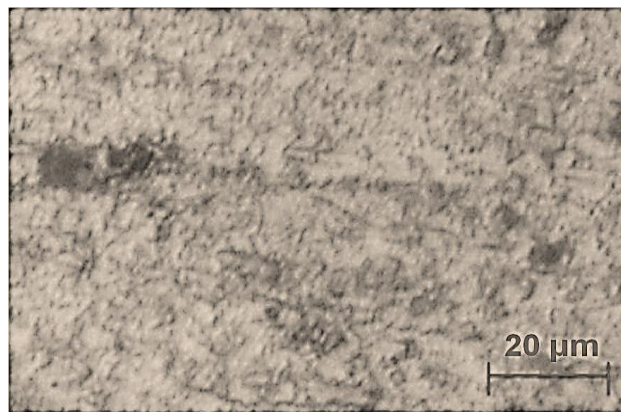


Figure 4.7. Optical microstructure of the as rolled Al-1100.

Figure 4.7 shows the optical microstructure of rolled Al-1100. It is observed that the average grain size is about 5.1  $\mu\text{m}$  and the material exhibits elongated grains along the rolling direction.

#### 4.1.3.3 Optical microstructure of as rolled Al-7075 alloy

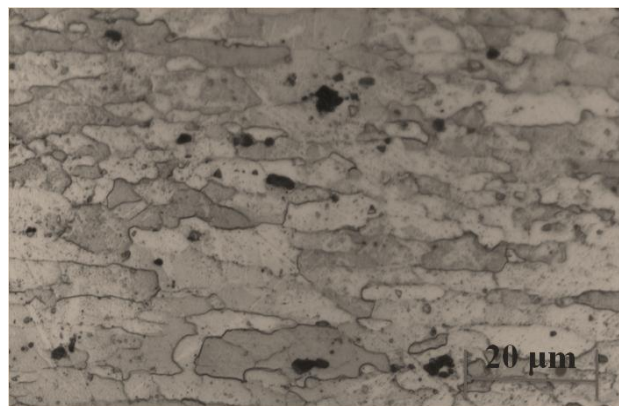


Figure 4.8. Optical microstructure of the as rolled Al-7075 alloy.

Figure 4.8 shows the optical microstructure of rolled Al-7075 alloy, can be observed that the average grain size is about  $13.4\ \mu\text{m}$  and the material exhibits an elongated grains along the rolling direction.

#### 4.1.3.4 SEM observation

Figure 4.9 (a-c) shows SEM images of the rolled Mg-2%Zn alloy, Mg-4%Zn and Mg-6%Zn alloy respectively. Large fraction of the newly deformed grains are formed along the rolling directions, with the presence of subgrains and deformation twins. Microstructure of the rolled alloys depicts bimodal grain size distribution with the combination of coarse and newly formed fine grains. Grain structure is rather homogeneous, but still some coarse grains are present. The average grain size found to be  $6.4\ \mu\text{m}$   $5.8\ \mu\text{m}$  and  $5.4\ \mu\text{m}$  in the Mg-2%Zn, Mg-4%Zn and Mg-6%Zn alloys respectively.

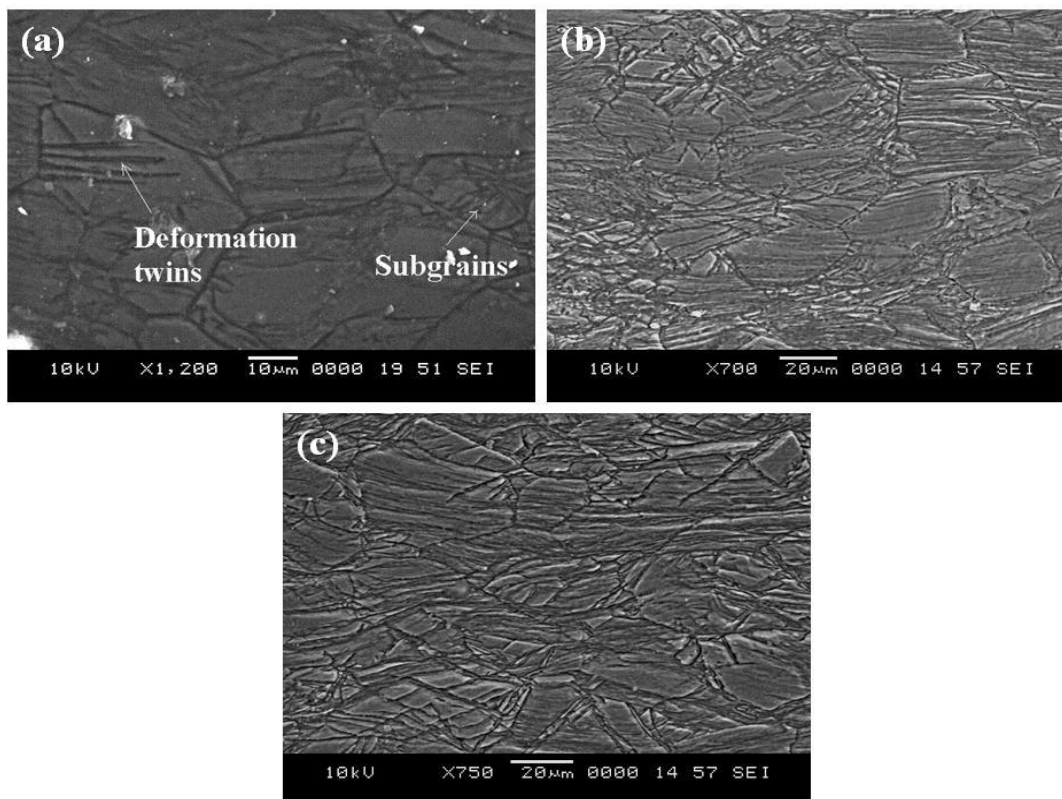


Figure 4.9. Scanning electron microscope (SEM) of rolled (a) Mg-2%Zn (b) Mg-4%Zn and (c) Mg-6%Zn alloy.

#### 4.1.3.5 Anodized Al sample

Al-1100 and Al-7075 alloys were anodized in electrolyte bath containing 15 % H<sub>2</sub>SO<sub>4</sub> solution with operating potential of 16 V at 3.5 A for 60 min at 18 °C.

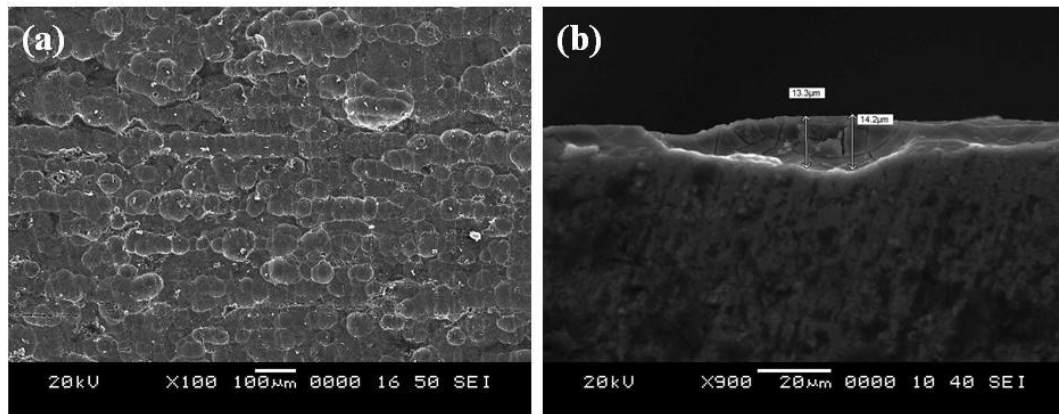


Figure 4.10. SEM micrographs of (a) Anodized Al sheet and (b) magnified image showing thickness of the alumina layer.

Figure 4.10 (a) shows (ND-RD plane) the formation of alumina on the surface of the Al sheet after anodization treatment and figure 4.10 (b) shows (TD-RD plane) the thickness of the alumina layer. Thickness of alumina found to be in the range of 10-12 μm.

#### 4.1.3.6 Property evolution of rolled alloys

Mechanical properties of the rolled Mg-(2-6)%Zn alloys, Al-1100 and Al-7075 alloy used in this study have been summarized in tables 4.3.

Table 4.3. Mechanical properties of rolled alloys

Properties/Alloys	Mg-2%Zn	Mg-4%Zn	Mg-6%Zn	Aluminium	Al-7075 alloy
Microhardness (HV)	74.9	80.4	75.9	90.2	166.2
Tensile strength (MPa)	172	210	188	183	314
Percentage Elongation (%)	4.1	6.5	8.3	16	21.1

Mechanical properties of Mg-Zn alloys increases with increase in the Zn content up to 4%. With further increase in Zn%, mechanical properties reduces. When the Zn mixed

with Mg, form large amount of (Mg-Zn) phases in the matrix and Mg-Zn rich deposited at grain boundaries. These phases increases the number of crack sources, therefore properties Mg-6%Zn alloy decreases (Dongsong et al. 2009).

## **4.2 Mg-Zn/Al and Mg-Zn/anodized Al multilayered composites**

### **4.2.1 Mg-2%Zn/Al and Mg-2%Zn/anodized Al multilayered composites**

Mg-2%Zn/Al and Mg-2%Zn/anodized Al multilayered composite was developed by ARB using Mg-2%Zn with pure Al and anodized Al. ARB was carried out at 300 °C up to five pass. Microstructural evolution of the ARB processed multilayered composite were investigated by SEM, EBSD and TEM. Mechanical properties were analyzed using microhardness and tensile tests. Corrosion behaviour was investigated using potentiodynamic polarization and immersion test. The results are briefed in the following sections.

#### **4.2.1.1 Microstructural observations**

Figure 4.11 shows SEM micrographs of the Mg-2%Zn/Al multilayered composite in the RD-TD plane after 5-pass ARB. It is observed from figure. 4.11 (a) that, there are no cracks or de-lamination along the interfaces of the multilayer, which indicate good bonding between Mg-2%Zn alloy and Al sheet. Average layer thickness was found to be in the range of 30-40  $\mu\text{m}$ . Slight waviness in the layers were observed due to high deformation. With the increase in the number of ARB passes, ultrafine grains are formed and are shown in figure. 4.11 (c-e). EDS analysis was done for different layers of the multilayered composite, the figure (I) Al layer (II) Mg-2%Zn layer (III) Inter face region. Grain refinement mechanism during ARB is attributed to grain subdivision due to deformation induced high angle grain boundaries and due to severe shears strain between strip and roller (Gashti et al. 2016).

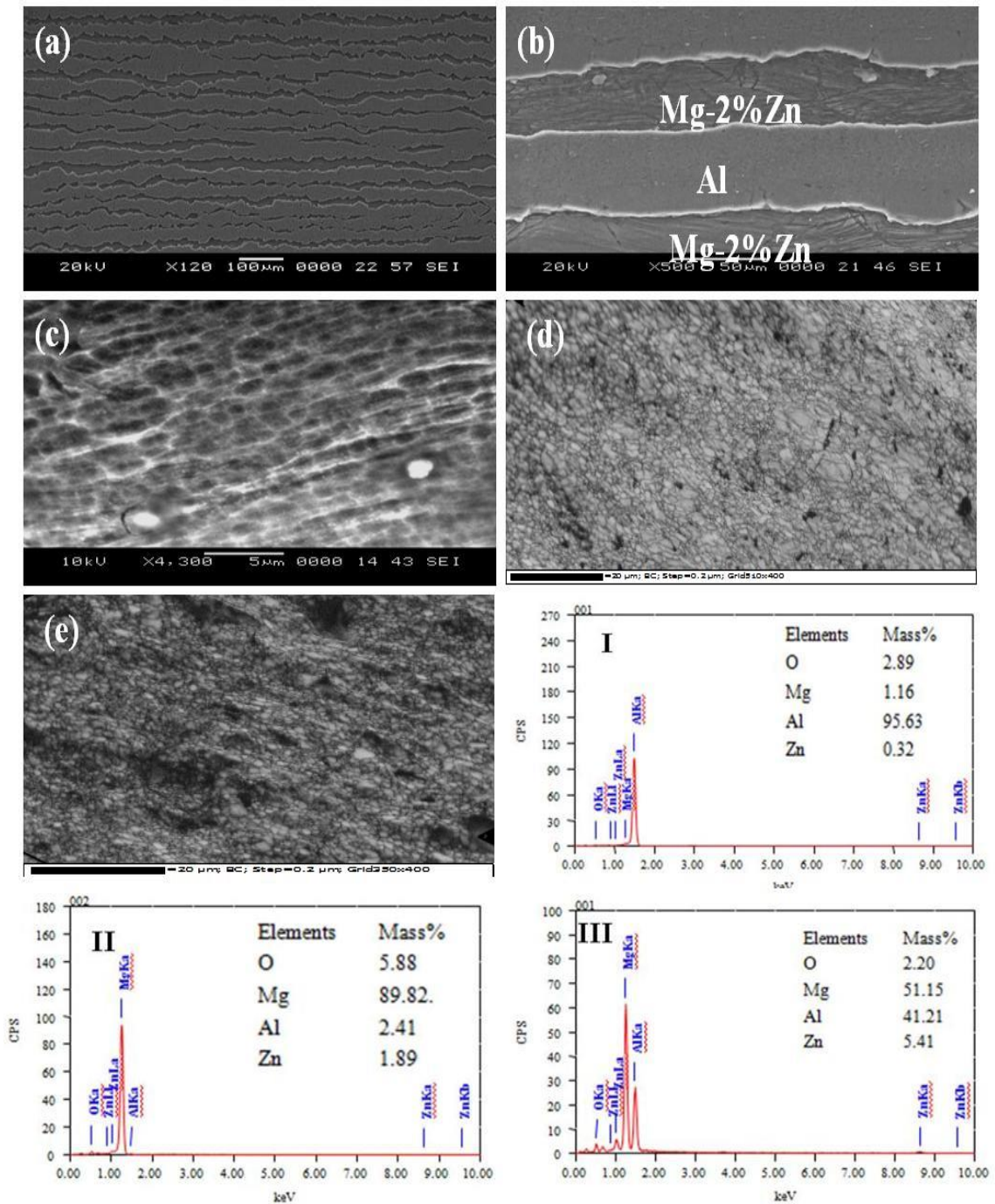


Figure 4.11. SEM micrographs of the ARB processed Mg-2%Zn/Al multilayered composite (a) five pass multilayered composite (b) magnified image of the different layers and grain structure (c) Mg-2%Zn layer (d) Al layer (e) anodized Al layer and EDS area analysis (I) Al layer (II) Mg-2%Zn layer (III) Interface region.

The total cumulative strain of the 5-pass ARB processed multilayered composite found to be 6.3. Grain refinement occurred because of multi-directional slip system, dislocation cells and subgrain structure is formed with a low angle grain boundaries.



As a result of dislocation accumulation, misorientation increases and gradual shift of low angle grain boundaries to high angle grain boundaries, which led to migration of new high angle grain boundaries and creation of UFG structure (Tsuji et al. 2003; Fattah-Alhosseini et al. 2016).

#### 4.2.1.2. EBSD analysis

Orientation image mapping (OIM) images were taken on RD-ND planes on Mg-2%Zn/Al and Mg-2%Zn/anodized Al multilayered composites samples subjected to 5-pass ARB process. Colors in the standard stereographic triangle correspond to crystallographic directions.

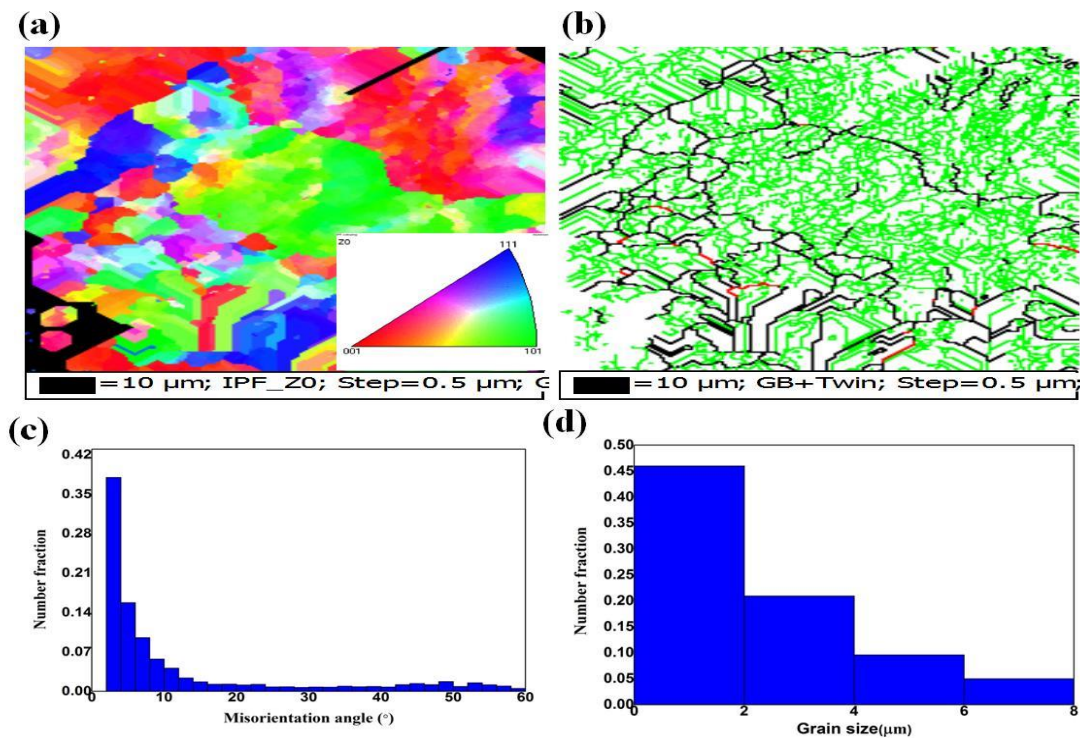


Figure 4.12. OIM images of Al layer in the 5-pass ARB processed Mg-2%Zn/Al multilayered composite (a) IPF map (b) Grain boundary map with twins (c) Misorientation angle distribution profile (d) Grain size distribution. Non-indexed points are shown as black pixels. In the grain boundary map, high angle boundaries (HAGBs) i.e. boundaries with misorientation angle more than  $15^\circ$  have been shown as black lines, while low angle boundaries (LAGBs) i.e. boundaries having misorientation angle of  $2^\circ$ - $15^\circ$  have been shown as green lines and twins have been marked in red colors. Inverse pole figure (IPF) map of the Al layer in the ARB

processed Mg-2%Zn/Al multilayered composite is shown in figure 4.12. As depicted from figure 4.12 (a), 5-pass ARB processed Al grains are directed uniformly in orientation, in the direction of rolling. Grain boundary map shown in figure. 4.12 (b) reveals fine grains with a fraction of HAGBs. At higher ARB pass, strain accumulated in the material increases, so that density of dislocations increases. As a result, fraction of HAGBs to LAGBs increases. Large lattice rotations occur around secondary phase particles during deformation which increases misorientations and thus produce new HAGBs (Baazamat et al. 2015). Percentage of twins was found to be 0.85%. Misorientation angle profile, as shown in figure 4.12 (c) consists of both LAGBs and HAGBs, which indicates that deformation is induced as result of dynamic recovery. Grain size variation profile (Figure. 4.12 d) exhibited an average grain size as 1.9  $\mu\text{m}$  in the Al layer of the multilayered composite.

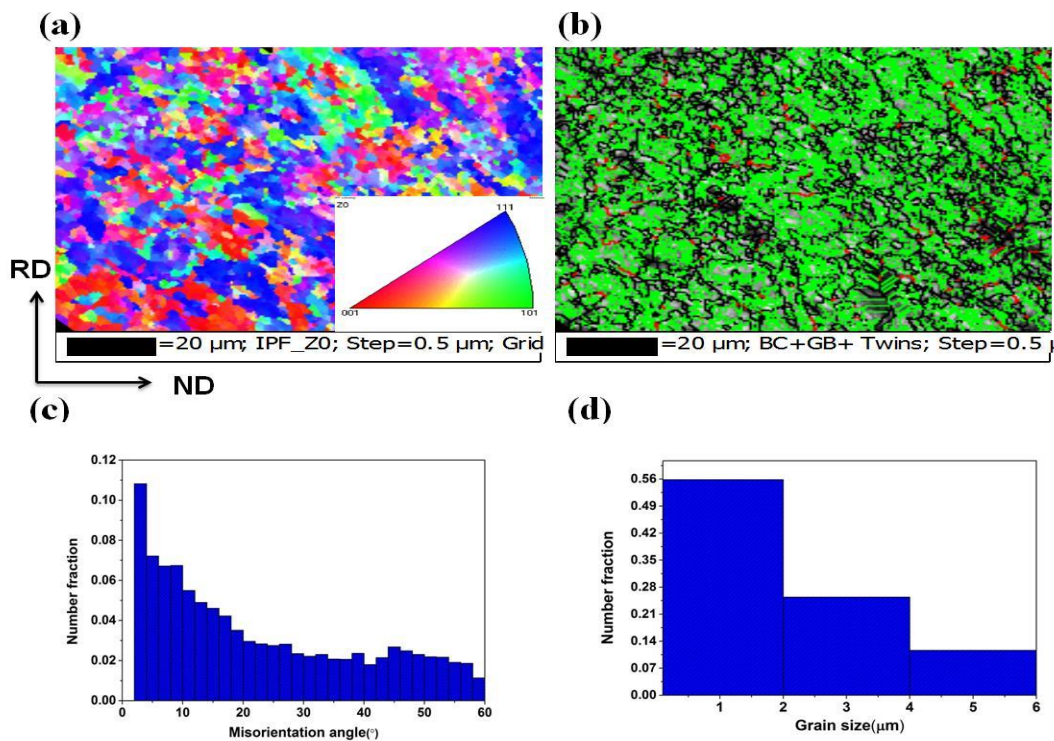


Figure 4.13. OIM images analysis of anodized Al layer in the 5-pass ARB processed Mg-2%Zn/Al multilayered composite (a) IPF map (b) Grain boundary map with twins (c) Misorientation angle distribution profile (d) Grain size distribution.

Inverse pole figure (IPF) map of the anodized Al layer in the ARB processed Mg-2%Zn/anodized Al multilayered composite is shown in figure 4.13 a. Grain boundary

map overlaid with twins is shown in figure 4.13 (b). EBSD image shows fine grains with a fraction of HAGBs. The mechanism of formation of UFG by ARB process is dynamic recrystallization, that results in the generation of sub-micron sized grains having high angle misorientation (Gashti et al. 2016). Percentage of twins was found to be 1.2% in the anodized Al layer of the 5-pass multilayered composite. At higher ARB pass, strain increases and as a result, misorientations of the deformation-induced boundaries are increased. With further increase in strain, these boundaries get converted to HAGBs. Misorientation angle distribution profile consisting of both LAGBs and HAGBs is shown in figure 4.13 (c). Grain size variation profile shown in figure 4.13 (d) exhibited average grain size as 1.3  $\mu\text{m}$  in the anodized Al layer in the Mg-2%Zn/anodized Al multilayered composite.

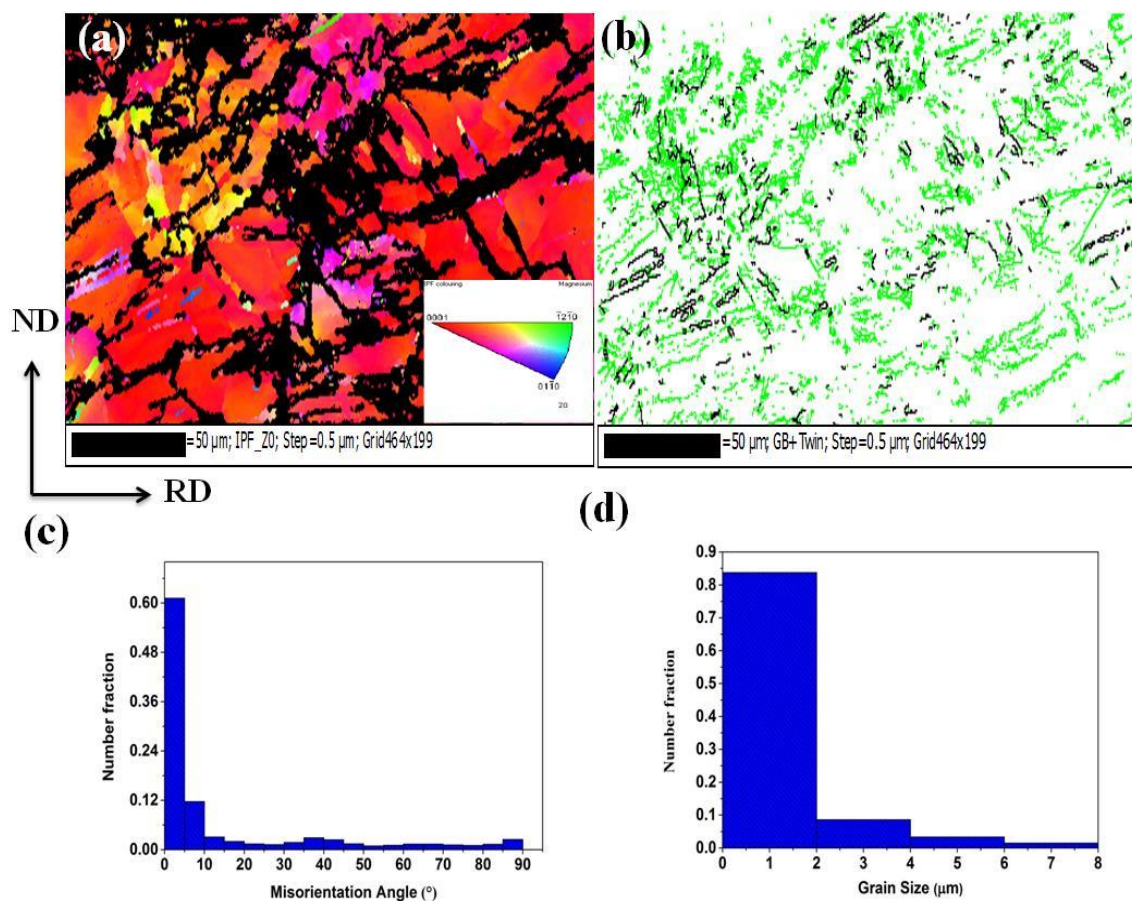


Figure 4.14. EBSD based analysis of Mg-2%Zn layer in the 5-pass ARB processed Mg-2%Zn/Al multilayered composite (a) IPF map (b) Grain boundary map with twins (c) Misorientation angle distribution profile (d) Grain size distribution.

EBSD results of Mg-2%Zn layer in the ARB processed Mg-2%Zn/Al multilayered composites are shown in Figure 4.14. IPF map (Figure 4.14 a) revealed that, grains are directed uniformly in  $\langle 0001 \rangle$  orientation in the direction of rolling. The grain boundary map (Figure 4.14 b) shows that the Mg-2%Zn layer consists of subgrains with a fraction of HAGBs due of dynamic recrystallization during ARB process. With higher ARB passes, number of LAGBs decreased with an increase in HAGBs. Fraction of recrystallized grains increased with higher strain due to nucleation of new grains during recrystallization, which resulted in a relatively uniform microstructure with ultra-fine grain. It is clearly observed that there are no twins formed in ARB processed Mg-2%Zn, which can be attributed to decrease in twin nucleation with decrease in grain size. It is reported that non-basal slips are activated for a fine grained Mg, resulting in suppression of twin generation and reduction in mechanical anisotropy by grain refinement (Chino et al. 2008). Deformation twins disappear in the Mg alloys, when the average grain size reaches to less than 2  $\mu\text{m}$ . Grain refinement mechanism during ARB is grain subdivision caused by plastic deformation where the course grains are subdivided into fine grain by deformation induced boundaries. The misorientation of the deformation induced boundaries subdivide the original grains, with increasing strain and most of the deformation induced boundaries become high angle at very high strain. Figure 4.14 (c) reveals the presence of both LAGBs and HAGBs in Mg-2%Zn layer which indicates that the deformation is induced as a result of dynamic recovery. Grain size variation plot (Figure 4.14 d) shows that 82% of the grains in the microstructure have grain size below 2  $\mu\text{m}$ . The average grain size is found to be 1  $\mu\text{m}$  in the Mg-2%Zn layer of the multilayered composite.

#### **4.2.1.3 TEM analysis**

Micrographs of TEM and their corresponding selected area diffraction patterns (SAED) along ND-RD plane of the ARB processed Mg-2%Zn/Al and Mg-2%Zn/anodized Al composites are illustrated in Figure 4.15. Ultra-fine grains (Figure 4.15 (b & d)) are clearly seen in the microstructure along with some regions showed dislocations (Figure 4.15 (a & c)), which is an indication of large misorientation. It should be emphasized

that the formation of the ultra-fine grains is regionally inhomogeneous in the highly strained materials (Saito et al. 1998).

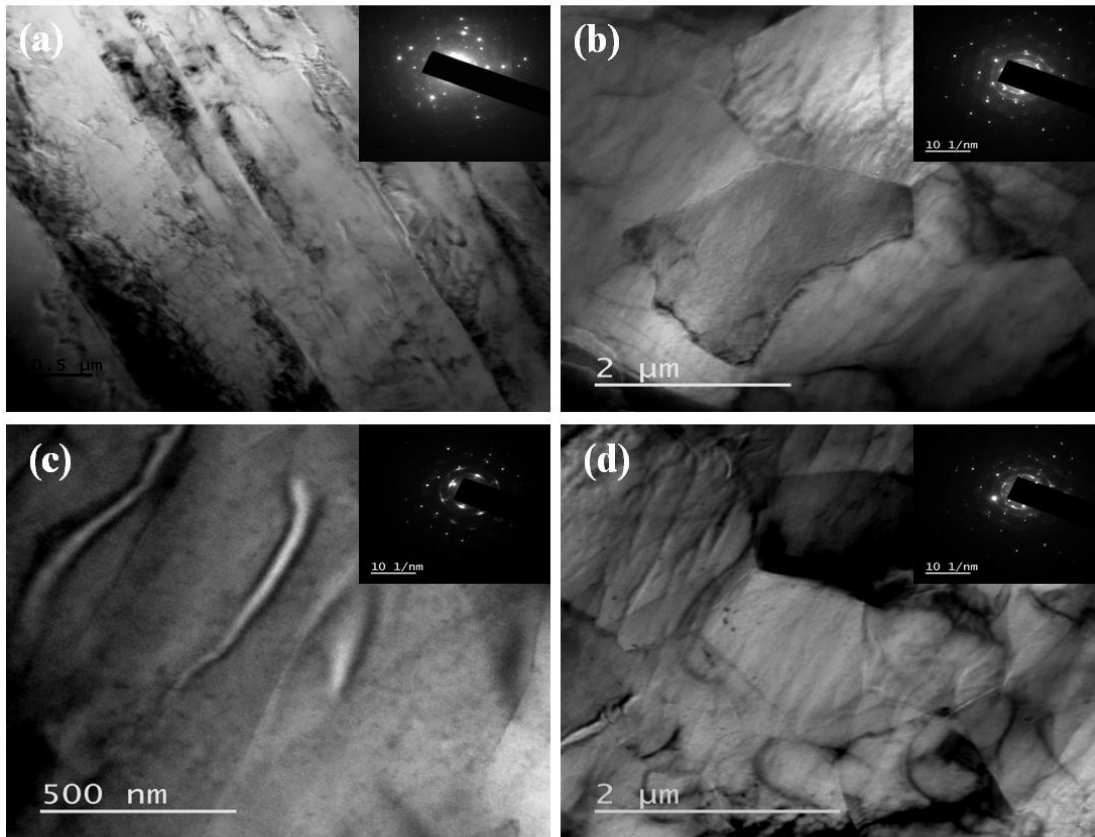


Figure 4.15. TEM micrographs and corresponding SAED patterns (a & b) Mg-2%Zn/Al (c & d) Mg-2%Zn/anodized Al multilayered composite.

Fraction of the ultra-fine grained region increased with increase in the number of ARB cycles due to higher strain. Figure 4.15 (b & d) shows the presence of dislocation density inside the ultra-fine grain, surrounded by strongly deformed boundaries. SAED patterns are in the form of rings which confirm the sub-grain structure in the composite with high angle misorientations. ARB processed composites are high strained materials due to which diffraction spots were found to be elongated and some diffraction spots did not form the rings due to presence of low angle grain boundaries.

#### 4.2.1.4 X-ray diffraction analysis

XRD patterns of the Mg-2%Zn/Al and Mg-2%Zn/anodized Al multilayered composite taken along the cross-section (TD-RD plane) is shown in Figure 4.16.

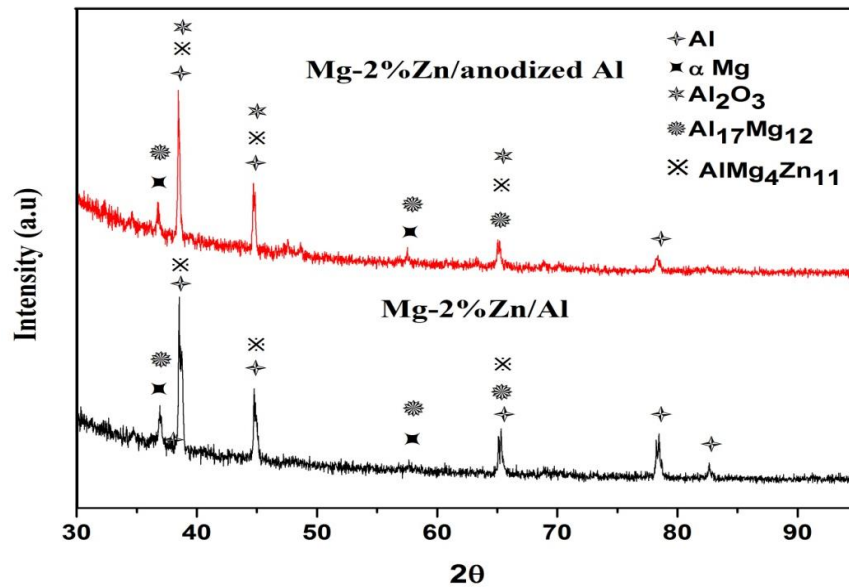


Figure 4.16. XRD patterns along the cross section of accumulative roll bonded multilayered composite.

XRD patterns of the composites revealed peaks indexed to Al,  $\alpha$ Mg,  $\text{Al}_{17}\text{Mg}_{12}$  and  $\text{AlMg}_4\text{Zn}_{11}$ . Mg-2%Zn/anodized Al composite shows the presence of  $\text{Al}_2\text{O}_3$ . Minor peak of  $\text{Al}_{17}\text{Mg}_{12}$ ,  $\text{AlMg}_4\text{Zn}_{11}$  and  $\text{Al}_2\text{O}_3$  appears after five ARB passes. As ARB proceeds and the layer thickness decreases, the number of interfaces per unit volume is raised. As a result, the intensity of intermetallic increases to some extent. Formation of intermetallics phases in multilayered composites attributed to high rolling strain occurred during ARB at 300 °C which increases the diffusion between different layers of the multilayered composite, grain boundaries area and dislocation density (Zhang and Acoff, 2007; Liu et al. 2012). This accelerates the elemental diffusion at interfaces and promotes the formation of intermetallic (Song et al. 1998).

#### 4.2.1.5 Density test

Density test was carried out according to Archimedes principle for wrought Mg-2%Zn, Al, anodized Al and accumulative roll bonded multilayered composite. Initially, the weight of the samples was measured in air and then measured under water. The density of the samples was calculated using equation 3.4, and is illustrated in table 4.4.

Table 4.4. Density test results.

Sample	Density (kg/m <sup>3</sup> )
Mg-2%Zn alloy	1759
Pure Al	2691
Anodized Al	2696
Mg-2%Zn/Al composite	2122
Mg-2%Zn/anodizedAl composite	2125

The 5-pass ARB processed Mg-2%Zn/Al and Mg-2%Zn/anodized Al composites are lighter in weight of about 21% as compared to Al-1100.

#### 4.2.1.6. Microhardness

Microhardness of the Mg-2%Zn, Al and anodized Al layers of the multilayered composite increases with increase in the number of ARB passes as shown in Figure 4.17.

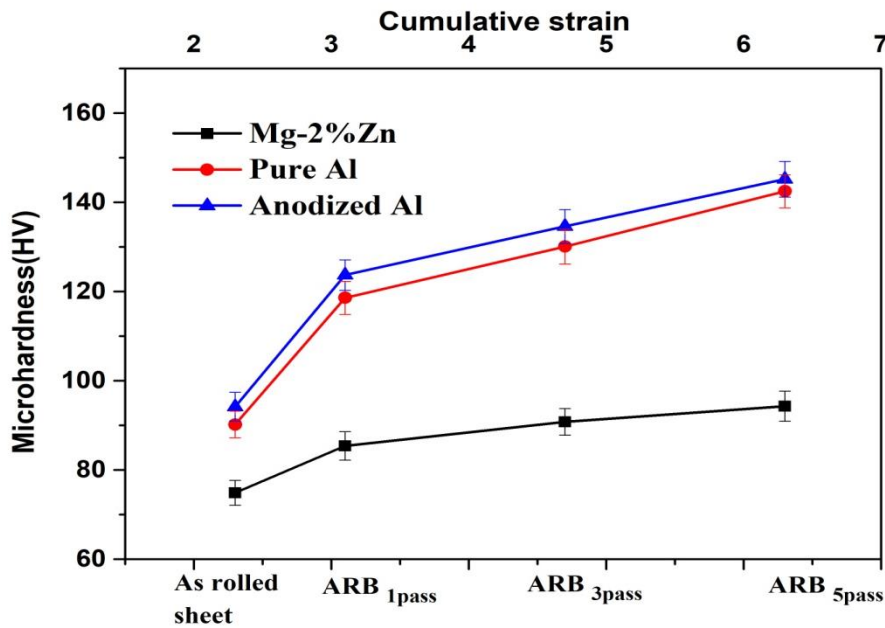


Figure 4.17. Microhardness variation in different layers of the Mg-2%Zn/Al and Mg-2%Zn/anodized Al composite with ARB passes.

During initial passes of ARB, the microhardness of the multilayered composite increases due to a high rate of strain hardening, this causes increase in dislocation density. At higher ARB passes, increase in microhardness values is due to combined effect of strain hardening and grain refinement. After five ARB passes, the microhardness of the Mg-2%Zn, Al and anodized Al layers are 1.25 times, 1.57 times and 1.54 times, respectively, higher, in comparison with their counterpart rolled alloys. Anodized Al layer in the Mg-2%Zn/anodized Al composite exhibited 1.8% higher hardness as compared to Al layer in the Mg-2%Zn/Al composite due to uniform distribution of harder alumina ( $\text{Al}_2\text{O}_3$ ) particles.

#### **4.2.1.7 Tensile strength**

Figure 4.18 (a) shows variation in tensile properties of the as rolled Al, Mg-2%Zn and roll bonded Mg-2%Zn/Al multilayered composite with different passes of ARB. It is observed that, as the number of ARB passes increases, yield strength (YS) and ultimate tensile strength (UTS) improves, and ductility reduces. During the initial passes of ARB, enhancement in UTS and YS can be attributed to strain hardening caused due to the strong obstacle provided to dislocation slip. But at the higher passes of ARB, improvement of strength is due to grain refinement. In the higher passes of the ARB, the work hardening effect diminishes and gradual evolution of UFG occurs. As the number of ARB passes increases, proportion of UFG in the microstructure increases. YS and UTS of the 5-pass ARB processed Mg-2%Zn/Al increased from 112 MPa to 162 MPa and 172 MPa to 246 MPa respectively. Improvement of YS and UTS is about 44.6% and 43.0% respectively as compared to rolled Mg-2%Zn alloy. Dislocations are generated at higher strain, which are pinned together and cause strengthening of the alloy. At higher ARB passes, the work hardening effect diminishes and ultra fine grains are created gradually which is more dominant in the strengthening mechanism.



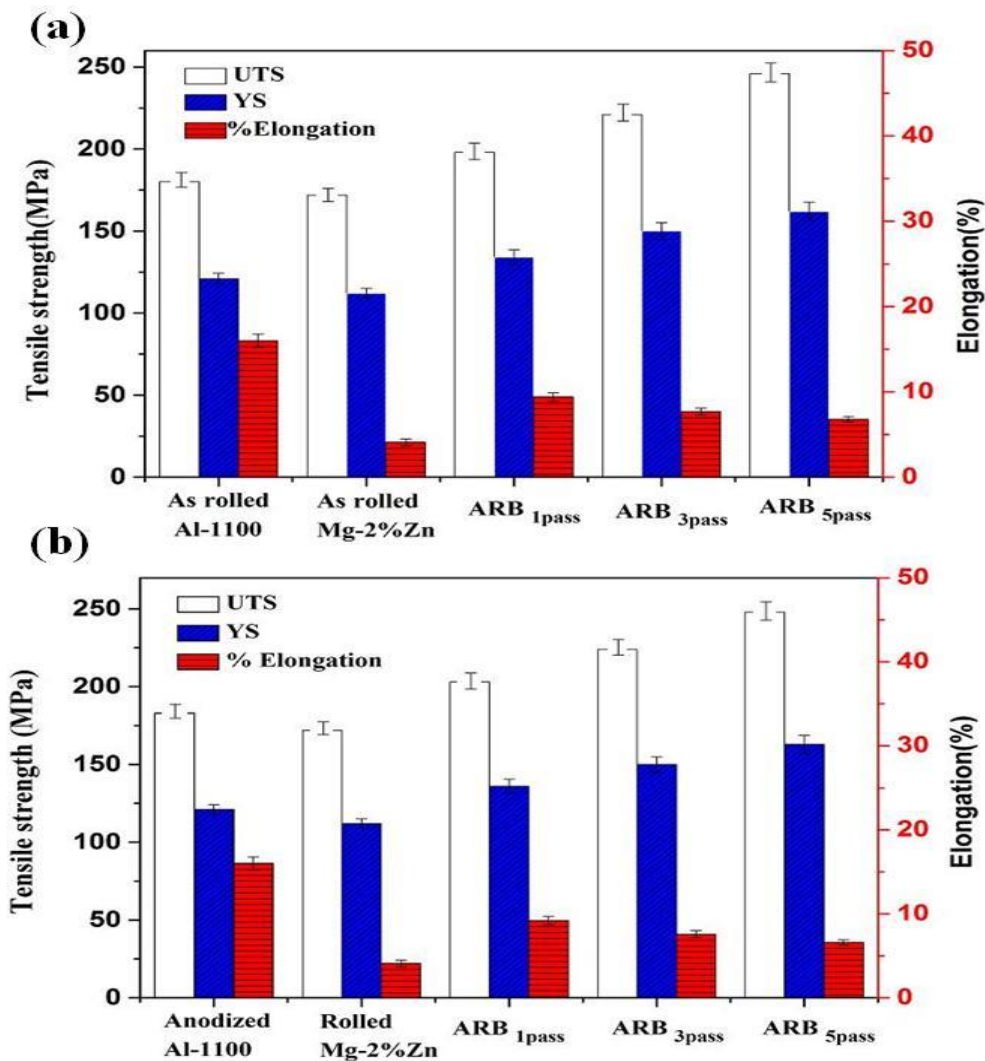


Figure 4.18. Variation of UTS, YS and percentage elongation of the multilayered composite with different ARB passes (a) Mg-2%Zn/Al composite (b) Mg-2%Zn/anodized Al composite.

Figure 4.18 (b) shows variation of tensile strength and ductility of Mg-2%Zn/anodized Al multilayered composite subjected to different ARB passes. The YS and UTS of the 5-pass ARB processed Mg-2%Zn/anodized Al increased from 112 MPa to 163 MPa and 172 MPa to 248 MPa respectively. Improvement in YS and UTS is about 45.5% and 44.1% respectively as compared to counterpart rolled Mg-2%Zn alloy. This improvement is due to strain hardening and grain refinement. Mg-2%Zn/anodized Al exhibited higher YS and UTS as compared to Mg-2%Zn/Al multilayered composite is due to the effect of alumina ( $Al_2O_3$ ) particles resulting from the anodization process, which acts as a barrier to dislocation movement. 5-pass ARB processed Mg-2%Zn/Al and Mg-

2%Zn/anodized Al multilayered composite exhibited 65.8% higher elongation than that of the Mg-2%Zn alloy (starting material). This can be attributed to amount of highly ductile element Al present in the multilayered composite. Percentage elongation decreases with the increase in the number of ARB passes (Figure 4.18 (a & b)) due to of strain hardening as well as UFG structure.

#### 4.2.1.8 Fractography

SEM micrographs of different layers of the composite fractured during tensile test is shown in Figure 4.19 (a & b).

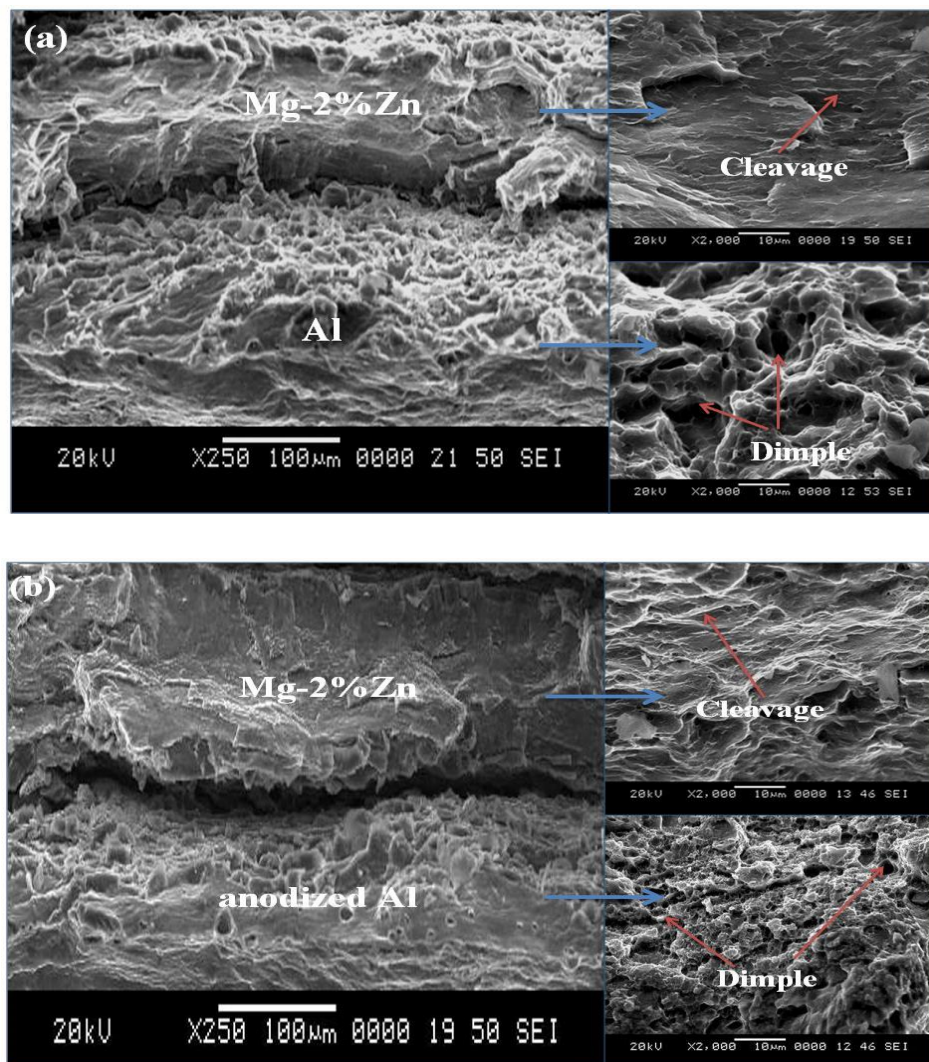


Figure 4.19. SEM micrographs of the fractured surface of 5-pass ARB processed (a) Mg-2%Zn/Al (b) Mg-2%Zn/anodized Al multilayered composite.

Magnified image of the Al and anodized Al layer in the 5-pass ARB processed Mg-2%Zn/Al and Mg-2%Zn/anodized Al composite reveals dimples as a result of ductile fracture. The dimples are formed by the nucleation, growth, and coalescence of microvoids (Callister and Rethwisch, 2008). When the elastic energy in the secondary phase particle is greater than the surface energy of the newly formed void surfaces, nucleation of voids occurred at dispersoid particles. These voids along with the grain boundary dislocations aid the secondary particle distribution within the matrix and also on the grain boundary regions which leads to coalescence of microvoids. Appearance of micro voids in the fracture surfaces are being affected by the state of shear stress. Therefore, the dimples are elongated which shows shear ductile failure (Barsoum and Faleskog, 2007) in the Al and anodized Al layer of the multilayered composites. However, Mg-2%Zn layer in the composite was fractured in the shear mode and free from dimples which appear to be transgranular brittle fracture due to hexagonal closed packed (HCP) structure. Shear fracture was observed in the interface regions between the layers. Thus, the composites Mg-2%Zn/Al and Mg-2%Zn/anodized Al exhibited shear ductile fracture.

#### **4.2.1.9 Potentiodynamic polarisation**

Electrochemical corrosion plots of as rolled Mg-2%Zn alloy, ARB processed Mg-2%Zn/Al and Mg-2%Zn/anodized Al composites in the solution of 0.1 M NaCl are shown in figure 4.20. Corrosion kinetics parameters such as corrosion potential ( $E_{\text{corr}}$ ), Tafel slopes ( $\beta_a$  &  $\beta_c$ ), corrosion current density ( $i_{\text{corr}}$ ) and corrosion rate (mm/y) were obtained from polarization plots and are tabulated in table 4.5. A shift of  $E_{\text{corr}}$  values was observed in noble direction after ARB processing and  $E_{\text{corr}}$  values were found about -1.63, -1.40 and -1.36  $V_{\text{SCE}}$  for wrought Mg-2%Zn alloy, Mg-2%Zn/Al and Mg-2%Zn/anodized Al respectively. A significantly lower corrosion current density ( $i_{\text{corr}}$ ) was observed for ARB processed composites as compared to wrought Mg-2%Zn alloys.

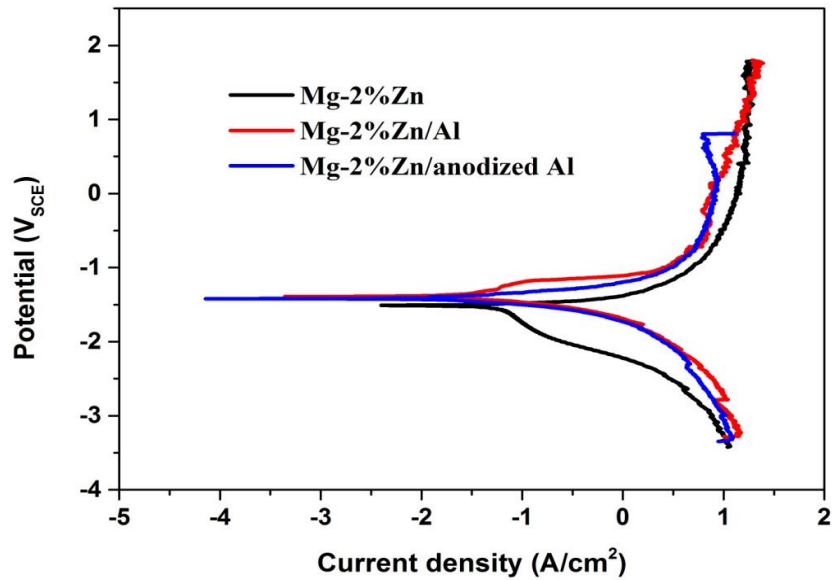


Figure 4.20. Potentiodynamic polarization curves of the as rolled Mg-2%Zn, Mg-2%Zn/Al and Mg-2%Zn/anodized Al multilayered composites.

Table 4.5. Electrochemical kinetic parameters

Materials	$E_{corr}$ (VSCE)	$I_{corr}$ ( $\mu\text{A}/\text{cm}^2$ )	$\beta_a$ (mV/decade)	$\beta_c$ (mV/decade)	Corrosion rate (mm/y)
Mg-2%Zn	-1.63	77.96	238.1	- 882.2	2.38
Mg- 2%Zn/Al	-1.36	32.73	372.4	-180.8	1.69
Mg-2%Zn/ anodized Al	-1.40	30.14	119.2	-172.9	1.49

High cathodic slope values were found for wrought Mg-2%Zn alloy as compared to ARB processed composites which indicate high evolution of  $\text{H}_2$  due to cathodic reduction reactions. To examine stable passivation behaviour of alloy and composite in exposed environments, passive current density provides a better representation of uniform and localised corrosion. A reduction of passive current density was observed for ARB processed composites compared to rolled Mg-2%Zn alloy.

Surface morphology after electrochemical polarization test in the solution of 0.1 M NaCl are shown in figure 4.21 for as rolled Mg-2%Zn alloy and Mg-2%Zn/Al and Mg-2%Zn/anodized Al multilayered composite. A significant dissolution of Mg-2%Zn

alloy layer was observed as compared to Al and anodized Al layer. However, Mg-2%Zn/anodized Al multilayered composite did not show any dissolution, like Mg-2%Zn/Al composite, because of anodization of Al before ARB process. A cracking tendency of anodized layer is observed due to high hardness of surface (alumina).

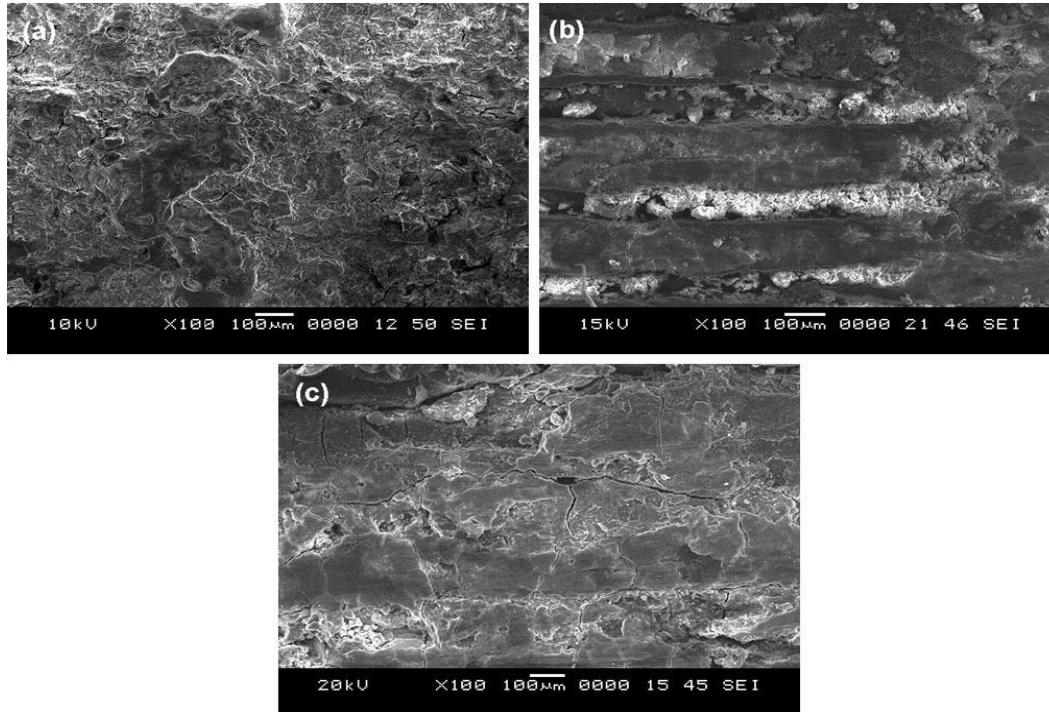


Figure 4.21. SEM micrographs of corroded (a) as rolled Mg-2%Zn (b) Mg-2%Zn/Al and (c) Mg 2%Zn/anodized Al composites after electrochemical test in a 0.1M NaCl solution.

#### 4.2.1.10 Immersion study

Hydrogen evolution rate and corresponding corrosion rate of the rolled Mg-2%Zn alloy and ARB processed multilayered composites are illustrated in Table 4.6. Hydrogen evolution drastically reduced about 45% and 58.8% in Mg-2%Zn/Al and Mg-2%Zn/anodized Al, respectively, as compared with Mg-2%Zn alloy. Degradation of Mg-2%Zn/Al multilayered composites is slower than rolled Mg-2%Zn alloy due to refined microstructure and the presence of  $\beta$  phases ( $Al_{12}Mg_{17}$  and  $AlMg_4Zn_{11}$ ).

Table 4.6. Immersion test results.

<b>Materials</b>	<b>Hydrogen evolution rate (ml/cm<sup>2</sup>/d)</b>	<b>Corrosion rate (mm/y)</b>
As rolled Mg-2%Zn	1.15	2.55
Mg-2%Zn/Al composite	0.75	1.40
Mg2%Zn/anodized Al composite	0.56	1.05

Further, the Mg-2%Zn/anodized Al composites showed less hydrogen evolution compared to Mg-2%Zn/Al multilayered composites due to presence of alumina (due to anodization before ARB process). Potentiodynamic polarisation (Table 4.5) and immersion test (Table 4.6) in 0.1 M NaCl solution showed similar trend in the corrosion rate.

#### **4.2.2 Mg-4%Zn/Al and Mg-4%Zn/anodized Al multilayered composites**

Mg-4%Zn/Al and Mg-4%Zn/anodized Al multilayered composite was developed by accumulative roll bonding (ARB) process using Mg-4%Zn with pure Al and anodized Al. The ARB was carried out at 300 °C up to five pass. A thorough microstructural characterization was performed on the composites by scanning electron microscope, electron backscatter diffraction (EBSD), transmission electron microscope, and phase analysis by x-ray diffraction. In addition, mechanical properties were evaluated by microhardness and tensile tests. Corrosion behavior of the multilayered composite was examined using electrochemical polarization and immersion test. The results are briefed in the following sections.

##### **4.2.2.1 Microstructural Analysis**

Figure 4.22 shows SEM micrographs of the Mg-4%Zn/Al composite on the RD-TD plane after 5-pass ARB process. Figure 4.22 (a & b) shows the alternat layers of Mg-4%Zn alloy and Al and there were no cracks or de-lamination along the interfaces of

the multilayers. Thickness of both, Mg-4%Zn and Al layers decreased gradually with increase in number of ARB passes and after 5-pass ARB pass, the thickness found to be 30-40  $\mu\text{m}$ . Ultrafine grains are depicted in the ARB processed Al layer (figure 4.22 c), anodized Al layer (figure 4.22 d), Mg-4%Zn layer (figure 4.22 e) in the Mg-4%Zn/Al and Mg-4%Zn/anodized Al multilayered composites. Grain refinement is due to (i) subdivision of the initial grains and formation of subgrain structure with low angle grain boundaries by multi-directional slip, (ii) misorientation increase and gradual transformation of low angle boundaries to high angle grain boundaries by dislocation accumulation, and (iii) migration of new high angle grain boundaries and formation of well-defined UFG structure (Xing et al. 2002).

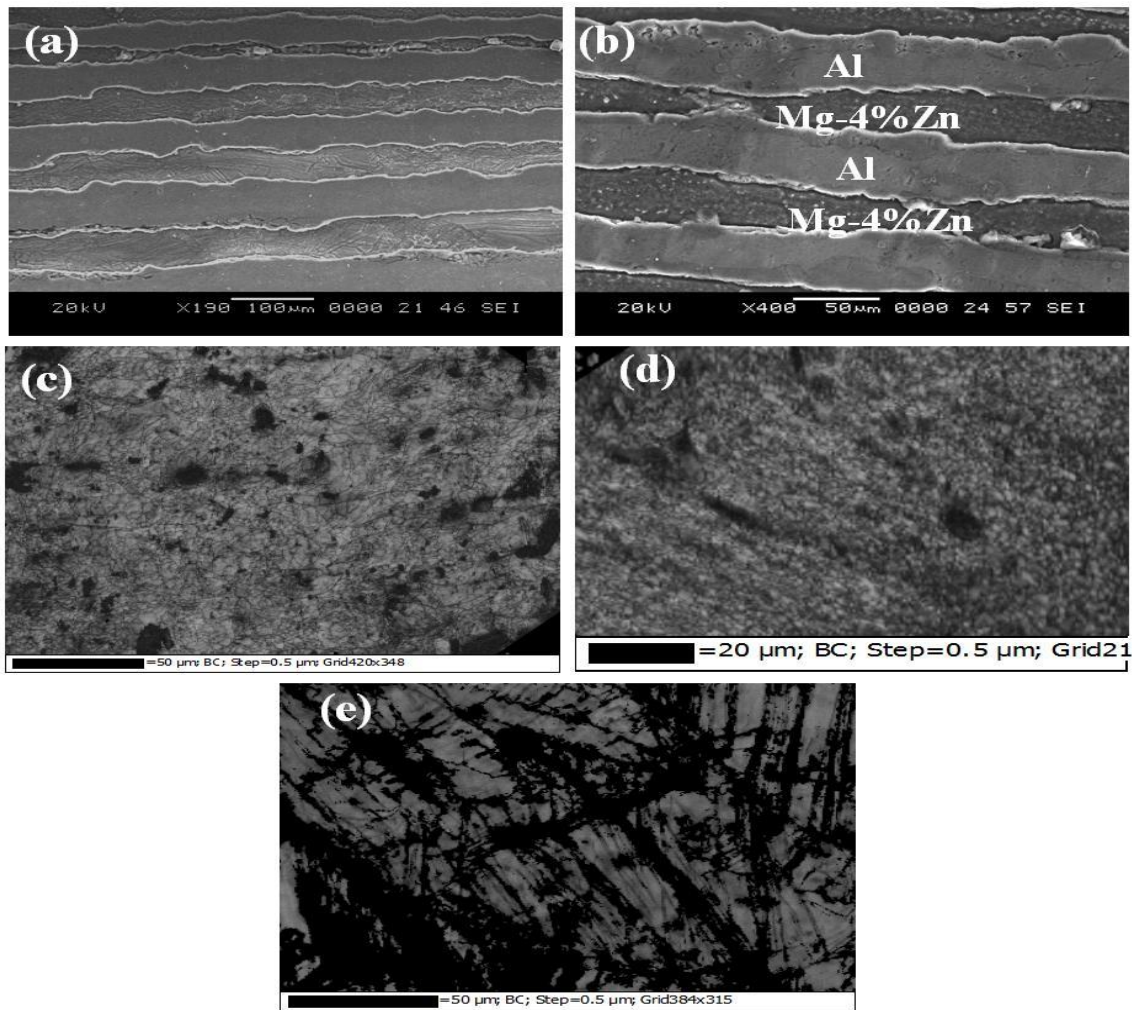


Figure 4.22. SEM micrographs of the Mg-4%Zn/Al multilayered composite (a) five pass multilayered composite (b) magnified image of different layers (c) Al layer (d) anodized Al layer (e) Mg-4%Zn layer.

Fraction of recrystallized grains increased with increase in strain due to the higher rate of nucleation of new grains during recrystallization, which resulted in a relatively uniform microstructure with ultra-fine grains. The dynamic recovery and recrystallization are the reason for the ultra-fine grain structure in the SPD processed metals (Jamaat and Toroghinejad, 2014; Humphreys and Hatherly, 2004).

#### 4.2.2.2. EBSD analysis

EBSD orientation mapping (RD-ND plane) was carried out on Mg-4%Zn/Al and Mg-4%Zn/anodized Al multilayered composites subjected to 5-pass ARB process (Figure 4.23, 4.24 and 4.25). Inverse pole figure (IPF) map of the Al layer in the ARB processed Mg-4%Zn/Al multilayered composite is shown in figure 4.23. As depicted from figure 4.23 (a), 5-pass ARB processed Al grains are directed uniformly in  $\langle 111 \rangle$  orientation in the direction of rolling.

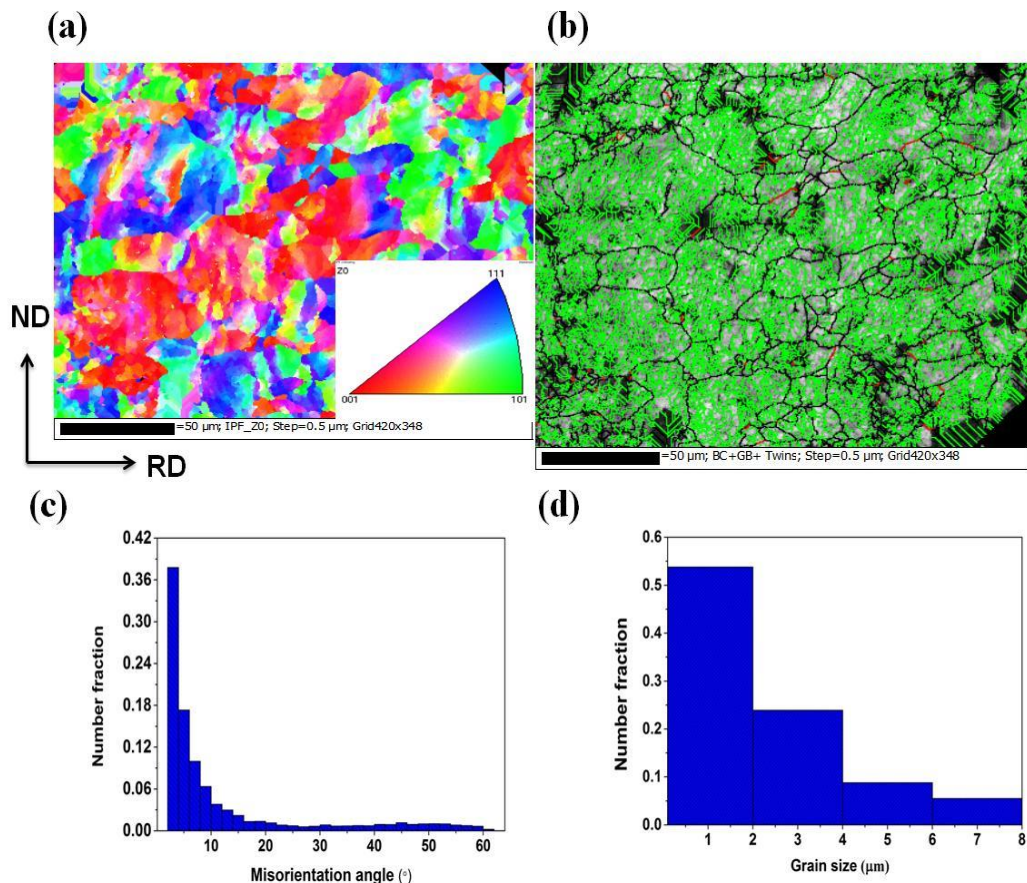


Figure 4.23. EBSD based analysis of Al layer in the Mg-4%Zn/Al multilayered composite (a) IPF map (b) Grain boundary map with twins (c) Misorientation angle distribution profile (d) Grain size distribution.



Grain boundary map shown in figure 4.23 (b) reveals fine grains with a fraction of HAGBs. The percentage of twins was found to be 0.7% as shown in figure 4.23 (b). The misorientation angle profile is as shown in figure 4.23 (c) consists of both LAGBs and HAGBs which indicates that deformation is induced as a result of dynamic recovery. Grain size variation profile (Figure 4.23 d) exhibited an average grain size as 1.5  $\mu\text{m}$  in the Al layer of multilayered composite.

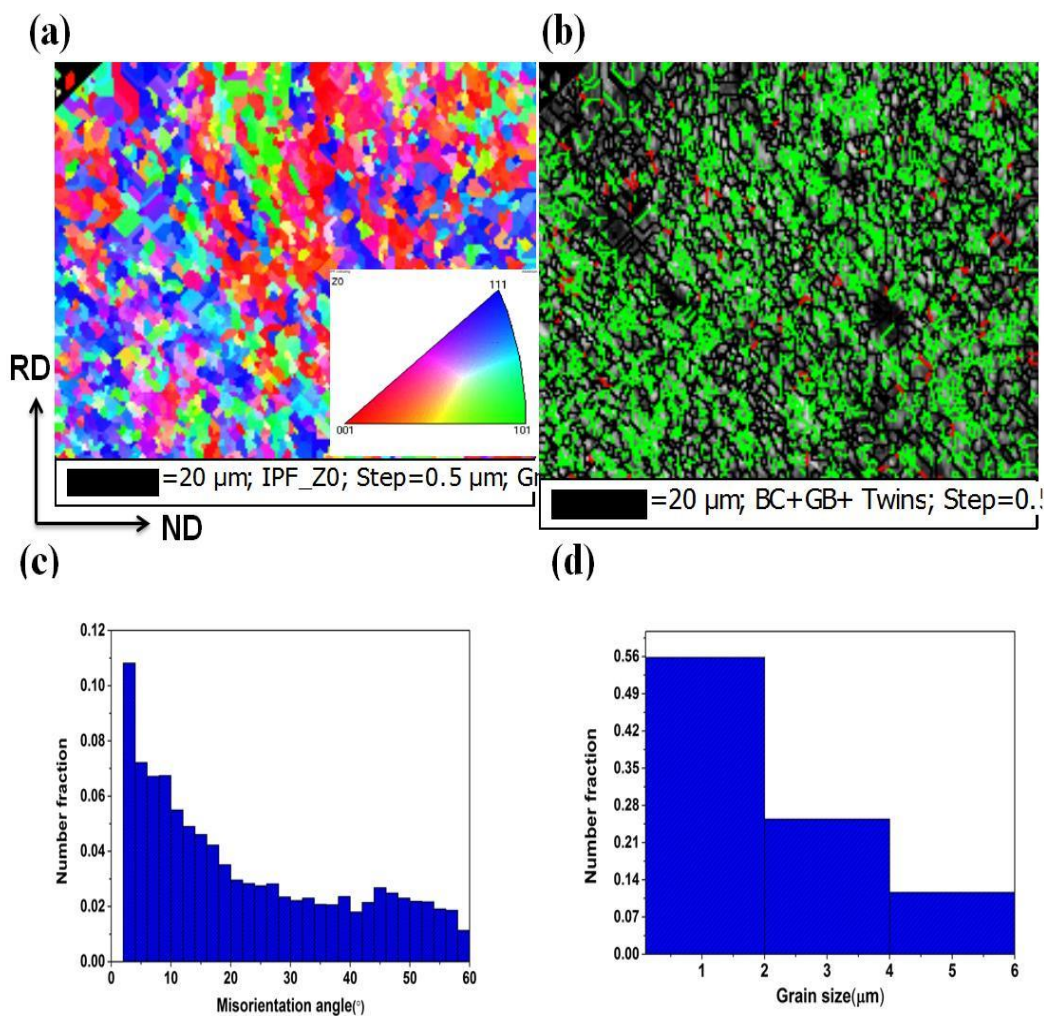


Figure 4.24. EBSD based analysis of anodized Al layer in the Mg-4%Zn/anodized Al multilayered composite (a) IPF map (b) Grain boundary map with twins (c) misorientation angle distribution profile (d) Grain size distribution.

Inverse pole figure (IPF) map of the anodized Al layer in the ARB processed Mg4%Zn/anodized Al multilayered composite is shown in figure 4.24 (a). Grain boundary map overlaid with twins is shown in figure 4.24 (b). EBSD image shows fine

grains with a fraction of HAGBs. The mechanism of formation of UFG by ARB process is by dynamic recrystallization that results in the generation of sub-micron sized grains having high angle misorientation (Roy et al. 2012) The percentage of twins was found to be 1.3% in the anodized Al layer of the 5-pass multilayered composite as shown in figure 4.24 (b). Misorientation angle distribution profile consisting of both LAGBs and HAGBs is shown in figure 4.24 (c). Grain size variation profile shown in figure 4.24 (d) exhibited average grain size as 1.3  $\mu\text{m}$  in the anodized Al layer in the Mg-4%Zn/anodized Al multilayered composite.

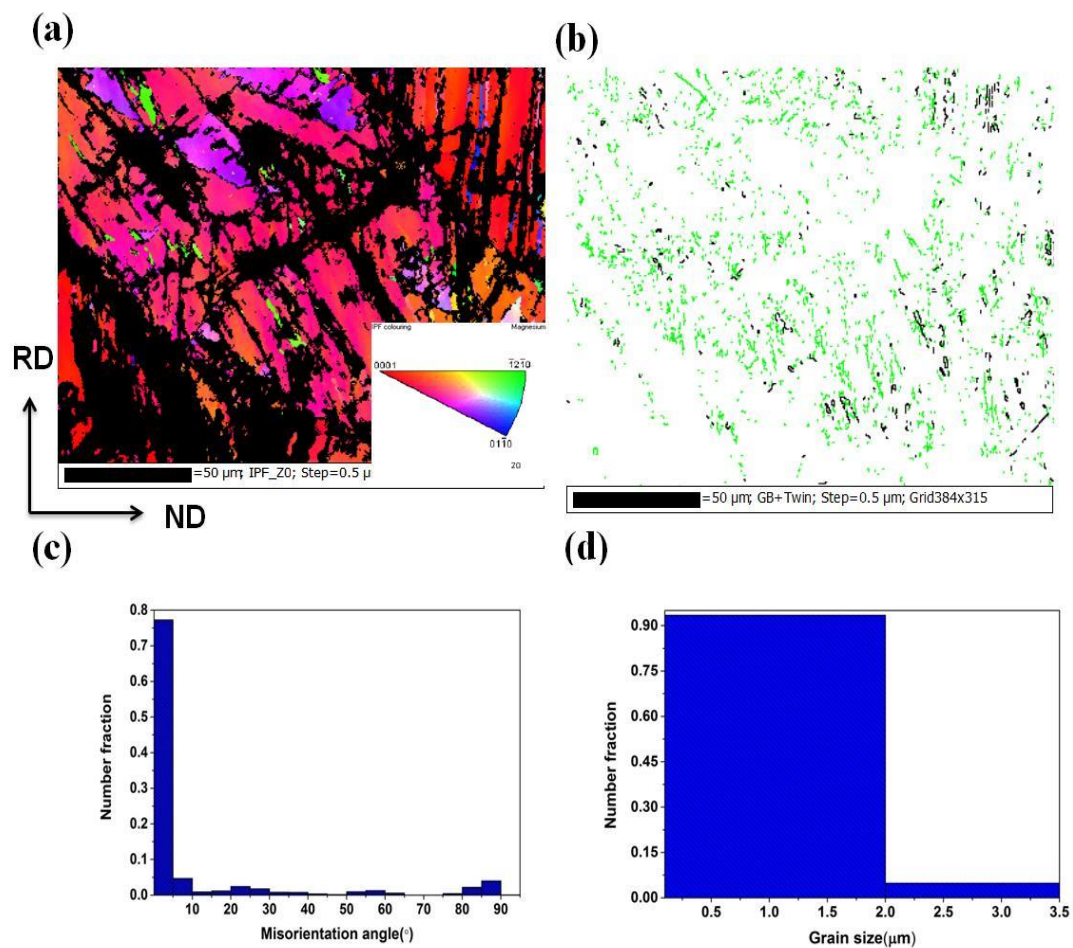


Figure 4.25. EBSD based analysis of Mg-4%Zn layer in the multilayered composite (a) IPF map (b) Grain boundary map with twins (c) misorientation angle distribution profile (d) Grain size distribution.

Inverse pole figure (IPF) map of the Mg-4%Zn layer in the ARB processed multilayered composite is shown in figure 4.25 (a). It is revealed that, Mg-4%Zn grains are directed uniformly in  $\langle 0001 \rangle$  orientation in the direction of rolling. Grain boundary map

overlaid with twins is shown in figure 4.25 (b). In the fine grained Mg alloys, slips are activated resulting in suppression of twin generation and reduction in mechanical anisotropy by grain refinement. Deformation twins disappear in the Mg alloys when the average grain size reaches less than 2  $\mu\text{m}$ . During ARB process, the original grains are divided into small crystals or domains by deformation induced boundaries and most of the deformation induced grain boundaries, become high angle at very high strain (Chino et al. 2008). As a result, misorientation angle distribution profile of the 5-pass ARB processed composites, shown in figure 4.25 (c), consists of both LAGBs and HAGBs. Grain size variation profile (Figure 4.25 d) shows the average grain size as 1  $\mu\text{m}$  in the Mg-4%Zn layer in the Mg-4%Zn/anodized Al multilayered composite.

#### 4.2.2.3 TEM analysis

Micrographs of TEM and their corresponding selected area diffraction patterns (SAED) (ND-RD plane) of the ARB processed Mg-4%Zn/Al and Mg-4%Zn/anodized Al composites are illustrated in figure 4.26.

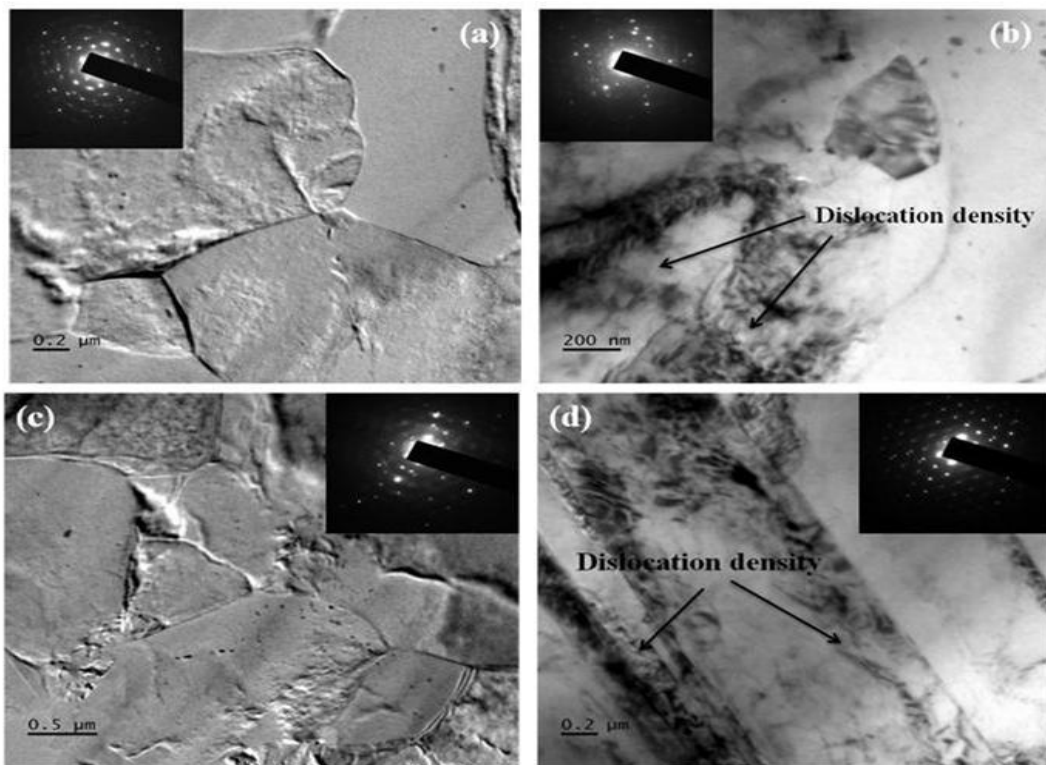


Figure 4.26. TEM micrographs and SAED patterns of the ARB processed Mg-4%Zn/Al (a & b) and Mg-4%Zn/anodized Al (c & d).

As can be seen, fine grains with dislocation tangles are present in the multilayered composites. The observed SAED patterns also depict ultra-fine grains and dislocation cells. The SAED patterns of both composites shows ring like pattern consisting of separate spots. This indicates fine grains with high angle boundaries.

#### 4.2.2.4 X-ray diffraction analysis

XRD patterns of the Mg-4%Zn/Al and Mg-4%Zn/anodized Al multilayered composite taken along the cross-section (TD plane) is shown in figure 4.27. Obtained results were compared with the data obtained from the Joint Committee on Powder Diffraction Standards (JCPDS).

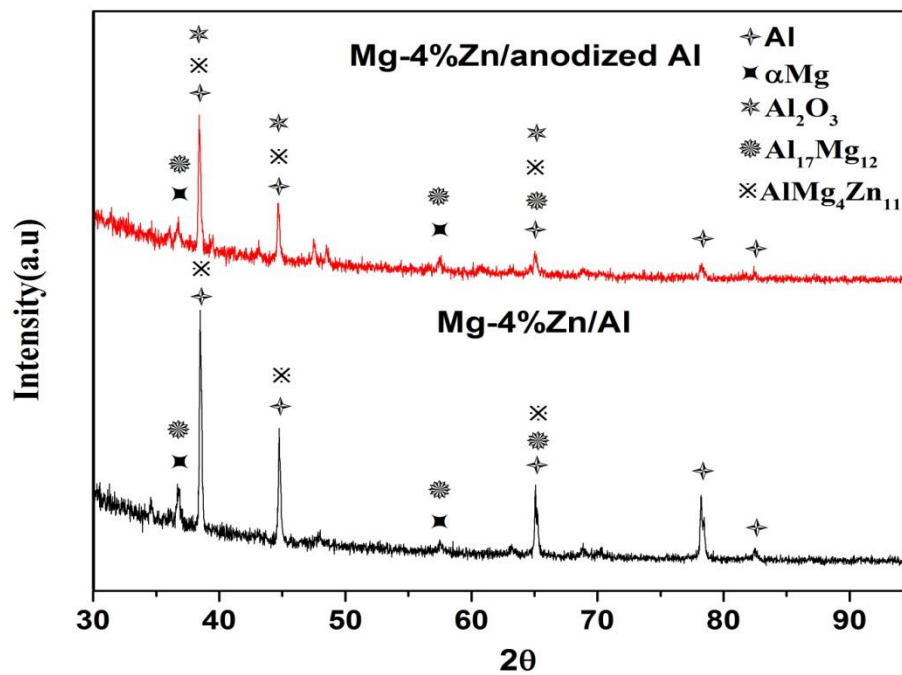


Figure 4.26. XRD patterns along the cross section of accumulative roll bonded multilayered composite.

XRD patterns revealed peaks indexed to Al,  $\alpha$ Mg, Al<sub>17</sub>Mg<sub>12</sub> and AlMg<sub>4</sub>Zn<sub>11</sub> in the multilayered composite. Mg-4%Zn/anodized Al composite shows the presence of Al<sub>2</sub>O<sub>3</sub>. Formation of intermetallics phases in multilayered composites attributed to high rolling strain during ARB at 300 °C which increases the diffusion between Mg-4%Zn and Al layers of the multilayered composite.

#### 4.2.2.5 Density test

Density test was carried out according to Archimedes principle for wrought Mg-4%Zn, Al, anodized Al and accumulative roll bonded multilayered composite. Initially, the weight of the samples was measured in air and under water. The calculated density is illustrated in table 4.7. The density of the roll bonded multilayered composites is 20.5% lighter in weight as compared to Al-1100.

Table 4.7. Density test results.

Sample	Density (kg/m <sup>3</sup> )
Mg-4%Zn alloy	1780
Al sheet	2691
Anodized Al sheet	2696
Mg-4%Zn/Al composite	2145
Mg-4%Zn/anodized Al composite	2147

#### 4.2.2.6 Microhardness test

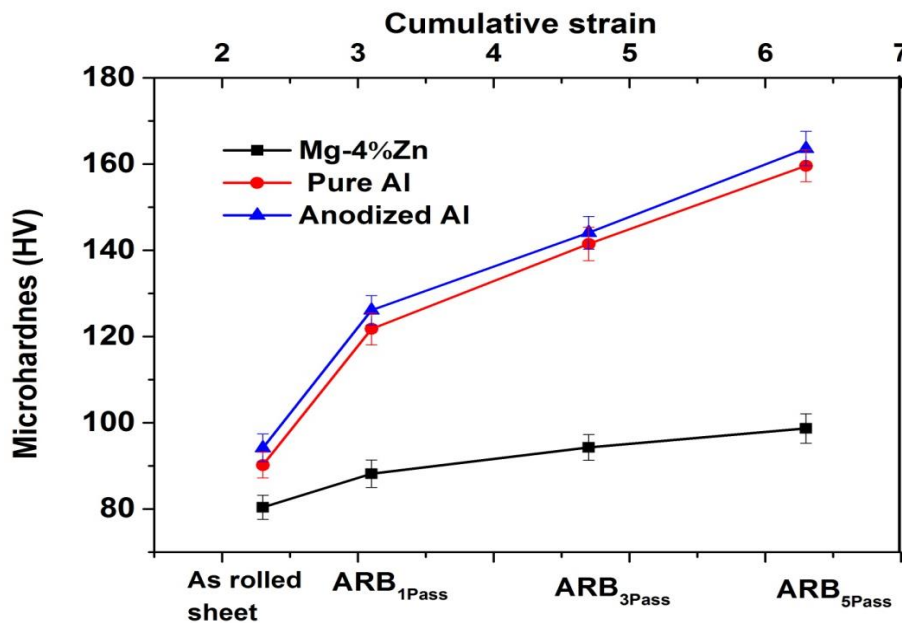


Figure 4.27. Microhardness variation in different layers of the Mg-4%Zn/Al and Mg-4%Zn/anodized Al composite with number of ARB passes.

Microhardness variations of Mg-4%Zn, Al and anodized Al layers after different ARB passes can be seen in figure 4.28. It is revealed that the microhardness values were increased with the increase in strain. After the first cycle, significant increase in hardness value could be observed which can be attributed to increase in the density of dislocations and their interactions. As the number of ARB passes increases, microhardness value increases due to strain hardening and grain refinement process. After five ARB passes, microhardness of the Mg-4%Zn layer, Al layer and anodized Al layer is about 1.2 times, ~ 1.76 times and ~1.73 times respectively, in comparison with counterpart rolled alloys. Anodized Al layer in the Mg-4%Zn/anodized Al composite exhibited higher hardness values as compared to Al layer in the Mg-4%Zn/Al composite due to uniform distribution of harder alumina ( $\text{Al}_2\text{O}_3$ ) particles.

#### **4.2.2.7 Tensile test**

Figure 4.29 (a) shows variation in tensile properties of the as rolled Al, Mg-4%Zn and roll bonded Mg-4%Zn/Al multilayered composite. It is observed that, YS and UTS improved considerably within number of ARB passes. During the early stages of ARB work hardening rate is dominant. After 2 pass, higher strength is achieved by grain structure and as the number of passes increases, gradual evolution of ultrafine grained structure plays the main role in strengthening. It is related to the increasing number of ultrafine grains and largely misoriented grain boundaries (Saito et al. 1998). Maximum yield strength and tensile strength reached to 189 MPa and 268 MPa respectively after fifth pass ARB process which is enhanced by 27.6% and 38.9% respectively in comparison to as rolled Mg-4%Zn alloy. It has been reported that strength variations in severely deformed composites are governed by two main strengthening mechanisms; first is strain hardening by dislocations and the second is grain boundary strengthening or grain refinement (Gubicza et al. 2007). Figure 4.29 (b) shows variation of tensile strength and ductility of Mg-4%Zn/anodized Al multilayered composite subjected to different ARB passes. Maximum YS and UTS of 191 MPa and 272 MPa was obtained after fifth pass ARB process.

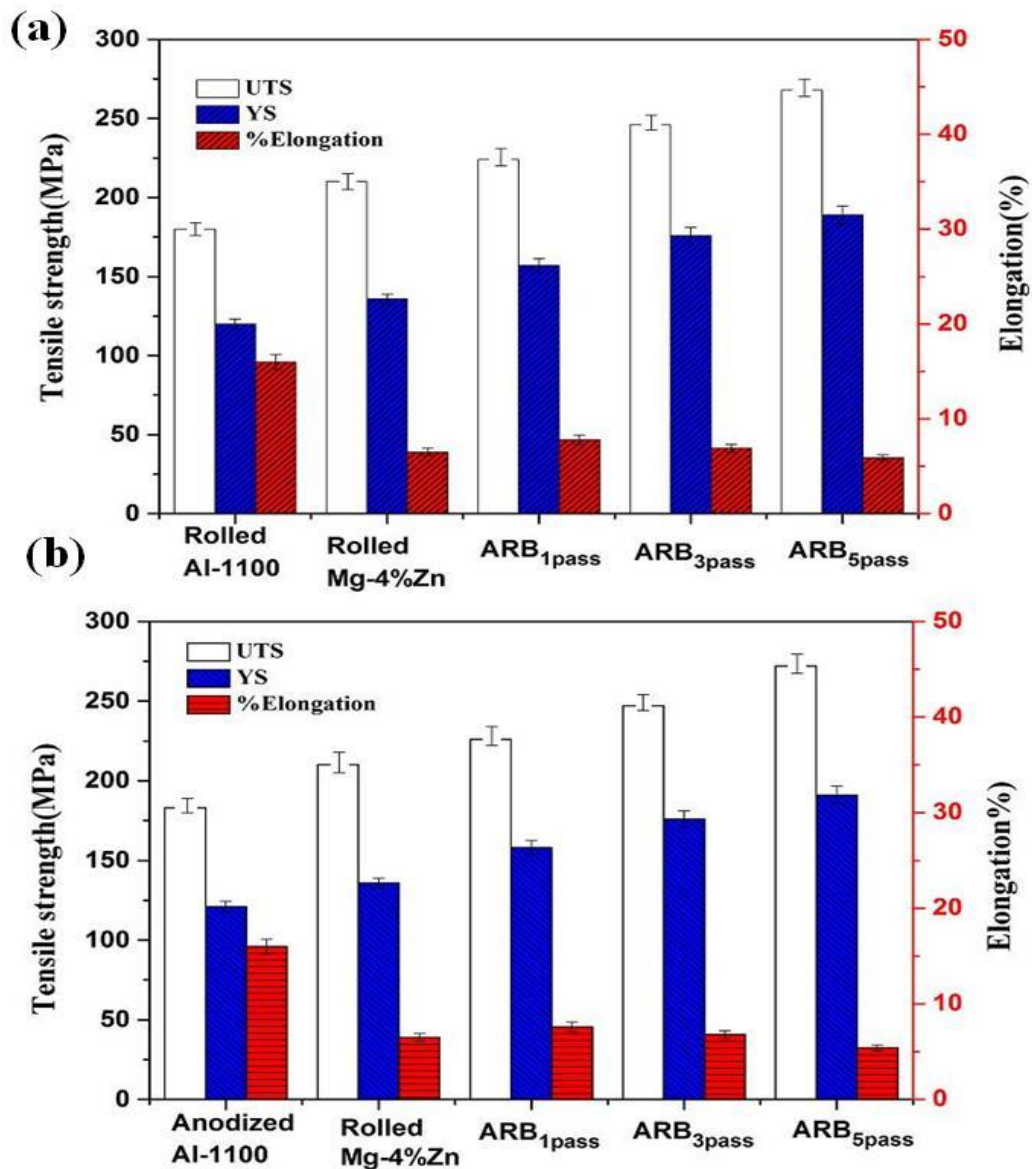


Figure 4.28. Variation of UTS, YS and percentage elongation of the multilayered composite with different ARB passes (a) Mg-4%Zn/Al composite (b) Mg-4%Zn/anodized Al composite.

Enhancement of YS and UTS is about 29.5% and 40.4% respectively in comparison to as rolled Mg-4%Zn alloy. YS and UTS of the Mg-4%Zn/anodized Al better as compared to Mg-4%Zn/Al composite is not only from strain hardening and grain refinement, but also, it is boosted by alumina particle ( $Al_2O_3$ ), resulted from the anodization process (Alizadeh, 2011). Alumina particle acts as a barrier to dislocation movement along with strain hardening and grain refinement in the Mg-4%Zn/anodized Al multilayered composite. During initial passes of ARB, percentage elongation of

multilayered composite is higher than that of the as rolled Mg-4%Zn alloy. After 3-pass ARB, the elongation gradually decreases due to strain hardening as well as UFG structure.

#### 4.2.2.8 Fractography

Fractographs after tensile test are shown in figure 4.30. Mg-4%Zn/Al and Mg-4%Zn/anodized Al composite exhibited a shear ductile fracture, having dimples and shear zones.

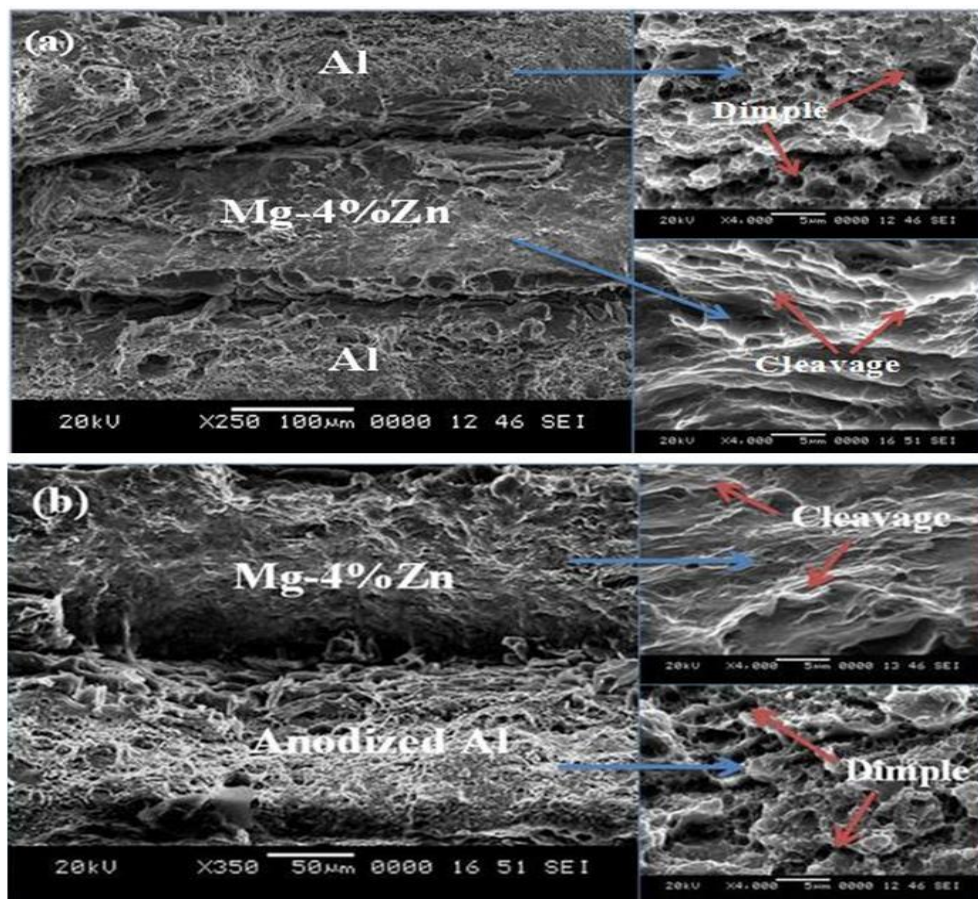


Figure 4.30. SEM micrographs of the fractured ARB processed (a) Mg-4%Zn/Al and (b) Mg-4%Zn/anodized Al multilayered composite.

Mg-4%Zn layer in composite was fractured in the shear mode and free from dimples which appear to be transgranular brittle fracture due to hexagonal closed packed (HCP) structure. The magnified image of the Al and anodized Al layer in the 5-pass ARB processed Mg-4%Zn/Al and Mg-4%Zn/anodized Al composite reveals dimples as a



result of ductile fracture (Hertzberg, 1989). The appearance of micro voids in the fractured surfaces are being affected by the state of shear stress. Therefore, the dimples are elongated which shows shear ductile failure.

#### 4.2.2.9 Potentiodynamic polarization

Figure 4.31 shows the polarization curves of the Mg-4%Zn alloy and multilayered composites in the solution of 0.1 M NaCl. Tafel fitting is a common method to analyze the polarization curves, from which the corrosion rate, corrosion current density ( $i_{\text{corr}}$ ) and corrosion potential ( $E_{\text{corr}}$ ) can be obtained. All the polarization curves were analyzed by Tafel fitting, and the estimated corrosion parameters are summarized in table 4.8. A shift of  $E_{\text{corr}}$  values was observed in noble direction after ARB processing and  $E_{\text{corr}}$  values were found to be -1.45, -1.32 and -1.28 V<sub>SCE</sub> for wrought Mg-4%Zn alloy, Mg-4%Zn/Al and Mg-4%Zn/anodized Al respectively. Multilayered composites exhibited less corrosion rate and corrosion current density as compared to as rolled Mg-4%Zn alloys.

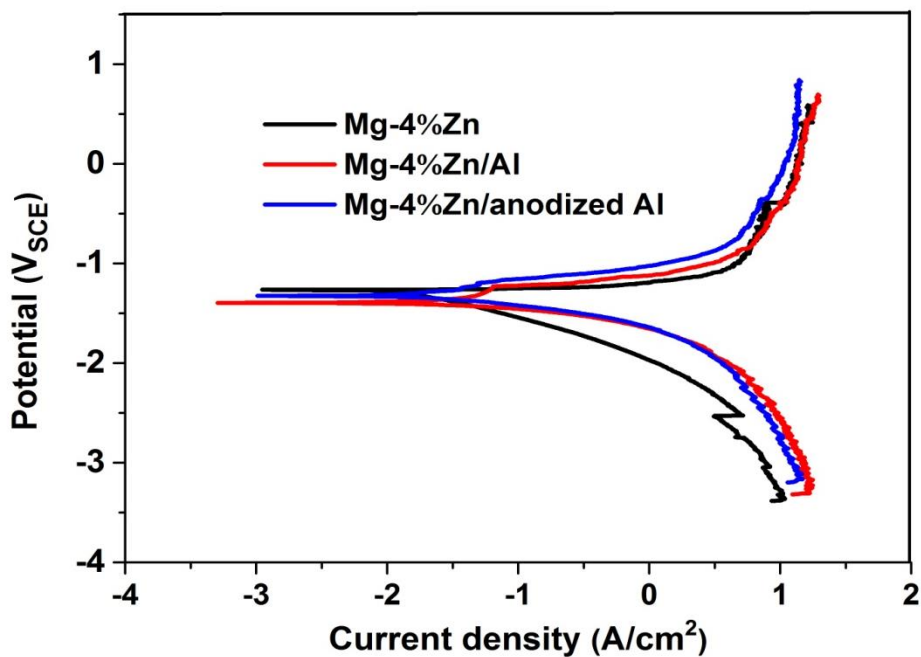


Figure 4.31. Potentiodynamic polarization curves of the Mg-4%Zn, Mg-4%Zn/Al and Mg-4% Zn/anodized Al.

Table 4.8. Potentiodynamic polarization curves data of the Mg-4%Zn, Mg-4%Zn/Al and Mg-4% Zn/anodized Al.

<b>Materials</b>	$E_{\text{corr}}$ (V <sub>SCE</sub> )	$i_{\text{corr}}$ ( $\mu\text{A}/\text{cm}^2$ )	$\beta_a$ (mV/decade )	$\beta_c$ (mV/decade )	<b>Corrosion rate (mm/y)</b>
Mg-4%Zn	-1.45	58.99	211.9	-285.4	1.77
Mg- 4%Zn/Al	-1.32	25.25	141.6	-188.6	1.30
Mg4%Zn/ anodized Al	-1.28	14.98	147.3	-168.2	0.74

Multilayered composite subjected to ARB process up to 5-passes exhibited grain size less than 1.5  $\mu\text{m}$ . These small sized grains create more grain boundaries that act as a corrosion barrier (Argade et al. 2012; Ralston and Birbilis, 2010). During ARB process, intermetallics ( $\text{Al}_{12}\text{Mg}_{17}$  and  $\text{AlMg}_4\text{Zn}_{11}$ ) formed are refined and uniformly distributed throughout the structure which acts as an anodic barrier to inhibit the overall corrosion. Lowest  $i_{\text{corr}}$  values were observed in Mg-4%Zn/anodized Al composite, due to uniform distribution of alumina ( $\text{Al}_2\text{O}_3$ ) resulted from the anodization process as well as microstructure with ultra-fine grains and  $\beta$  phases ( $\text{Al}_{12}\text{Mg}_{17}$  and  $\text{AlMg}_4\text{Zn}_{11}$ ) formed during ARB process.

Surface morphology after electrochemical polarization test in 0.1 M NaCl solution is shown in figure 4.32. Severe corrosion, as well as, some of the pits and cracks were observed on the surface of the rolled Mg-4%Zn alloy, as shown in figure 4.32 (a). Layer-wise corrosion can be observed on the multilayered composite. Bright areas shown in figure 4.32 (b), which is Mg-4%Zn layer, signifies the highest rate of corrosion (magnesium hydroxide). However, Mg-4%Zn/anodized Al multilayered composite did not show any severe dissolution like in Mg-4%Zn/Al composite because of anodization of Al before ARB process as shown in figure 4.32 (c).

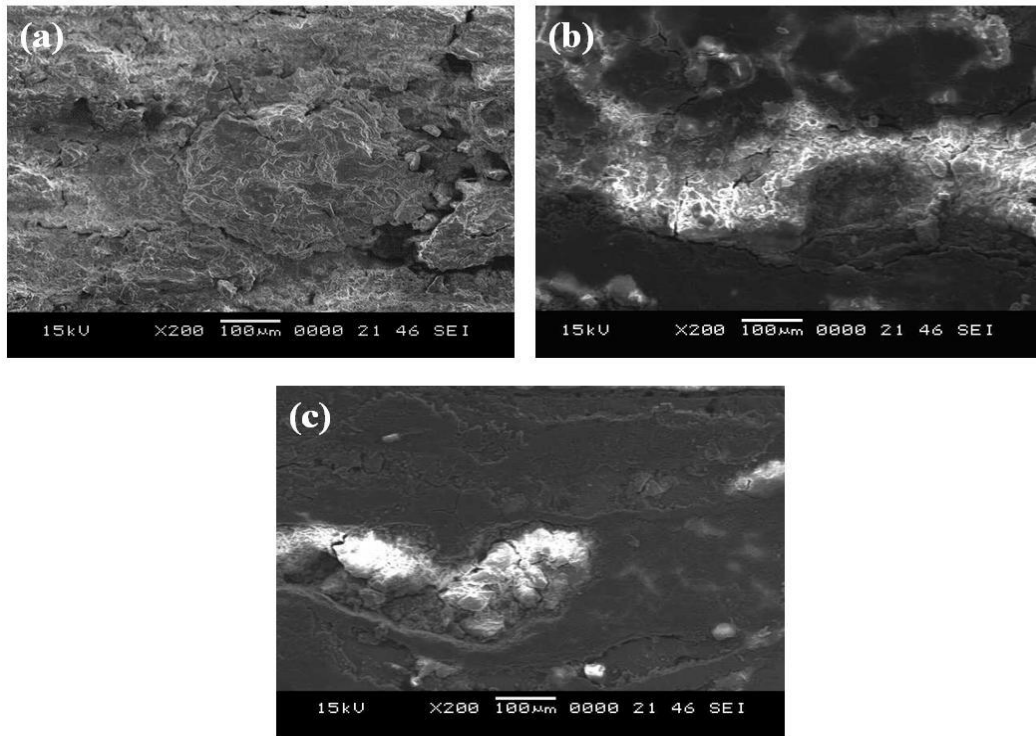


Figure 4.32. SEM micrographs of corroded (a) rolled Mg-4%Zn (b) Mg-4%Zn/Al and (c) Mg 4%Zn/anodized Al after electrochemical test in a 0.1 M NaCl solution.

#### 4.2.2.10 Immersion test

Hydrogen evolution rate and corresponding corrosion rate of the wrought Mg-4%Zn alloy and ARB processed multilayered composites are illustrated in table 4.9.

Table 4.9. Immersion test results.

Materials	Hydrogen evolution rate (ml/cm <sup>2</sup> /d)	Corrosion rate (mm/y)
Mg-4%Zn	1.02	2.26
Mg-4%Zn/Al	0.58	1.09
Mg-4%Zn/anodized Al	0.32	0.59

Hydrogen evolution drastically reduced to about 43.1% and 68.6% in Mg-4%Zn/Al and Mg-4%Zn/anodized Al respectively as compared with as rolled Mg-4%Zn alloy. The degradation of the ARB processed multilayered composite is slower than in wrought

Mg-4%Zn alloy, due to refined microstructure and the presence of  $\beta$  phases ( $\text{Al}_{12}\text{Mg}_{17}$  and  $\text{AlMg}_4\text{Zn}_{11}$ ). Further, Mg-4%Zn/anodized Al composite showed less hydrogen evolution compared to Mg-4%Zn/Al multilayered composite due to presence of alumina.

#### **4.2.3 Mg-6%Zn/Al and Mg-6%Zn/anodized Al multilayered composites**

Mg-6%Zn/Al and Mg-6%Zn/anodized-Al multilayered composite are developed using ARB. Mg-6%Zn alloy is roll bonded with pure Al and anodized Al at 300 °C up to 5-pass to develop multilayered composites. Microstructural characterization was done using scanning electron microscope, energy-dispersive X-ray spectroscopy, electron back scattered diffraction and transmission electron microscope and phase analysis by x-ray diffraction. In addition, mechanical properties were evaluated by microhardness and tensile strength tests. Corrosion behavior of the multilayered composite was examined using electrochemical polarization and immersion test.

##### **4.2.3.1 Microstructural Analysis**

SEM micrographs of the 5-pass ARB processed Mg-6%Zn/ anodized Al multilayered composite, shows alternative layers of Mg-6%Zn and anodized Al depicted in figure 4.33. Absence of cracks or de-lamination along the interfaces of the multilayer composite indicate good bonding between Mg-6%Zn alloy and anodized Al, but slight waviness layer structure was observed. Thickness of the multilayered composite decreases with increase in number of ARB passes and finally, 5-pass ARB processed composite layer thickness was found to be in the range of 40-50  $\mu\text{m}$ . Ultrafine grains are depicted in the ARB processed Al layer (figure 4.33 c), anodized Al layer (figure 4.33 d), Mg-6%Zn layer (figure 4.33 e) in the Mg-6%Zn/Al and Mg-6%Zn/anodized Al multilayered composites. Energy dispersive spectroscopy data shows the area comparison evaluation in the alternate layers of Al (region I) and Mg-6%Zn (region II) at the interface of Mg-6%Zn and Al (region III).

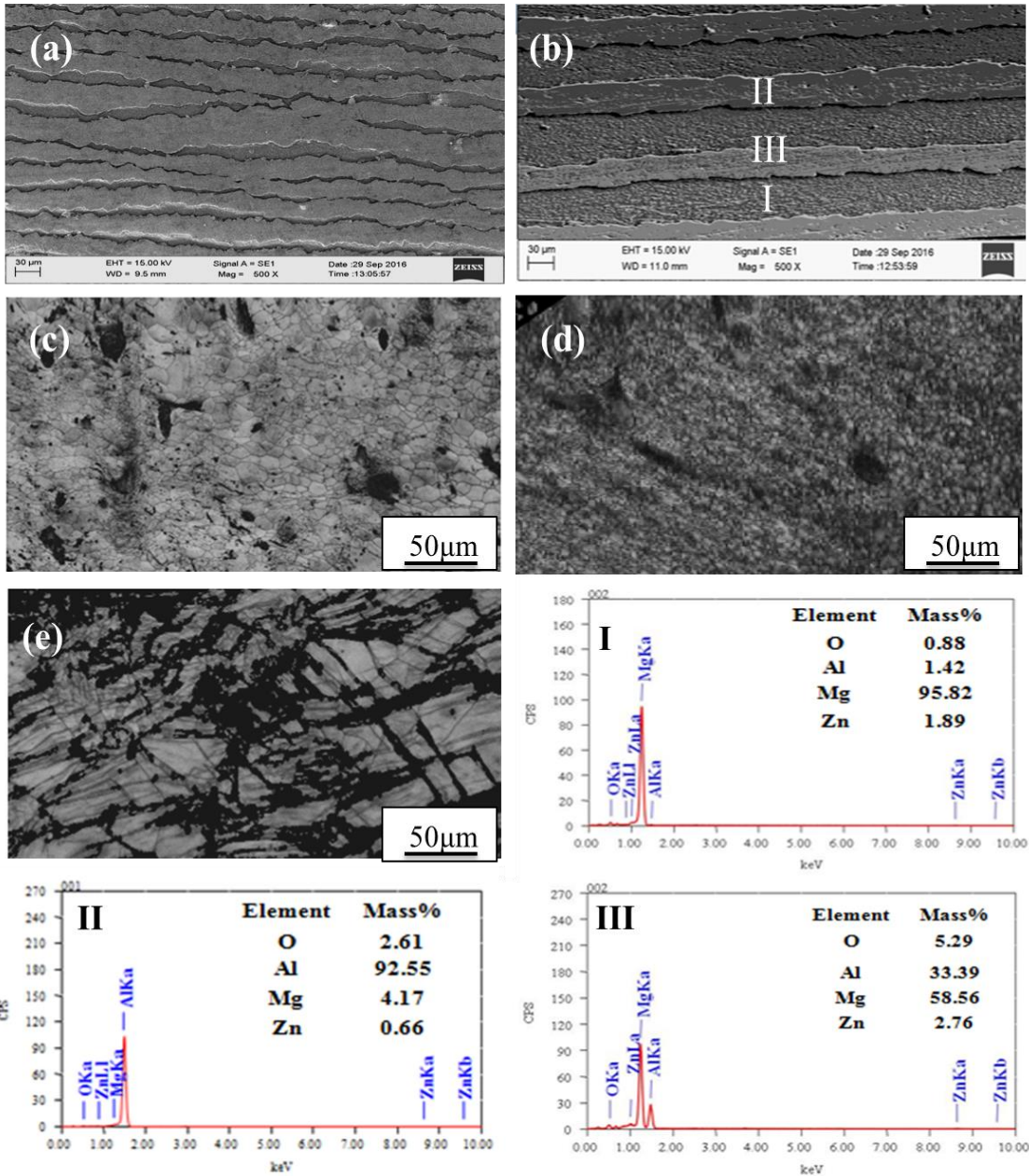


Figure 4.33. SEM micrographs of (a) 5-pass ARB processed Mg-6%Zn/anodized Al multilayered composite (b) Magnified image (c) Micrographs revealing the grains in Al layer (d) Anodized Al layer (e) Mg-6%Zn layer and (I) EDS of the Mg-6%Zn layer (II) anodized Al layer (III) Interphase between Mg-6%Zn/anodized Al layer.

Mg-2%Zn layers in the multilayered composite undergoes a necking and finally ruptured because of brittleness characteristics of Mg alloys. Normally, the plastic instabilities caused by different flow properties of constituent phases make the relatively hard phase to neck and finally to rupture during the deformation of dissimilar metals (Wu et al. 2010; Yazar, et al. 2005). Microstructure of Mg-6%Zn layer, Al and

anodized Al layer revealed ultrafine grains due to grain subdivision and shear strain between strip and roller during ARB process (Lee et al. 2002). Fraction of recrystallized grains increased with increase in strain due to the higher rate of nucleation of new grains during recrystallization, which resulted in a relatively uniform microstructure with ultra-fine grains.

#### 4.2.3.2. EBSD analysis

EBSD analysis of the Al layer (on ND-RD plane) in the 5-pass ARB Mg-6%Zn/Al multilayered composites is shown in figure 4.33. Figure 4.34 (a) shows the inverse pole figure map where standard stereographic triangle corresponds to various crystallographic directions indicated by various colors.

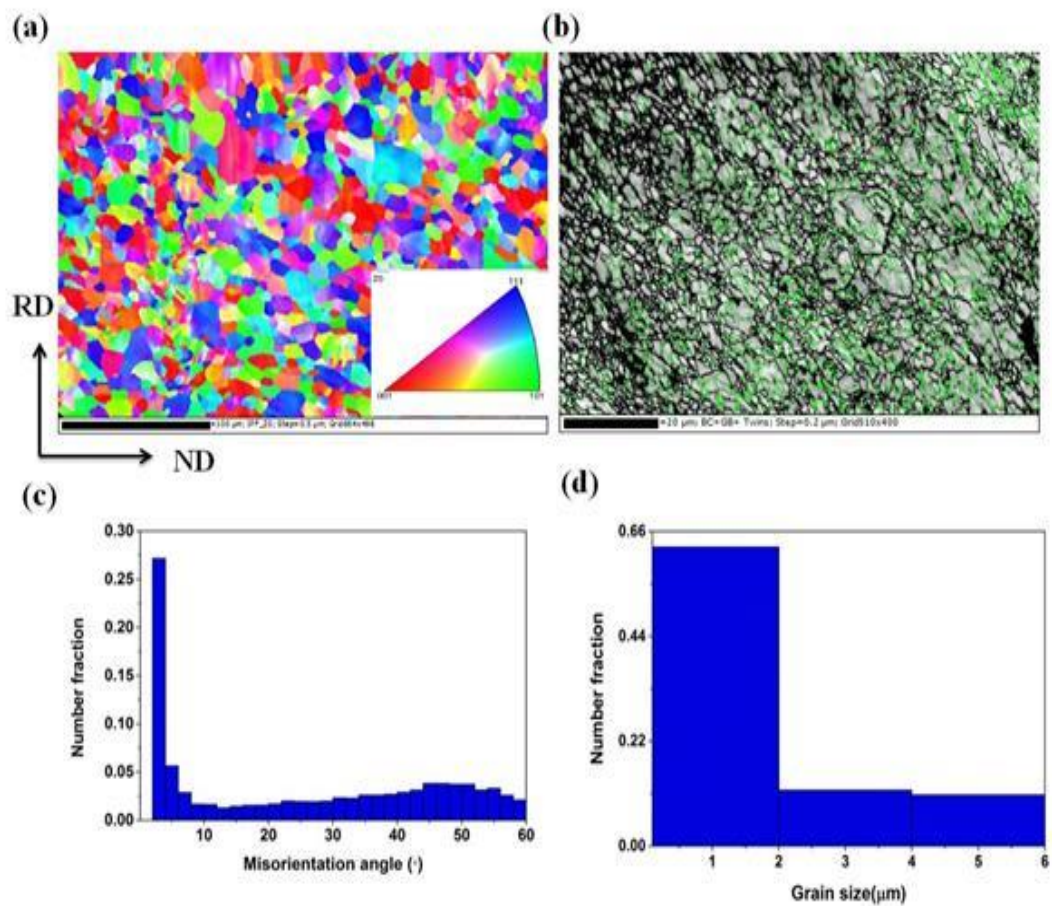


Figure 4.34. EBSD based analysis of Al layer in the Mg-6%Zn/Al multilayered composite (a) IPF map (b) Misorientation angle distribution profile (c) Grain boundary map with twins (d) Grain size distribution.

Grains are directed in the direction of rolling, which is  $\langle 001 \rangle$  orientation. Misorientation angle distribution profile (Figure 4.34 b) revealed some fraction of high angle grain boundaries (HAGB) due large strain during deformation process with ARB passes. If the number of ARB passes increases, density of dislocations increases which results in increased fraction of high angle boundaries (Hansen and Juul, 2011). At the higher ARB passes, the area of grain boundaries increased due to internal energy in the deformed material (Lee et al. 2002). Grain boundary map overlaid with twins is shown in figure 4.34 (c). Percentage of twins has been calculated from the HKL channel 5 software and found to be 1.3 % and occurs along with some shear bands. The average grain size was found to be  $1.8 \mu\text{m}$  as plotted in figure 4.34 (d).

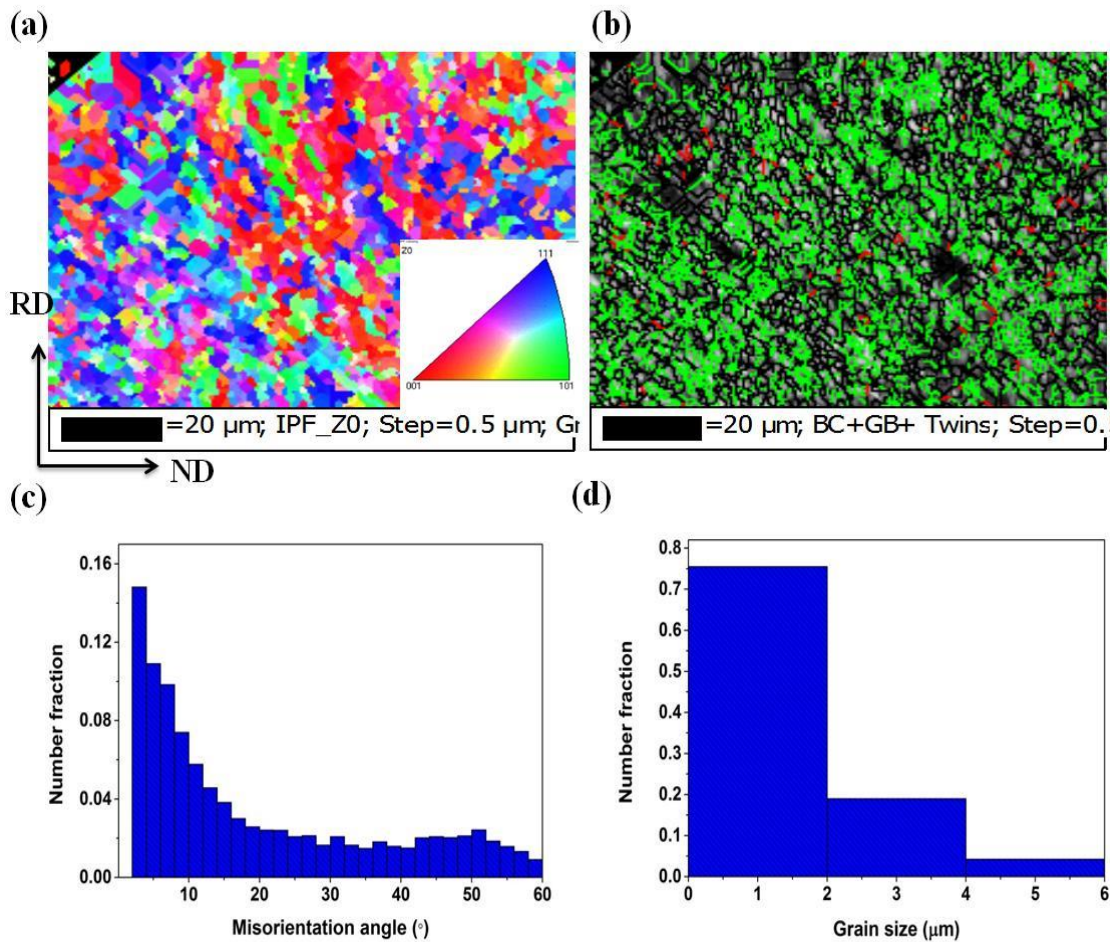


Figure 4.35. EBSD based analysis of anodized Al layer in the Mg-6%Zn/anodized Al multilayered composite (a) IPF map (b) Misorientation angle distribution profile (c) IPF map overlaid with grain boundaries and twins (d) Grain size distribution.

Figure 4.35 depicts EBSD analysis of the anodized Al layer (on ND-RD plane) in the Mg-6%Zn/anodized Al multilayered composite. IPF map (Figure 4.35 a) revealed that anodized Al layer grains are directed uniformly in  $\langle 001 \rangle$  orientation in the direction of rolling. Misorientation angle distribution profile (Figure 4.35 b) consists of subgrains with a fraction of HABs due to occurrence of dynamic recrystallization during ARB process. Grain boundary map overlaid with twins is shown in figure 4.35 (c) which consists of equiaxed grains with some fraction of HABs. The percentage of twins found to be 1.4%. Grain size variation profile (Figure 4.35 d) exhibited average grain size of 1.6  $\mu\text{m}$ .

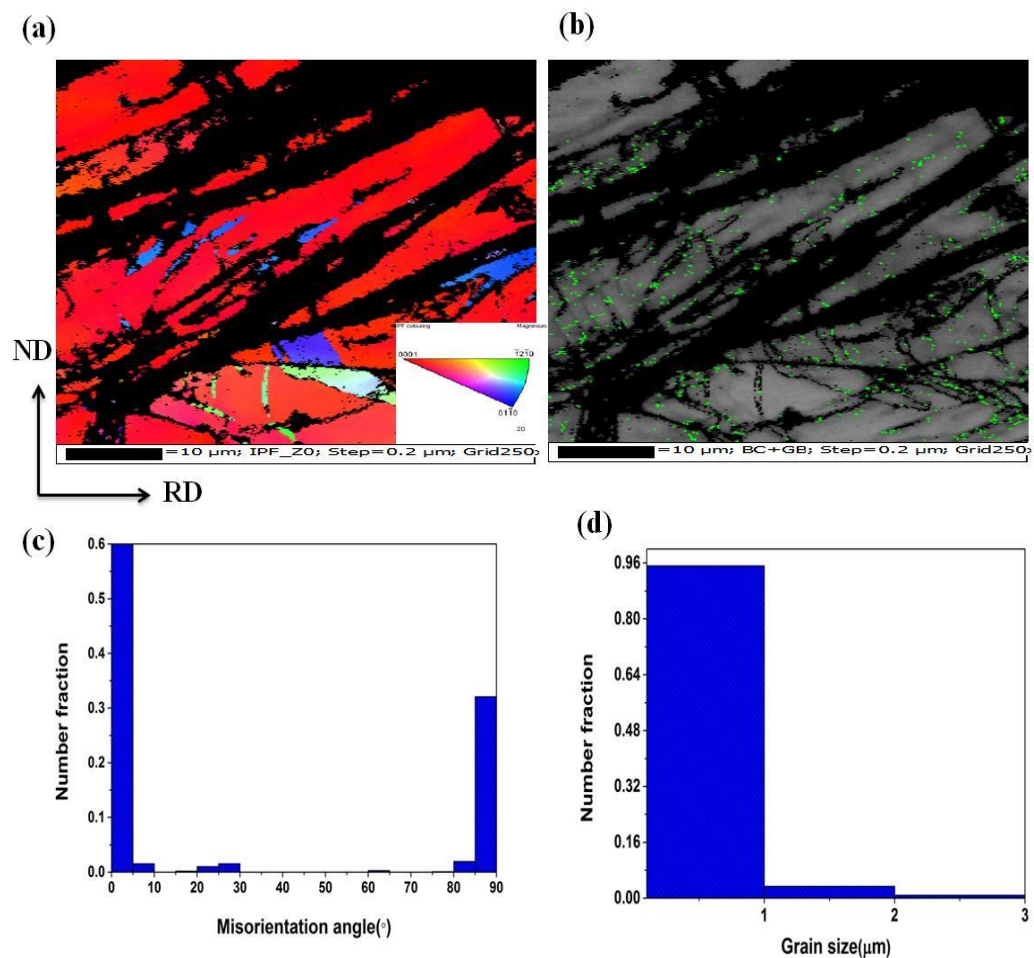


Figure 4.36. EBSD based analysis of Mg-6%Zn layer in the multilayered composite (a) IPF map (b) Grain boundary map overlaid with twins (c) misorientation angle distribution profile (d) Grain size distribution.

Figure 4.36 depicts EBSD based analysis of the Mg-6%Zn layer (ND-RD plan) in the multilayered composites. IPF map (figure 4.36 a) revealed that grains are directed



uniformly in  $\langle 0001 \rangle$  orientation in the direction of rolling. Misorientation angle distribution profile (figure 4.36 b) exhibited both LAGBs and HAGBs in Mg-6%Zn layer in the multilayered composite. Figure 4.36 (c) shows, uniform distribution of ultra fine grains and did not shows any twins because when the grain size decreases, the twin nucleation decreases. Grain size variation profile (Figure 4.36 d) exhibited average grain size of 0.6  $\mu\text{m}$ . Fraction of recrystallized grains increased with increase in strain due to the higher rate of nucleation of new grains during recrystallization, which resulted in a relatively uniform microstructure with fine grains. In the fine grained Mg alloys, slips are activated resulting in suppression of twins and reduction in mechanical anisotropy by grain refinement. Deformation twins disappear in the Mg alloys, when the average grain size reduces to  $< 2 \mu\text{m}$  (Chino et al. 2008).

#### 4.2.3.3 TEM analysis

TEM micrographs of the Mg-6%Zn/Al and Mg-6%Zn/anodized Al multilayered composite revealed fine grains with high degree of misorientation as shown in figure 4.37 a & b.

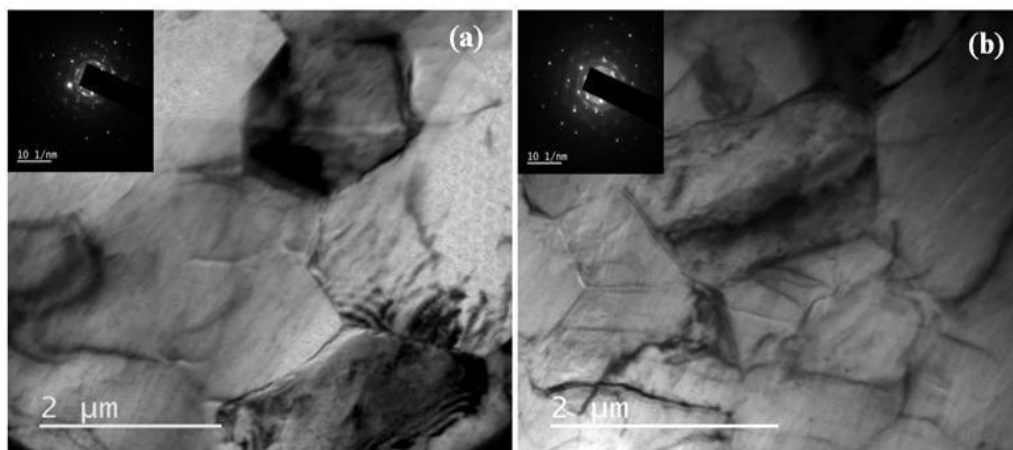


Figure 4.37. TEM micrographs and SAED patterns of the 5-pass ARB processed (a) Mg-6%Zn/Al (b) Mg-6%Zn/anodized Al multilayered composite.

Density of dislocations can be observed inside the grains. During ARB process, high strain is introduced, resulting in subdivision of grains, due to formation of planar dislocation boundaries and incidental dislocation boundaries. Higher misorientations form across these dislocation boundaries and spacing of boundaries reduces, which helps to create fine grains. SAED patterns revealed the formation of rings, which

confirms the fine grain structure in the multilayered composites. Grain refinement is because of dynamic recrystallization.

#### 4.2.3.4 X-ray diffraction analysis

XRD results for the phase constituents along the cross section of 5-pass ARB processed multilayered composites are shown in figure 4.38.

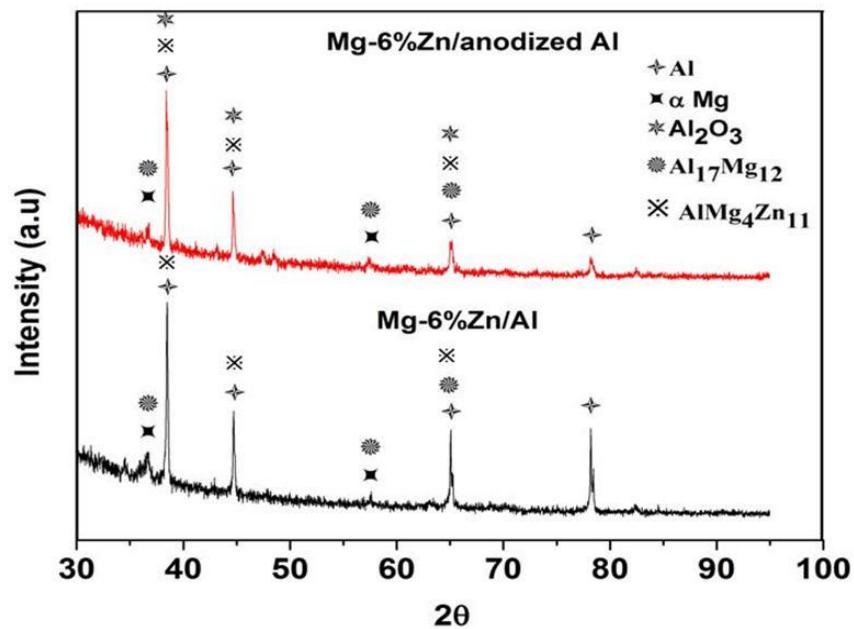


Figure 4.38. XRD analysis along the cross section of ARB processed multilayered composite.

Results were compared with the data obtained from the Joint Committee on Powder Diffraction Standards (JCPDS). Multilayered composites revealed peaks of Al,  $\alpha$ Mg, Al<sub>17</sub>Mg<sub>12</sub> and AlMg<sub>4</sub>Zn<sub>11</sub>. Multilayered composite exhibited intermetallic compounds due to inter diffusion between Al, Mg and Zn because of high strain during ARB at 300 °C. Mg-6%Zn/anodized Al multilayered composite exhibited Al<sub>2</sub>O<sub>3</sub> peak due to anodization on the Al sheet before ARB process.

#### 4.2.3.5 Density

Density test results are illustrated in table 4.10. Mg-6%Zn/Al and Mg-6%Zn/anodized Al multilayered composites were found to be 21.6% times light weight as compared to pure Al.

Table 4.10. Density test results.

Materials	Density (kg/m <sup>3</sup> )
Mg-6%Zn alloy	1781
Al sheet	2691
Anodized Al sheet	2696
Mg-6%Zn/Al composite	2109
Mg-6%Zn/anodized Al composite	2112

#### 4.2.3.6 Microhardness

Microhardness variation of multilayered composite (Figure 4.39) depicted that, as the number of ARB passes increases, microhardness of Mg-6%Zn, Al and anodized Al layers increases.

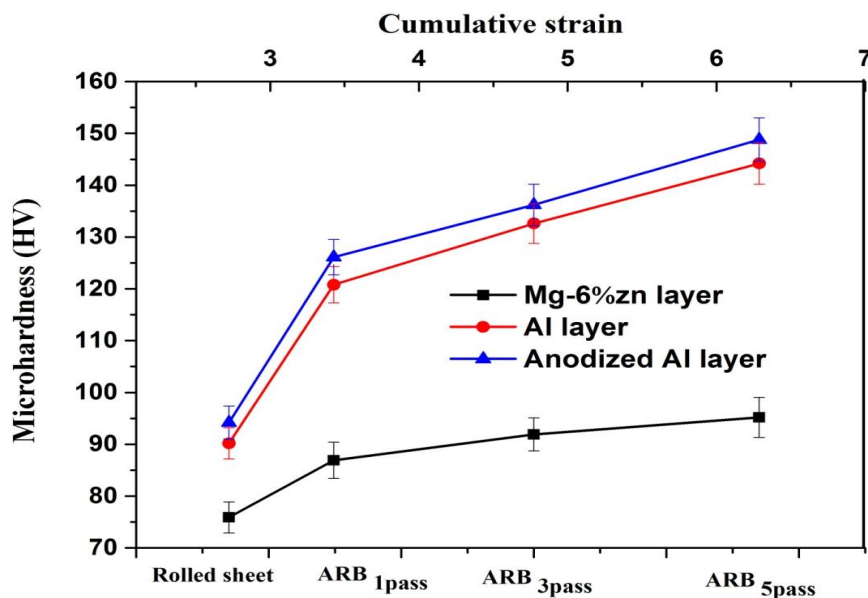


Figure 4.39. Microhardness variation of composite layers of the Mg-6%Zn, Al and anodized Al at different ARB passes.

During initial passes of ARB process, improvement of hardness was attributed to strain hardening (based on the density of dislocations and interactions between them) during ARB process. Cumulative strain accumulated in the roll bonded samples can be given by equation 3.3. Cumulative strain was found to be 3.2, 4.7 and 6.3 for 1, 3 and 5 pass

ARB multilayered composites, respectively. After the first pass, microhardness increased rapidly which is due to the work hardening as a result of increased dislocations density. Improvement of microhardness at higher passes of ARB is due to combined effect of dislocation density increment and grain refinement. Microhardness of the 5-pass multilayered composite layers increased to 95.2 HV for Mg-2%Zn, 144.2 HV for Al and 148.8 HV for anodized Al. Microhardness of the multilayered composites is also affected by the presence of intermetallic ( $\text{Al}_{17}\text{Mg}_{12}$  and  $\text{AlMg}_4\text{Zn}_{11}$ ) formed during ARB process. In the case of Mg-6%Zn/anodized Al multilayered composites harder alumina particles are distributed uniformly in the microstructure during ARB process and act as a barrier to the dislocation movement.

#### **4.2.3.7 Tensile strength test**

Variation of UTS, YS and elongation of Mg-6%Zn/Al and Mg-6%Zn/anodized Al composites at different ARB passes are shown in Figure 4.40 (a & b). As can be seen, the strength of multilayered composite increases with increase in number of ARB passes. Mg-6%Zn/Al composite exhibited improved YS and UTS of about 1.52 and 1.34 times and also Mg-6%Zn/anodized Al composite exhibited improved YS and UTS by of about 1.46 and 1.36 times, respectively, as compared to rolled Mg-6%Zn alloy. Improvement of strength in initial passes of ARB is due to strain hardening or dislocation strengthening mechanism. Strength improvement at the higher ARB passes is due to formation of fine grain structure, largely misoriented grain boundaries (Terada et al. 2007) and formation of intermetallic phases (Schmidt et al. 2011). At higher ARB passes, work hardening effect gradually decreases, as the number of fine grains with high-angle boundaries increases. Total elongation decreases with increasing number of ARB passes. During the initial passes, the composites exhibited higher elongation because of the presence of highly ductile element Al in the equal quantity with Mg-6%Zn. At the higher passes, the total elongation decreases due to strain hardening and refined grains.

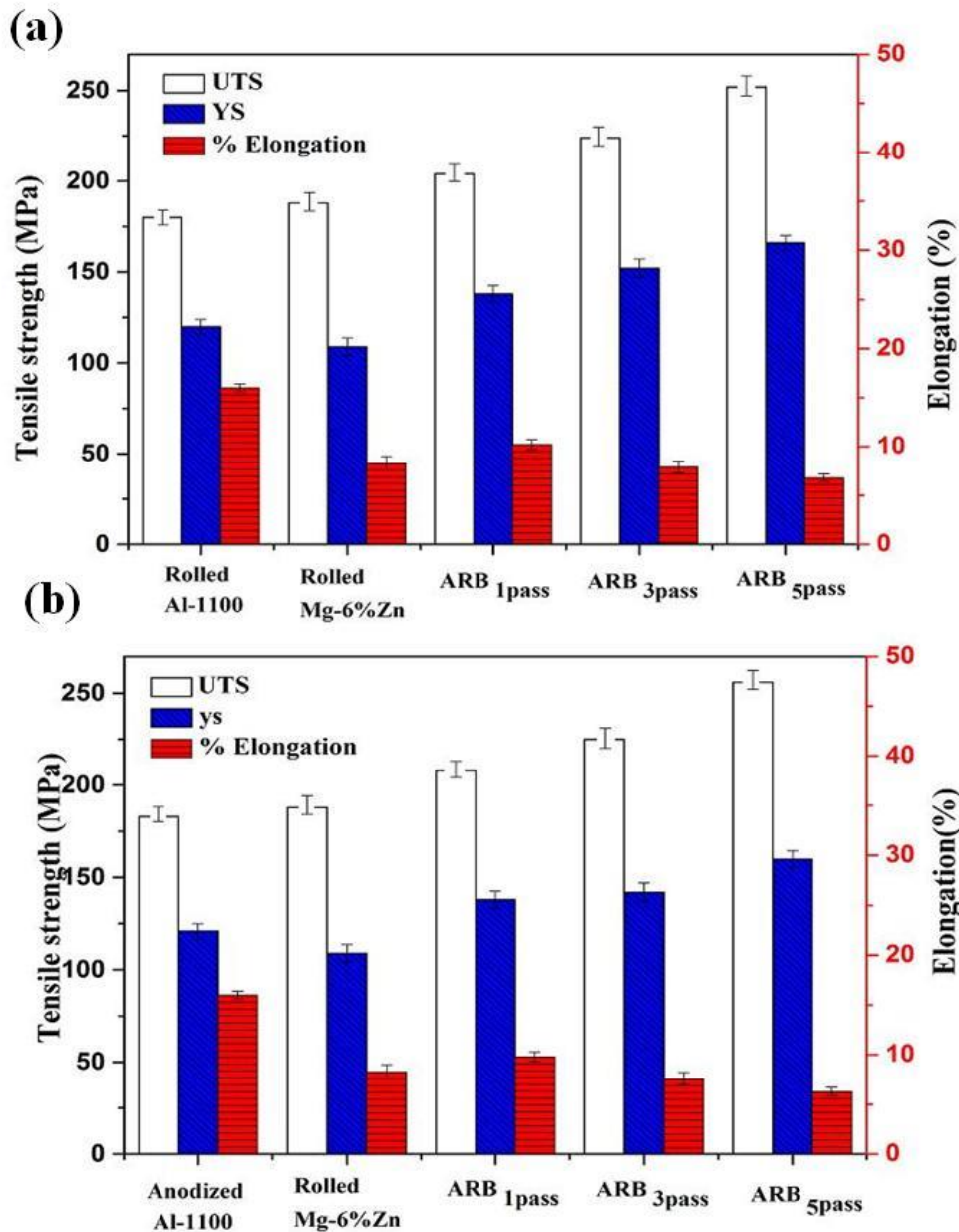


Figure 4.40. UTS, YS and percentage elongation for various ARB passes of multilayered composite (a) Mg-6%Zn/Al (b) Mg-6%Zn/anodized Al.

UTS of Mg-6%Zn/anodized Al composite is 1.58% higher as compared to Mg-6%Zn/Al composite due to the presence of alumina particle (anodization treatment). Alumina particle helps to increase the strength by pinning the dislocations and impeding their motion resulting in enhanced dislocation density and dislocation interactions which increases work hardening and strength (Jamaati et al. 2012). Not only strain hardening and grain refinement, but also the reinforcement effect in the

matrix caused by intermetallics formed during ARB process (Chang et al. 2012; Parisa et al. 2015; Ahmadi et al. 2014).

#### 4.2.3.8 Fractography

Fracture surface of tensile tested 5-pass ARB processed Al, anodized Al and Mg-6%Zn layers are shown in figure 4.41. Al layer and anodized Al layer in the Mg-6%Zn/Al and Mg-6%Zn/anodized Al multilayered composite depicts typical ductile failure illustrated by dimples, as shown in figure 4.41 (a) and (b) respectively. Ductile fracture begins with the nucleation, growth, and coalescence of microvoids. Presence of shallow and small elongated microvoids affected by shear stress during ARB process confirms the shear ductile fracture.

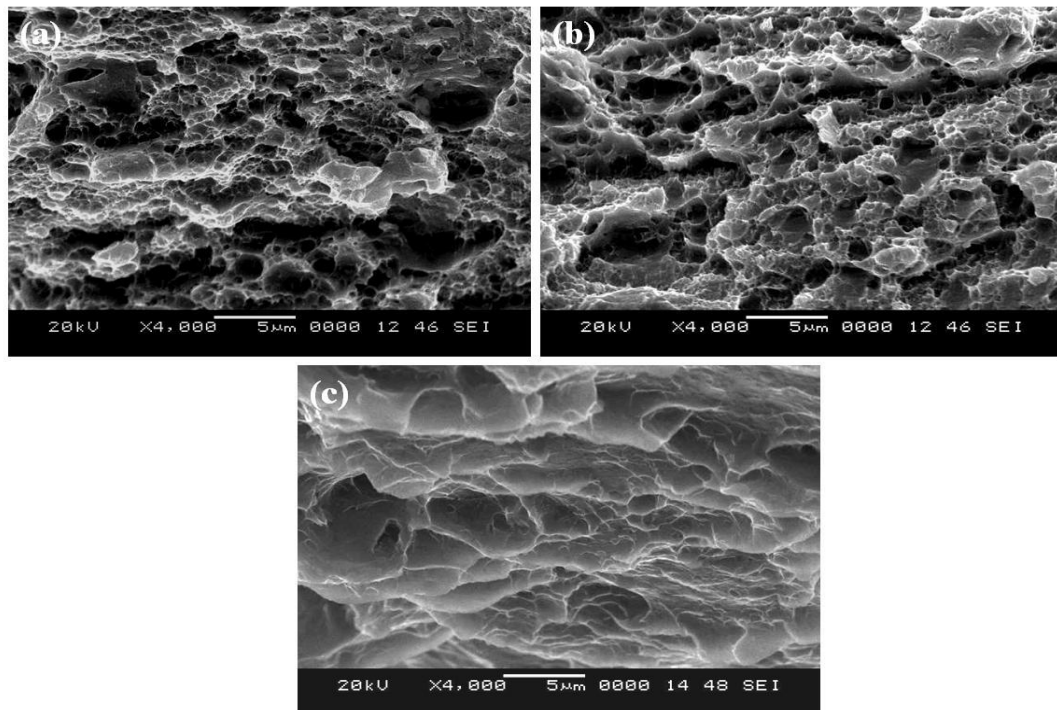


Figure 4.41. Fracture profile of the 5-pass ARB processed multilayered composite layers (a) Al (b) Anodized Al and (c) Mg-6%Zn.

Mg-6%Zn layer in the multilayered composite depicts (Figure 4.41 c) bright lines in the fracture surface which are indication of cleavage fracture. Mg-6%Zn layers were fractured in the shear mode and without forming dimples which appear to be transgranular brittle fracture.

#### 4.2.3.9 Potentiodynamic polarization

Potentiodynamic polarization curves of the Mg-6%Zn, Mg-6%Zn/Al and Mg-6% Zn/anodized Al are shown in figure 4.42. Calculated potentiodynamic polarization test results from the polarization curves are summarized in table 4.11. Corrosion current density ( $I_{\text{corr}}$ ) of the as rolled Mg-6%Zn alloy, 5-pass ARB processed Mg-6%Zn/Al and Mg-6%Zn/anodized Al multilayered composites is  $16.19 \mu\text{A}/\text{cm}^2$ ,  $9.8 \mu\text{A}/\text{cm}^2$  and  $5.5 \mu\text{A}/\text{cm}^2$  respectively.

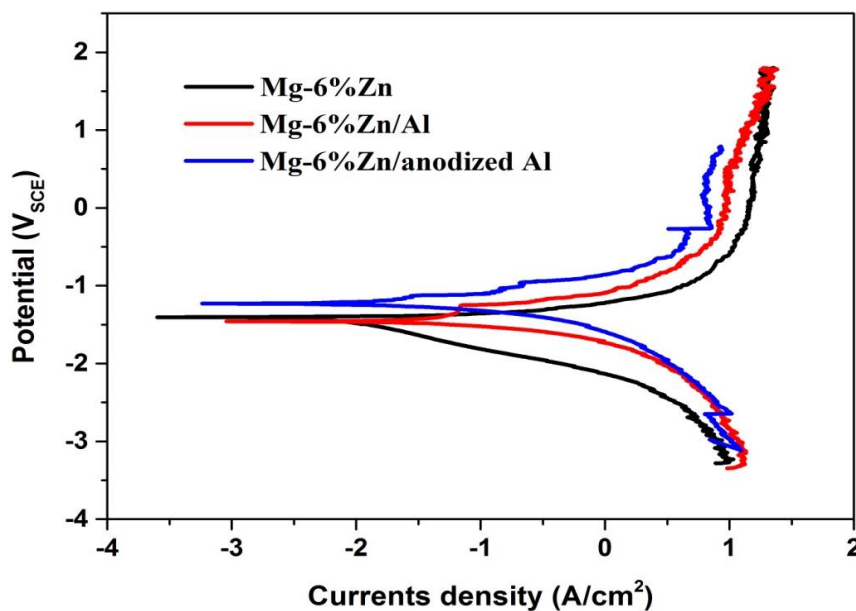


Figure 4.42. Potentiodynamic polarization curves of the Mg-6%Zn, Mg-6%Zn/Al and Mg-6% Zn/anodized Al.

Meanwhile, a shift of the corrosion potential ( $E_{\text{corr}}$ ) toward noble direction was observed as shown in table 4.11. Corrosion rate was calculated from the EC-LAB software which showed that the corrosion rate of Mg-6%Zn/Al and Mg-6%Zn/anodized Al multilayered composites exhibited 0.35 mm/y and 0.20 mm/y which is about by 1.4 and 2.45 times as compared to rolled Mg-6%Zn alloy (0.49 mm/y). Fine grains create more grain boundaries that act as a corrosion barrier. Mg-6%Zn alloy containing multilayered composite exhibited higher corrosion resistance is due to higher amount of Zn in the composite (Mozaffari et al. 2010).

Table 4.11. Potentiodynamic polarization results.

Materials	$E_{\text{corr}}$ ( $V_{\text{SCE}}$ )	$i_{\text{corr}}$ ( $\mu\text{A}/\text{cm}^2$ )	$\beta_a$ (mV/decade)	$\beta_c$ (mV/decade)	Corrosion rate (mm/y)
As rolled Mg-6%Zn alloy	-1.53	16.19	175.8	302.7	0.49
Mg-6%Zn/Al composite	-1.39	9.8	98.0	127.3	0.35
Mg-6%Zn/ anodizedAl composite	-1.32	5.5	63.5	143	0.20

Presence of higher content of Zn in the multilayered composites resulted in the formation of ZnO, which can enhance the protectiveness of the passive film and kinetics of passivation, there by inhibiting corrosion. During ARB process, intermetallics ( $\text{Al}_{12}\text{Mg}_{17}$  and  $\text{AlMg}_4\text{Zn}_{11}$ ) formed due to bonding and  $\text{Al}_2\text{O}_3$  particles from anodization treatment, are refined and uniformly distributed throughout the structure which acts as an anodic barrier to inhibit the overall corrosion.

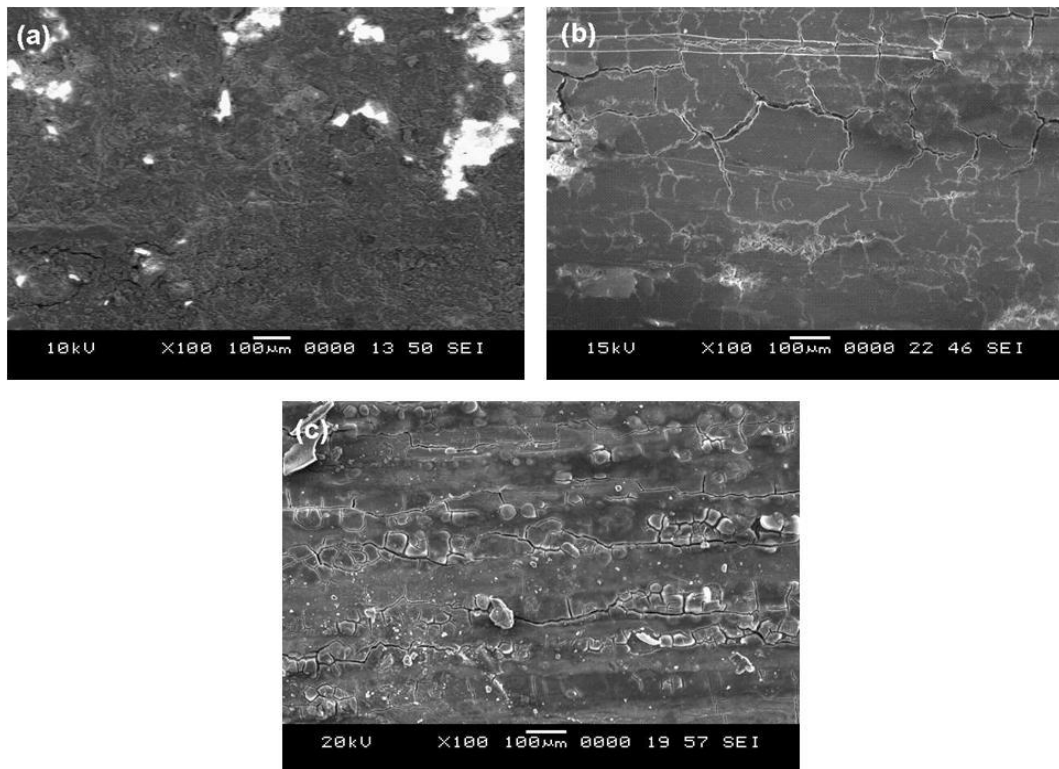


Figure 4.43. SEM micrographs of corroded (a) rolled Mg-6%Zn (b) Mg-6%Zn/Al and (c) Mg-6%Zn/anodized Al after electrochemical test in a 0.1 M NaCl solution.



Rolled Mg-6%Zn alloy revealed severe corrosion throughout the structure showing pits and cracks, as shown in figure 4.43 (a). Mg-6%Zn layer revealed corrosion products which consist of mainly magnesium hydroxide reported by Huang et al. (2003). Mg-6%Zn/Al multilayered composite exhibits layer-wise corrosion, however, Mg-6%Zn/anodized Al multilayered composite (Figure 4.43 b) did not show any severe dissolution like Mg-6%Zn/Al composite but some cracks found on the surface because of anodization of Al before ARB process as shown in figure 4.43 (c).

#### 4.2.3.10 Immersion test

Hydrogen evolution rate and corresponding corrosion rate of the wrought Mg-6%Zn alloy and ARB processed Mg-6%Zn/Al and Mg-6%Zn/Al composite are illustrated in table 4.12.

Table 4.12. Immersion test results.

<b>Materials</b>	<b>Hydrogen evolution rate (ml/cm<sup>2</sup>/d)</b>	<b>Corrosion rate (mm/y)</b>
Rolled Mg-6%Zn	0.28	0.62
Mg-6%Zn/Al	0.24	0.43
Mg-6%Zn/anodized Al	0.21	0.36

Higher hydrogen evolution was noticed in the Mg-6%Zn alloy (0.82 ml/cm<sup>2</sup>/d) as compared to Mg-6%Zn/Al (0.28 ml/cm<sup>2</sup>/d) and Mg-6%Zn/anodized Al composite (0.21 ml/cm<sup>2</sup>/d). Corrosion rate calculated from hydrogen evolution for 5-pass ARB processed multilayered composite is less than rolled Mg-6%Zn alloy due to refined microstructure, the presence of  $\beta$  phases ( $Al_{12}Mg_{17}$  and  $AlMg_4Zn_{11}$ ) and due to presence of alumina. Potentiodynamic polarisation (table 4.11) and immersion testing (table 4.12) in 0.1 M NaCl solution showed similar trend of corrosion rate.

#### 4.2.4 Summary

Mg-(2-6)%Zn/Al and Mg-(2-6)%Zn/anodized Al multilayered composites were developed by ARB at 300 °C up to five pass successfully. Microstructure, mechanical

properties and corrosion behaviour of the multilayered composites were investigated and summarized as follows.

Developed multilayered composites exhibited about 20% lighter weight as compared to as rolled Al-1100.  $Al_{17}Mg_{12}$  and  $AlMg_4Zn_{11}$  and  $Al_{17}Mg_{12}$ ,  $AlMg_4Zn_{11}$  and  $Al_2O_3$  Intermetallics were found in the 5-pass ARB processed Mg-(2-6%)Zn/Al and Mg-(2-6%)Zn/anodized Al multilayered composites in the XRD analysis.

EBS and TEM analysis showed that UFG with high angle misorientation in the microstructure. Average grain size was found to be (a) 1.9  $\mu m$ , 1.3  $\mu m$  and 1.04  $\mu m$  for Al and anodized Al and Mg-2%Zn layers (b) 1.5  $\mu m$ , 1.3  $\mu m$  and 1  $\mu m$  for Al and anodized Al and Mg-4%Zn layers (c) 1.8  $\mu m$ , 1.6  $\mu m$  and 0.6  $\mu m$  for Al and anodized Al and Mg-6%Zn layers respectively in the multilayered composite. As the number of ARB passes increases, microhardness of different layers of the Mg-(2-6%)Zn/Al and Mg-(2-6%)Zn/anodized Al multilayered composite increases. Mg-4%Zn/Al and Mg-4%Zn/anodized Al composite gives better microhardness values as compared to composite containing 2% Zn and 6% Zn.

It is observed that, as the number of ARB passes increased, YS and UTS improves, and ductility reduces. Mg-4%Zn/Al and Mg-4%Zn/anodized Al composite gives better strength as compared to other two composite systems. In the anodized multilayered composites, uniform distribution of  $Al_2O_3$  particle helps to increase the strength by pinning the dislocations and impeding their motion resulting in enhanced dislocation density and dislocation interactions. Fractured surfaces of the Al and anodized Al layers of the composite are characterized by dimples and exhibited shear ductile fracture and Mg-Zn layer exhibited transgranular brittle fracture in the multilayered composites.

Potentiodynamic polarization and immersion study revealed that Mg-Zn/Al multilayered composite exhibited highest corrosion resistance as compared to as rolled Mg-Zn alloy. It is mainly due to UFG structure, intermetallics ( $Al_{12}Mg_{17}$  and  $AlMg_4Zn_{11}$ ) formed are refined and uniformly distributed throughout the structure which acts as an anodic barrier to inhibit the overall corrosion. Mg-Zn/anodized Al

showed better corrosion resistance as compared to Mg-Zn/Al, due to uniform distribution of alumina ( $\text{Al}_2\text{O}_3$ ) resulted from the anodization process. Mg-6%Zn/Al and Mg-6%Zn/anodized Al exhibited higher corrosion resistance is due to higher amount of Zn in the composite. Obtained result is due to presence of stronger passivating alloying elements Zn & Al. Presence of higher content of Zn in the multilayered composites results in the formation of large amount of ZnO, which can enhance the protectiveness of the passive film and kinetics of passivation there by inhibiting the corrosion.

### **4.3 Mg-Zn/Al-7075 and Mg-Zn/anodized Al-7075 multilayered composites**

#### **4.3.1 Mg-2%Zn/Al-7075 and Mg-2%Zn/anodized Al-7075 multilayered composites**

Multilayered Mg-2%Zn/Al-7075 and Mg-2%Zn/anodized Al-7075 composites were produced by accumulative roll bonding (ARB) process using Mg-2%Zn with Al-7075 and anodized Al-7075 alloys up to four passes at 350 °C. The structure, mechanical property and corrosion behaviors of the multilayered composites have been evaluated by means of scanning electron microscopy, electron backscattered diffraction, transmission electron microscope, X-ray diffraction, mechanical testing, potentiodynamic and immersion test.

##### **4.3.1.1 Microstructural analysis**

SEM micrographs of the Mg-2%Zn/Al-7075 multilayered composite after four ARB passes are shown in figure 4.44. Microstructure of roll bonded composite reveals alternative layers of Mg-2%Zn and Al-7075. There were no cracks or de-lamination along the interfaces of the multilayer which indicate good bonding between Mg-2%Zn alloy and Al-7075 (Figure 4.44 a). Thicknesses of both Mg-2%Zn layer and Al-7075 layer decreased gradually with increase in number of ARB passes. Layer thickness was found to be in the range of 50-60  $\mu\text{m}$  and slight waviness layer structure was observed due to high deformation with successive ARB passes (Figure 4.44 b). Fine grains are observed in Al-7075 layer and Mg-2%Zn layer in 4-pass multilayered composites is as shown in figure 4.44 (c) and (d). Energy dispersive spectroscopy (EDS) data shows alternate layers of anodized Al-7075 layer (Figure 4.44 e) and Mg-4%Zn layer (Figure 4.44 f). Mechanism for grain refinement during ARB is grain subdivision caused by plastic deformation where the original grains are subdivided into fine grains by deformation-induced boundaries (Toth and Gu, 2014).

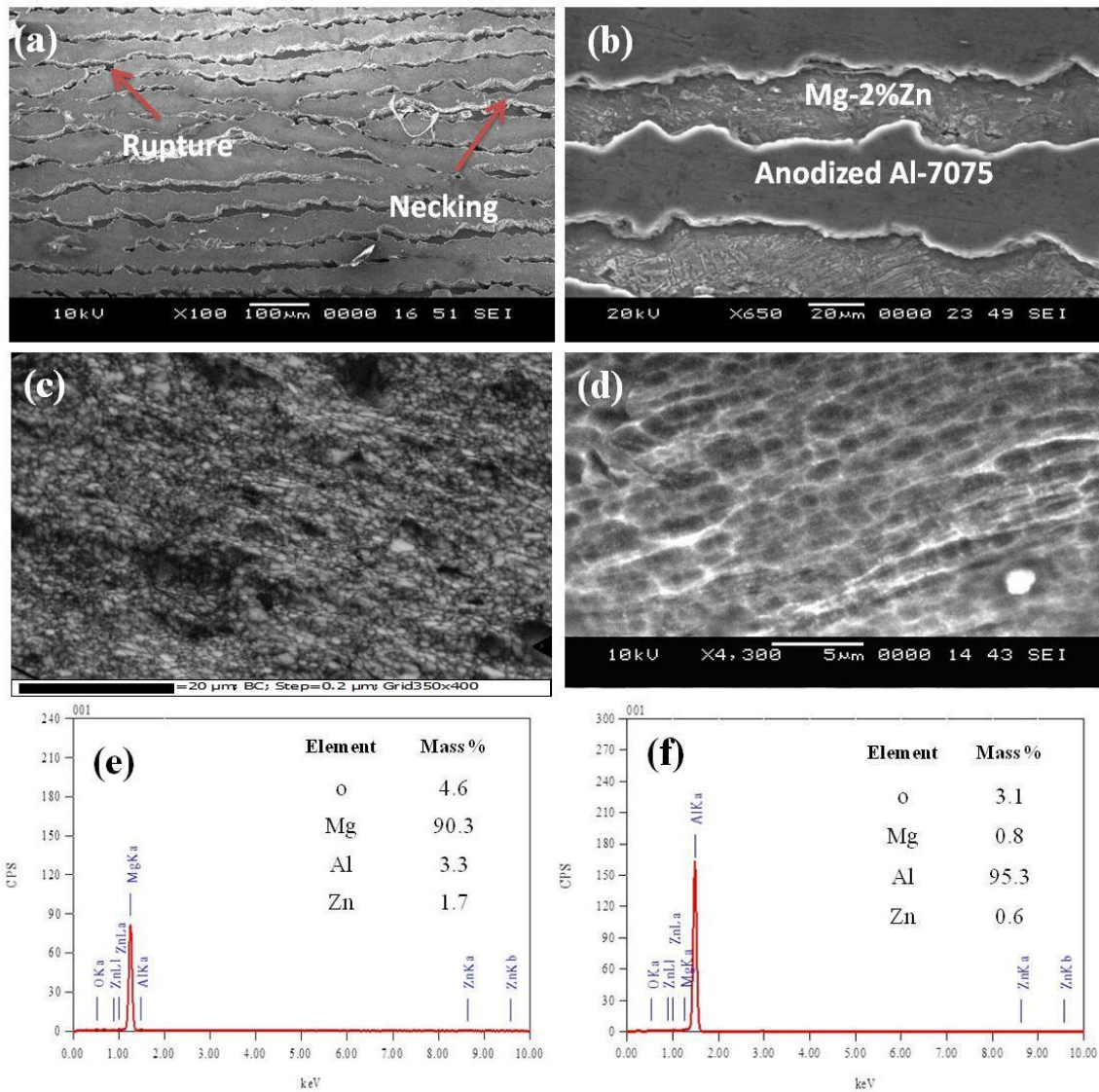


Figure 4.44. SEM micrographs of (a) 4-pass accumulative roll bonded Mg-2%Zn/Al-7075 multilayered composite (b) Enlarged image of multilayered composite (c) Al-7075 layer (c) Mg-2%Zn layer showing ultrafine grains (e) EDS of the Mg-2%Zn layer (f) EDS of the Al-7075 layer.

#### 4.3.1.2 EBSD analysis

Inverse pole figure (IPF) map of the Al-7075 layer in the ARB processed Mg-2%Zn/Al-7075 multilayered composite is shown in figure 4.45 (a). Colours in the standard stereographic triangle correspondence to the crystallographic directions. Non-indexed points are shown as black pixels. In the grain boundary map (Figure 4.45 b), low angle

boundaries are represented in green lines, while high angle boundaries are represented in black lines and twins are marked in red colors.

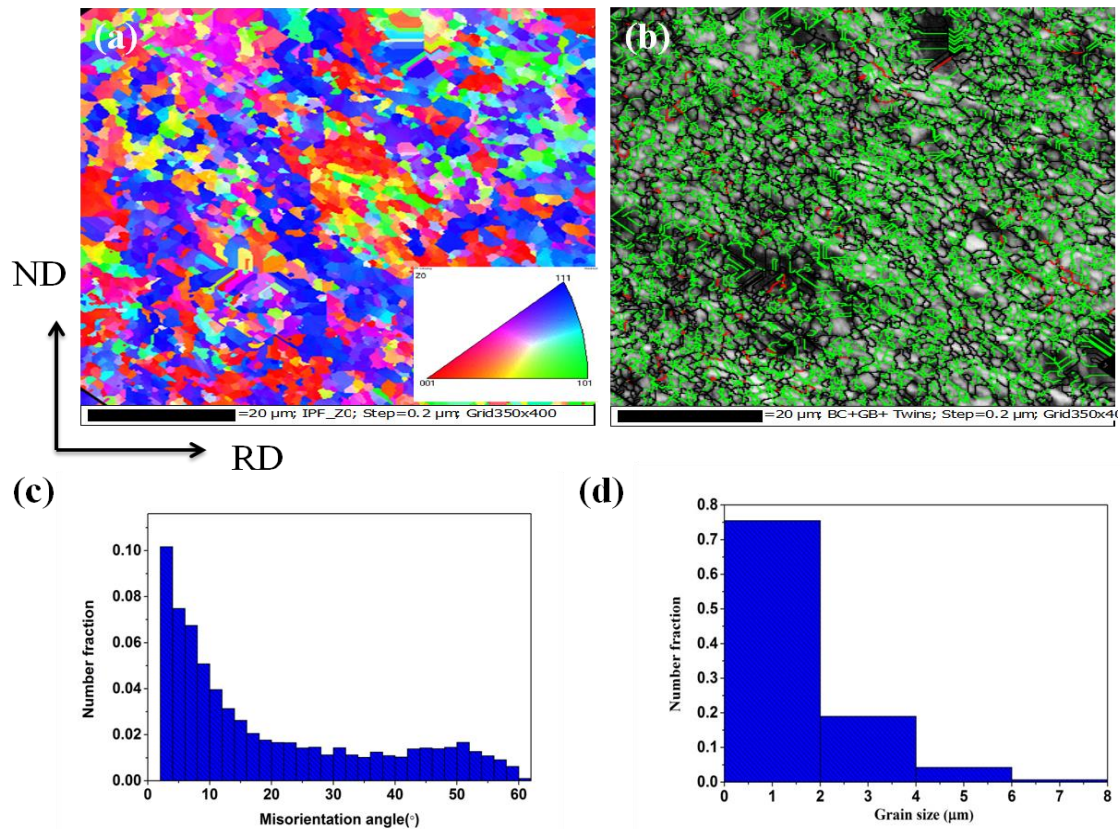


Figure 4.45. EBSD based analysis of Al-7075 layer in the 4-pass ARB processed Mg-2%Zn/Al-7075 multilayered composite (a) IPF map (b) Grain boundary map with twins (c) Misorientation angle distribution profile (d) Grain size distribution.

Al-7075 layer in the Mg-2%Zn/Al-7075 composites consists of fine (sub) grains with a fraction of high angle boundaries. As the number of ARB passes increases, strain accumulated in the material increases. As a result, subgrain boundaries gradually transforms from low angle grain boundaries (LAGBs) into high-angle grain boundaries (HAGBs). Figure 4.45 (b) depicts HAGBs in Al-7075 layer of the Mg-2%Zn/Al-7075 multilayered composite. Percentage of twins was found to be 1.67% in the Al-7075 layer due to strain hardening. Misorientation angle profile (Figure 4.45 c) consists of both LAGBs and HAGBs which indicates deformation is induced as result of dynamic recovery. It is observed (Figure 4.45 d) that 75% of the grains in the microstructure have grain size below 2 μm. Average grain size was found to be 1.3 μm in the Al-7075 layer in the multilayered composite.

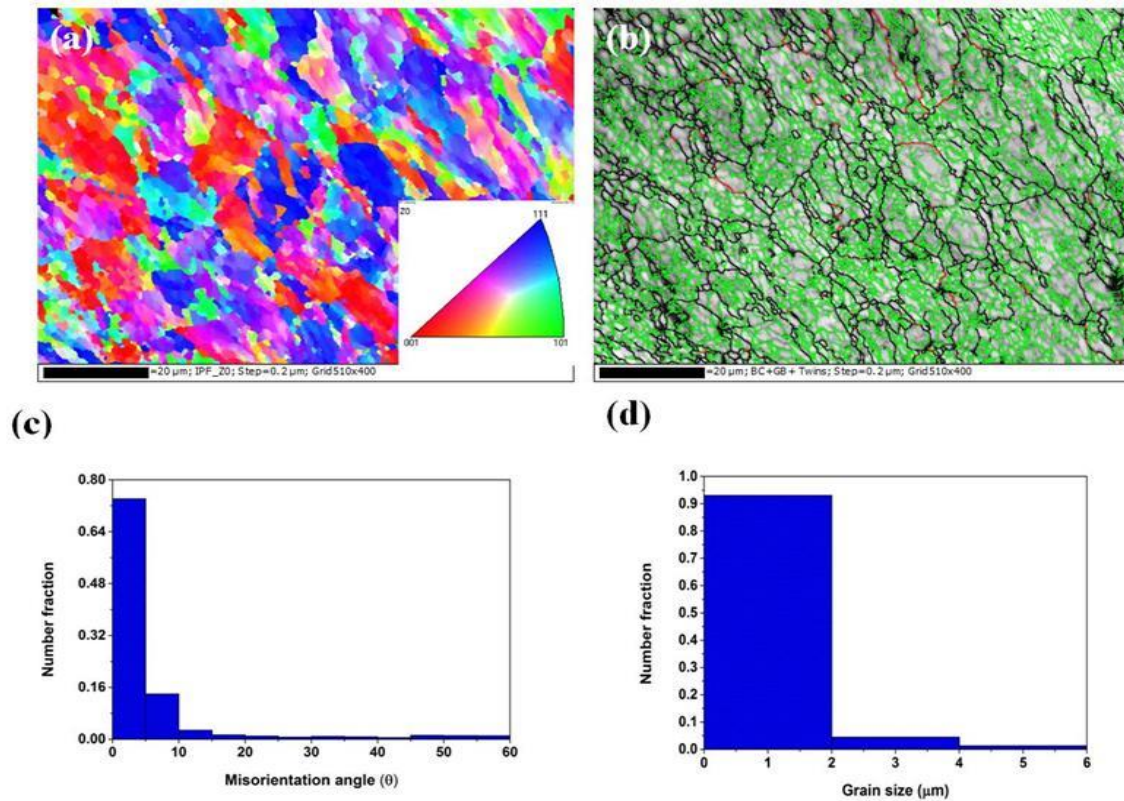


Figure 4.46. EBSD based analysis of anodized Al-7075 layer in the 4-pass ARB processed Mg-2%Zn/anodized Al-7075 multilayered composite (a) IPF map (b) Grain boundary map with twins (c) Misorientation angle distribution profile (d) Grain size distribution.

Inverse pole figure (IPF) map (Figure 4.44 a) composed of elongated grains directed uniformly in  $\langle 111 \rangle$  orientation in the rolling direction. Grain boundary map, as shown in Figure 4.46 (b), reveals fine grains with a fraction of HAGBs. With higher ARB passes, strain accumulated in the material is high so that density of dislocations is more in the materials. As a result, fraction of low-angle boundaries is converted into high-angle boundaries. Percentage of twins in the anodized Al-7075 layer of the multilayered composite was found to be 0.45%. Misorientation angle profile, as shown in figure 4.46 (c), consists of both LAGBs and HAGBs which indicates that deformation is induced as a result of dynamic recovery. A significant fraction ( $\sim 90\%$ ) of grains have diameter  $< 2 \mu\text{m}$  as shown in figure 4.46 (d), the average grain size found to be  $0.73 \mu\text{m}$ .

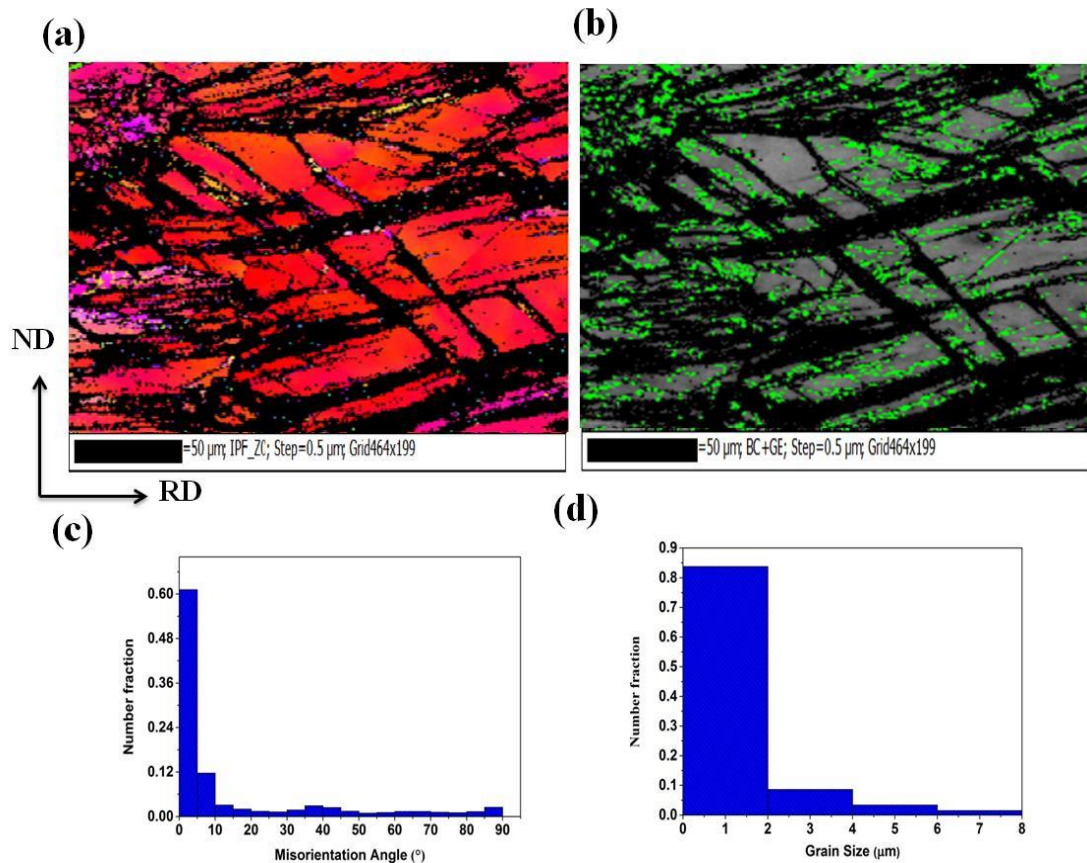


Figure 4.47. EBSD based analysis of Mg-2%Zn layer in the 4-pass ARB processed Mg-2%Zn/Al-7075 multilayered composite (a) IPF map (b) Grain boundary map with twins (c) Misorientation angle distribution profile (d) Grain size distribution.

EBSD results of Mg-2%Zn layer in the ARB processed Mg-2%Zn/Al-7075 multilayered composites are shown in figure 4.47. Inverse pole figure (IPF) map of the Al-7075 layer is shown in figure 4.47 (a). Grain boundary map (Figure 4.47 b) shows that Mg-2%Zn layer consists of subgrains, with a fraction of HABs due to dynamic recrystallization occurred during ARB process. It is clearly observed that there are no twins formed in ARB processed Mg-2%Zn, which can be attributed to decrease in twin nucleation with decrease in grain size. It is reported that non-basal slips are activated for a fine grained Mg, resulting in suppression of twin generation and reduction in mechanical anisotropy by grain refinement. Deformation twins disappear in the Mg alloys, when the average grain size reaches to less than 2 μm. Figure 4.47 (c) reveals the presence of both LAGBs and HAGBs in Mg-2%Zn layer of the Mg-2%Zn/Al-7075 multilayered composite which indicates that deformation is induced as a result of



dynamic recovery. Grain size variation plot (Figure 4.47 d) shows that 82% of the grains in the microstructure have grain size below 2  $\mu\text{m}$ . Average grain size is found to be 1  $\mu\text{m}$  in the Mg-2%Zn layer of the multilayered composite.

#### 4.3.1.3 TEM analysis

Figure 4.48 reveals TEM micrographs associated with selected area electron diffraction (SAED) patterns of the 4-pass ARB processed Mg-2%Zn/Al-7075 (a & b) and Mg-2%Zn/anodized Al-7075 (c & d).

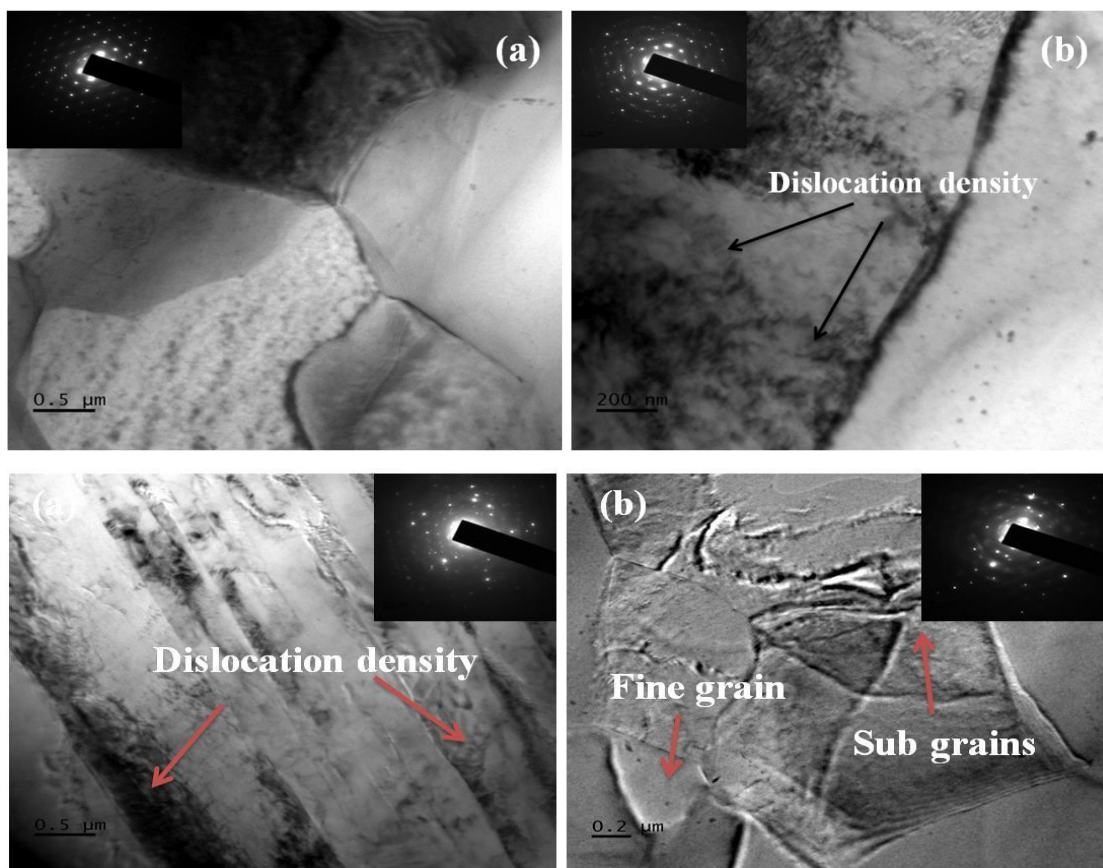


Figure 4.48. TEM micrographs and SAED patterns of the ARB processed Mg-2%Zn/Al-7075 (a & b) and Mg-2%Zn/anodized Al-7075 (c & d).

TEM micrograph clearly shows that formation of ultrafine grained microstructure comprising of dense dislocation tangles. During ARB process, due to high strain, subdivision of grains occurs due to formation of planar dislocation boundaries and incidental dislocation boundaries. Higher misorientations form across these dislocation boundaries and spacing of boundaries reduces, which helps to create fine grains (Gashti

et al. 2016). SAED patterns are in the form of rings which confirm the sub-grain structure in the Mg-2%Zn/Al-7075 composite with high angle misorientations. ARB processed composites are high strained materials due to which diffraction spots are elongated and some diffraction spots do not form the rings which is due to presence of low angle grain boundaries.

#### 4.3.1.4 XRD analysis

Figure 4.49 shows the XRD patterns taken from the cross-section of the Mg-2%Zn/Al-7075 multilayered composite. XRD patterns revealed peaks indexed to Al,  $\alpha$ Mg,  $\text{Al}_{17}\text{Mg}_{12}$  and  $\text{AlMg}_4\text{Zn}_{11}$ . As the number of ARB passes increases, layer thickness decreases and thus, number of interfaces per unit volume increases, thereby inter diffusion between the different layers occurs.

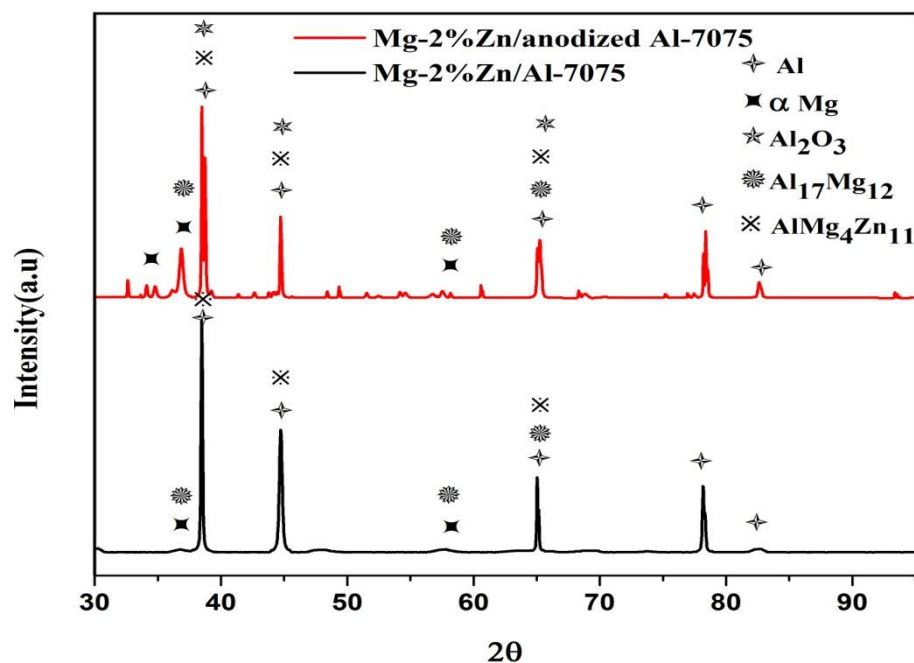


Figure 4.49. XRD patterns along the cross section of accumulative roll bonded Mg-2%Zn/Al-7075 multilayered composites.

Important feature of the XRD patterns is that the peak of  $\text{Al}_{17}\text{Mg}_{12}$  and  $\text{AlMg}_4\text{Zn}_{11}$  appears after four passes of ARB. The reason for the formation of these intermetallic phases is the intense straining during ARB at 350 °C that causes the increase in number of grain boundaries and dislocation density. This accelerates the elemental diffusion at

interfaces and promotes the formation of intermetallic (Tsuji et al. 2003; Jafarian et al. 2015).

#### 4.3.1.5 Density test

Density values of various alloy combinations, as obtained by density test is illustrated in table 4.13.

Table 4.13. Density test results.

Materials	Density (kg/m <sup>3</sup> )
Mg-2%Zn alloy	1759
Al-7075 alloy	2775
Anodized Al-7075	2778
Mg-2%Zn/Al-7075 composite	2295
Mg-2%Zn/anodized Al-7075 composite	2297

Roll bonded Mg-2%Zn/Al-7075 and Mg-2%Zn/anodized Al-7075 multilayered composite (Mg-2%Zn/Al-7075) exhibited weight saving of 20.9% as compared to Al-7075 alloy.

#### 4.3.1.6 Microhardness test

Figure 4.50 demonstrates the variations in the microhardness values in different layers of multilayered composites. As the number of ARB passes increases, microhardness of the Mg-2%Zn, Al and anodized Al layers of the multilayered composite increases. After four ARB passes, microhardness of the Mg-2%Zn layer, Al-7075 layer and anodized Al-7075 layer reached to 97.6 HV (1.3 times), 250.1 HV (1.50 times) and 256.2 HV (1.50 times) respectively, in comparison with their counterpart rolled alloys.

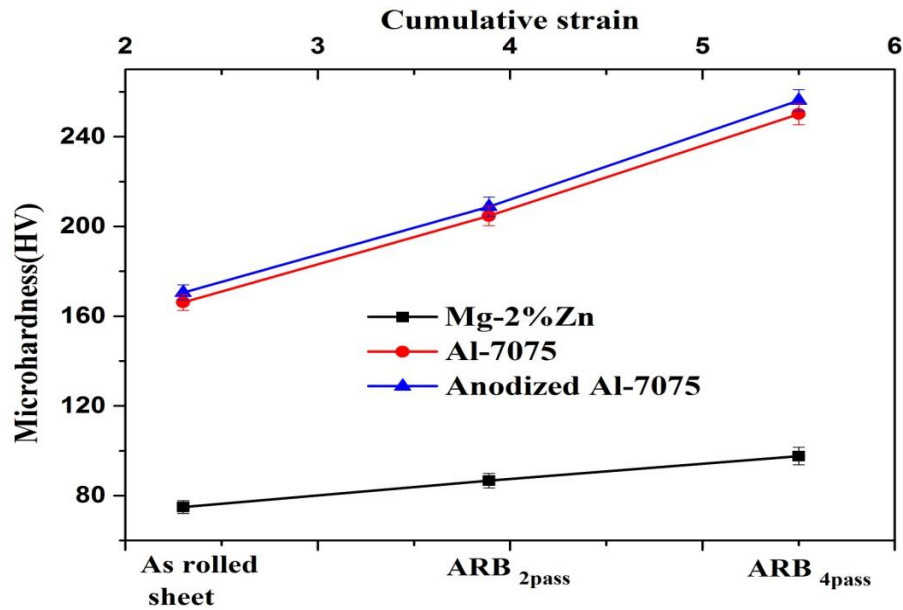


Figure 4.50. Microhardness variation in Mg-2%Zn, Al-7075 and anodized Al-7075 layers during different passes of the ARB process.

Significant increase in hardness at relatively low strains can be attributed to strain hardening, i.e., the increase in the density of the dislocations and their interactions. At higher ARB passes, increase in microhardness values is due to combined effect of strain hardening, grain refinement and intermetallics (Parisa et al. 2015). Anodized Al layer in the Mg-2%Zn/anodized Al-7075 composite exhibited higher hardness values as compared to Al layer in the Mg-2%Zn/Al-7075 composite due to uniform distribution of harder alumina ( $Al_2O_3$ ) particles in the aluminium layer. During the ARB process, the alumina particles increased dislocation density and their interfaces.

#### 4.3.1.7 Tensile strength test

Figure 4.51 (a) shows variation in tensile strength of the as rolled Mg-2%Zn, Al-7075, and roll bonded Mg-2%Zn/Al-7075 multilayered composite. UTS and YS of the multilayered composite increases with the increase in number of ARB pass. During initial passes of ARB, predominant strengthening mechanism is strain hardening. But at higher passes of ARB, improvement of strength is due to grain refinement where ultra-fine grains retard the dislocation movements, mechanism known as dislocation strengthening as explained by Hall-Petch equation. Also formation of intermetallic phases in the multilayered composite helps to improve the strength.

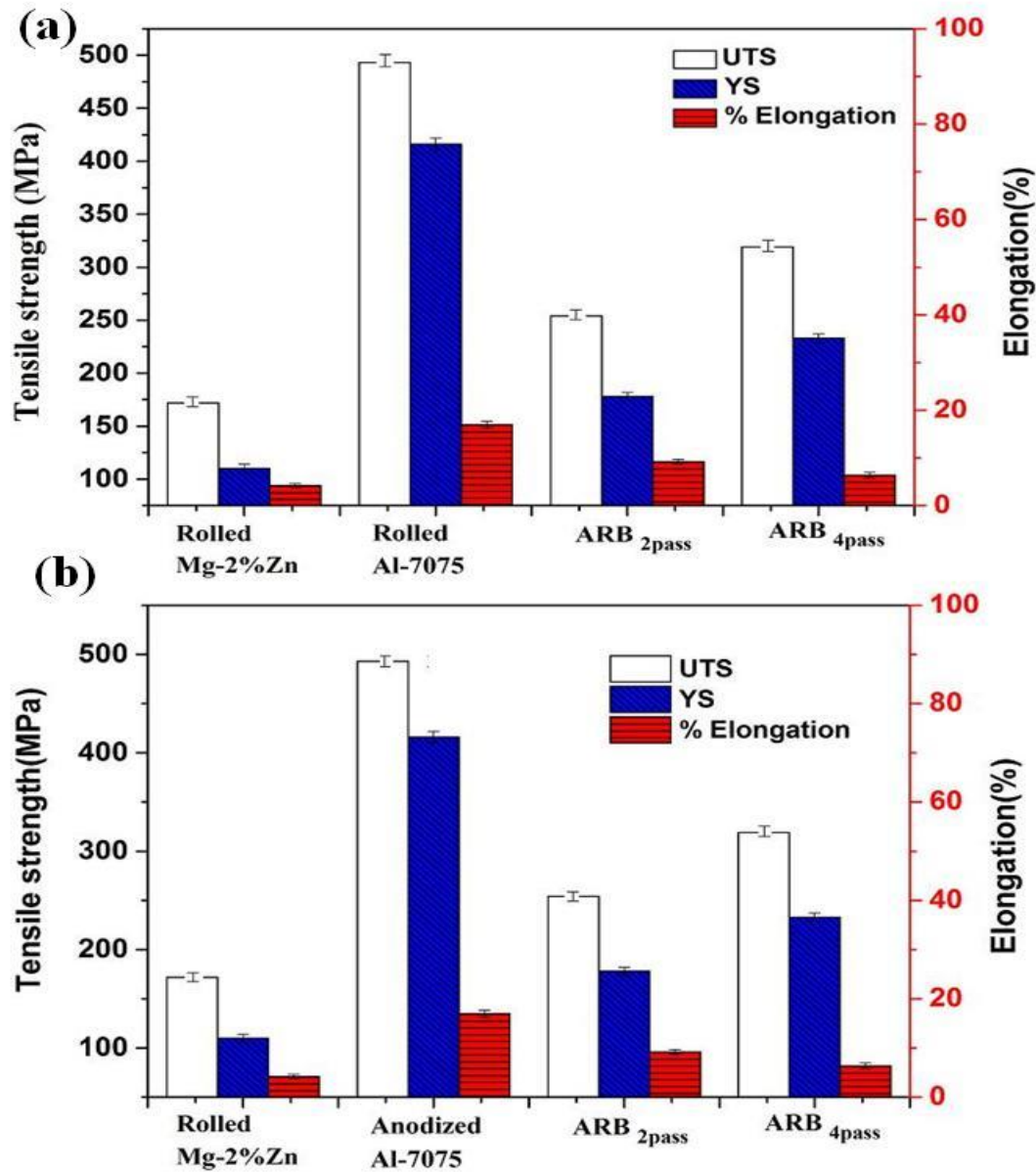


Figure 4.51. Variations of UTS, YS and percentage elongation of the multilayered composite with different ARB passes (a) Mg-2%Zn/Al-7075 (b) Mg-2%Zn/anodized Al-7075 composite.

First cycle had a significant effect on the tensile strength due to strain hardening process during ARB process. YS and UTS were improved, and after four pass, they were about 2 times (220 MPa) and 1.82 times (314 MPa) higher than that of the rolled M-2%Zn alloy. Figure 4.51 (b) shows the YS, UTS and elongation to failure of the as-rolled sheets and different ARB passed Mg-2%Zn/anodized Al-7075 composite. The YS and UTS increases when the number of ARB passes increases, whereas elongation decreases. YS and UTS of Mg-2%Zn/anodized Al-7075 after 4-passes reached to 233.6

MPa, 319.0 MPa which are 2.11 times, 1.85 times of the as-rolled Mg-2%Zn alloy. Enhanced strength and hardness with increase in the number of ARB passes is due to strain hardening and grain refinement during ARB process (Hidalgo et al. 2016). During initial passes of ARB, strength and hardness improved due to strain hardening and formation of subgrains. At higher passes, strength and hardness is controlled by the continuous development of ultrafine grains with high-angle grain boundaries. Meanwhile, the improved hardness of anodized Al-7075 layer is affected by the presence of Al<sub>2</sub>O<sub>3</sub> particles which constraint the localized deformation during indentation.

#### 4.3.1.8 Fractography

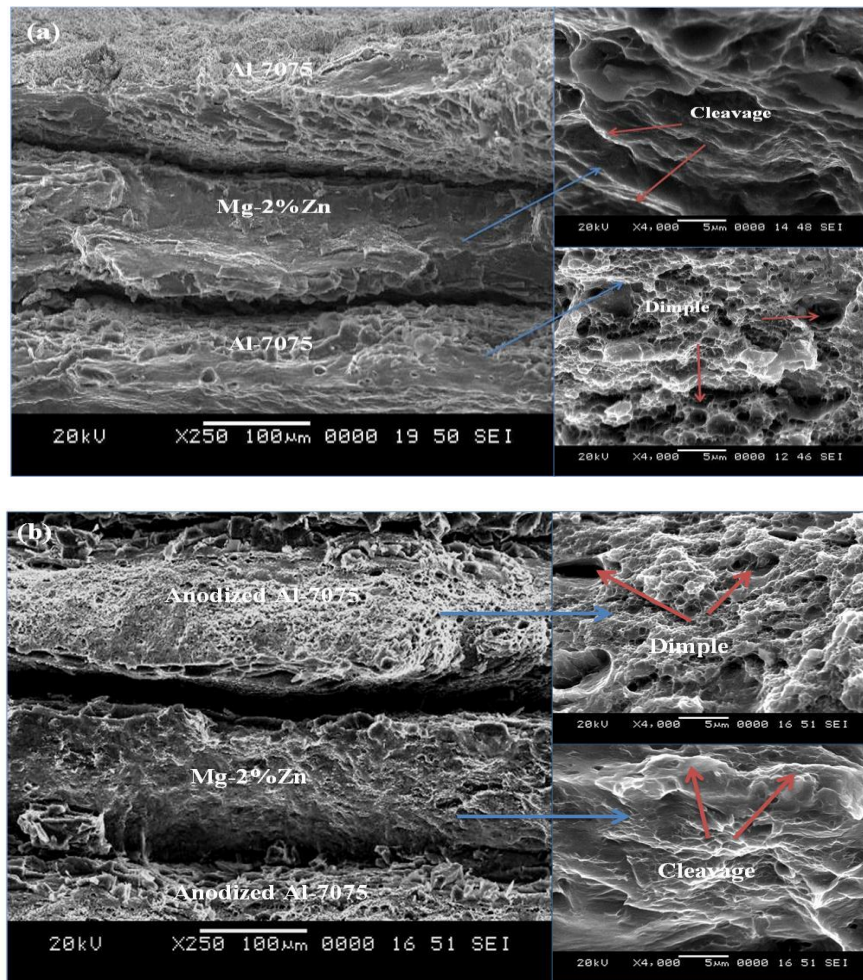


Figure 4.52. SEM micrographs of the fractured surface of 4-pass ARB processed (a) Mg-2%Zn/Al-7075 (b) Mg-2%Zn/anodized Al-7075 multilayered composite.

Fracture surfaces of 4-pass ARB-processed Mg-2%Zn/Al-7075 and Mg-2%Zn/anodized Al-7075 multilayered composites were shown in Figure 4.52 (a & b). Magnified image of the Al-7075 and anodized Al-7075 layers in the 4-pass ARB processed Mg-2%Zn/Al-7075 and Mg-2%Zn/anodized Al-7075 composite reveals dimples as a result of ductile fracture. Appearance of micro voids in the fracture surfaces are being affected by the state of shear stress. The shear ductile fracture is characterized by shallow small elongated shear dimples, which are oriented along the shear direction. Therefore, the dimples are elongated which shows shear ductile failure (Barsoum and Faleskog, 2007). However, Mg-2%Zn layer in composite was fractured in the shear mode and free from dimples which appear to be transgranular brittle fracture due to hexagonal closed packed (HCP) structure.

#### 4.3.1.9 Potentiodynamic polarisation

Typical Potentiodynamic polarization curves of Mg-2%Zn alloy and Mg-2%Zn/Al-7075 and Mg-2%Zn/anodized Al-7075 multilayered composite in 0.1M NaCl solution are shown in figure 4.53. Corrosion potential of multilayered composite is shifted to more positive value in comparison with the Mg-2%Zn Al alloy.

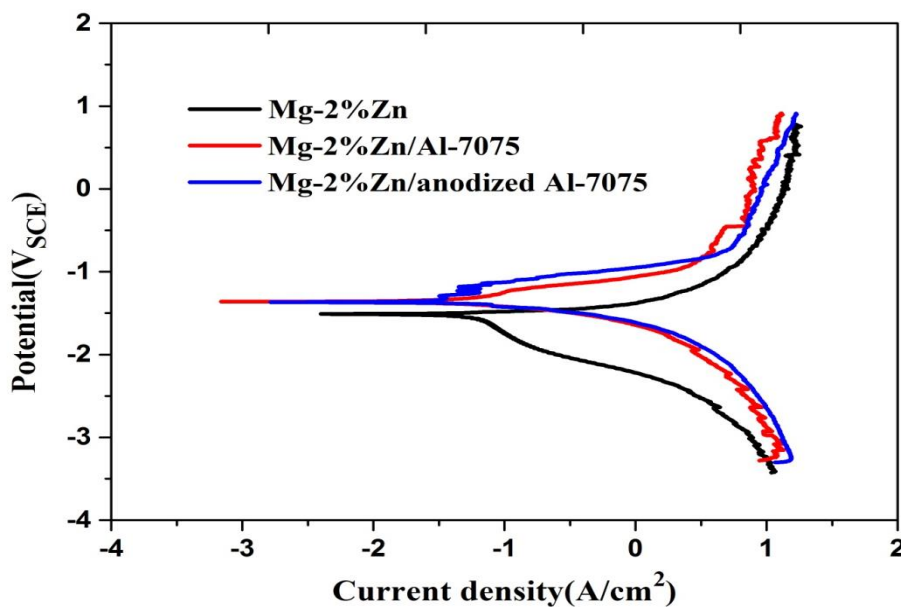


Figure 4.53. Potentiodynamic polarization curves of the Mg-2%Zn, Mg-2%Zn/Al-7075 and Mg-4% Zn/anodized Al-7075 multilayered composite.

Significant lower corrosion current density ( $i_{\text{corr}}$ ) was observed for ARB processed composite as compared to wrought Mg-2%Zn alloy (shown in Table 4.14). High cathodic slope values were found for wrought Mg-2%Zn alloy, which indicate high evolution of  $\text{H}_2$  due to cathodic reduction reactions.

Table 4.14. Electrochemical kinetic parameters of the rolled Mg-2%Zn alloy and multilayered composites.

Materials	$E_{\text{corr}}$ ( $\text{V}_{\text{SCE}}$ )	$i_{\text{corr}}$ ( $\mu\text{A}/\text{cm}^2$ )	$\beta_a$ ( $\text{mV}/\text{decade}$ )	$\beta_c$ ( $\text{mV}/\text{decade}$ )	Corrosion Rate ( $\text{mm}/\text{y}$ )
Mg-2%Zn	-1.63	77.96	238.1	- 882.2	2.3
Mg-2%Zn/Al-7075	-1.32	46.9	246.9	- 203.0	1.09
Mg-2%Zn/ anodized Al-7075	-1.26	25.96	141.3	-202.3	0.62

Formation of ultrafine grained structure results in reduced  $i_{\text{corr}}$  and corrosion rate in the Mg-2%Zn/Al-7075 multilayered composite. Smaller grain size increases the total grain boundary area, as a consequence, increases the surface protective films. Electrochemical corrosion study showed that the corrosion resistance of the Mg-2%Zn/Al-7075 multilayered composite is better than Mg-2%Zn alloys due to decreased cathodic kinetics, growth of protective passive film due to ultrafine grain structure and formation of additional  $\beta$  phases in the form of  $\text{Al}_{12}\text{Mg}_{17}$  and  $\text{AlMg}_4\text{Zn}_{11}$  (Aung and Zhou, 2010).

Surface morphology after electrochemical polarization test in the solution of 0.1 M NaCl for Mg-2%Zn alloy and Mg-2%Zn/Al-7075 multilayered composite, is shown in figure 4.54. As rolled Mg-2%Zn alloy is uniformly corroded, a few pits and cracks can be observed in figure 4.54 (a). ARB processed multilayered composites exhibited totally different corrosion morphology as compared to Mg-2%Zn alloy figure 4.54 (b).



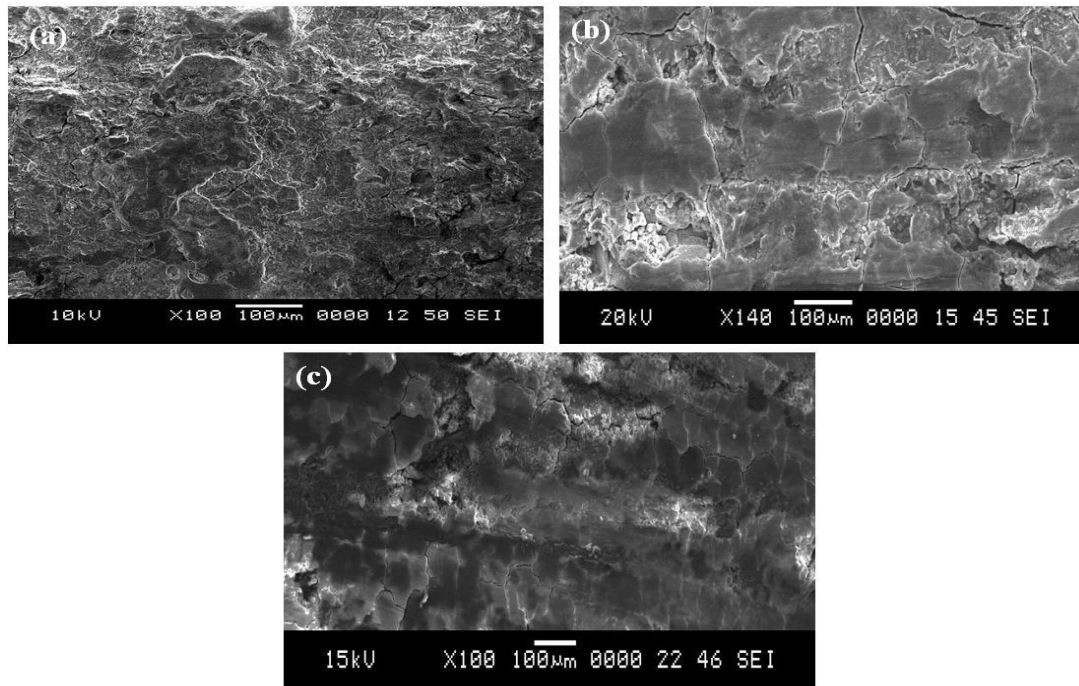


Figure 4.54. SEM micrographs of corroded (a) Mg-2%Zn alloy (b) Mg-2%Zn/Al-7075 (c) Mg-2%Zn/anodized Al-7075 multilayered composites after electrochemical test in a 0.1M NaCl solution.

In ARB processed composite, significant dissolution of Mg-2%Zn alloy in NaCl solution was observed in the Mg-2%Zn/Al-7075 multilayered composite. Corrosion product (hydroxide film) is observed only on the surface Mg-2%Zn alloy layer. Slight corrosion of Mg-2%Zn/anodized Al-7075 multilayered composite was observed due to anodization and is depicted in figure 4.54.

#### 4.3.1.10 Immersion test

Table 4.15 shows the corrosion rate of the alloys after 5 days of immersion in 0.1 M NaCl. After 5 days of immersion in 0.1 M NaCl, the average corrosion rate for Mg-2%Zn, Mg-2%Zn/Al-7075, and Mg-2%Zn/anodized Al-7075 was determined to be 2.55, 1.17 and 0.64 mm/y, respectively.

Table 4.15. Immersion test results.

<b>Materials</b>	<b>Hydrogen evolution rate (ml/cm<sup>2</sup>/d)</b>	<b>Corrosion rate (mm/y)</b>
Mg-2%Zn	1.15	2.55
Mg-2%Zn/Al-7075	0.65	1.17
Mg-2%Zn/anodized Al-7075	0.36	0.64

Hydrogen evolution of the Mg-2%Zn/Al-7075 and Mg-2%Zn/anodized Al-7075 composite samples reduced about 2.17 and 3.98 times as compared with Mg-2%Zn alloy. Degradation of the ARB processed multilayered composite is more slower than wrought Mg-2%Zn alloy due to refined microstructure and the presence of  $\beta$  phases ( $Al_{12}Mg_{17}$  and  $AlMg_4Zn_{11}$ ). Further, the Mg-2%Zn/anodized Al-7075 composite showed less hydrogen evolution due to presence of alumina.

#### **4.3.2 Mg-4%Zn/Al-7075 and Mg-4%Zn/anodized Al-7075 multilayered composites**

Mg-4%Zn/Al-7075 and Mg-4%Zn/anodized Al-7075 multilayered composite was produced by accumulative roll bonding process up to four passes at 350 °C. Samples are characterized for microstructure using SEM, EBSD, TEM and XRD. Mechanical properties were evaluated by microhardness test and tensile strength tests. Corrosion behavior of the multilayered composite was examined using electrochemical polarization and immersion test. The results are briefed in the following sections.

##### **4.3.2.1 Microstructural analysis**

SEM micrographs of the Mg-4%Zn/anodized Al-7075 multilayered composites are shown in Figure 4.55. It revealed no void and crack at the interface of Mg-4%Zn and anodized an Al-7075 alloy which means that the good bonding established between the layers.

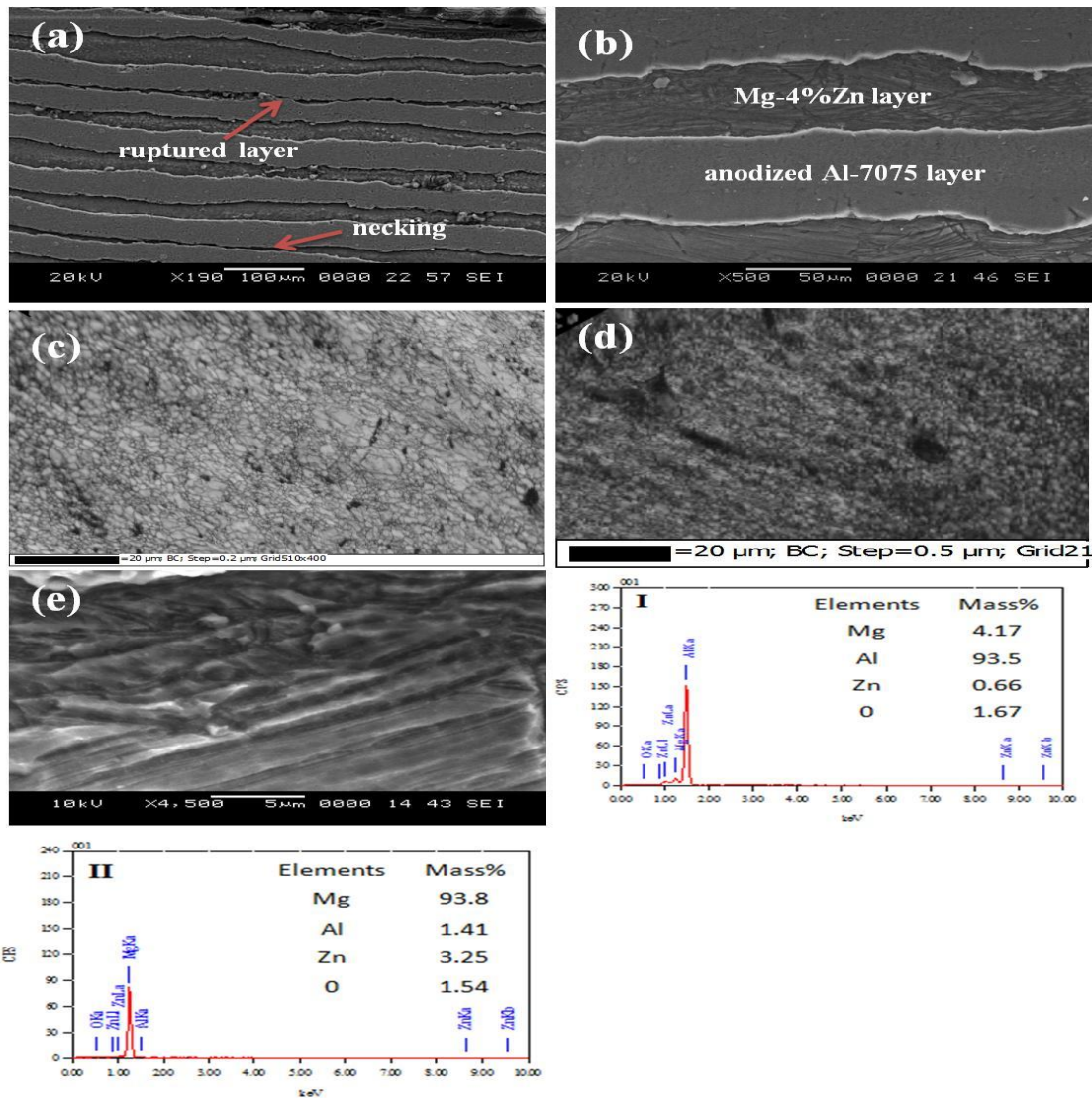


Figure 4.55. SEM micrographs of the ARB processed Mg-4%Zn/anodized Al multilayered composite (a) five pass multilayered composite (b) magnified image of the different layers (c) Al layer (d) anodized Al layer (e) Mg-2%Zn layer and EDS (I) anodized Al layer (II) Mg-2%Zn layer.

Thickness of both, Mg-4%Zn layer and anodized Al layer was found to be in the range of 50-60 µm (Figure 4.55 b) with slight waviness. Energy dispersive spectroscopy (EDS) data shows alternate layers of anodized Al-7075 layer (region I) and Mg-4%Zn layer (region II). Normally, plastic instabilities caused by different flow properties of constituent phases make the hard phase to form necking and finally to rupture during the co-deformation of dissimilar metals (Wu et al. 2010; Yazar et al. 2005). In the present investigation, Mg-4%Zn layers in the Mg-4%Zn/anodized Al-7075 multilayered composite undergoes a necking and finally ruptured because of brittleness

characteristics of Mg alloys. Microstructure of the Al-7075 layer (Figure 4.55 c), anodized Al-7075 layer (Figure 4.55 d) and Mg-4%Zn layer (Figure 4.55 e) reveals ultrafine grains formation due to grain subdivision and shears strain between strip and roller during ARB process. Fraction of recrystallized grains increased with increase in strain due to higher rate of nucleation of new grains during recrystallization, which resulted in a relatively uniform microstructure with ultra-fine grains.

#### 4.3.2.2 EBSD analysis

Figure 4.56 (a) shows the EBSD inverse pole figure (IPF) maps of Al-7075 layer microstructure illustrating reasonably homogeneous and consists of equiaxed grains.

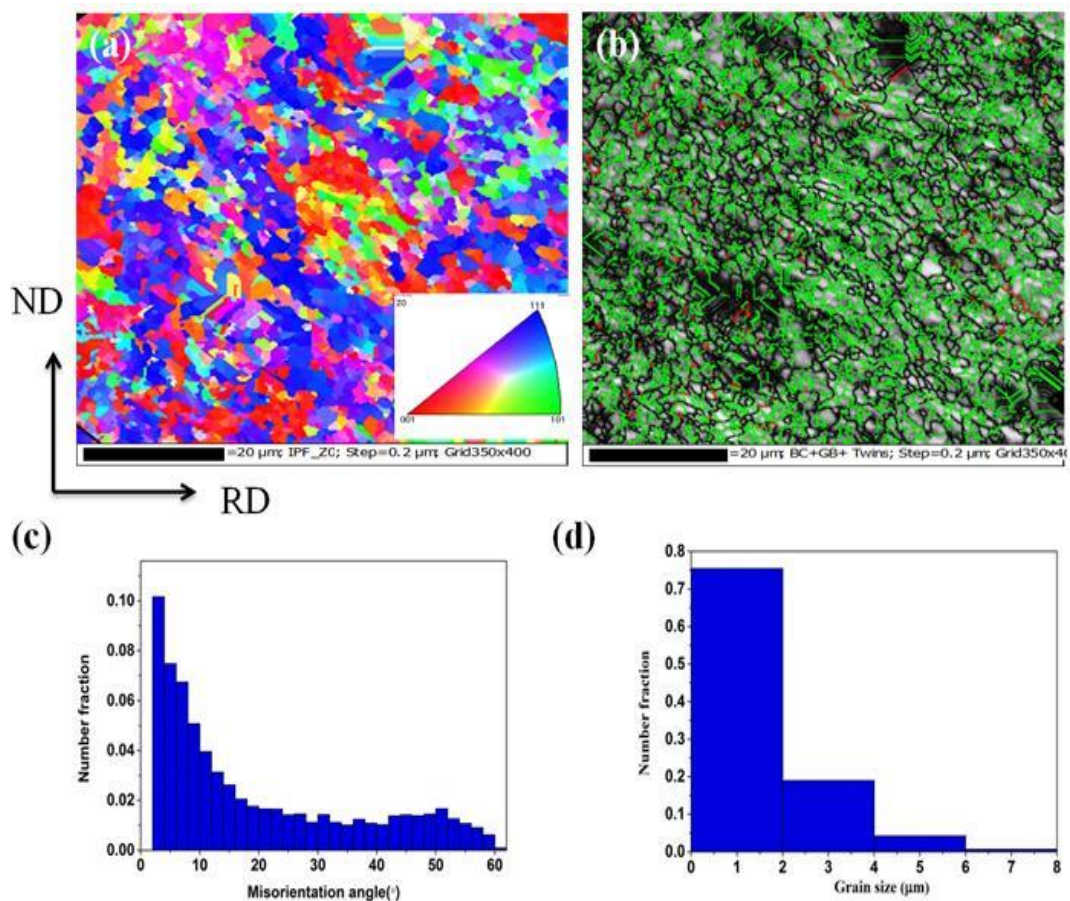


Figure 4.56. EBSD based analysis of Al-7075 layer in the 4-pass ARB processed Mg-4%Zn/Al-7075 multilayered composite (a) IPF map (b) Grain boundary map with twins (c) Misorientation angle distribution profile (d) Grain size distribution.

Grains are orientated in the direction of rolling, which is  $\langle 111 \rangle$  orientation. Figure 4.56 (b) depicts HAGBs in Al-7075 layer of the Mg-2%Zn/Al-7075 multilayered composite. Percentage of twins was found to be 1.67% in the Al-7075 layer due to strain hardening. Misorientation angle profile (Figure 4.56 c) consists of both LAGBs and HAGBs which indicates deformation is induced as a result of dynamic recovery. It is observed (Figure 4.56 d) that 75% of the grains in the microstructure have grain size below 2  $\mu\text{m}$ . Average grain size was found to be 1.3  $\mu\text{m}$  in the Al-7075 layer in the multilayered composite.

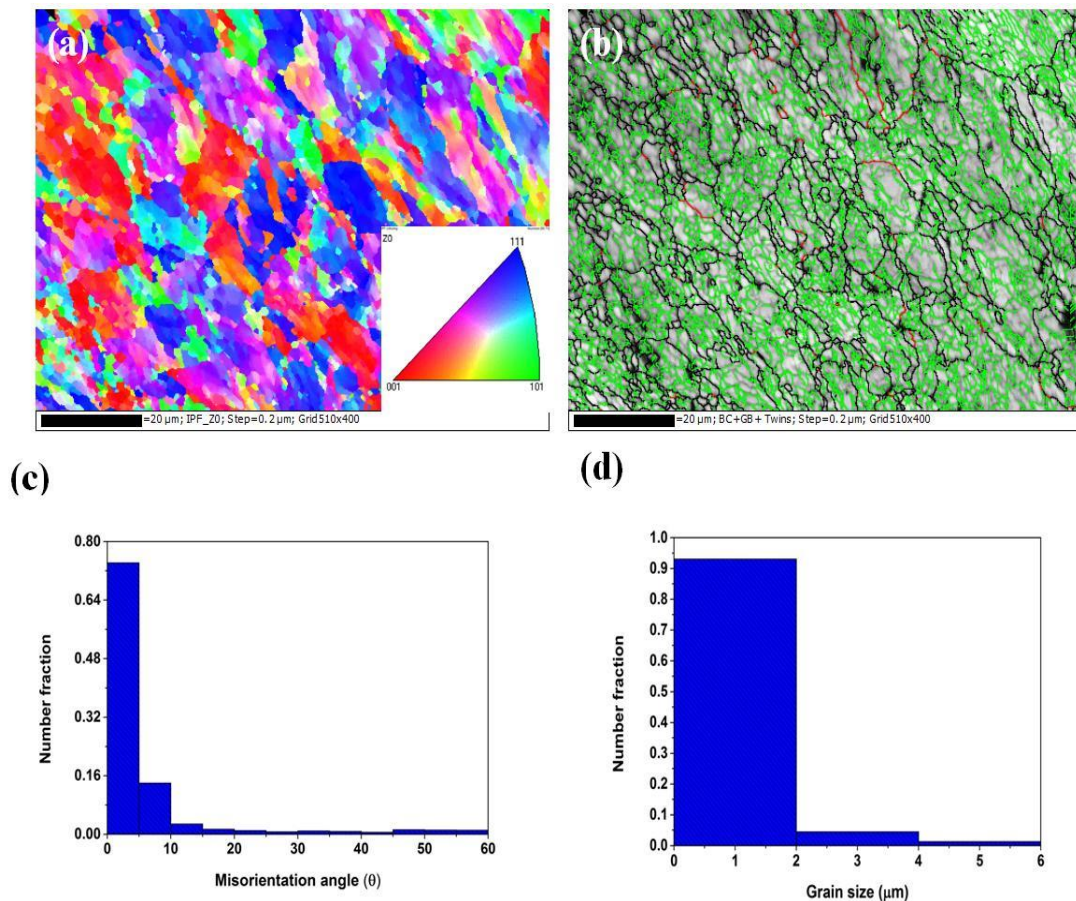


Figure 4.57. EBSD based analysis of anodized Al-7075 layer in the Mg-4%Zn/anodized Al-7075 multilayered composite (a) IPF map (b) Grain boundary map with twins (c) Misorientation angle distribution profile (d) Grain size distribution.

Figure 4.57 (a) shows the EBSD inverse pole figure (IPF) maps of anodized Al-7075 layer in the Mg-4%Zn/anodized Al-7075 multilayered composite. It shows ultra fine grains, which are orientated in the direction of rolling. Grain boundary map (Figure 4.57 b) revealed both high angle grain boundaries (HAGB) and low angle boundaries

(LAGB) which indicates that deformation is induced as result of dynamic recrystallization during ARB process. At higher strain, low angle grain boundaries (LAGBs) were converted into high angle grain boundaries (HAGBs). Percentage of twins and grain size was calculated from the HKL channel 5 software. The twins are found to be 0.45 % as shown in figure 4.57 (c). Misorientation angle distribution profile consists of grain size variation profile (Figure 4.57 d), shows around 90% of grains have diameter  $< 2 \mu\text{m}$  and an average grain size found to be  $0.73 \mu\text{m}$ .

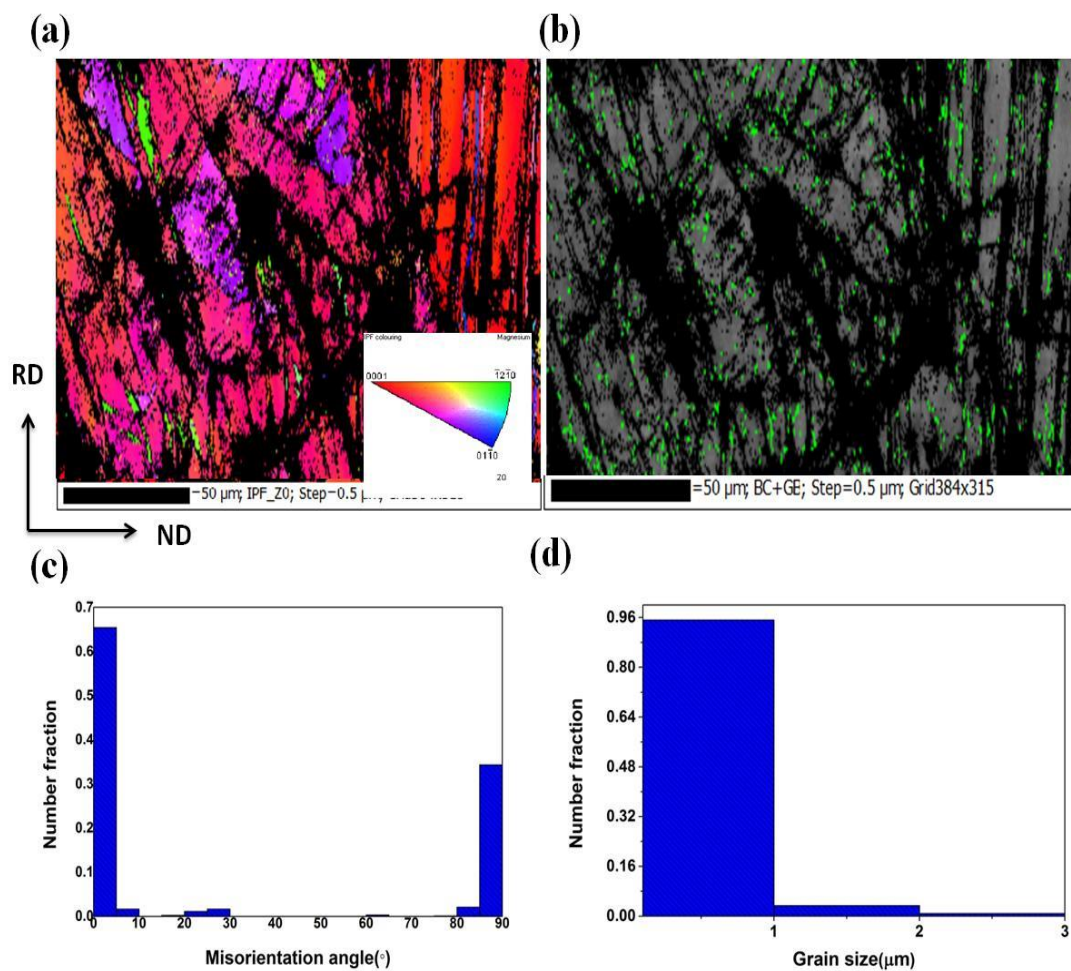


Figure 4.58. EBSD based analysis of Mg-4%Zn layer in the 4-pass ARB processed Mg-4%Zn/Al-7075 multilayered composite (a) IPF map (b) Grain boundary map with twins (c) Misorientation angle distribution profile (d) Grain size distribution.

Inverse pole figure (IPF) map of Mg-4%Zn layer (Figure 4.58 a) shows that, grains are oriented in  $\langle 0001 \rangle$  along the direction of rolling. Grain boundary map consists of fine grains with a fraction of both HAGBs and LAGBs and are overlaid with twins and are

shown in figure 4.58 (b). At HAGBs increase with decrease in LAGBs at higher ARB passes. At higher strain, ratio of recrystallized grains increases due to high rate of recrystallization, thus homogenous microstructure with UFG are achieved. Twins are suppressed with the activation of slip systems, thus mechanical anisotropy by grain refinement. Misorientation angle distribution profile (Figure 4.58 c), consists of both LAGBs and HAGBs. Grain size variation profile (Figure 4.58d) shows 92% of the grains are below 2  $\mu\text{m}$ , an average grain size found to be 1  $\mu\text{m}$ .

#### 4.3.2.3 TEM analysis

TEM microstructure and corresponding selected area electron diffraction (SAED) observed in rolling plane of the 4-pass ARB processed multilayered composite is shown in figure 4.59. Ultra-fine grains are revealed in the microstructure of the multilayered composite and some regions showed dislocations, which is an indication of large misorientation (Figure 4.59 a & b). It should be emphasized that the formation of the ultra-fine grains is regionally inhomogeneous in the highly strained materials (Saito et al .1998).

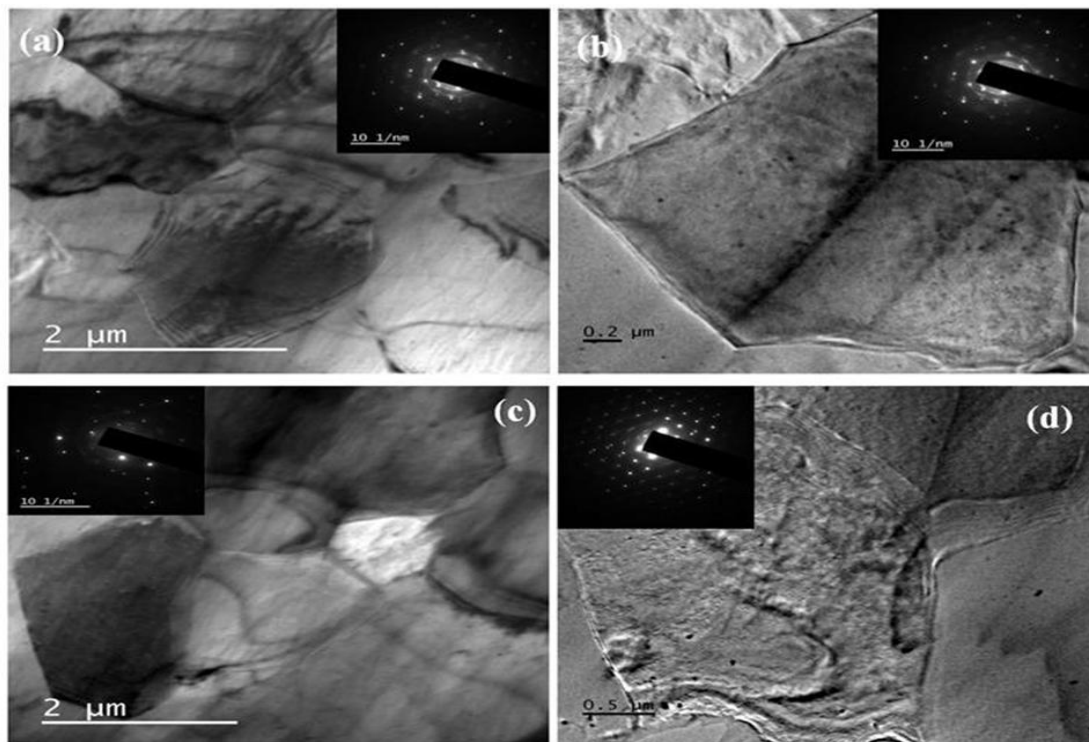


Figure 4.59. TEM micrographs and SAED patterns of the 4-pass ARB processed (a & b) Mg-4%Zn/Al-7075, (c & d) Mg-4%Zn/anodized Al-7075 multilayered composite.

At higher ARB passes, fraction of the ultra-fine grained regions is increased due to higher strain. Figure 4.59 (c & d) shows dislocation density inside the ultra-fine grain and are surrounded by strongly deformed boundaries. SAED patterns are in the form of rings which confirm the sub-grain structure in the Mg-2%Zn/Al-7075 and Mg-2%Zn/anodized Al-7075 composites with high angle misorientations. Diffraction spots are elongated and some diffraction spots do not form the rings, which is due to presence of low angle grain boundaries at higher strains.

#### 4.3.2.4 X-ray diffraction analysis

Figure 4.60 shows the XRD results along RD-TD plane of 4-pass ARB processed multilayered composite.

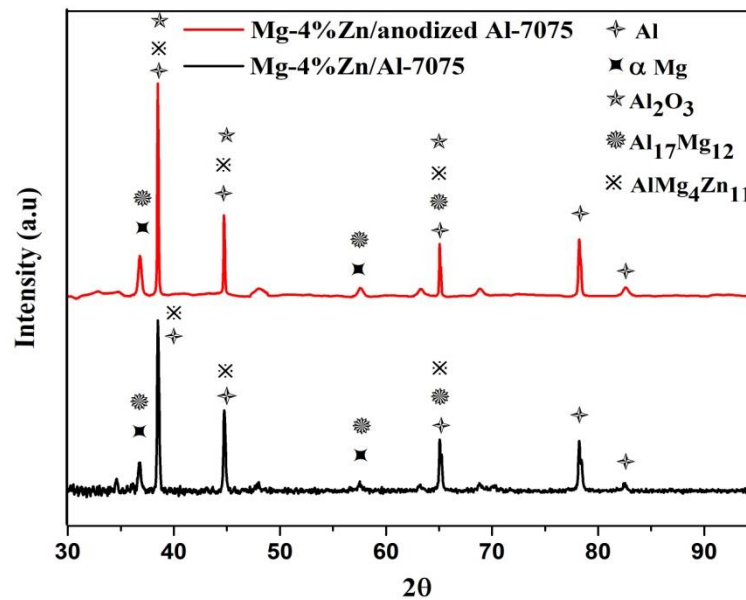


Figure 4.60. XRD patterns along the cross section of the 4-pass ARB processed multilayered composite.

XRD patterns revealed peaks indexed to Al,  $\alpha$ Mg, Al<sub>17</sub>Mg<sub>12</sub> and AlMg<sub>4</sub>Zn<sub>11</sub> in the Mg-4%Zn/Al composite. If the number of ARB pass increases the volume of the intermetallic increases. Al<sub>17</sub>Mg<sub>12</sub> and AlMg<sub>4</sub>Zn<sub>11</sub> intermetallics are found in the Mg-4%Zn/anodized Al-7075 multilayered composite, as well as Al<sub>2</sub>O<sub>3</sub> due to anodization treatment on Al-7075 alloy sheet before ARB process.



#### 4.3.2.5 Density Test

Density test results are shown in table 4.16. ARB processed Mg-4%Zn/Al-7075 and Mg-4%Zn/anodized Al-7075 roll bonded multilayered composite exhibited 1.23 times lighter weight as compared to Al-7075 alloy.

Table 4.16. Density test results.

Materials	Density Kg/m <sup>3</sup>
As rolled Mg-4%Zn	1780
Al-7075 alloy	2775
Anodized Al-7075 sheet	2778
Mg-4%Zn/Al-7075 composite	2252
Mg-4%Zn/anodized Al-7075 composite	2256

#### 4.3.2.6 Microhardness

Figure 4.61 shows the microhardness variation of different layers in the multilayered composite with respect to the number of ARB passes.

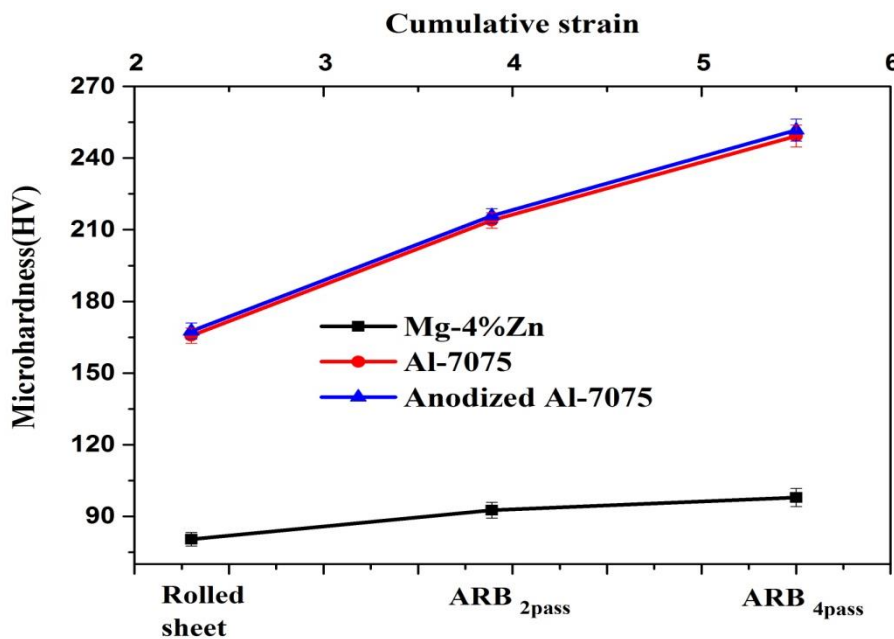


Figure 4.61. Microhardness variation of the rolled and Mg-4%Zn/anodized Al-7075 multilayered composite after different numbers of ARB passes.

Microhardness increased with increase in the strain. After four ARB passes, the microhardness of the Mg-4%Zn layer, Al-7075 layer and anodized Al-7075 layer reached to 97.9 HV, 249.3 HV and 251.7 HV respectively. Role of increase in microhardness is more at initial stages as compared to higher ARB passes. Thus increase in dislocation density and decrease in the average boundary spacing was contributed to hardening of the material in the initial passes. In addition, alumina particle present in the multilayered composites due to anodization treatment also contributing to improvement in the microhardness of the anodized Al-7075 layer.

#### **4.3.2.7 Tensile strength**

Figure 4.62 (a) shows variation in tensile strength of the as rolled Mg-4%Zn, Al-7075, and roll bonded Mg-4%Zn/Al-7075 multilayered composite. YS and UTS of the 4-pass ARB processed Mg-4%Zn/Al-7075 increased from about 136 MPa to 228 MPa and 210 MPa to 318 MPa respectively. Improvement of YS and UTS is due to bonding with very high strength Al-7075 alloy as well as strain hardening and grain refinement (Amirkhanlou et al. 2013; Parisa et al. 2015). Dislocations are generated at higher strain, which are pinned together and cause strengthening of the alloy. At higher ARB passes, work hardening effect diminishes and ultra fine grains are created gradually which is more dominant in the strengthening mechanism. Figure 4.62 (b) shows the yield strength, ultimate tensile strength and elongation to failure of the as-rolled sheets and different ARB passed Mg-4%Zn/anodized Al-7075 composite. YS and UTS increased from about 136 MPa to 230 MPa and 210 MPa to 322 MPa respectively. Obtained high strength is due to alumina particles present in the composite. Alumina particles act as a barrier to dislocation movement, causing enhancement of strength. With increase in the number of ARB passes, the total elongation decreases due to increase of work hardening, suppression of dislocation movement and formation ultra fine grains. ARB processed composites exhibited total elongation of 6.4% and 6.2% which is almost same as that of the starting material Mg-4%Zn alloy.

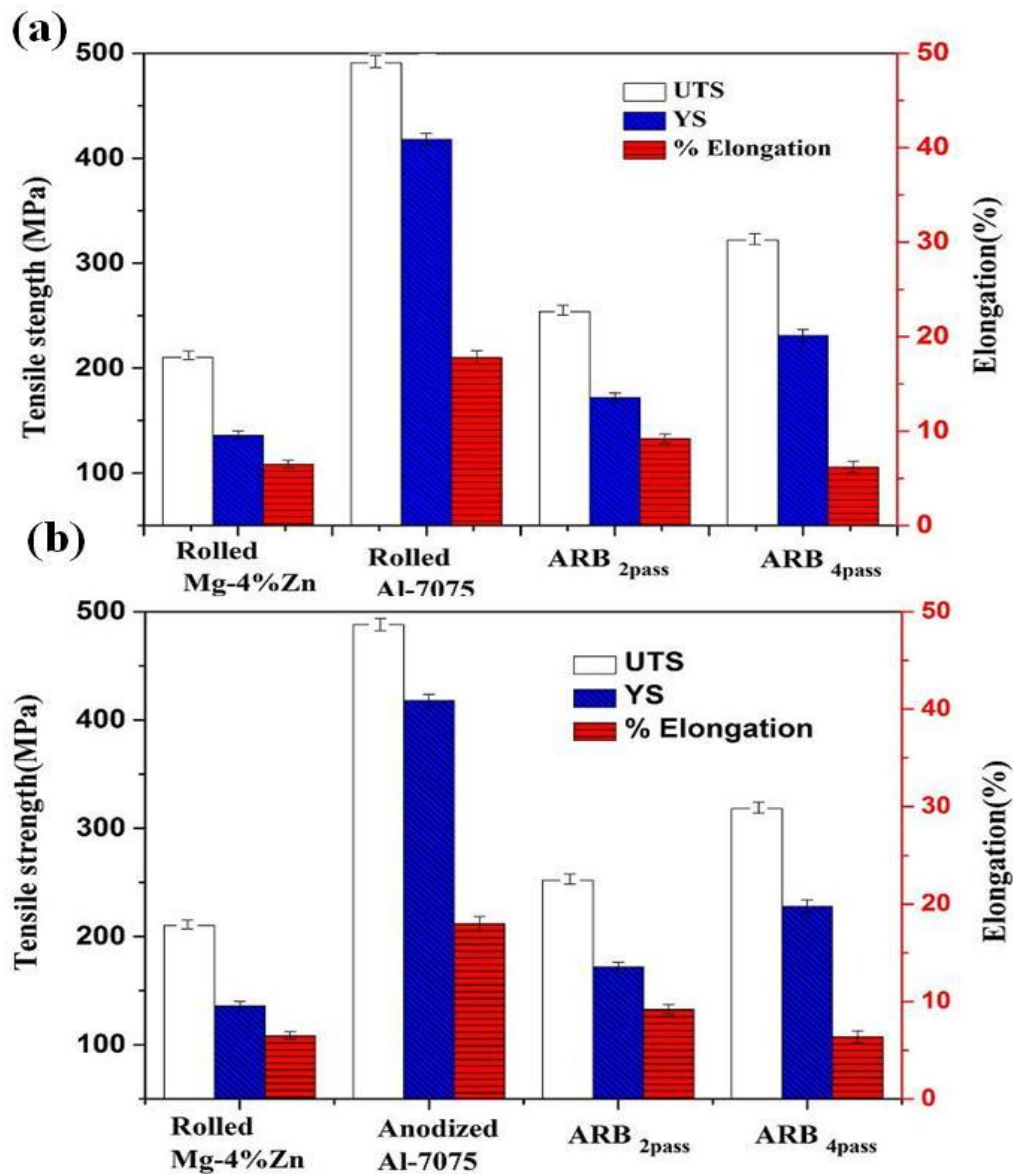


Figure 4.62. Variations of UTS, YS and percentage elongation of the multilayered composite with different ARB passes (a) Mg-4%Zn/Al-7075 (b) Mg-4%Zn/anodized Al-7075 composite.

#### 4.3.2.8 Fractography

Fracture surfaces of the multilayered composites layers are shown in figure 4.63. The Al-7075 and anodized Al-7075 layers reveal the dimples in the structure (Figure 4.63 a & b), which is the indication of ductile fracture. Ductile fracture takes place by nucleation, growth and coalescence of microvoids which leads to crack. From the

observation, it can be seen that dimples are elongated which is being affected by the state of shear stress, which demonstrates shear ductile failure in the Al-7075 and anodized Al-7075 layers.

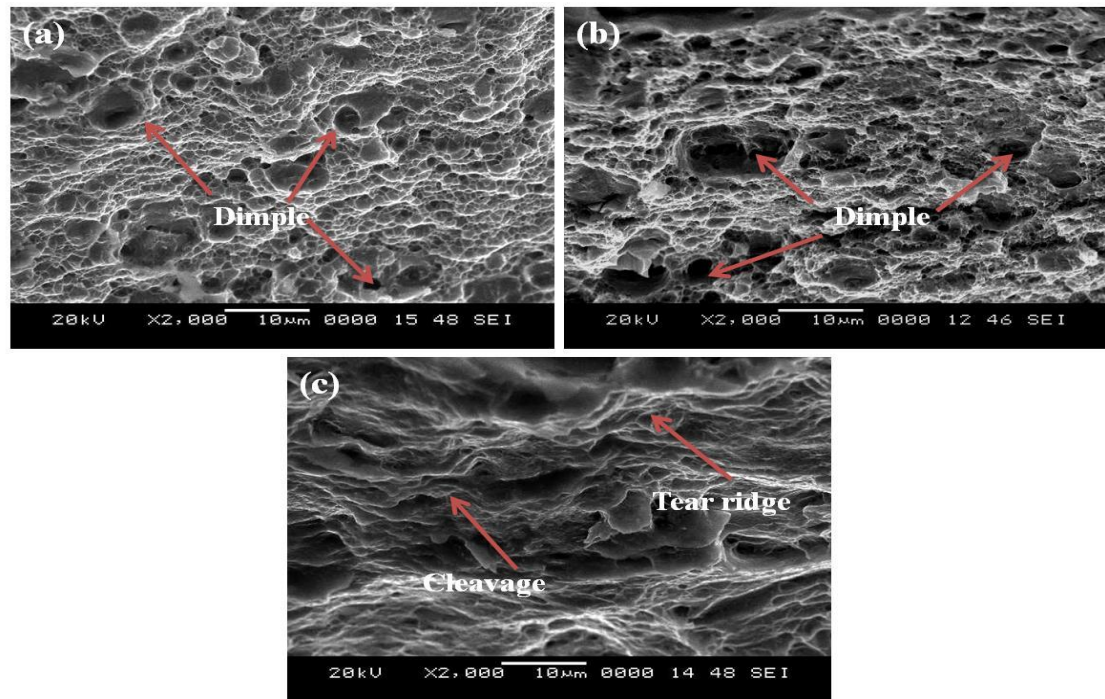


Figure 4.63. SEM micrographs of the fractured surface of the multilayered composites layers (a) Al-7075 (b) anodized Al-7075 (c) Mg-4%Zn layer.

However, Mg-4% Zn layers (Figure 4.63 c) were fractured in the shear mode and free from dimples which appear to be cleavage or transgranular brittle fracture due to hexagonal closed packed structure. Transgranular brittle fracture is characterized by some tear ridges and smooth facets.

#### 4.3.2.9 Potentiodynamic polarization

Potentiodynamic polarization plots of Mg-4%Zn alloy, ARB processed Mg-4%Zn/Al-7075 and Mg-4%Zn/anodized Al-7075 multilayered composites in the solution of 0.1 M NaCl are shown in figure 4.64. Calculated potentiodynamic polarization test results from the polarization curves are summarized in table 4.17. Potentiodynamic polarization plot shows the corrosion potential in passive regions indicating a higher passivation exhibited in the ARB processed multilayered composites as compared to

rolled Mg-4%Zn alloy. Corrosion current density ( $I_{\text{corr}}$ ) of the 4-pass ARB processed multilayered composites is  $30.14 \mu\text{A}/\text{cm}^2$  and  $24.85 \mu\text{A}/\text{cm}^2$  meanwhile shifts the corrosion potential ( $E_{\text{corr}}$ ) toward noble direction as observed in table 4.17.

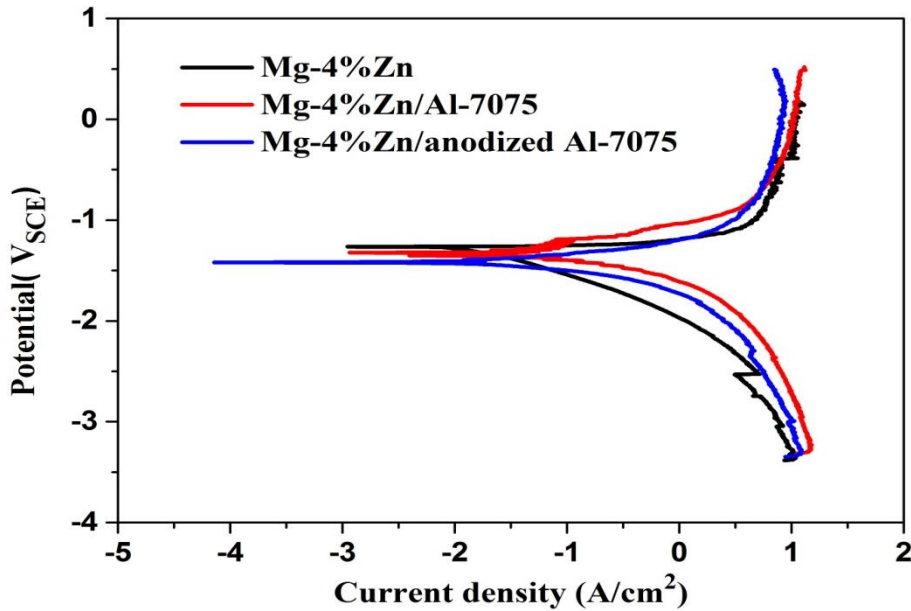


Figure 4.64. Potentiodynamic polarization curves of the Mg-4%Zn and 4-pass ARB processed multilayered composites.

Table 4.17. Potentiodynamic polarization test results.

Materials	$E_{\text{corr}}$ ( $\text{V}_{\text{SCE}}$ )	$i_{\text{corr}}$ ( $\mu\text{A}/\text{cm}^2$ )	$\beta_a$ ( $\text{mV}/\text{decade}$ )	$\beta_c$ ( $\text{mV}/\text{decade}$ )	Corrosion rate ( $\text{mm}/\text{y}$ )
Mg-4%Zn	-1.45	58.99	211.9	-285.4	1.77
Mg-4%Zn/Al-7075	-1.40	30.14	119.1	-172.9	0.73
Mg-4%Zn/anodized Al-7075	-1.283	24.85	125.1	-170.9	0.65

Corrosion rate was calculated from the EC-LAB software, it is revealed that Mg-4%Zn/Al-7075 (0.73 mm/y) improved about 2.42 times and Mg-4%Zn/anodized Al-7075 multilayered composites (0.65 mm/y) improved about 2.72 times as compared to

rolled Mg-4%Zn alloy (1.77 mm/y). Fine grains create more grain boundaries that act as a corrosion barrier. Intermetallics ( $\text{Al}_{12}\text{Mg}_{17}$  and  $\text{AlMg}_4\text{Zn}_{11}$ ) formed due to bonding, are uniformly distributed throughout the structure. These act as an anodic barrier to inhibit the overall corrosion.

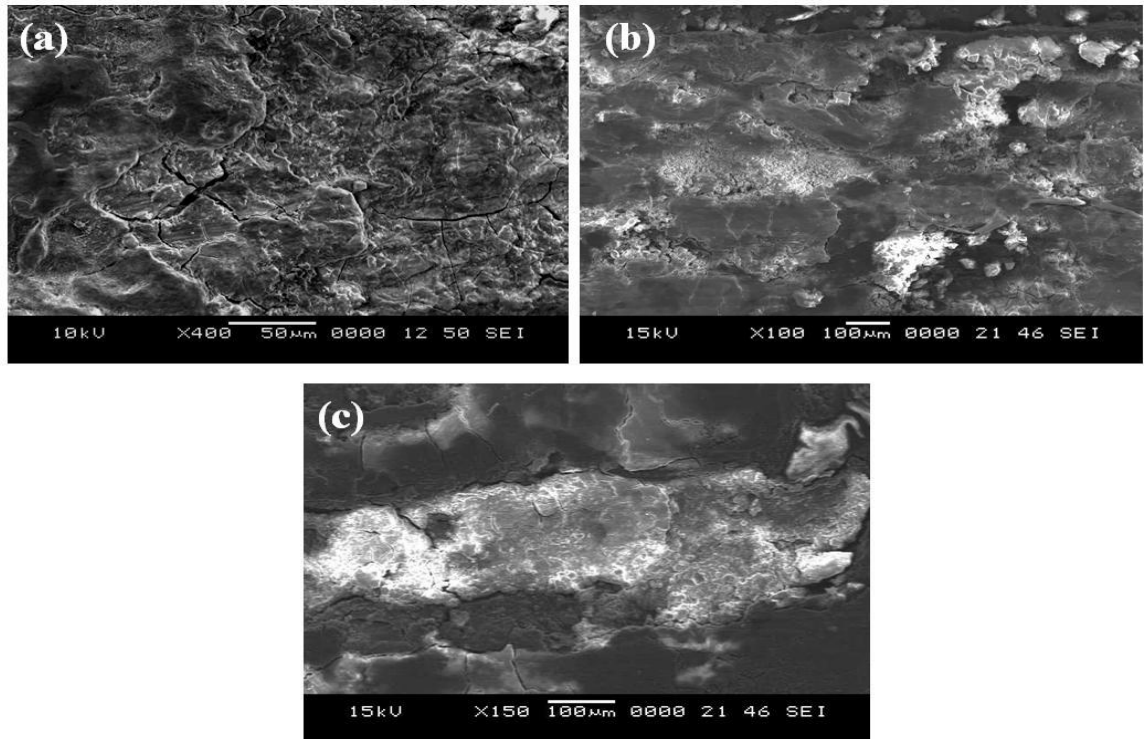


Figure 4.65. Surface morphologies of the corroded (a) Mg-4%Zn alloy (b) Mg-4%Zn/Al-7075 (c) Mg-4%Zn/Al-7075 multilayered composites.

Rolled Mg-4%Zn alloy revealed severe corrosion throughout the structure, some of the pits and cracks were observed (Figure 4.65). The Mg-4%Zn/Al-7075 and Mg-4%Zn/anodized Al-7075 multilayered composite exhibits layer-wise corrosion, Mg-4%Zn layer revealed corrosion products is mainly (magnesium hydroxide) as compared to Al-7075 layer. However, Mg-4%Zn/anodized Al-7075 multilayered composite did not show any severe dissolution like in Mg-Zn/Al-7075 composite because of anodization of Al before ARB process. Cracking tendency of anodized layer was found due to higher hardness and brittle nature of alumina surface.

#### 4.3.2.10 Immersion test

Hydrogen evolution rate and corresponding corrosion rate of the wrought Mg-4%Zn alloy and ARB processed composites are illustrated in Table 4.18.

Table 4.18. Immersion test results.

<b>Materials</b>	<b>Hydrogen evolution rate (ml/cm<sup>2</sup>/d)</b>	<b>Corrosion rate (mm/y)</b>
Rolled Mg-4%Zn alloy	1.02	2.26
Mg-4%Zn/Al-7075 composite	0.52	0.92
Mg-4%Zn/anodized Al-7075 composite	0.45	0.62

Higher hydrogen evolution was noticed for the Mg-4%Zn alloy (1.02 ml/cm<sup>2</sup>/d) as compared to Mg-4%Zn/Al-7075 (0.52 ml/cm<sup>2</sup>/d) and Mg-4%Zn/anodized Al-7075 composite (0.45 ml/cm<sup>2</sup>/d). The corrosion rate calculated from hydrogen evolution for 4-pass ARB processed multilayered composite is 3.64 times lesser than rolled Mg-4%Zn alloy due to refined microstructure and also due to presence of  $\beta$  phases ( $\text{Al}_{12}\text{Mg}_{17}$  and  $\text{AlMg}_4\text{Zn}_{11}$ ) and alumina. Potentiodynamic polarisation (Table 4.17) and immersion testing (Table 4.18) in 0.1 M NaCl solution showed similar trend in the corrosion rate.

#### 4.3.3 Mg-6%Zn/Al-7075 and Mg-6%Zn/anodized Al-7075 multilayered composites

Multilayered composite of Mg-6%Zn/Al-7075 and Mg-6%Zn/anodized Al-7075 was produced by accumulative roll bonding (ARB) using Mg-6%Zn with Al-7075 alloy and anodized Al-7075 alloy. ARB was carried out at 350 °C up to four pass. Microstructural evolution, mechanical properties and corrosion behaviour of ARB processed multilayered composite were investigated using various characterization techniques. The results are briefed in the following sections.

### 4.3.3.1 Microstructural analysis

Figure 4.66 shows the SEM micrographs in RD–TD planes of the ARB processed multilayered composite after 4-pass.

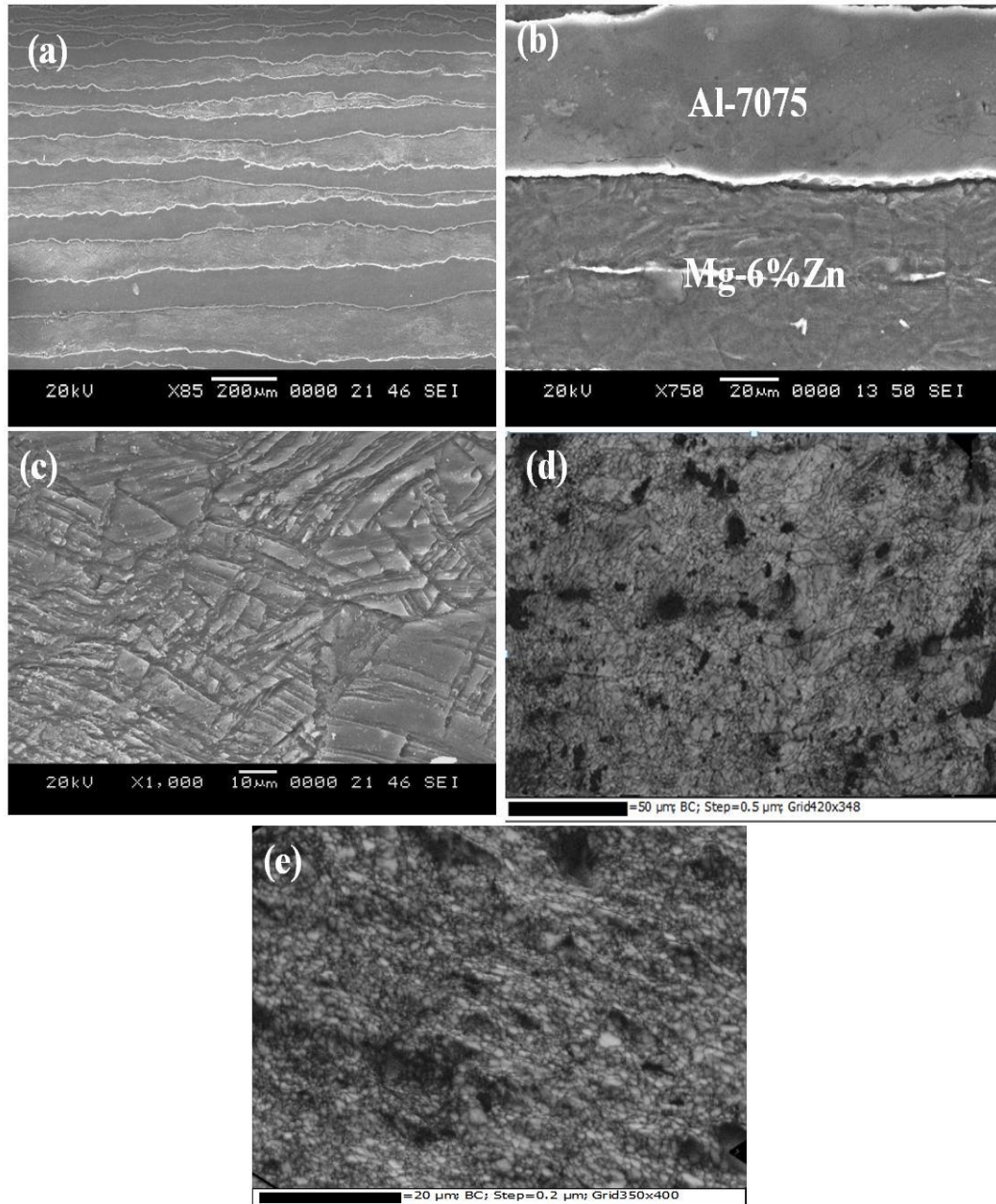


Figure 4.66. SEM micrographs of the ARB processed Mg-6%Zn/Al-7075 multilayered composite (a) five pass multilayered composite (b) magnified image of the different layers and grain structure (c) Mg-6%Zn layer (d) Al layer (e) anodized Al layer.



It reveals good bonding between the Mg-6%Zn and Al-7075 layers, as there are no cracks or delimitation between the interfaces. Slight waviness layer structure was observed along with necking and ruptured regions in the Mg-6%Zn layers because of high plastic deformation (Semiatin et al. 1979). Because of the brittleness of Mg, cracks were seen on Mg-6%Zn surface. Magnified SEM image of the multilayered composite (Figure 4.66 b) and the average layer thickness was found to be in the range of 50-60  $\mu\text{m}$ . Ultrafine grains are observed in Al layers ARB processed samples are in Figure 4.66 (c-e). Grain refinement mechanism during ARB is grain subdivision due to deformation induced high angle grain boundaries and also due to severe shears strain between strip and roller (Gashti et al. 2016). Total cumulative strain of the 4-pass ARB processed multilayered composite was calculated according to equation 3.3 and found to be 5.8.

#### 4.3.3.2 EBSD analysis

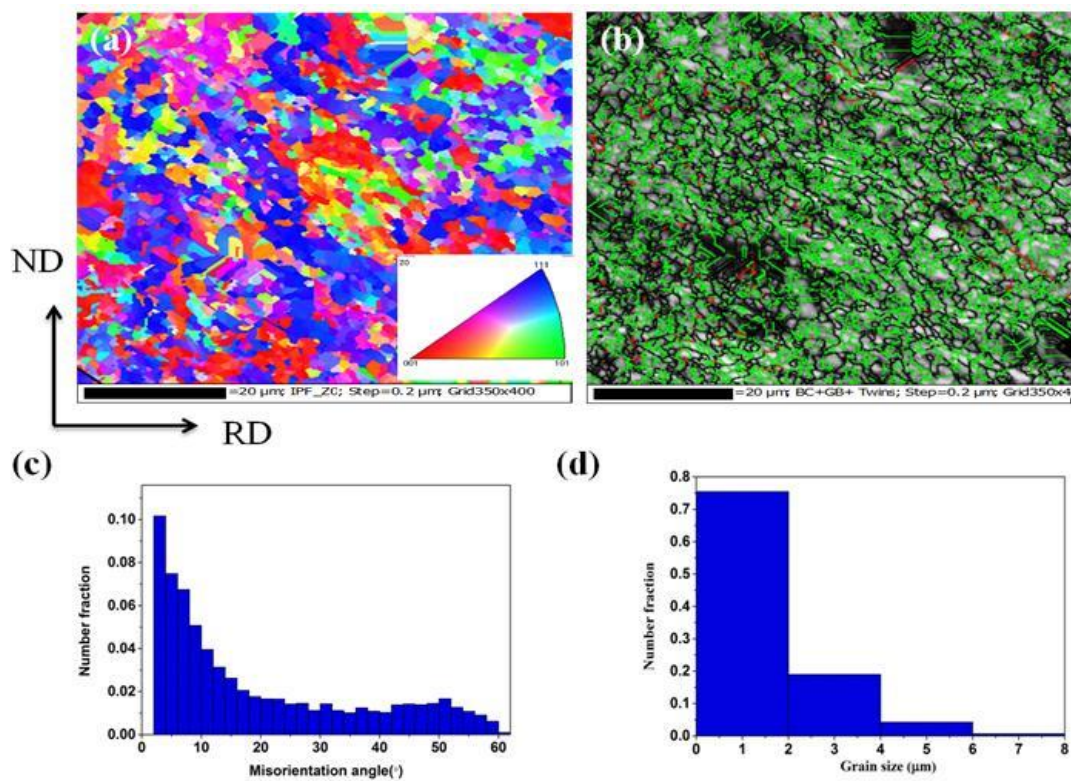


Figure 4.67. EBSD based analysis of Al-7075 layer in the 4-pass ARB processed Mg-6%Zn/Al-7075 multilayered composite (a) IPF map (b) Grain boundary map with twins (c) Misorientation angle distribution profile (d) Grain size distribution.

Microstructural evolution is depicted from the EBSD analysis of 4-pass ARB-processed multilayered composites layers (on RD-ND plane) is shown in Figure (4.67 - 4.69). Figure 4.67 (a) shows the EBSD inverse pole figure (IPF) maps of Al-7075 layer microstructure illustrating reasonably homogeneous and consists of equiaxed grains. Grains are orientated in the direction of rolling, which is  $\langle 111 \rangle$  orientation. Figure 4.67 (b) depicts HAGBs in Al-7075 layer of the Mg-2%Zn/Al-7075 multilayered composite. Percentage of twins was found to be 1.67% in the Al-7075 layer due to strain hardening. It is observed (Figure 4.67 d) that 75% of the grains in the microstructure have grain size below 2  $\mu\text{m}$ . The average grain size was found to be 1.3  $\mu\text{m}$  in the Al-7075 layer in the multilayered composite.

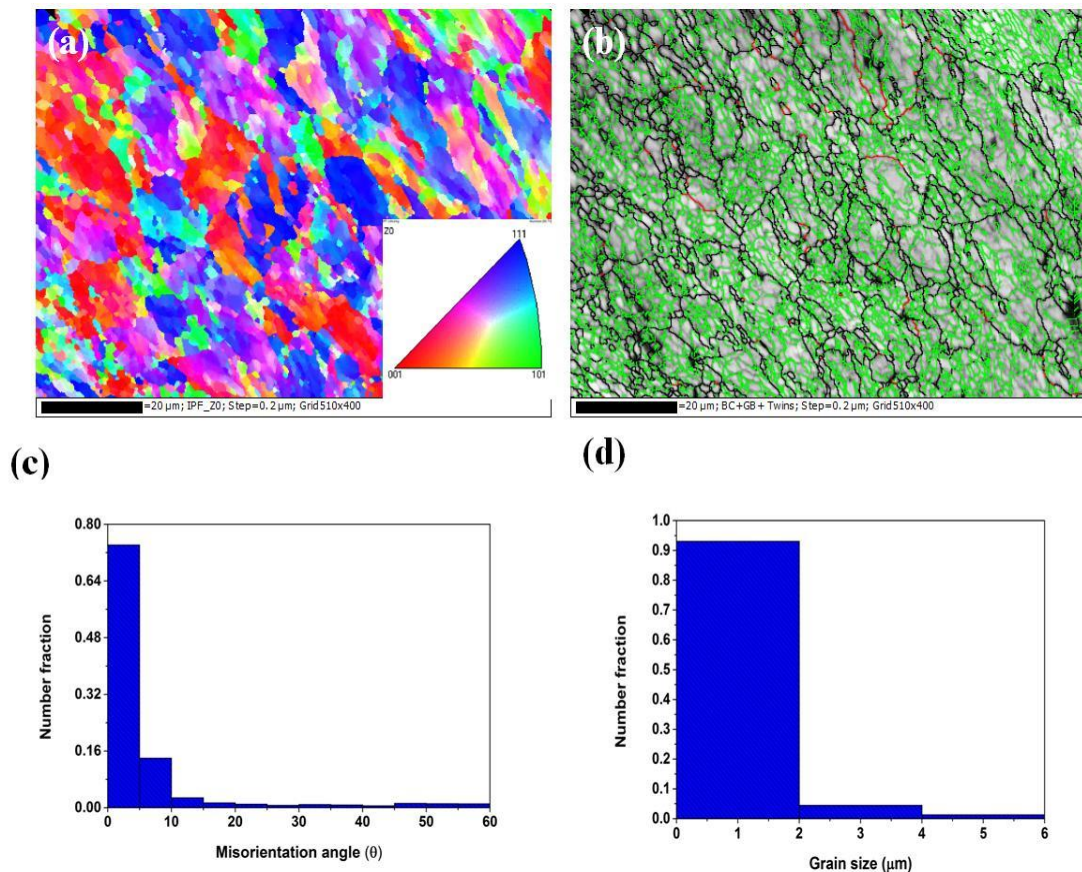


Figure 4.68. EBSD based analysis of anodized Al-7075 layer in the Mg-6%Zn/anodized Al-7075 multilayered composite (a) IPF map (b) Grain boundary map with twins (c) Misorientation angle distribution profile (d) Grain size distribution.

Figure 4.68 (a) shows the EBSD inverse pole figure (IPF) maps of Al-7075 layer, which shows ultra fine grains are orientated in the direction of rolling. From the figure 4.68 (b), percentage of twins was estimated to be 0.45 %. Misorientation angle profile (figure 4.67 c) consists of both LAGBs and HAGBs. Misorientation angle distribution profile consists of grain size variation profile (Figure 4.68 d) shows, around 90% of grains have diameter  $< 2 \mu\text{m}$  and an average grain size found to be  $0.73 \mu\text{m}$ .

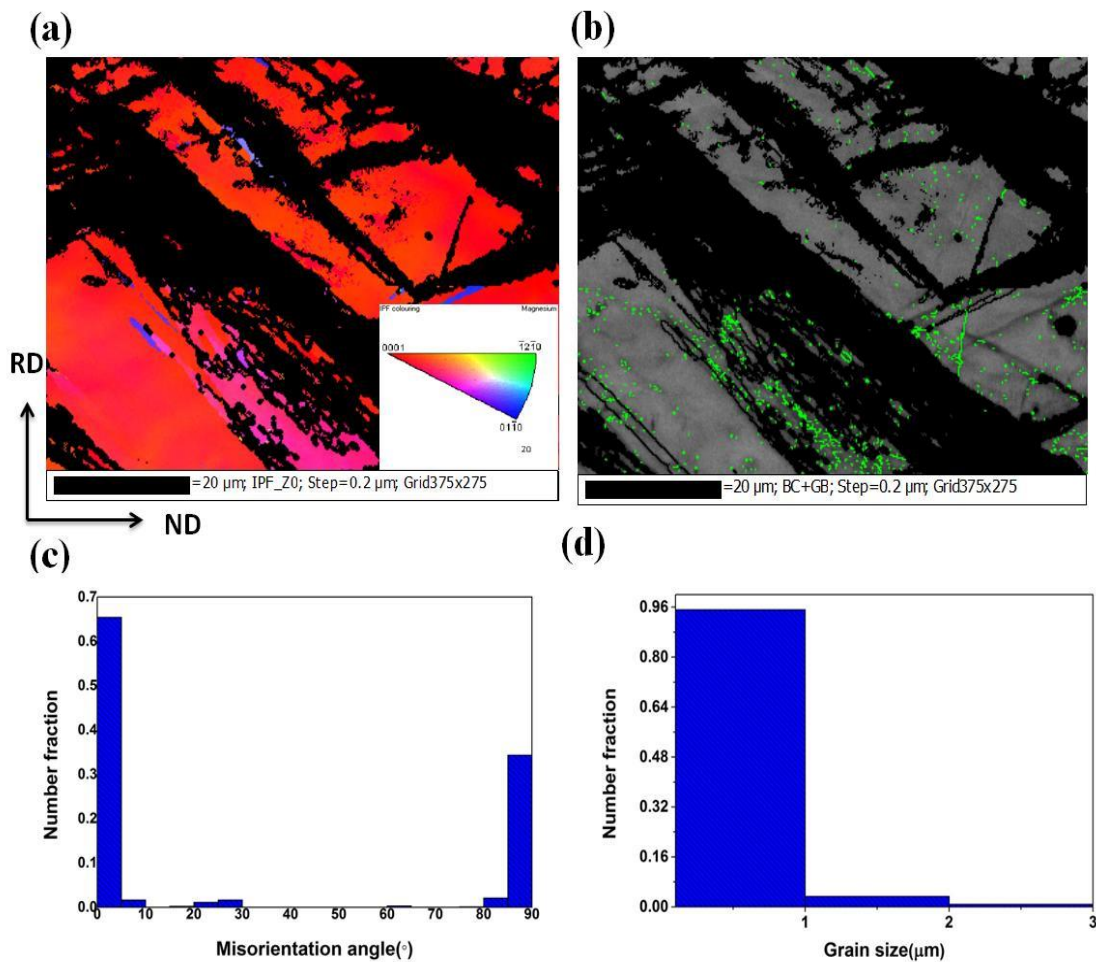


Figure 4.69. EBSD based analysis of Mg-6%Zn layer in the 4-pass ARB processed Mg-6%Zn/Al-7075 multilayered composite (a) IPF map (b) Grain boundary map with twins (c) Misorientation angle distribution profile (d) Grain size distribution.

Inverse pole figure (IPF) map of the Mg-6%Zn layer (Figure 4.69 a) reveals that, grains are directed uniformly in  $\langle 0001 \rangle$  orientation in the direction of rolling. Grain boundary map overlaid with twins is shown in figure 4.69 (b) which consists of fine grains with a fraction of both HAGBs and LAGBs. Misorientation angle distribution profile (Figure 4.69 c), consists of both LAGBs and HAGBs. But, no twins were seen in Mg-2%Zn

layer and the average grain size of  $0.6\ \mu\text{m}$  was observed in Mg-2%Zn layer of 4 pass ARB sample and it depicted in figure 4.69 (d).

#### 4.3.3.3 TEM analysis

Micrographs of TEM and their corresponding selected area diffraction patterns (SAED) (ND-RD plane) of the ARB processed Mg-6%Zn/Al-7075 and Mg-6%Zn/anodized Al-7075 composites are illustrated in figure 4.70.

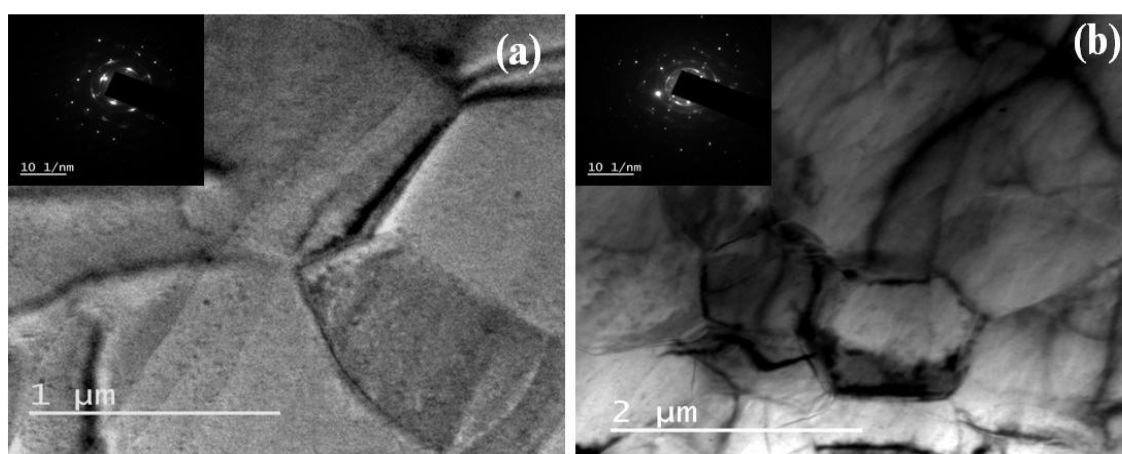


Figure 4.70. TEM micrographs and SAED patterns of the ARB processed (a) Mg-6%Zn/Al-7075 and (b) Mg-6%Zn/anodized Al-7075.

As can be seen, fine grains with dislocation tangles are present in the multilayered composites. The observed SAED patterns also depict ultra-fine grains and dislocation cells. The SAED patterns of both composites shows ring like pattern consisting of separate spots. This indicates ultra fine grains with high angle boundaries and it also confirms the EBSD analysis.

#### 4.3.3.4 X-ray diffraction analysis

The results of XRD analysis were carried out on the RD–TD plane of the ARB processed sheets are shown in figure 4.71. XRD patterns revealed (Figure 4.71) peaks indexed to Al,  $\alpha\text{Mg}$ ,  $\text{Al}_{17}\text{Mg}_{12}$  and  $\text{AlMg}_4\text{Zn}_{11}$  in the Mg-6%Zn/Al-7075 composite and Mg-6%Zn/anodized Al-7075 composite shows the Al,  $\alpha\text{Mg}$ ,  $\text{Al}_{17}\text{Mg}_{12}$  and  $\text{AlMg}_4\text{Zn}_{11}$  along with  $\text{Al}_2\text{O}_3$ . Important feature of the patterns is that a small peak of  $\text{Al}_{17}\text{Mg}_{12}$ ,

AlMg<sub>4</sub>Zn<sub>11</sub> and Al<sub>2</sub>O<sub>3</sub> appears after four pass. As the ARB proceeds and the layer thickness decreases, the number of interfaces per unit volume is raised.

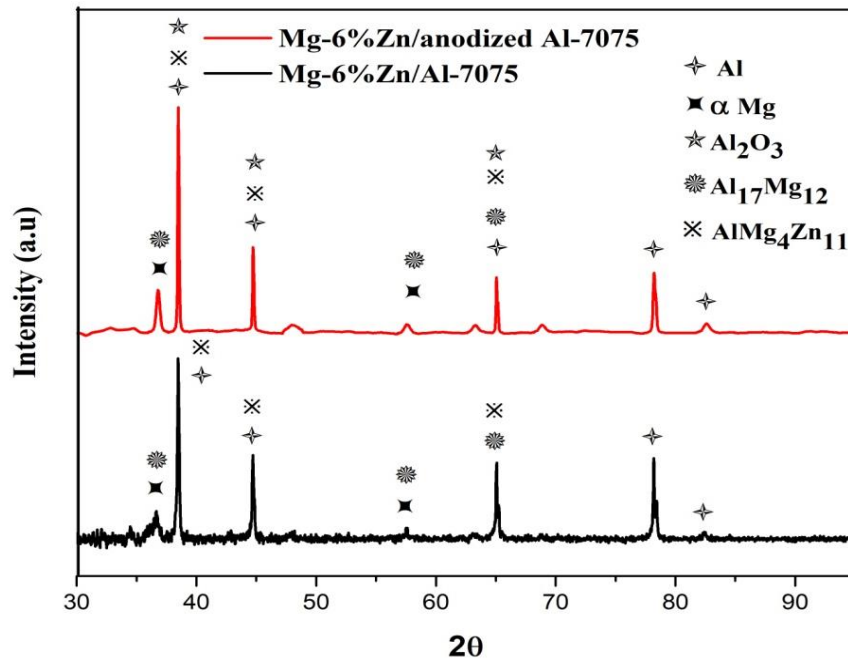


Figure 4.71. XRD patterns along the cross section of accumulative roll bonded multilayered composite.

As a result, the intensity of intermetallic increases to some extent as the ARB cycles is increased. The formation of intermetallics phases in multilayered composites attributed to high rolling strain during ARB at 350 °C which increases the diffusion between different layers of the multilayered composite, grain boundaries area and dislocation density (Zhang et al. 2007; Liu et al. 2012). This accelerates the elemental diffusion at interfaces and promotes the formation of intermetallic (Song et al. 1998).

#### 4.3.3.5 Density test

Density test, which follows Archimedes principle was performed on rolled and accumulative roll bonded multilayered composites and the results are illustrated in Table 4.19.

Table 4.19. Density test results

Materials	Density Kg/m <sup>3</sup>
As rolled Mg-6%Zn	1781
Al-7075 alloy	2775
Anodized Al-7075 sheet	2776
Mg-6%Zn/Al-7075 composite	2166
Mg-6%Zn/anodized Al-7075 composite	2170

Roll bonded Mg-6%Zn/Al-7075 and Mg-6%Zn/anodized Al-7075 multilayered composite exhibited weight saving of 21.8% and 21.9% respectively, as compared to Al-7075 alloy.

#### 4.3.3.6 Microhardness

Figure 4.72 shows the Vickers microhardness variations of Mg-6%Zn, Al-7075 and anodized Al-7075 layers of the multilayered composite at the different passes of the ARB process.

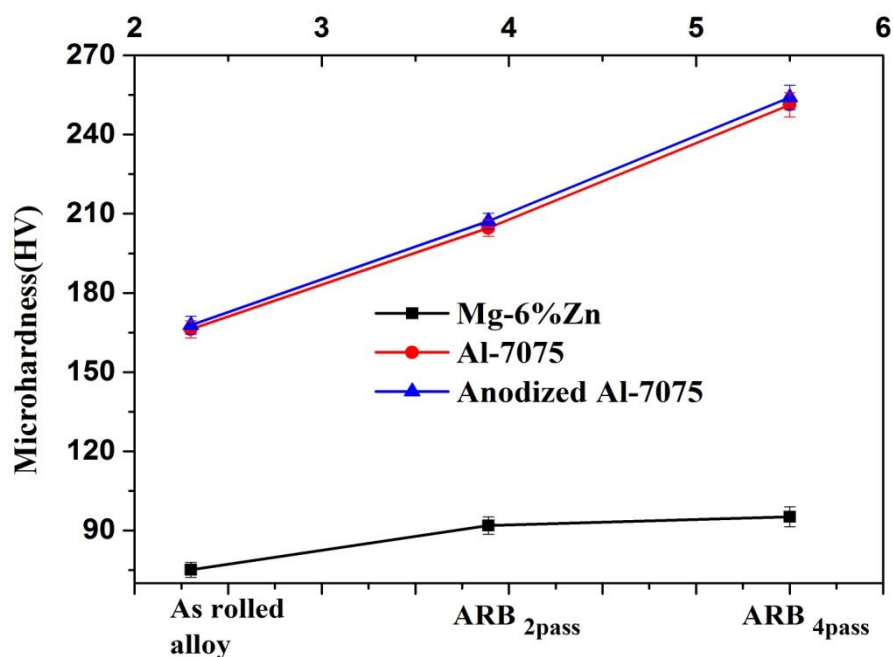


Figure 4.72. Microhardness variation of Mg-6%Zn, Al-7075 and anodized Al-7075 layers during different passes of the ARB process.

It illustrates that by increasing the ARB passes, the microhardness of ARB processed multilayered composite layers was increased. After four ARB passes, the microhardness of the Mg-6%Zn layer, Al-7075 layer and anodized Al-7075 layer reached to 95.2 HV (1.26 times), 251.3 HV (1.501 times) and 254.1 HV (1.51 times) respectively. The increase rate of microhardness in the primary passes of ARB is attributed to the high rate of strain hardening (based on the density of dislocations and interactions between them). At higher ARB passes, increase in microhardness values is due to combined effect of strain hardening and grain refinement (Wang et al. 2016). The anodized Al-7075 layer in the Mg-6%Zn/anodized Al-7075 composite exhibited higher hardness values as compared to Al-7075 layer in the Mg-6%Zn/Al-7075 composite due to uniform distribution of harder alumina ( $\text{Al}_2\text{O}_3$ ) particles in the aluminium layer.

#### **4.3.3.7 Tensile strength**

Tensile properties have been evaluated for different pass ARB processed Mg-6%Zn/Al-7075 composite and Mg-6%Zn/anodized Al-7075 composite as shown in Figure 4.73 (a & b). Figure 4.73(a) shows variation of tensile strength and ductility of Mg-6%Zn/Al-7075 multilayered composite subjected to different ARB passes. The characteristic nature of these plots show that YS and UTS were improved and after the four ARB pass were about 1.64 times (224 MPa) and 1.68 times (316 MPa) higher than that of the rolled M-6%Zn alloy. Variations of the strength in the severely deformed materials are governed by strain hardening by dislocations and grain refinement (Tsuji et al. 1999; Huang et al. 2008). Figure 4.73(b) shows variation of tensile strength and ductility of Mg-6%Zn/anodized Al-7075 multilayered composite subjected to different ARB passes. The maximum YS and UTS were improved and after the four ARB pass were about 1.66 times (226 MPa) and 1.70 times (320 MPa) higher than that of the rolled M-6%Zn alloy. The YS and UTS of the Mg-6%Zn/anodized Al-7075 are superior that that of Mg-6%Zn/Al-7075 composite.

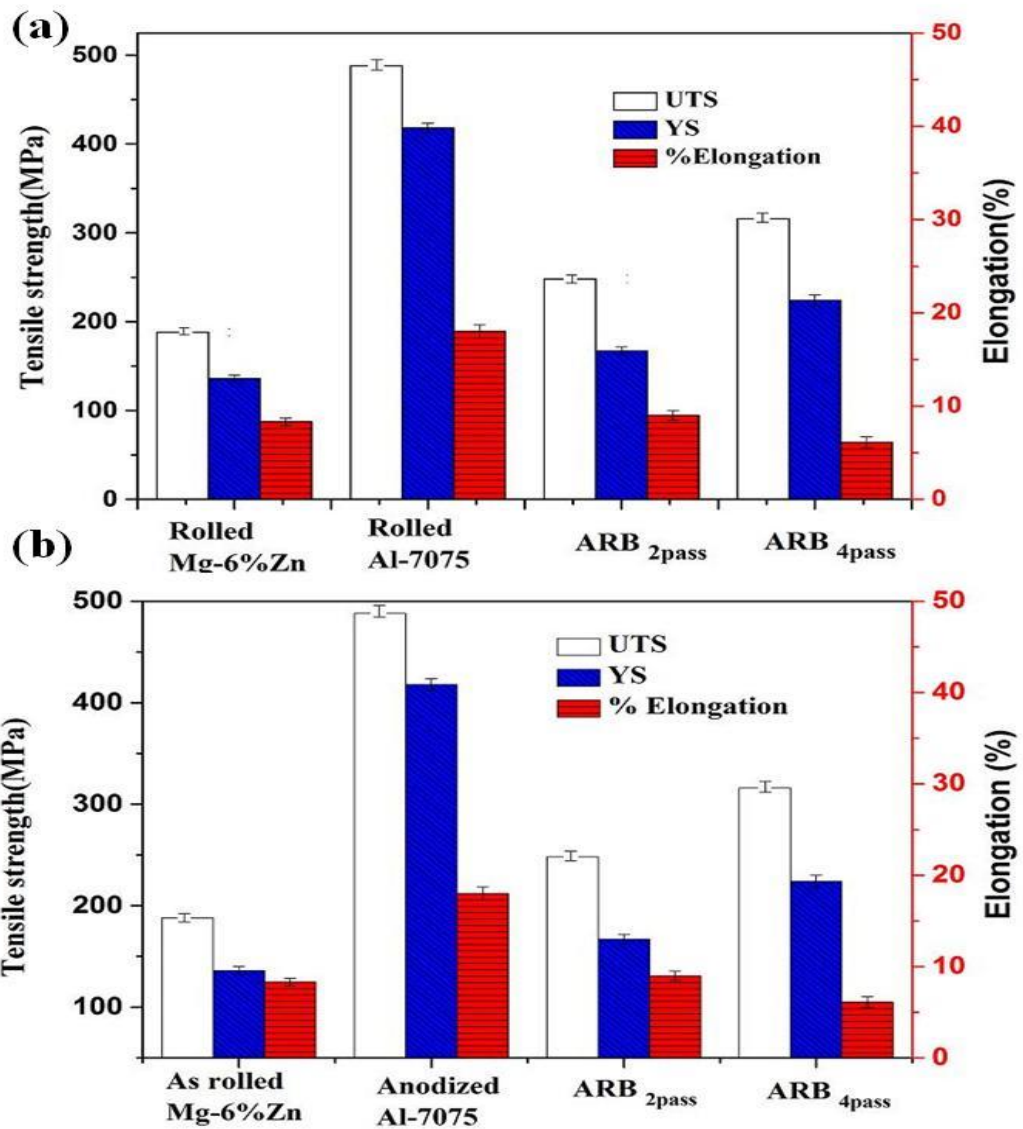


Figure 4.73. Variation of UTS, YS and percentage elongation of the multilayered composite with different ARB passes (a) Mg-6%Zn/Al-7075 composite (b) Mg-6%Zn/anodized Al-7075 composite.

Thus it attributed to strain hardening, grain refinement and also from alumina particle ( $Al_2O_3$ ) resulted from the anodization process (Alizadeh, 2011).

#### 4.3.3.8 Fractography

Fracture surface of tensile tested 4-pass ARB processed Al-7075, anodized Al-7075 and Mg-6%Zn layers are shown in Figure 4.74. The principal of fracture mechanism at all layers of the Mg-6%Zn/Al-7075 and Mg-6%Zn/anodized Al-7075 multilayered



composites was considered, found that Al-7075 layer and anodized Al-7075 layer depicts typical ductile failure illustrated by dimples, as shown in figure 4.74 (a) and (b) respectively.

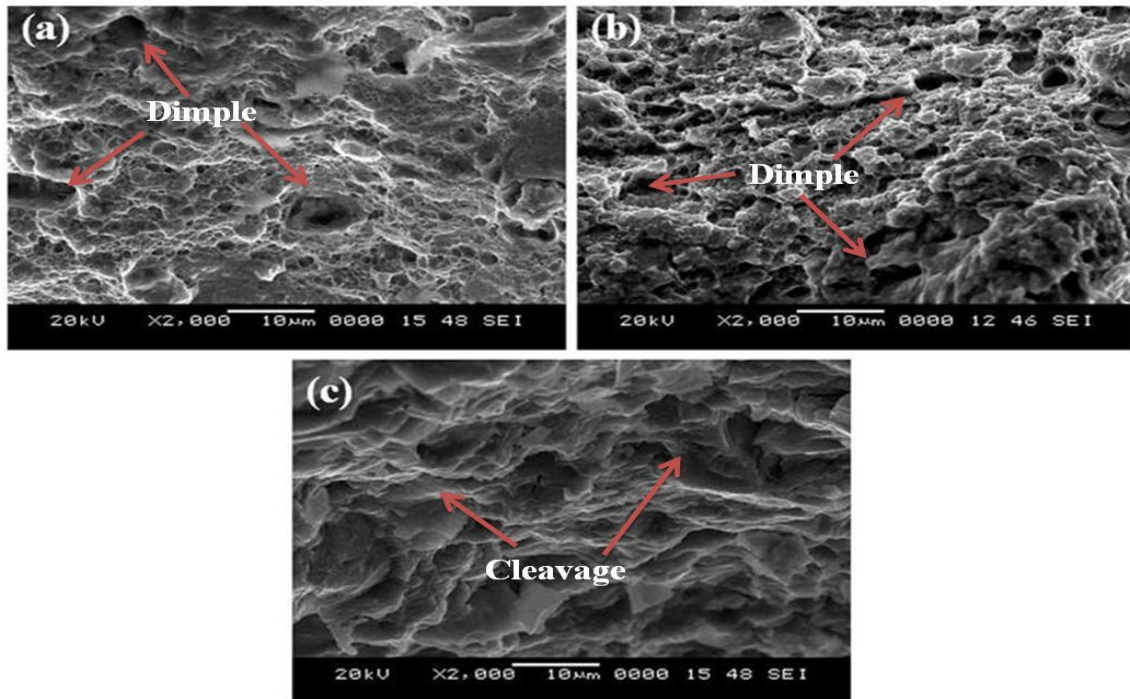


Figure 4.74. SEM micrographs of the fractured surface of 5-pass ARB processed (a) Mg-4%Zn/Al (b) anodized Al multilayered composite.

Elongated dimples on the fractured surface of the Al-7075 layer and anodized Al-7075 layer which evidently illustrate that the failure mode is shear ductile rupture. When the failure is influenced by shear stress, the voids tend to be elongated, consequently, parabolic depressions form on the fracture surfaces. However, Mg-6%Zn layers (Figure 4.74 d) were fractured in the shear mode and free from dimples, it reveals bright lines in the fracture surface which is the indication of cleavage fracture.

#### 4.3.3.9 Potentiodynamic polarization

Potentiodynamic polarization curves were recorded to evaluate the corrosion properties of the Mg-6%Zn, Mg-6%Zn/Al-7075 and Mg-6% Zn/anodized Al-7075 (Figure 4.75). Calculated potentiodynamic polarization test results from the polarization curves are summarized in table 4.20.

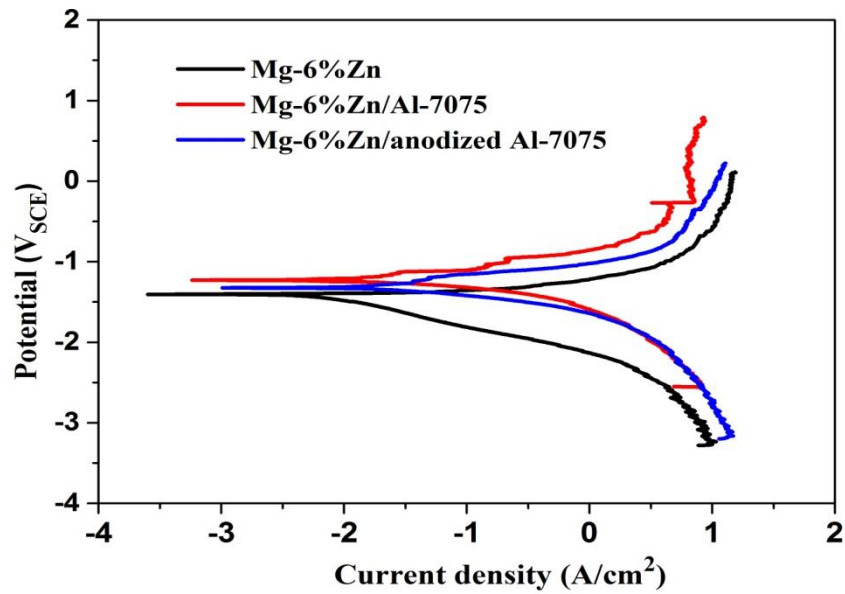


Figure 4.75. Potentiodynamic polarization curves of the Mg-6%Zn, Mg-6%Zn/Al-7075 and Mg-2% Zn/anodizedAl-7075 multilayered composite.

Table 4.20. Potentiodynamic polarization test results.

Materials	$E_{\text{corr}}$ ( $V_{\text{SCE}}$ )	$i_{\text{corr}}$ ( $\mu\text{A}/\text{cm}^2$ )	$\beta_a$ ( $\text{mV}/\text{decade}$ )	$\beta_c$ ( $\text{mV}/\text{decade}$ )	Corrosion rate ( $\text{mm}/\text{y}$ )
Mg-6%Zn alloy	-1.53	16.1	175.8	302.7	0.49
Mg-6%Zn/Al-7075 composite	-1.17	15.3	107.9	-117.6	0.38
Mg-4%Zn/anodized Al-7075 composite	-1.28	14.9	147.3	-168.2	0.36

Corrosion resistance of the multilayered composite is dramatically improved due to UFG structure; fine sized grains create more grain boundaries that act as a corrosion barrier. During ARB process, intermetallics ( $\text{Al}_{12}\text{Mg}_{17}$  and  $\text{AlMg}_4\text{Zn}_{11}$ ) formed due to bonding with anodized Al-7075 alloy are refined and uniformly distributed throughout the structure which acts as an anodic barrier to inhibit the overall corrosion and anodization treatment on Al-7075 alloy before ARB process. Lowest  $i_{\text{corr}}$  values were

observed in Mg-6%Zn/anodized Al-7075 as compared to Mg-6%Zn/Al-7075, due to uniform distribution of alumina ( $\text{Al}_2\text{O}_3$ ) resulted from the anodization process along with ultra-fine grains and composites contains  $\beta$  phases ( $\text{Al}_{12}\text{Mg}_{17}$  and  $\text{AlMg}_4\text{Zn}_{11}$ ) formed during ARB process.

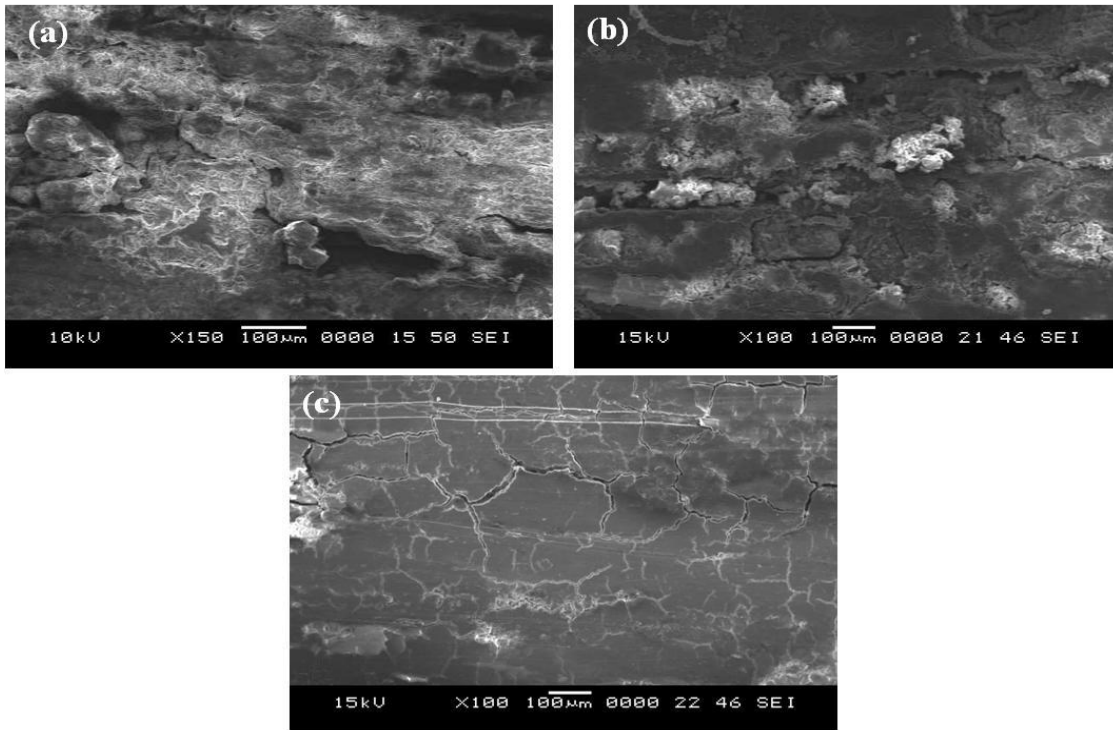


Figure 4.76. SEM micrographs of corroded (a) rolled Mg-6%Zn (b) Mg-6%Zn/Al-7075 and (c) Mg-6%Zn/anodized Al-7075 after electrochemical test in a 0.1 M NaCl solution.

Surface morphology after electrochemical polarization test in 0.1 M NaCl solution is shown in figure 4.76. Severe corrosion, as well as, some of the pits and cracks were observed on the surface of the rolled Mg-6%Zn alloy, as shown in figure 4.76 (a). The layer-wise corrosion can be observed on the multilayered composite. Bright area shown in Mg-6%Zn alloy signifies the high rate of corrosion (magnesium hydroxide). However, Mg-6%Zn/Al-7075 (Figure 4.76b) and Mg-6%Zn/anodized Al-7075 (Figure 4.76 c) multilayered composite did not show any severe dissolution like Mg-6%Zn alloy.

#### 4.3.3.10 Immersion test

Hydrogen evolution rate and corresponding corrosion rate of the wrought Mg-6%Zn alloy and ARB processed Mg-6%Zn/Al-7075 and Mg-2%Zn/anodized Al-7075 composite in 0.1 M NaCl are illustrated in table 4.21.

Table 4.21. Immersion test results.

Materials	Hydrogen evolution rate (ml/cm <sup>2</sup> /d)	Corrosion rate (mm/y)
Mg-6%Zn	0.28	0.62
Mg-6%Zn/Al-7075	0.25	0.45
Mg-6%Zn/anodized Al-7075	0.23	0.41

The corrosion rate calculated from hydrogen evolution for multilayered composite is less than rolled Mg-6%Zn alloy due to refined microstructure and the presence of  $\beta$  phases ( $Al_{12}Mg_{17}$  and  $AlMg_4Zn_{11}$ ) and distribution of alumina particles.

#### 4.3.4 Summary

Mg-(2-6)%Zn/Al-7075 and Mg-(2-6)%Zn/anodized Al-7075 multilayered composites were processed by accumulative roll bonding process at 350 °C up to four passes successfully. Microstructure, mechanical properties and corrosion behaviour of the multilayered composites was investigated. Following summaries has been derived from the obtained results.

Developed multilayered composites exhibited found to be 21% lighter weight as compared to Al-7075 alloy. XRD analysis revealed the presence of  $Al_{17}Mg_{12}$  and  $AlMg_4Zn_{11}$  and  $Al_{17}Mg_{12}$ ,  $AlMg_4Zn_{11}$  and  $Al_2O_3$  intermetallics in the four pass ARB processed Mg-(2-6)%Zn/Al-7075 and Mg-(2-6)%Zn/anodized Al-7075 multilayered composites.

EBSD and TEM analysis showed the UFG with high angle misorientation in the microstructure. The average grain size was found to be (a) 1.3  $\mu$ m, 1  $\mu$ m and 1  $\mu$ m for

Al-7075 and anodized Al-7075 and Mg-2%Zn layers in the Mg-2%Zn/Al-7075 and Mg-4%Zn/anodized Al-7075 multilayered composite (b) 1.3  $\mu\text{m}$ , 0.73  $\mu\text{m}$  and 1  $\mu\text{m}$  for Al-7075 and anodized Al-7075 and Mg-4%Zn layers of the Mg-4%Zn/Al-7075 and Mg-4%Zn/anodized Al-7075 composite (c) 1.3  $\mu\text{m}$ , 0.73  $\mu\text{m}$  and 0.6  $\mu\text{m}$  for Al-7075 and anodized Al-7075 and Mg-6%Zn layers of the Mg-6%Zn/Al-7075 and Mg-6%Zn/anodized Al-7075 multilayered composite.

As the number of ARB passes increases, microhardness of the different layers of Mg-(2-6%)Zn/Al-7075 and Mg-(2-6%)Zn/anodized Al-7075 multilayered composite increases. The Mg-4%Zn/Al-7075 and Mg-4%Zn/anodized Al-7075 composite gives better microhardness values as compared to Mg-2%Zn/Al-7075, Mg-2%Zn/anodized Al-7075 and Mg-6%Zn/Al-7075 and Mg-6%Zn/anodized Al-7075.

It is observed that, YS and UTS of the composites followed the same trend as the microhardness with increases in ARB passes. YS and UTS of the Mg-4%Zn/Al-7075 (228 MPa and 318 MPa) and Mg-4%Zn/anodized Al-7075 (230 MPa and 322 MPa) exhibited better strength as compared to other two composite systems. Tensile properties for anodized multilayered composites are better than for those without anodized composites due to uniform distribution of alumina particle helps to increase the strength by pinning the dislocations and impeding their motion resulting in enhanced dislocation density and dislocation interactions. Fractured surfaces of Al-7075 and anodized Al-7075 layers of the composite are characterized by dimples and exhibited shear ductile fracture and Mg-Zn layer exhibited transgranular brittle fracture in the multilayered composites.

Potentiodynamic polarization and immersion study revealed that the Mg-(2-6)% Zn/Al-7075 multilayered composite exhibited highest corrosion resistance as compared to rolled Mg-Zn alloys. It is mainly due to development of UFG structure and during ARB process, intermetallics ( $\text{Al}_{12}\text{Mg}_{17}$  and  $\text{AlMg}_4\text{Zn}_{11}$ ) formed is refined and uniformly distributed throughout the structure which acts as an anodic barrier to inhibit the overall corrosion. Higher corrosion resistance of Mg-Zn/anodized Al-7075 as compared to Mg-Zn/Al-7075 is due to uniform distribution of alumina ( $\text{Al}_2\text{O}_3$ ) resulted from the

anodization process. Mg-6%Zn/Al-7075 and Mg-6%Zn/anodized Al-7075 exhibited higher corrosion resistance as compared to lower Zn alloying composites like Mg-(2-4)%Zn/Al-7075 and Mg-(2-4)%Zn/anodized Al-7075. Higher content of Zn in the multilayered composites results in the formation of large amount of ZnO, which can enhance the protectiveness of the passive film and kinetics of passivation there by inhibiting the corrosion.

## **4.4 Mg-Zn/Ce/Al hybrid composite**

### **4.4.1 Mg-2%Zn/Ce/Al hybrid composite**

Mg-2%Zn/Ce/Al hybrid composite was developed using Mg-2%Zn alloy with Al and Ce particle through accumulative roll bonding (ARB) process at 300 °C up to five pass. Uniaxial tensile and hardness tests were performed on ARB processed samples. SEM equipped with EDS and EBSD and TEM was used for microstructure observation and phase analysis was done by XRD was used for microstructural observation. Microhardness and tensile tests were carried out on ARB processed specimens. In addition, Corrosion behavior of the hybrid composite was examined using electrochemical polarization test and immersion test. Results obtained from the present work are presented and described in this section.

#### **4.4.1.1 Microstructural observations**

Figure 4.77 shows SEM micrographs along the RD–TD planes of the 5-pass ARB-processed Mg-2%Zn/Ce/Al hybrid composite and results from EDS analysis. It revealed the good bonding between the Mg-2%Zn, Ce and Al, there were no cracks or de-lamination along the interfaces. Mg-2%Zn layers in the Mg-2%Zn/0.2%Ce/Al hybrid composite (Figure 4.77 a) undergoes a necking and finally ruptured because of brittleness characteristics of Mg alloys. Plastic instabilities caused by different flow properties of constituent phases make the harder phase to neck and finally rupture during the co-deformation of dissimilar metals (Min et al. 2006). Figure 4.77 (b) shows the alternate layers of Mg-2%Zn and Al. After 5-pass ARB process, thickness of layers found to be 30-40 µm. EDS data (Figure 4.77 c & d) shows cerium particles in the hybrid composite. Microstructure of the Mg-2%Zn layer (Figure 4.77 e) and Al layer (Figure 4.77 f) reveals the ultrafine grains due to grain subdivision and shears strain between strip and roller during ARB process. During ARB process, grain refinement took place, mechanism was reported as (i) because of multi-directional slip system, dislocation cells and subgrain structure is formed with a low angle grain boundaries. As a result of dislocation accumulation, misorientation increases and gradual shift of low angle grain boundaries to high angle grain boundaries. Migration of new high angle grain boundaries, thus creation of UFG structure.

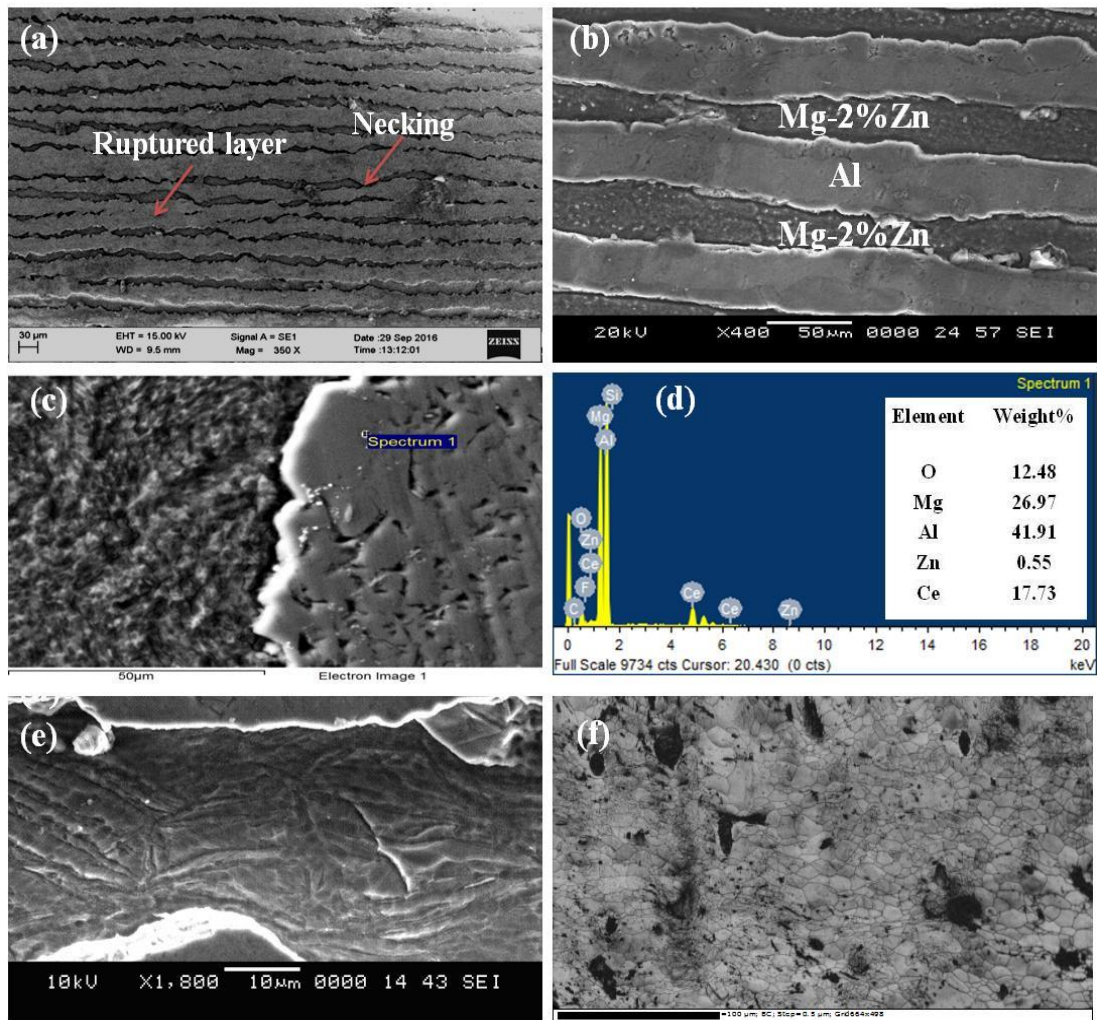


Figure 4.77. SEM micrographs of 5-pass ARB processed (a) Mg-2%Zn/Ce/Al hybrid composite (b) Magnified image (c & d) EDS of cerium particle (e) Microstructure of the Mg-2%Zn layer (f) Microstructure of the Al layer.

#### 4.4.1.2 EBSD analysis

Microstructure development of 5-pass ARB processed Mg-2%Zn/Ce/Al hybrid composite (on RD-ND plane) was carried out using EBSD analysis as shown in figure 4.78 & 4.79. The colors in the inverse pole figure (IPF) map represent the crystallographic orientations parallel to the normal direction. The standard stereographic triangle reveals a correspondence between colors and crystallographic orientations. Low angle grain boundaries (LAGB) are depicted as green lines (misorientations between 2-15°), high angle grain boundaries (HAGB) as black lines



(misorientations above  $15^\circ$ ) and twins are depicted in red colors. Figure 4.78 depicts EBSD based analysis of the Al layer in the hybrid composite.

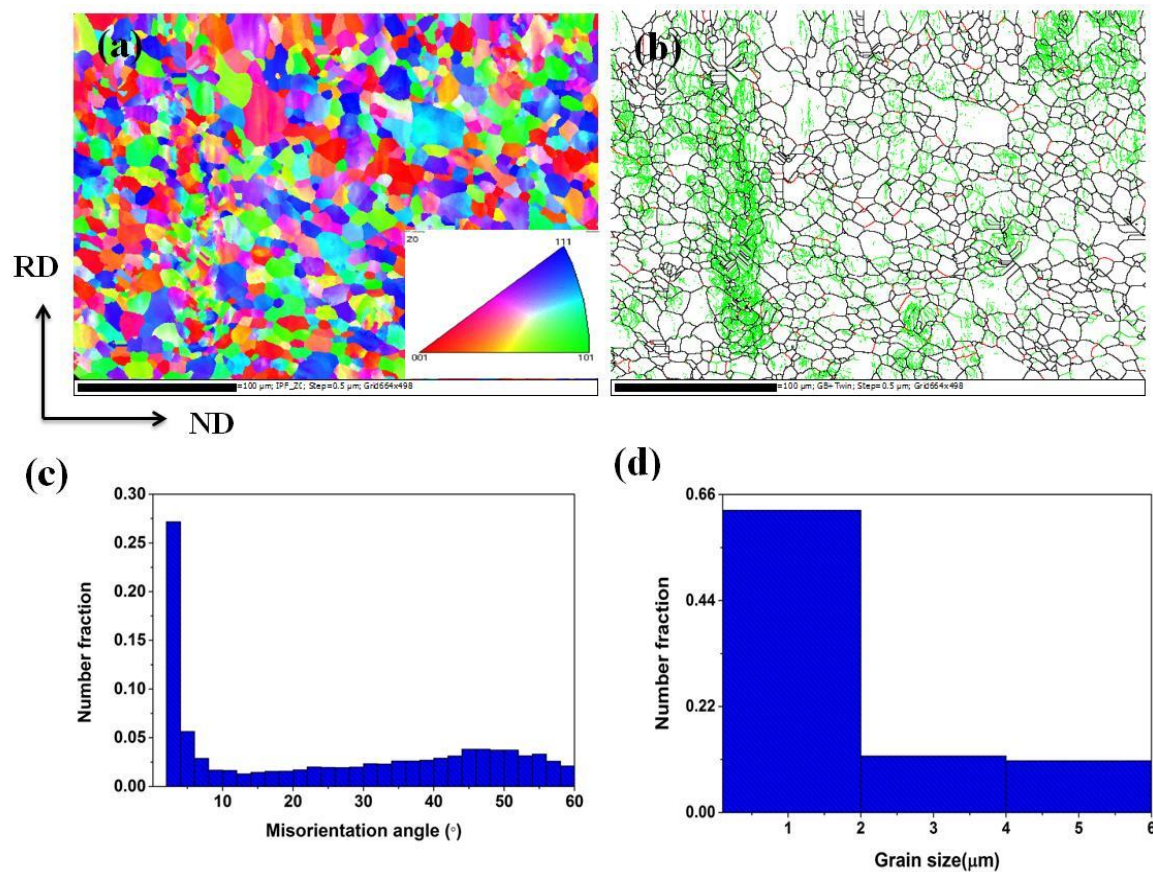


Figure 4.78. EBSD based analysis of Al layer in the Mg-2%Zn/Ce/Al hybrid composite (a) IPF map (b) Misorientation angle distribution profile (c) IPF map, grain boundary map with twins (d) Grain size distribution.

IPF map (Figure 4.78 a) revealed that grains are directed uniformly in  $\langle 001 \rangle$  orientation in the direction of rolling. Misorientation angle distribution profile (Figure 4.78 b) consists of subgrains with a fraction of HABs due of dynamic recrystallization during ARB process. Grain boundary map overlaid with twins is shown in figure 4.78 (c) which consists of equiaxed grains with some fraction of HABs. The percentage of twins found to be 2.3%. Grain size variation profile (Figure 4.78 d) exhibited average grain size of  $1.8 \mu\text{m}$ .

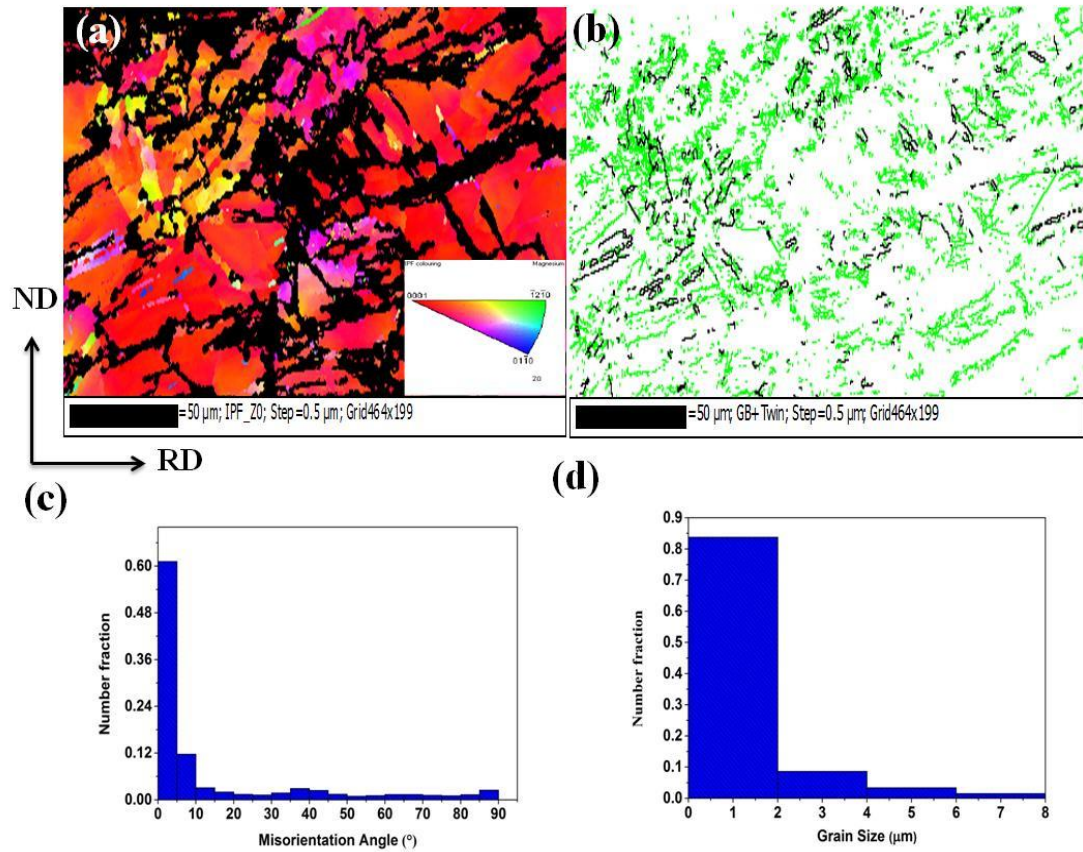


Figure 4.79. EBSD based analysis of Mg-2%Zn layer in the 5-pass ARB processed Mg-2%Zn/Ce/Al hybrid composite (a) IPF map (b) Grain boundary map with twins (c) Misorientation angle distribution profile (d) Grain size distribution.

EBSD results of Mg-2%Zn layer in the ARB processed Mg-2%Zn/Al-7075 multilayered composites are shown in Figure 4.79. IPF map (Figure 4.79 a) revealed that grains are directed uniformly in  $\langle 0001 \rangle$  orientation in the direction of rolling. The grain boundary map (Figure 4.79 b) shows that the Mg-2%Zn layer consists of subgrains with a fraction of HABs due of dynamic recrystallization during ARB process. Figure 4.79 (c) reveals the presence of both LAGBs and HAGBs in Mg-2%Zn layer of the Mg-2%Zn/Ce/Al multilayered composite which indicates deformation is induced as result of dynamic recovery. Grain size variation plot (Figure 4.79 d) shows that 82% of the grains in the microstructure have grain size below 2  $\mu\text{m}$ . The average grain size is found to be 1  $\mu\text{m}$  in the Mg-2%Zn layer in the multilayered composite.

#### 4.4.1.3 TEM analysis

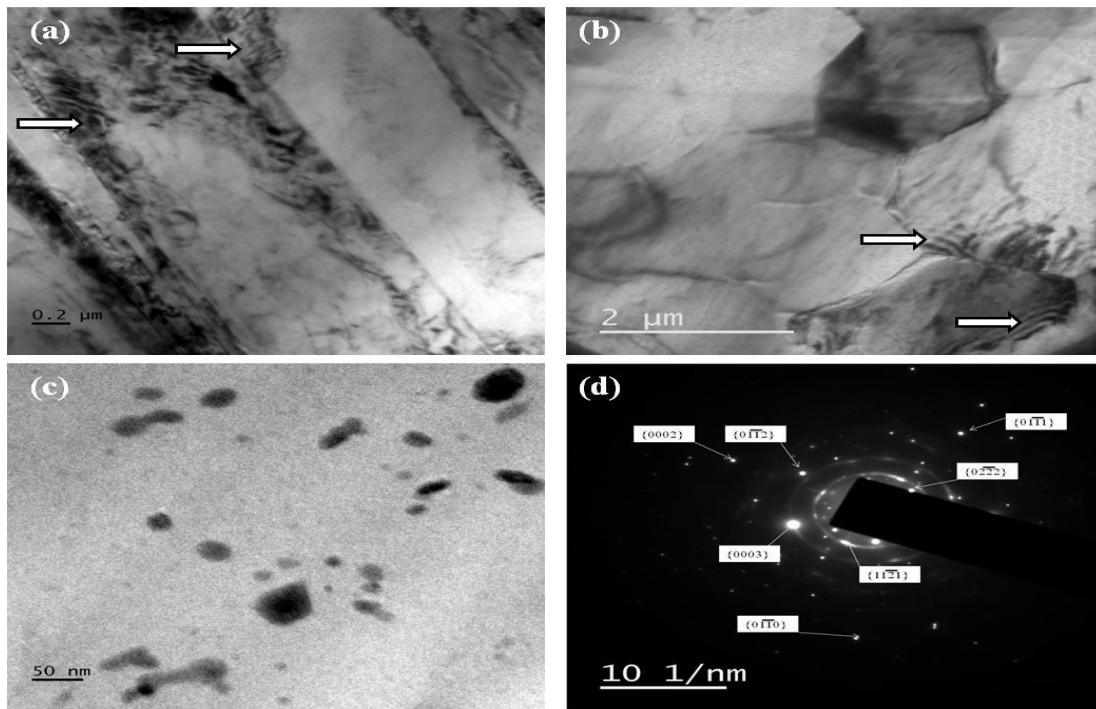


Figure 4.80. TEM micrographs and SAED patterns of the 5-pass ARB processed Mg-2%Zn/Ce/Al hybrid composite.

Figure 4.80 shows TEM bright-field image (on RD-ND plane) and corresponding selected area electron diffraction (SAED) of 5-pass ARB processed Mg-2%Zn/Ce/Al hybrid composite. Some of the strain zones and tangled dislocations are revealed (Figure 4.80 a) in the composite. Figure 4.80 b shows the formation of ultrafine grains with typical dislocation sub-structure containing sub-grains bordered by high angle sub-boundaries. Fraction of ultra-fine grained regions increased with increasing the number of ARB cycles due to higher strain. Higher magnification image (Figure 4.80 b) shows the dislocation density inside the ultra-fine grain and surrounded by strongly deformed boundaries. Figure 4.80 (c) shows uniform distribution of Ce particles in the hybrid composite. SAED patterns are in the form of diffused rings like pattern with extra spots, which indicating the sub-grain structure with high angle boundaries. Also, as the number of ARB cycles increased the SAD pattern became more ring-like, showing the increase of a portion of high angle boundary (Chino et al. 2008).

#### 4.4.1.4 X-ray diffraction analysis

XRD patterns (RD-TD plane) of 5-pass ARB processed Mg-2%Zn/0.2%Ce/Al hybrid composite is shown in figure 4.81.

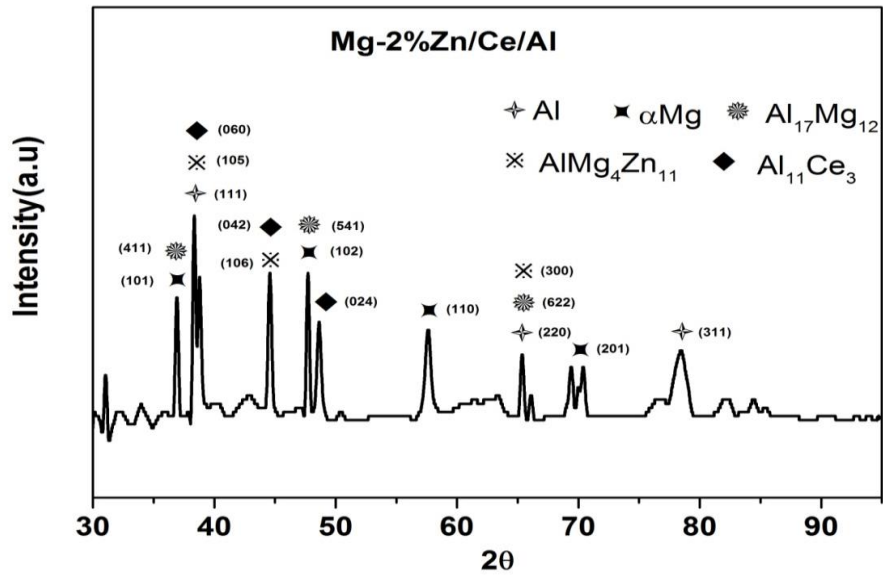


Figure 4.81. XRD patterns along the cross section of the Mg-2%Zn/Ce/Al hybrid composite

XRD results indicated the presence of mainly three intermetallic phases, which are  $\text{Al}_{17}\text{Mg}_{12}$ ,  $\text{AlMg}_4\text{Zn}_{11}$  and  $\text{Al}_{11}\text{Ce}_3$ . Addition of Ce leads to the formation of the  $\text{Al}_{11}\text{Ce}_3$ . During ARB process, diffusion of elements between the layers occurs due to high pressure (50% reduction) and temperature (350 °C) as well bonded because of mechanical bonding. Intermetallics are formed in the interface region, as the number of ARB passes increases the area of the interface region increases.

#### 4.4.1.5 Density

Calculated density test results are illustrated in table 4.22.

Table 4.22. Density test results.

Sample	Density ( $\text{kg/m}^3$ )
Mg-2%Zn alloy	1759
Al-1100	2691
Mg-2%Zn/Ce/Al composite	2116

Developed Mg-2%Zn/Ce/Al hybrid composite exhibited 1.21 times light weight as compared to pure Al.

#### 4.4.1.6 Microhardness

Microhardness variations in Al and Mg-2%Zn layers at different ARB passes can be seen in figure 4.82. It is revealed that the microhardness values were increased with the increase in strain. After the first cycle, a significant increase has been observed in the hardness value, can be attributed to increase in the density of dislocations and their interactions. As the number of ARB passes increases, microhardness values increases because of strain hardening and as well as grain refinement process. Microhardness of the Al-1100 and Mg-2%Zn layers of 5-pass multilayered composite layers reached to 157.7 Hv (~1.74 times) and 99.9 Hv (~ 1.33 times) respectively in comparison to its counterpart as rolled alloys.

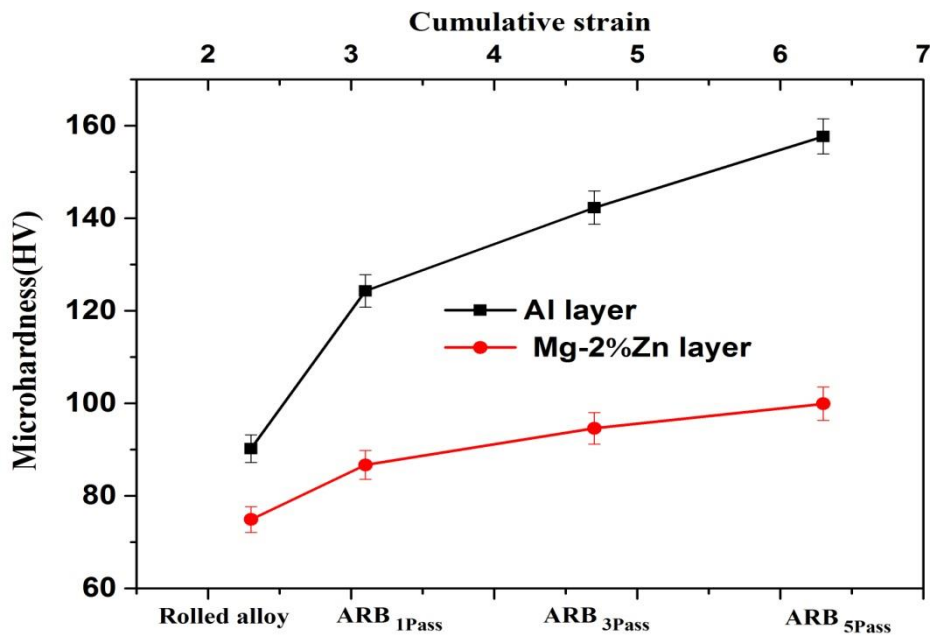


Figure 4.82. Microhardness variation of the rolled and Mg-2%Zn/Ce/Al hybrid composite after different numbers of ARB passes.

Presence of the cerium particles in the hybrid composite aids in activation the strengthening mechanisms. During the ARB, cerium particles increases dislocation density in the matrix/reinforcement interfaces due to strain incompatibility between the matrix and particle, and the difference in thermal expansion during ARB process and

during cooling. Therefore, the hardness value of hybrid composite sample was higher than that of the monolithic alloys (Mohammad et al. 2014).

#### 4.4.1.7 Tensile strength

Figure 4.83 illustrates the variation of the tensile strength (UTS), yield strength (YS) and elongation of the hybrid composite samples corresponding to the number of ARB passes. It can be seen that, with increase in the number of ARB passes, the UTS increases. UTS and YS of the Mg-2%Zn/Ce/Al hybrid composite after 5-passes reached to 238 MPa and 172 MPa respectively which is 38% and 56% higher than that of Mg-2%Zn alloy (172 MPa and 110 MPa). It is reported that two major mechanisms control the strengthening of ARB processed materials are strain hardening and grain refinement. During the initial passes, the strength is generally attributed to dislocation strengthening in which dislocations are pinned together and cause strengthening of the alloy.

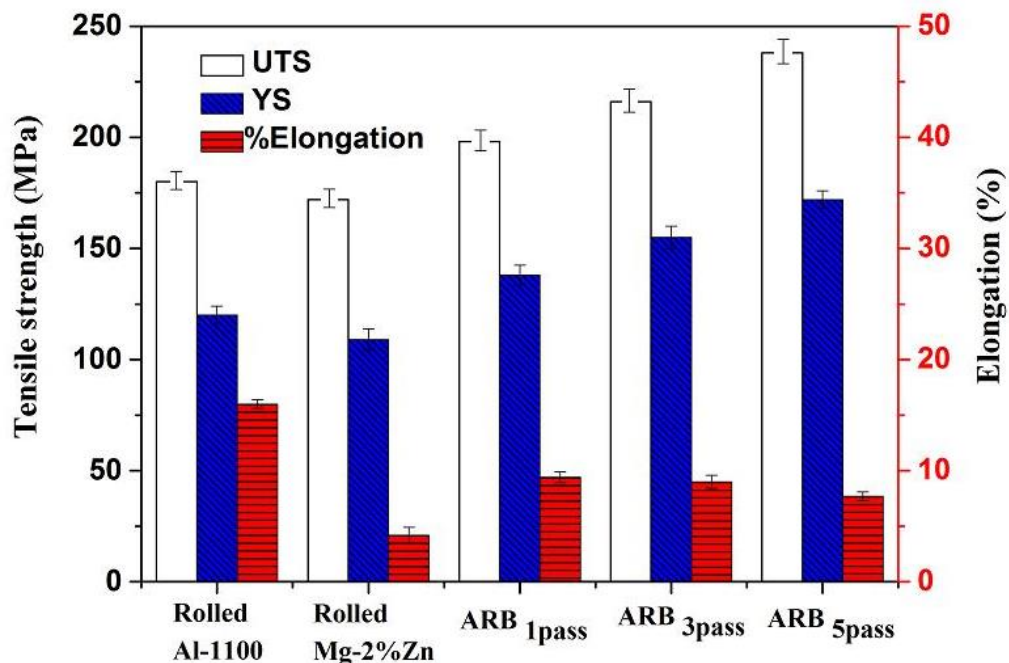


Figure 4.83. Variation of UTS, YS and percentage elongation of the Mg-2%Zn/Ce/Al hybrid composite with different ARB passes.

Effect of dislocation strengthening decreases and further increase in strength, is due to formation of ultrafine-grained structure with highly misoriented grains (Toroghinejad

et al. 2014 b). In the present study, obtained high strength in the Mg-2%Zn/0.2%Ce/Al hybrid composite, is not only due to mentioned mechanism, but also due to cerium particle reinforcement (Ma et al. 2003). It has been reported that load transfers from the matrix to the reinforcement particles by accommodation of shear stresses at the composite interfaces leading to an increase of strength (Pagounis and Lindroos, 1998). Reinforcement particles accelerating the formation of ultrafine grains by preventing grain growth (Jamaati et al. 2012). Dislocations, are generated around reinforcement particles in matrix are considered as one of the main strengthening mechanisms that contributes in strengthening of severe plastic deformation processed materials. The total elongation decreases as the number of ARB passes increases due to work hardening effect and grain refinement. 5-pass ARB processed Mg-2%Zn/Ce/Al hybrid composite exhibited total elongation of 1.8 times higher than starting material Mg-2%Zn alloy. It is mainly due to equal quantity of highly ductile Al present in the hybrid composite and also due to Ce particle reinforcement.

#### 4.4.1.8 Fractography

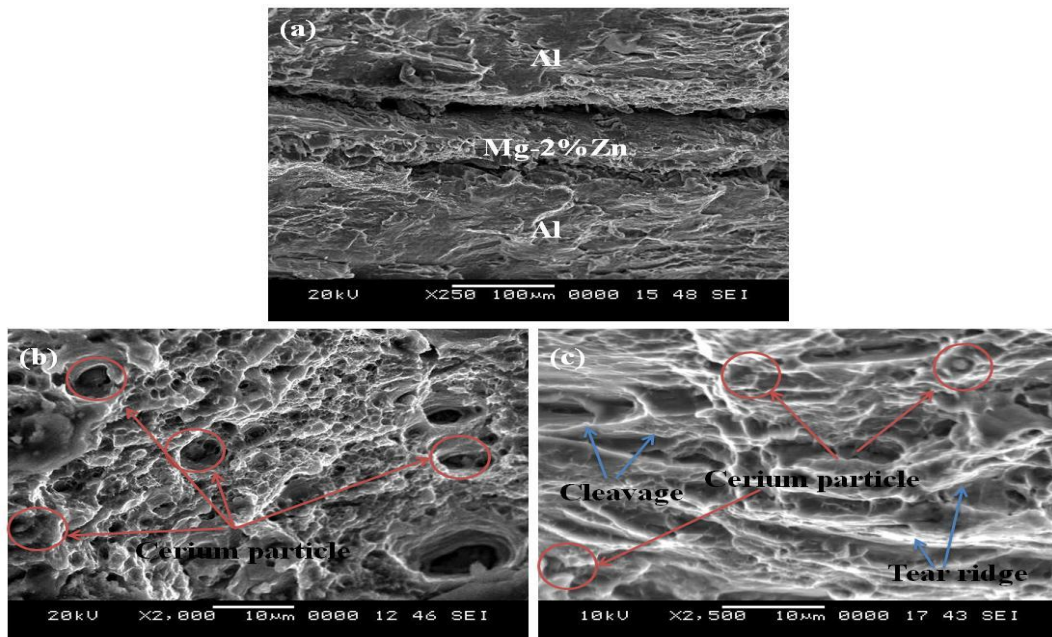


Figure 4.84. SEM micrographs of the fractured surface of the (a) 5-pass ARB processed Mg-2%Zn/Ce/Al hybrid composite (b) Al layer (c) Mg-2%Zn layer.

Fracture surface of the 5-pass ARB processed Mg-2%Zn/Ce/Al hybrid composite is shown in figure 4.84 a. Fracture analysis of composites is governed by fracture of reinforcement particles, detachment of interface and nucleation and growth of dimples (Jamaati et al. 2011). Al layer in the hybrid composite depicts typical ductile failure illustrated by number of dense and deep dimples, as shown in figure 4.84 b. This kind of fracture occurred due to nucleation, growth, and coalescence of microvoids. Presence of shallow shear dimples and elongated microvoids found clearly on the fracture surface are affected by shear stress during ARB process. It confirms shear ductile fracture, where the final failure takes place by the shearing of the intervoid ligaments (Shaarbaf and Toroghinejad, 2008). Figure 4.84 b depicts shallow dimples and a few Ce particles. Mg-2%Zn layer (Figure 4.84 c) in the hybrid composite depicts tear ridges and cleavages in the fracture surface which is indication for cleavage fracture. Mg-2%Zn layers were fractured in the shear mode and free from voids which appear to be transgranular brittle fracture.

#### 4.4.1.9 Potentiodynamic polarization

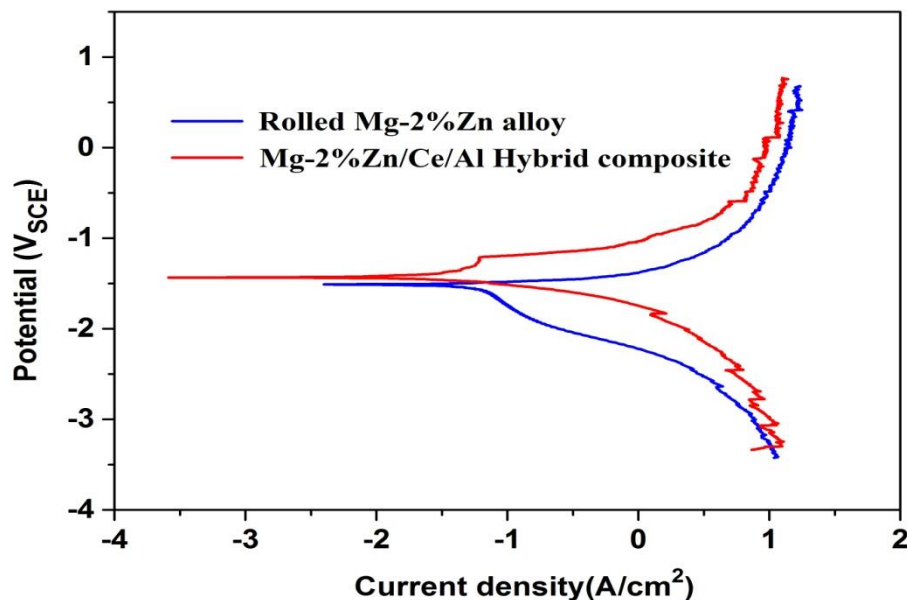


Figure 4.85. Potentiodynamic polarization curves of the Mg-2%Zn and 5-pass ARB processed Mg-2%Zn/Ce/Al hybrid composite.

Potentiodynamic polarization curves were recorded to evaluate the corrosion properties of the wrought alloy and Mg-2%Zn/Ce/Al hybrid composite in the 0.1 M NaCl as



shown in figure 4.85. Polarization curves were analyzed by Tafel fitting. Corrosion kinetics parameters such as corrosion potential ( $E_{\text{corr}}$ ), tafel slopes ( $\beta_a$  &  $\beta_c$ ), corrosion current density ( $i_{\text{corr}}$ ) and corrosion rate (mpy) were obtained from polarization plots are summarized in table 4.23.

Table 4.23. Potentiodynamic polarization test results.

Materials	$E_{\text{corr}}$ (V <sub>SCE</sub> )	$i_{\text{corr}}$ ( $\mu\text{A}/\text{cm}^2$ )	$\beta_a$ (mV/decade)	$\beta_c$ (mV/decade)	Corrosion rate (mm/y)
Mg-2%Zn	-1.63	77.96	238.1	-882.2	2.37
Mg- 2%Zn/0.2%C e/Al	-1.42	34.53	670.3	-178.7	0.72

Multilayered composite sample subjected to ARB process up to 5-pass exhibited UFG structure ( $< 2 \mu\text{m}$ ). These small sized grains create more grain boundaries that act as a corrosion barrier (Song et al. 1998). During ARB process, intermetallics ( $\text{Al}_{12}\text{Mg}_{17}$ ,  $\text{AlMg}_4\text{Zn}_{11}$  and  $\text{Al}_{11}\text{Ce}_4$ ) formed due to bonding with Al are refined and uniformly distributed throughout the structure which acts as an anodic barrier to inhibit the overall corrosion (Pardo et al. 2008).

Surface morphology after electrochemical polarization test in the solution of 0.1 M NaCl are shown in figure 4.86 for Mg-2%Zn and Mg-2%Zn/Ce/Al hybrid composite. A significant dissolution of Mg-2%Zn alloy (Figure 4.86 a) was observed as compared to Mg-2%Zn/Ce/Al hybrid composite.

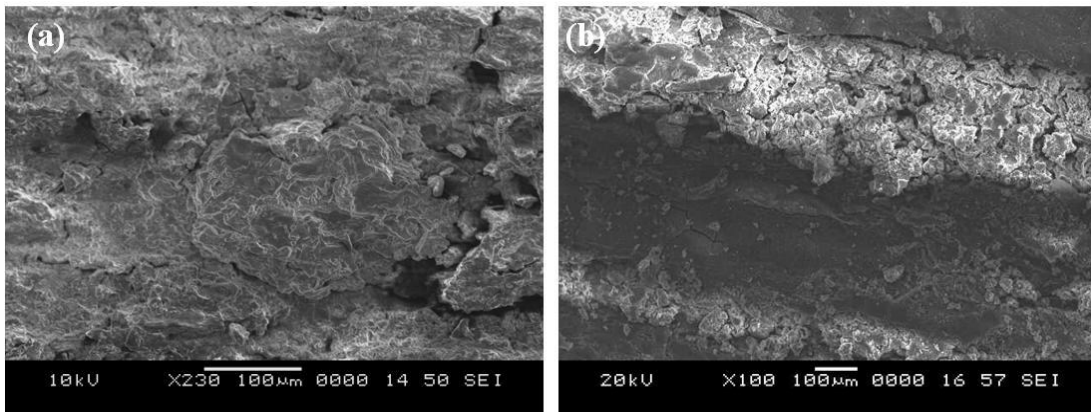


Figure 4.86. SEM micrographs of corroded (a) Mg-2%Zn (b) Mg-2%Zn/Ce/Al hybrid composite after electrochemical test in a 0.1 M NaCl solution.

Mg-2%Zn/Ce/Al hybrid composite exhibits layer-wise corrosion and bright region of Mg-2%Zn layer shown in figure 4.86 (b) which is covered with magnesium hydroxide, similar observations reported by Huang et al. 2003. Addition of Ce particle during ARB process helps to form  $Al_{11}Ce_3$  phase (Figure 4.81), which increases the stability of passive films and thus attributes to improve the corrosion resistance of the Mg-2%Zn/Ce/Al hybrid composite (Yan et al. 2016).

#### 4.4.1.10 Immersion test

Hydrogen evolution rate and corresponding corrosion rate of the wrought Mg-2%Zn alloy and ARB processed Mg-2%Zn/Ce/Al hybrid composite are illustrated in Table 4.24.

Table 4.24. Immersion test results.

Materials	Hydrogen evolution rate (ml/cm <sup>2</sup> /d)	Corrosion rate (mm/y)
Rolled Mg-2%Zn alloy	1.1	2.44
Mg-2%Zn/Ce/Al Hybrid composite	0.46	0.85

Higher hydrogen evolution was noticed for the Mg-2%Zn alloy (1.1 ml/cm<sup>2</sup>/d) as compared to Mg-2%Zn/Ce/Al hybrid composite (0.46 ml/cm<sup>2</sup>/d). The corrosion rate calculated from hydrogen evolution for composite is 2.8 times less than rolled Mg-2%Zn alloy due to refined microstructure and the presence of  $\beta$  phases ( $Al_{12}Mg_{17}$ ,  $AlMg_4Zn_{11}$  and  $Al_{11}Ce_4$ ). The potentiodynamic polarisation (Table 4.23) and immersion testing (Table 4.24) in 0.1 M NaCl solution showed similar trend of corrosion rate.

#### 4.4.2 Mg-4%Zn/Ce/Al Hybrid composite

Mg-4%Zn/Ce/Al hybrid composite was developed using Mg-4%Zn alloy with Al and Ce particle through accumulative roll bonding process at 300 °C up to five pass. Microstructural characterization, mechanical properties, and corrosion tests were performed on the roll bonded samples and the results are summarise as follows

#### 4.4.2.1 Microstructure analysis

Figure 4.87 shows SEM micrographs of the Mg-4%Zn/Ce/Al hybrid composite on the RD-TD plane after 5-pass ARB process.. Thickness of both, Mg-4%Zn layer and Al layer decreased gradually with increase in number of ARB passes. Average layer thickness was found to be in the range of 30-40  $\mu\text{m}$  and slight waviness layer was observed due to high deformation on increasing the ARB passes, resulted in ultrafine grains (Figure 4.87 (c & d)). Grain refinement mechanism during ARB is grain subdivision due to deformation induced by high angle grain boundaries and also due to severe shear strain between strip and roller.

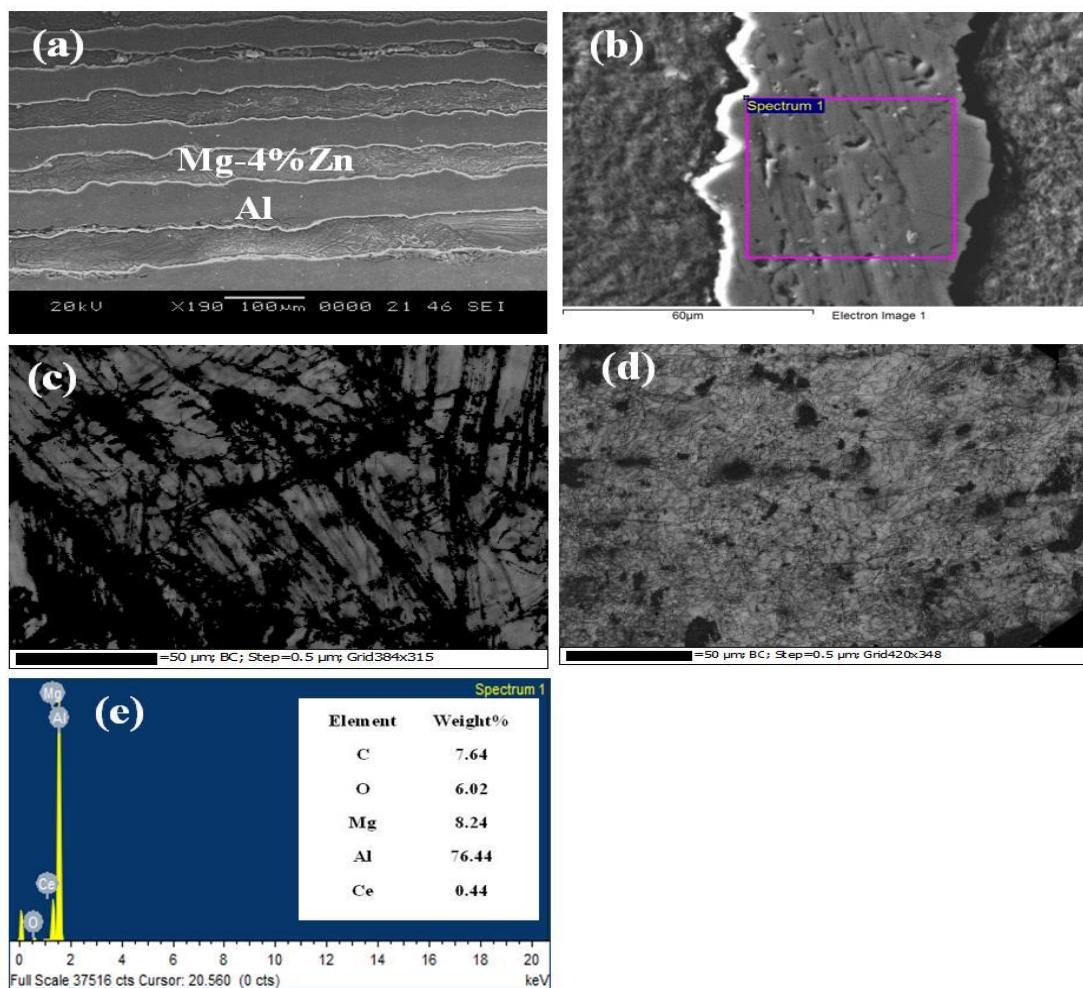


Figure 4.87. SEM micrographs of 5-pass ARB processed (a) Mg-4%Zn/Ce/Al Hybrid composite (b) Magnified image (c) Microstructure of the Mg-4%Zn layer (d) Microstructure of the Al layer (e) EDS of cerium particle.

The cerium particles distribution were observed on the surface of the Al layer (Figure 4.87 b) and EDS analysis (Figure 4.87 e) revealed that 0.44 % cerium on the selected area of Mg-4%Zn/Ce/Al hybrid composite.

#### 4.4.2.2 EBSD analysis

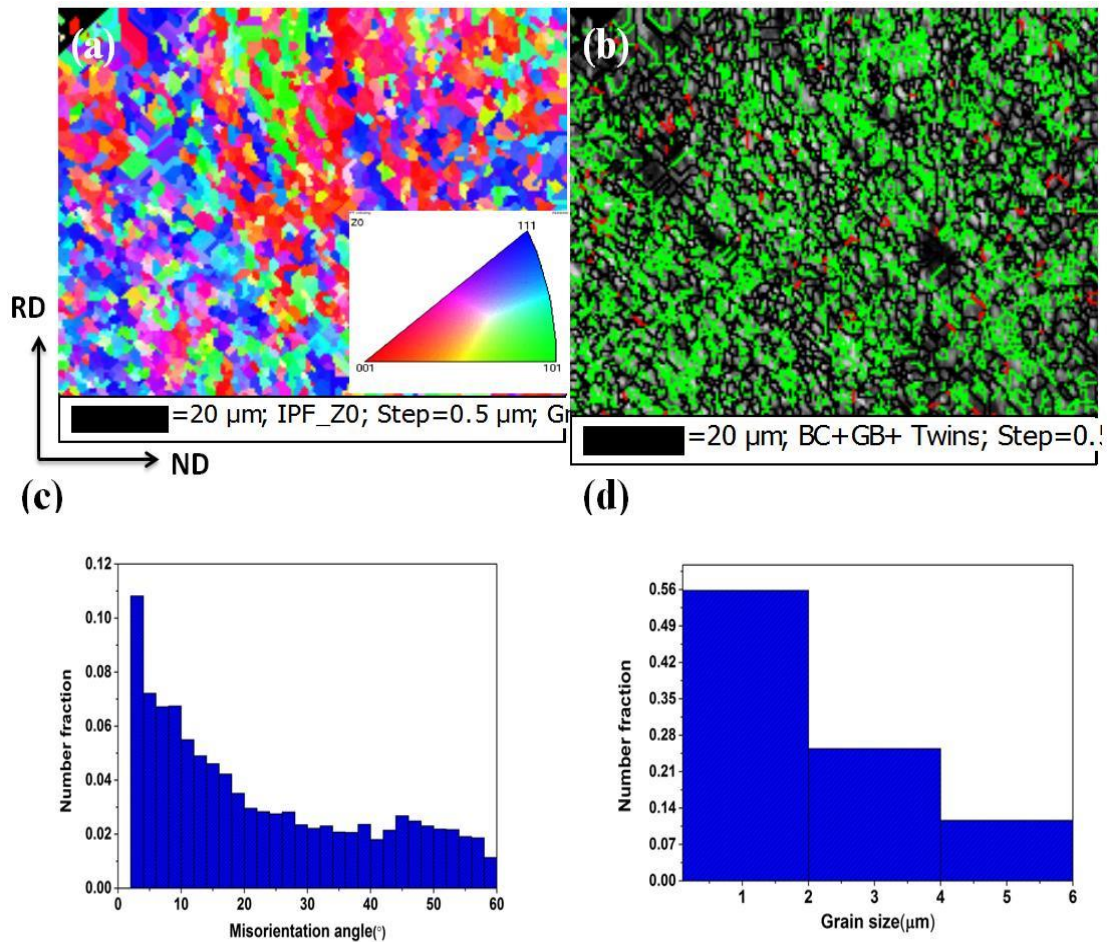


Figure 4.88. EBSD based analysis of Al layer in the Mg-4%Zn/Ce/Al hybrid composite (a) IPF map (b) Misorientation angle distribution profile (c) IPF map, grain boundary map with twins (d) Grain size distribution.

Inverse pole figure (IPF) map of the Al layer in the ARB processed Mg-4%Zn/Ce/Al hybrid composite is shown in Figure 4.88 (a). Grain boundary map overlaid with twins is shown in figure 4.88 (b). The percentage of twins was found to be 1.3%. Misorientation angle distribution profile consisting of both LAGBs and HAGBs is shown in figure 4.88(c). Grain size variation profile shown in figure 4.88 (d) exhibited average grain size as 1.3  $\mu\text{m}$  in the Al layer in the Mg-4%Zn/Ce/Al hybrid composite.

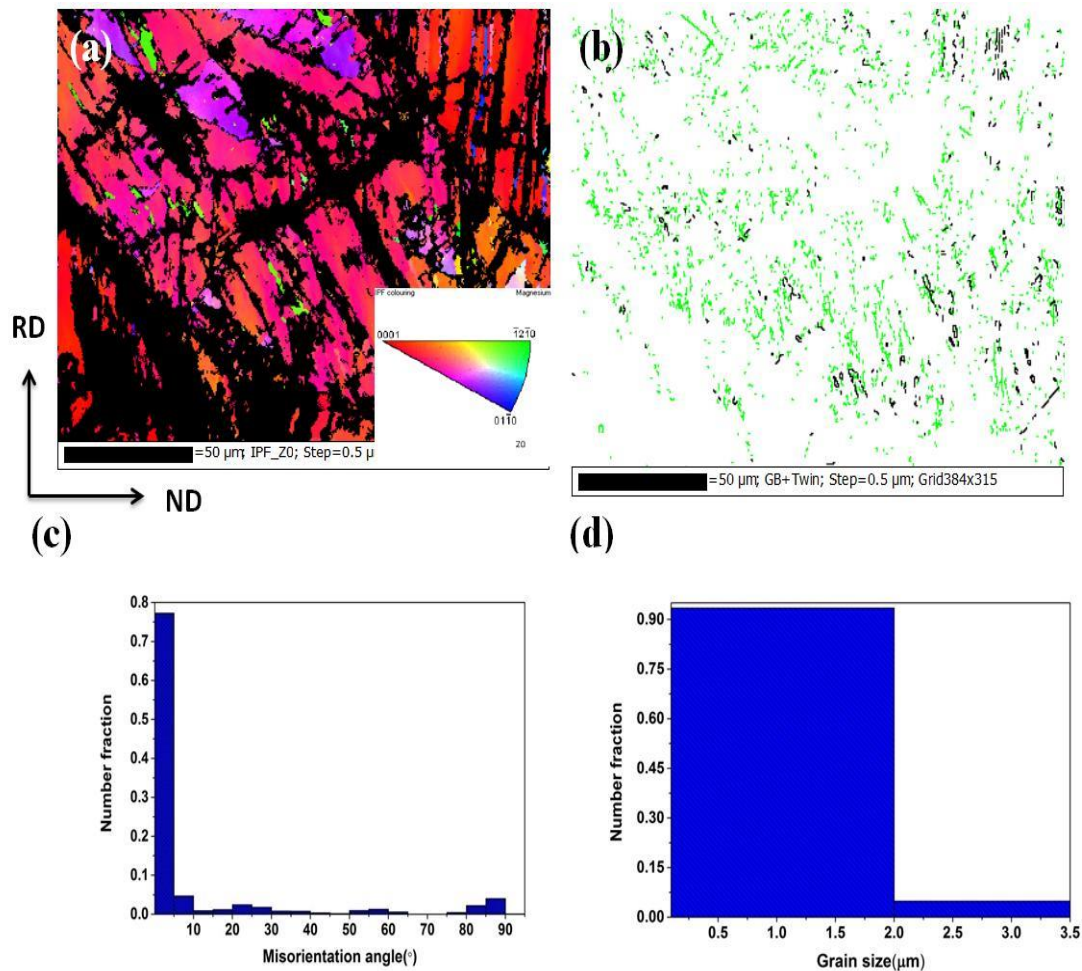


Figure 4.89. EBSD based analysis of Mg-2%Zn layer in the 5-pass ARB processed Mg-4%Zn/Ce/Al hybrid composite (a) IPF map (b) Grain boundary map with twins (c) Misorientation angle distribution profile (d) Grain size distribution.

Inverse pole figure (IPF) map of the Mg-4%Zn layer in the ARB processed hybrid composite is shown in figure 4.89 (a). It is revealed that, Mg-4%Zn grains are directed uniformly in  $\langle 0001 \rangle$  orientation in the direction of rolling. Grain boundary map overlaid with twins is shown in figure 4.89 (b). As a result, misorientation angle distribution profile of the 5-pass ARB processed composites, shown in figure 4.89 (c), consists of both LAGBs and HAGBs. Grain size variation profile (Figure 4.89 d) shows the average grain size of 1  $\mu\text{m}$  in the Mg-4%Zn/Ce/Al hybrid composite.

#### 4.4.2.3 TEM analysis

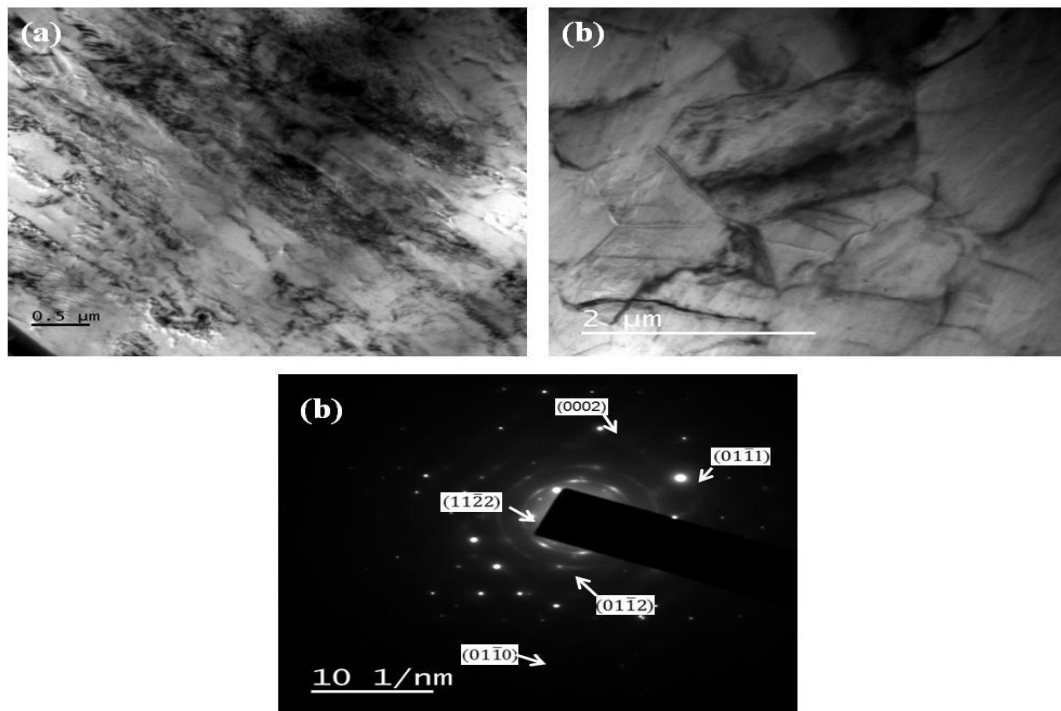


Figure 4.90. TEM micrographs and SAED patterns of the 5-pass ARB processed Mg-4%Zn/Ce/Al hybrid composite.

Micrographs of TEM and their corresponding selected area diffraction patterns (SAED) (ND-RD plane) of the ARB processed Mg-4%Zn/Ce/Al hybrid composite are illustrated in Figure. 4.11. Micrograph (Figure 4.90 a) revealed some strain regions and dislocation tangles which is an indication of large misorientation. As can be seen, fine grains with dislocation tangles are present in the composites (Figure 4.90 b). The SAED patterns of composite shows ring like pattern consisting of separate spots as shown in figure 4.90 (c), This indicates fine grains with high angle boundaries.

#### 4.4.2.4 X-ray diffraction analysis

XRD patterns (RD-TD plane) of 5-pass ARB processed Mg-4%Zn/Ce/Al hybrid composite is shown in figure 4.91.

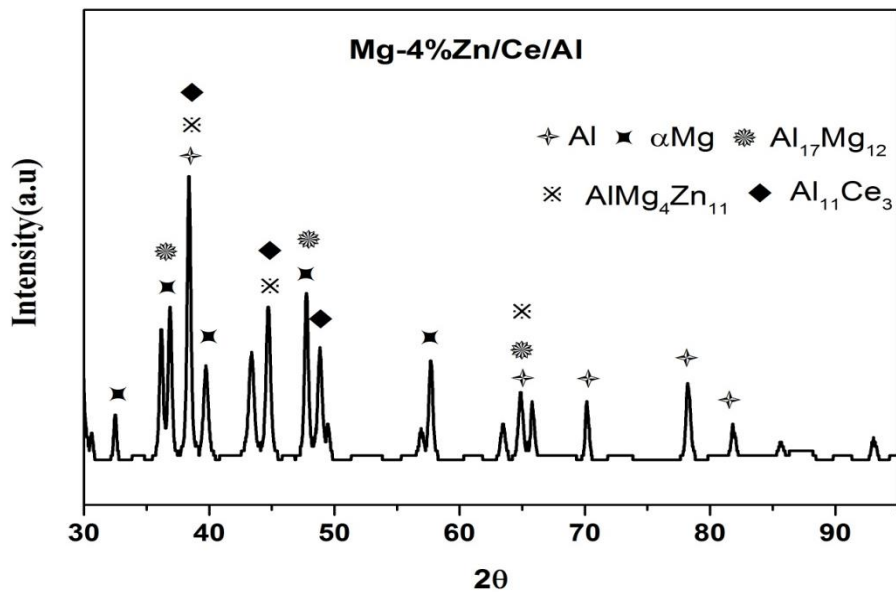


Figure 4.91. XRD patterns along the cross section of the Mg-4%Zn/Ce/Al hybrid composite

Results indicate mainly three intermetallic phases of  $\text{Al}_{17}\text{Mg}_{12}$ ,  $\text{AlMg}_4\text{Zn}_{11}$  and  $\text{Al}_{11}\text{Ce}_3$ . The addition of Ce leads to the formation of the  $\text{Al}_{11}\text{Ce}_3$ . During ARB process, Mg-4%Zn, Ce and Al were diffused due to high pressure (50% reduction) and temperature (300 °C) and bonded because of mechanical bonding. Intermetallics are formed in the interface region. Interface region increased with the increase in ARB passes..

#### 4.4.2.5 Density test

Calculated density test results are illustrated in table 4.25.

Table 4.25. Density test results

Sample	Density ( $\text{kg/m}^3$ )
Al	2691
Mg-4%Zn alloy	1780
Mg-4%Zn/Ce/Al Hybrid composite	2157

Roll bonded Mg-4%Zn/Ce/Al hybrid composites exhibited 1.24 times less weight as compared to pure Al.

#### 4.4.2.6 Microhardness

As the number of ARB passes increases, microhardness of the Mg-4%Zn and Al layers increases linearly as shown in figure 4.92.

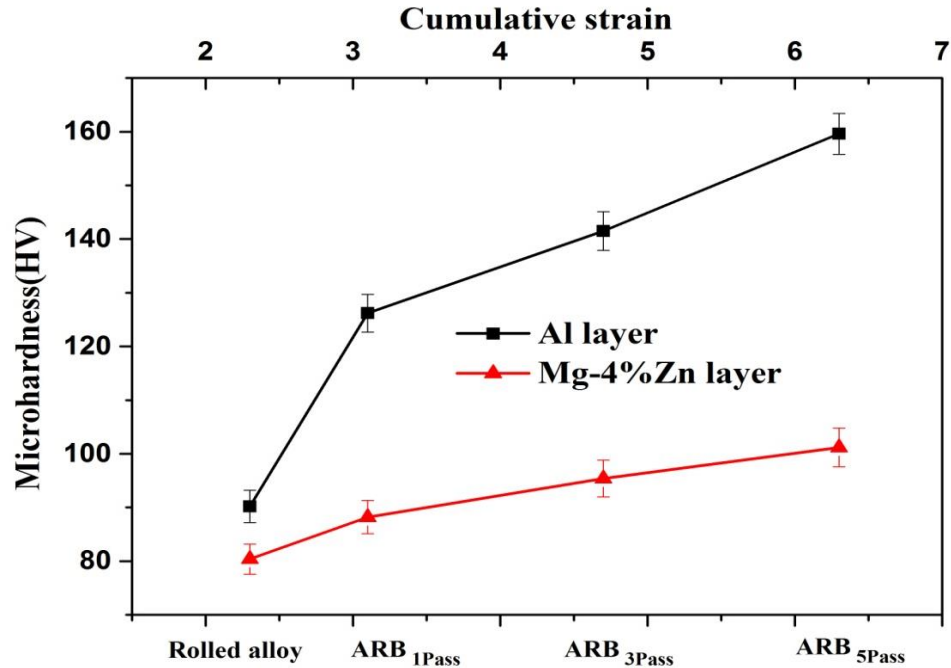


Figure 4.92. Microhardness variation of the rolled and Mg-4%Zn/Ce/Al hybrid composite after different numbers of ARB passes.

During initial passes of ARB, the microhardness of the multilayered composite increases due to a high rate of strain hardening this causes increase in dislocation density. At higher ARB passes, increase in microhardness values is due to combined effect of strain hardening and grain refinement. After 5-pass ARB process, the microhardness of the Mg-4%Zn layer and Al layer increases about 1.25 times and 1.76 times respectively, as compared to counterpart rolled alloys. Presence of the cerium particles in the hybrid composite during the ARB process, activate the strengthening mechanisms. It is observed that Mg-4%Zn/Ce/Al hybrid composite exhibited higher hardness as compared to Mg-2%Zn/Ce/Al composite due to increased Zn content which acts as grain refiner.



#### 4.4.2.7 Tensile strength test

It is observed that, as the number of ARB passes increases, yield strength (YS) and ultimate tensile strength (UTS) improves and ductility reduces as shown in figure 4.93.

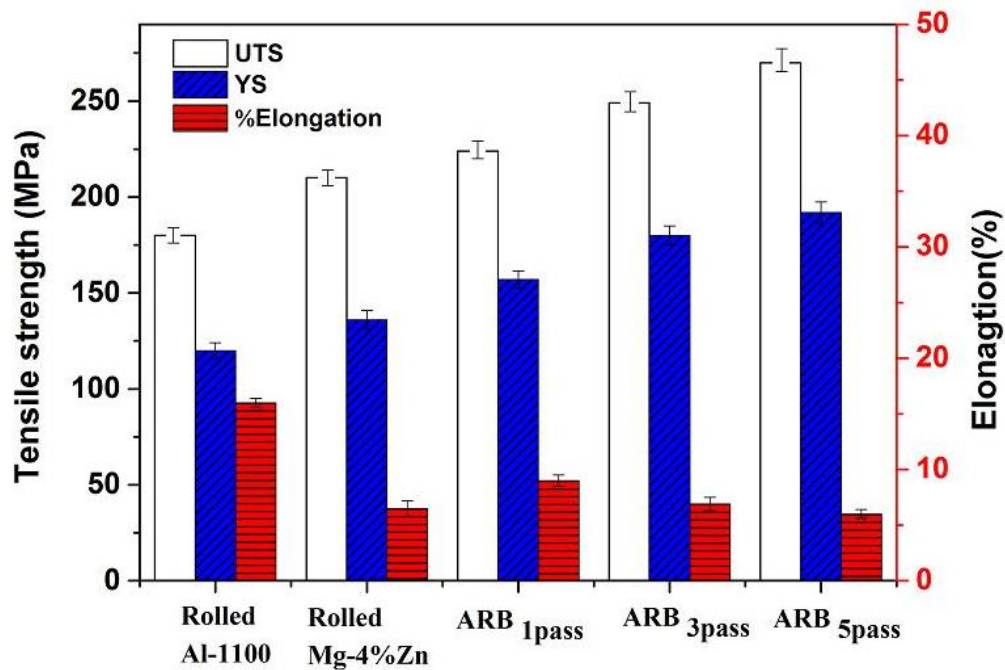


Figure 4.93. Variation of UTS, YS and percentage elongation of the Mg-4%Zn/Ce/Al hybrid composite with different ARB passes.

During the initial passes of ARB, enhancement in UTS and YS can be attributed to strain hardening caused due to the strong obstacle provided to dislocation slip. But at the higher passes of ARB, improvement of strength is due to grain refinement. In the higher passes of the ARB, the work hardening effect diminishes and gradually evolution of UFG occurs. As the number of ARB passes increases, proportion of UFG in the microstructure increases (Wang et al. 2016). UTS and YS of the 5-pass Mg-4%Zn/Ce/Al hybrid composite is enhanced by 28.5% and 41.1% respectively in comparison to as rolled Mg-4%Zn alloy. Dislocations generated around reinforcement particles in matrix, are considered as one of the main strengthening mechanisms that contributes in strengthening of severe plastic deformation processed materials. It is noted that, increased amount of Zn in the Mg-4%Zn/Ce/Al hybrid composite attributed to higher strength as compared to Mg-2%Zn/Ce/Al hybrid composite because of the

higher amount of Zn, which act as grain refiners. With increase in ARB passes, percentage of elongation reduces.

#### 4.4.2.8 Fractography

Fracture surface of tensile tested 5-pass ARB processed Al and Mg-4%Zn layers are shown in figure 4.94 (a). Al layer in the Mg-4%Zn/Ce/Al hybrid composite depicts typical ductile failure illustrated by dimples, as shown in figure 4.94 (b). Ductile fracture begins with the nucleation, growth, and coalescence of microvoids. Presence of shallow and small elongated microvoids affected by shear stress during ARB process which was confirms shear ductile fracture. Mg-4%Zn layer in the multilayered composite depicts bright (Figure 4.94 c) lines in the fracture surface which is indication of cleavage fracture. Mg-4%Zn layers were fractured in the shear mode and free from dimples which appear to be transgranular brittle fracture.

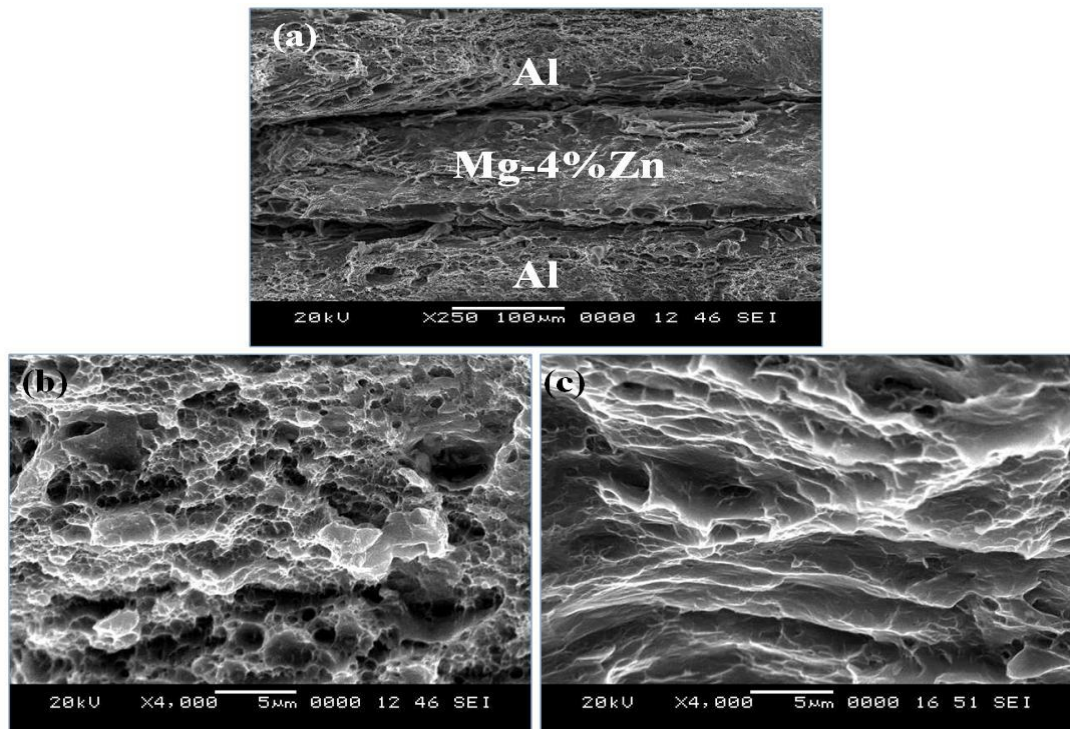


Figure 4.94. SEM micrographs of the fractured surface of the (a) 5-pass ARB processed Mg-4%Zn/Ce/Al hybrid composite (b) Al layer (c) Mg-4%Zn layer.

#### 4.4.2.9 Potentiodynamic polarization

Potentiodynamic polarization test results calculated from the polarization curves are summarized in table 4.26.

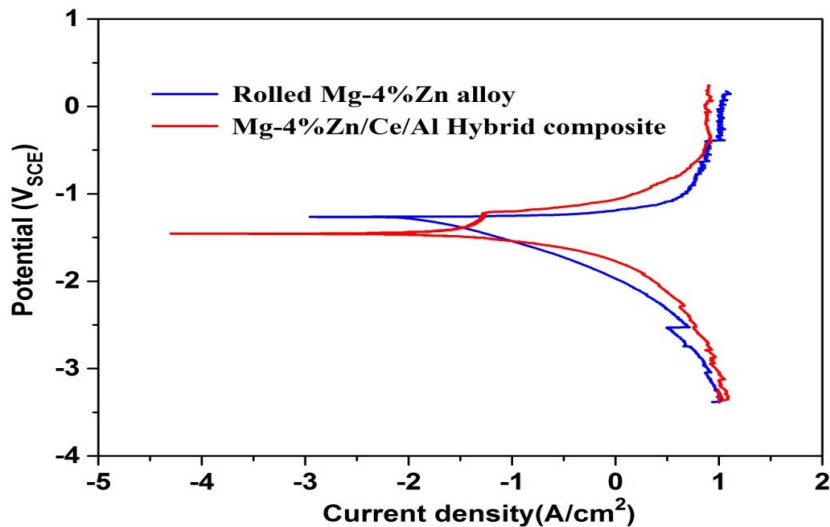


Figure 4.95. Potentiodynamic polarization curves of the Mg-4%Zn and 5-pass ARB processed Mg-4%Zn/Ce/Al hybrid composite.

Corrosion current density ( $I_{corr}$ ) of the rolled Mg-4%Zn alloy and 5-pass ARB processed Mg-4%Zn/Ce/Al hybrid composite is  $58.99 \mu\text{A}/\text{cm}^2$  and  $34.85 \mu\text{A}/\text{cm}^2$  meanwhile shifts the corrosion potential ( $E_{corr}$ ) toward noble direction was observed in figure 4.95. Potentiodynamic polarization plot shows the corrosion potential in passive regions indicating a higher passivation exhibited in the ARB processed multilayered composites as compared to rolled Mg-4%Zn alloy.

Table 4.26. Potentiodynamic polarization test results.

Materials	$E_{corr}$ (V <sub>SCE</sub> )	$i_{corr}$ ( $\mu\text{A}/\text{cm}^2$ )	$\beta_a$ (mV/decade)	$\beta_c$ (mV/decade)	Corrosion rate (mm/y)
Mg-4%Zn alloy	-1.45	58.9	211.9	-285.4	1.77
Mg-4%Zn/Ce/Al hybrid composite	-1.44	29.68	688.3	-170.0	0.75

Hybrid composite sample subjected to ARB process up to 5-pass exhibited UFG structure ( $<1 \mu\text{m}$ ). These small sized grains create more grain boundaries that act as a

corrosion barrier. During ARB process, intermetallics ( $\text{Al}_{12}\text{Mg}_{17}$ ,  $\text{AlMg}_4\text{Zn}_{11}$  and  $\text{Al}_{11}\text{Ce}_3$ ) formed due to bonding with Al alloy are refined and uniformly distributed throughout the structure which acts as an anodic barrier to inhibit the overall corrosion.

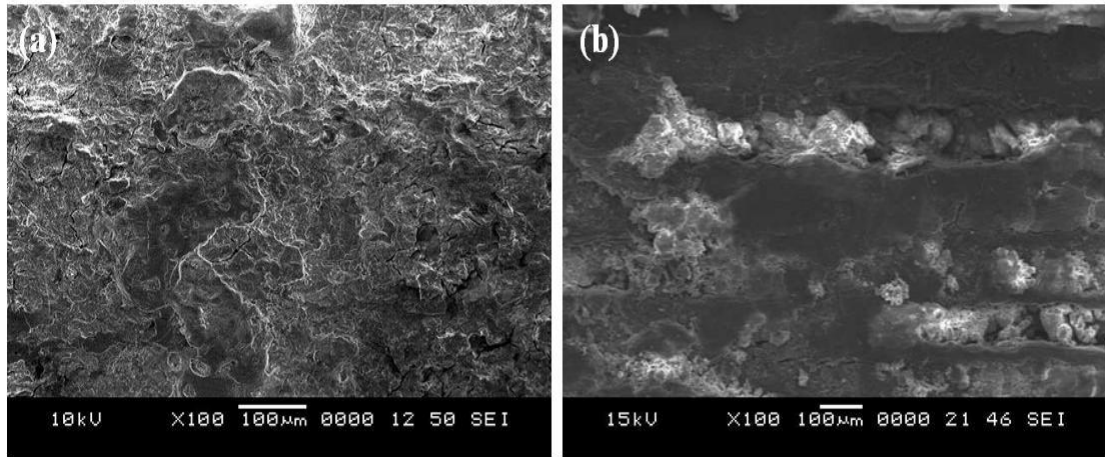


Figure 4.96. SEM micrographs of corroded (a) Mg-4%Zn (b) Mg-4%Zn/Ce/Al hybrid composite.

Surface morphology after electrochemical polarization test in the solution of 0.1 M NaCl are shown in figure 4.96. Addition of Ce particle during ARB process helps to form  $\text{Al}_{11}\text{Ce}_3$  phase (Figure 4.91), similar results are reported by Huang et al. 2003. It increases the stability of passive films and thus attributes to improvement in the corrosion resistance of the Mg-4%Zn/Ce/Al hybrid composite (Yan et al. 2016).

#### 4.4.2.10 Immersion test

Higher hydrogen evolution was noticed for the Mg-4%Zn alloy ( $0.82 \text{ ml/cm}^2/\text{d}$ ) as compared to Mg-4%Zn/Ce/Al hybrid composite ( $0.43 \text{ ml/cm}^2/\text{d}$ ).

Table 4.27. Immersion test results.

Materials	Hydrogen evolution rate ( $\text{ml/cm}^2/\text{d}$ )	Corrosion rate ( $\text{mm/y}$ )
Rolled Mg-4%Zn alloy	0.82	1.86
Mg-4%Zn/Ce/Al hybrid composite	0.43	0.77

Corrosion rate calculated from hydrogen evolution for 5-pass ARB processed hydrogen composite is 2 times less than rolled Mg-4%Zn alloy due to refined microstructure and the presence of  $\beta$  phases ( $\text{Al}_{12}\text{Mg}_{17}$ ,  $\text{AlMg}_4\text{Zn}_{11}$  and  $\text{Al}_{11}\text{Ce}_3$ ). The potentiodynamic polarisation (Table 4.26) and immersion testing (Table 4.27) in 0.1 M NaCl solution showed similar trend in the corrosion rate.

#### **4.4.3 Mg-6%Zn/Ce/Al hybrid composite**

Mg-6%Zn/Ce/Al hybrid composite was developed using Mg-6%Zn alloy with Al and Ce particle through accumulative roll bonding process at 300 °C up to five pass. Uniaxial tensile test and hardness measurement were carried out on roll bonded specimens. SEM equipped with EDS and EBSD, TEM and phase analysis by XRD was used for microstructural characterization. Mechanical properties of the ARB processed hybrid composites were evaluated using microhardness and tensile strength tests. In addition, Corrosion behavior of the hybrid composite was examined using electrochemical polarization test. The results obtained from the present work are presented and described in this section.

##### **4.4.3.1 Microstructure evaluation**

SEM micrographs of the Mg-6%Zn/Ce/Al hybrid composite after 5-pass ARB process is as shown in Figure 4.97. There were no cracks or de-lamination along the interfaces of the Mg-6%Zn and Al layers of the composites, indicating the good interfacial bonding introduced by ARB process (Figure 4.97 a). The thickness of Mg-6%Zn and Al layers were found to be in the range of 30-40  $\mu\text{m}$ . Energy dispersive spectroscopy (EDS) data shows interface between Mg-6%Zn and Al layer and also cerium particles were observed from the Figure 4.19(b). The microstructure of the Mg-6%Zn layer (Figure 4.97 c) and Al layer (Figure 4.97 d) reveals the ultrafine grains due to grain subdivision and shears strain between strip and roller during ARB process. Fraction of recrystallized grains increased with increase in strain due to higher rate of nucleation of new grains during recrystallization, which resulted in a relatively uniform microstructure with ultra-fine grains.

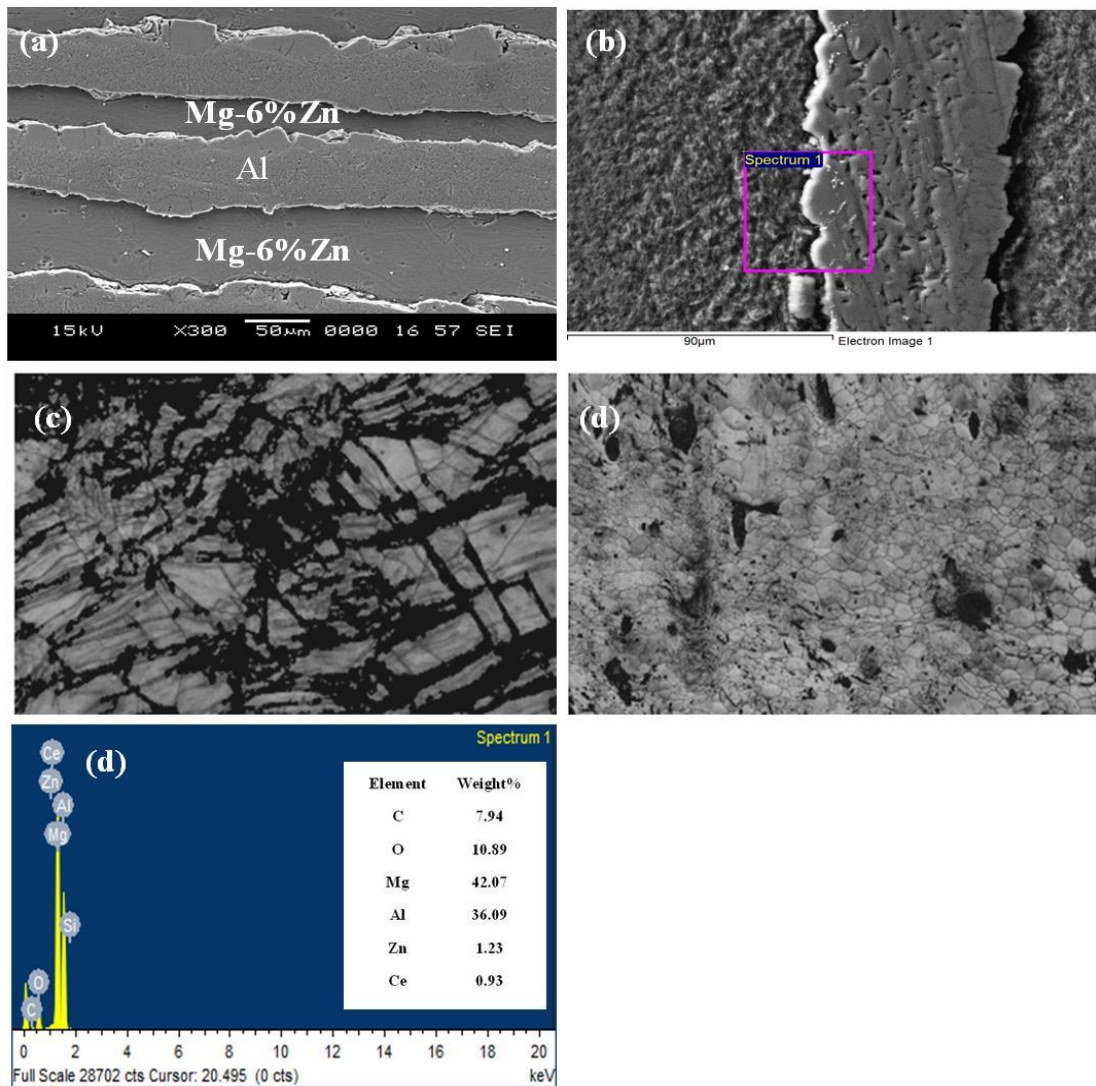


Figure 4.97. SEM micrographs of 5-pass ARB processed (a) Mg-6%Zn/Ce/Al hybrid composite (b) Magnified image (c) Microstructure of the Mg-6%Zn layer (d) Microstructure of the Al layer. (e) EDS of cerium particle.

#### 4.4.3.2 EBSD analysis

Figure 4.98 shows EBSD orientation mapping of Al layer of the 5-pass Mg-6%Zn/Ce/Al hybrid composite. Inverse pole figure (IPF) map (Figure 4.98 a) composed of elongated grains directed uniformly in  $\langle 111 \rangle$  orientation in the rolling direction. Grain boundary map (Figure 4.98 b) reveals fine grains with a fraction of HAGBs. At higher ARB passes, strain accumulated in the material is high so that density of dislocations is more in the materials. As a result, fraction of low-angle boundaries is converted in to high-angle boundaries. Percentage of twins in the Al layer of the hybrid

composite was found to be 0.45%. Grain size variation plot (Figure 4.98 d) shows a significant fraction (~90%) of grains having diameter of  $< 2 \mu\text{m}$  and the average grain size found to be  $0.73 \mu\text{m}$ .

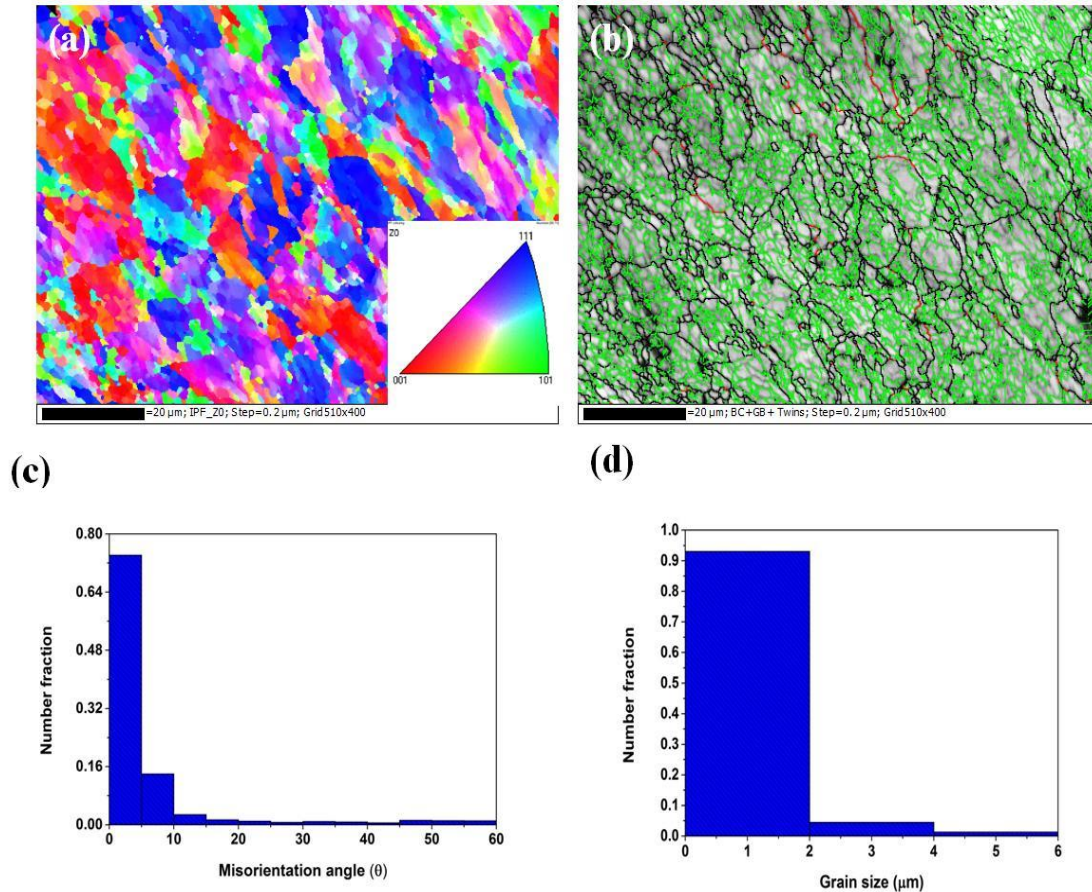


Figure 4.98. EBSD based analysis of Al layer in the Mg-6%Zn/Ce/Al hybrid composite (a) IPF map (b) Misorientation angle distribution profile (c) IPF map, grain boundary map with twins (d) Grain size distribution.

Figure 4.99 depict EBSD based analysis of the Mg-6%Zn layer in the hybrid composites. IPF map (Figure 4.99 a) shows, the grains are directed uniformly in  $\langle 0001 \rangle$  orientation in the direction of rolling. Grain boundary map (Figure 4.99 b) reveals fine grains with a fraction of HAGBs. Misorientation angle distribution profile (Figure 4.99 c) exhibited both LAGBs and HAGBs in Mg-6%Zn layer in the multilayered composite. Deformation twins disappear in the Mg alloys, when the average grain size reaches to  $< 2 \mu\text{m}$ . Grain size variation profile exhibited average grain size of  $0.6 \mu\text{m}$  as shown in figure 4.99 (d).

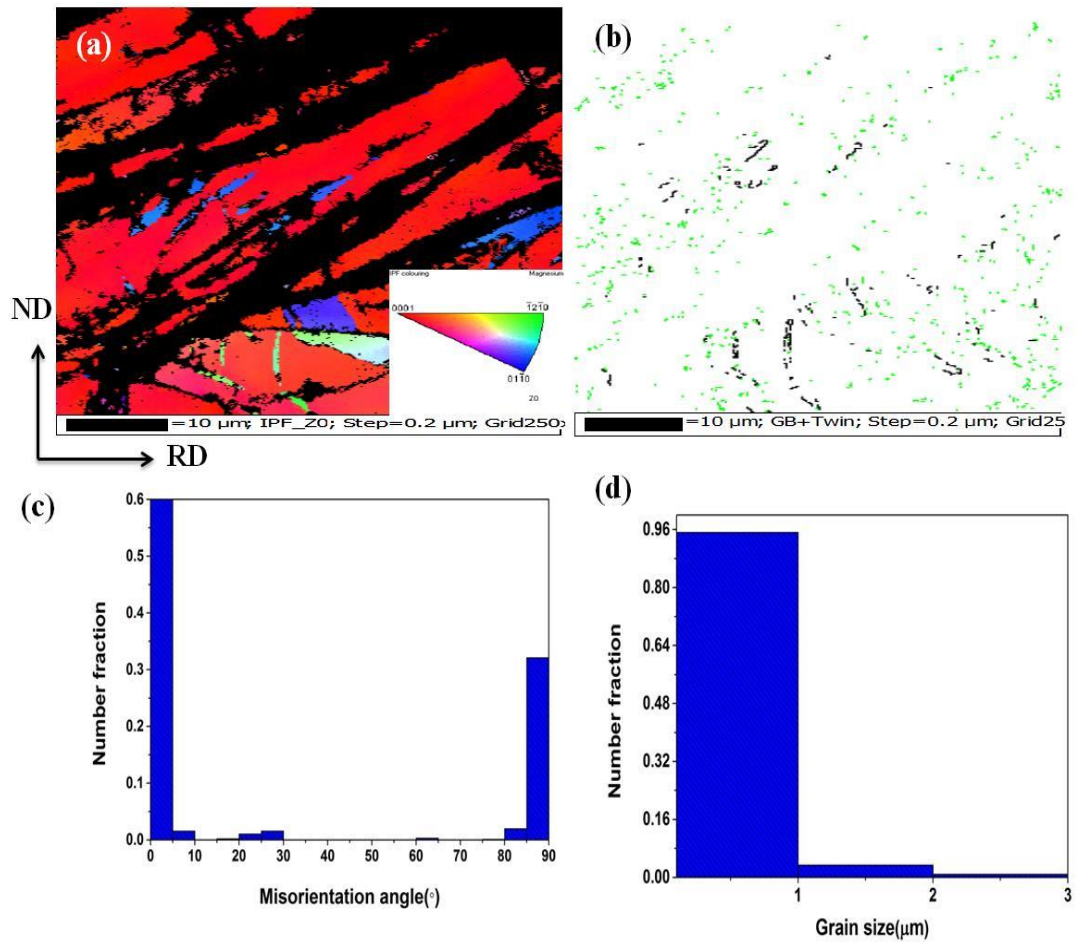


Figure 4.99. EBSD based analysis of Mg-6%Zn layer in the 5-pass ARB processed Mg-6%Zn/Ce/Al hybrid composite (a) IPF map (b) Grain boundary map with twins (c) Misorientation angle distribution profile (d) Grain size distribution.

#### 4.4.3.3 TEM analysis

TEM microstructure and corresponding selected area electron diffraction (SAED) observed at rolling plane of the 5-pass ARB processed Mg-6%Zn/Ce/Al hybrid composite is shown in figure 4.100. Ultra-fine grains are clearly revealed in the microstructure and some regions showed dislocations (Figure 4.100 a), which is an indication of large misorientation. It should be emphasized that the formation of the ultra-fine grains is regionally inhomogeneous in the highly strained materials.



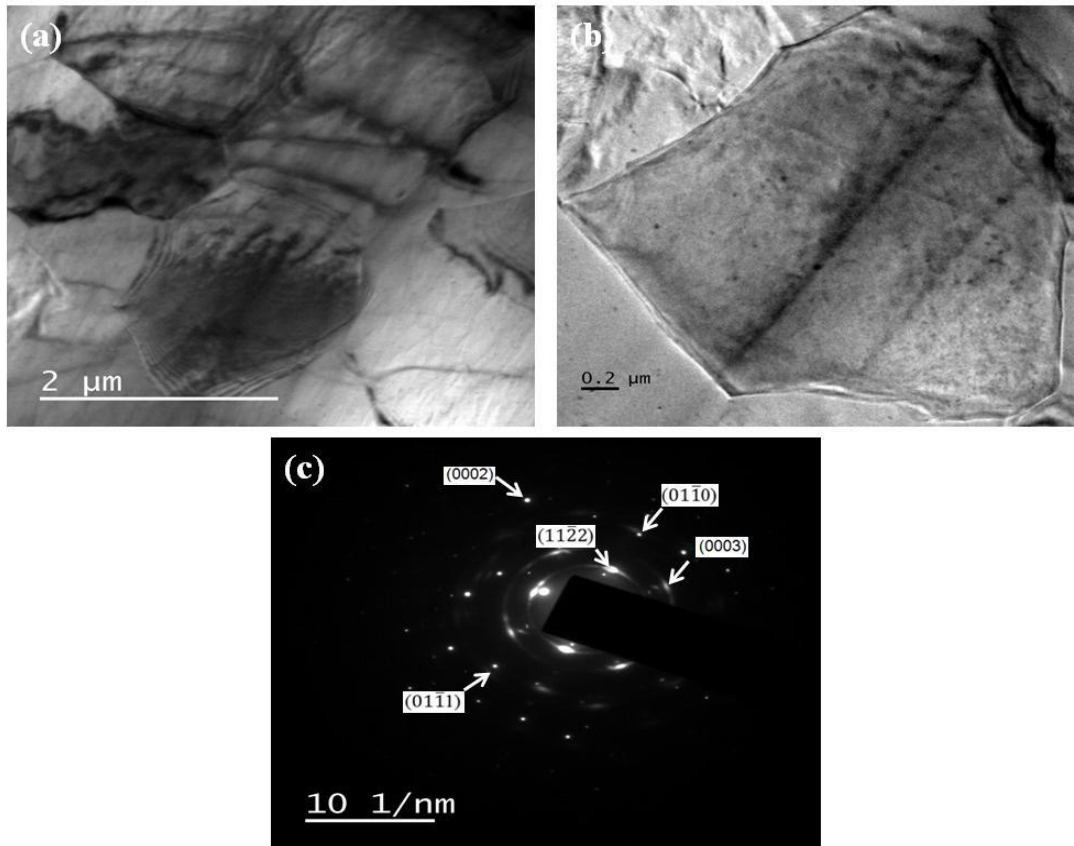


Figure 4.100. TEM micrographs and SAED patterns of the 5-pass ARB processed Mg-6%Zn/Ce/Al hybrid composite.

Fraction of ultra-fine grained regions increased with increasing the number of ARB cycles due to higher strain. Higher magnification image (Figure 4.100 b) shows the dislocation density inside the ultra-fine grain and surrounded by strongly deformed boundaries. SAED patterns are in the form of rings which confirm the sub-grain structure in the Mg-6%Zn/Ce/Al hybrid composite (Figure 4.100 c) with high angle misorientations.

#### 4.4.3.4 X-ray diffraction analysis

XRD patterns (RD-TD plane) of 5-pass ARB processed Mg-6%Zn/Ce/Al hybrid composite is shown in figure 4.101.

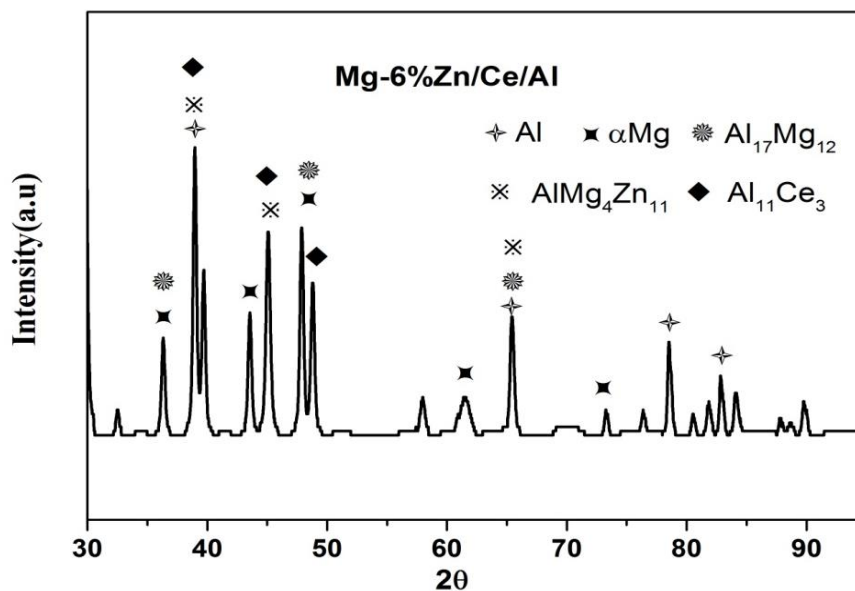


Figure 4.101. XRD patterns along the cross section of the Mg-6%Zn/Ce/Al hybrid composite.

Results indicated mainly three intermetallic phases Al<sub>17</sub>Mg<sub>12</sub>, AlMg<sub>4</sub>Zn<sub>11</sub> and Al<sub>11</sub>Ce<sub>3</sub>. The addition of Ce leads to the formation of the Al<sub>11</sub>Ce<sub>3</sub> is clearly observed in XRD analysis. During ARB process, Mg-6%Zn, Ce and Al were diffused due high pressure (50% reduction) and temperature (300 °C) and bonded because of mechanical bonding. Intermetallics are formed in the interface region. Area of the interface region increases with the increase of the number ARB passes.

#### 4.4.3.5 Density

Calculated density test results are summarized in table 4.28.

Table 4.28. Density test results

Sample	Density (kg/m <sup>3</sup> )
Al	2691
Mg-6%Zn alloy	1781
Mg-6%Zn/Ce/Al Hybrid composite	2119

#### 4.4.3.6 Microhardness

Microhardness of the Mg-6%Zn and Al alloy layers of the hybrid composite increases with increase in ARB passes is as shown in figure 4.102.

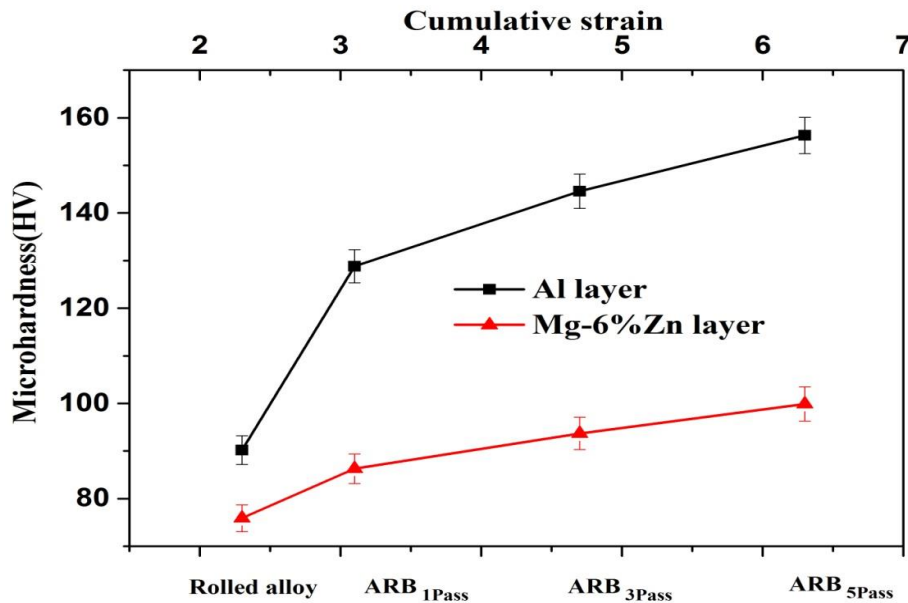


Figure 4.102. Microhardness variation of the rolled and Mg-6%Zn/Ce/Al hybrid composite after different numbers of ARB passes.

After the first pass, microhardness increased rapidly which is due to the work hardening, as a result of increased dislocations density. As the number of ARB passes increases, the microhardness found to increased because of strain hardening and grain refinement process. Microhardness of the 5-pass multilayered composite layers reached to 99.9 HV (~1.31 time) and 156.3 HV (~ 1.73 times), respectively. The presence of the cerium particles in the hybrid composite during the ARB process, activate the strengthening mechanisms. During the ARB, the cerium particles increased dislocation density in the matrix/reinforcement interfaces due to strain between the matrix and particle as well as due to difference in thermal expansion during ARB process (Mohammad et al. 2014). Therefore, hardness value of hybrid composite sample was higher than that of the monolithic alloys.

#### 4.4.3.7 Tensile strength test

Variation of tensile strength (UTS), yield strength (YS) and elongation of the Mg-6%Zn/Ce/Al hybrid composite at different ARB passes are shown in figure 4.103.

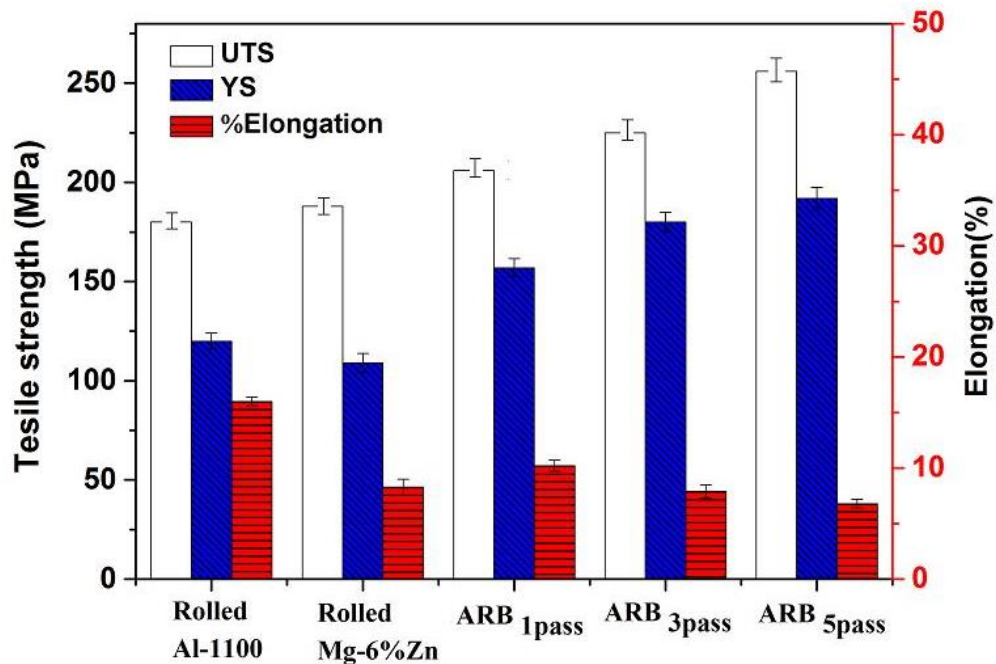


Figure 4.103. Variation of UTS, YS and percentage elongation of the Mg-6%Zn/Ce/Al hybrid composite with different ARB passes.

As can be seen, the strength of multilayered composite increases with increase in number of ARB passes. YS and UTS of the hybrid composite improved to 1.76 times and 1.36 times than that of rolled Mg-6%Zn alloy respectively. Strength improvement in initial passes of ARB process attributed to strain hardening or dislocation strengthening mechanism. Strength improvement at the higher ARB passes is due to formation of ultrafine grain structure (Hall-Petch effect), largely misoriented grain boundaries, and formation of intermetallic phases. At higher ARB passes, work hardening effect gradually decreases, as the number of ultrafine grains with high-angle boundaries increases. Total elongation decreases with increasing number of ARB passes. In addition, the high strength observed in the Mg-6%Zn/Ce/Al hybrid composite is not only due to mentioned mechanism but also due to cerium particle reinforcement. Pagounis and Lindroos, 1998 reported that load transfers from the matrix to the reinforcement particles by accommodation of shear stresses at the composite interfaces leading to an increase of strength. Reinforcement particles accelerate formation of ultrafine grains by preventing grain growth. Dislocations are generated around reinforcement particles in the matrix are considered as one of the main strengthening mechanisms that contributes in strengthening of severe plastic deformation processed materials.

#### 4.4.3.8 Fractography

Fractographs after tensile test are shown in figure 4.104. It shows that Mg-6%Zn/Ce/Al hybrid composite exhibited a shear ductile fracture, having dimples and shear zones (Figure 4.104 a).

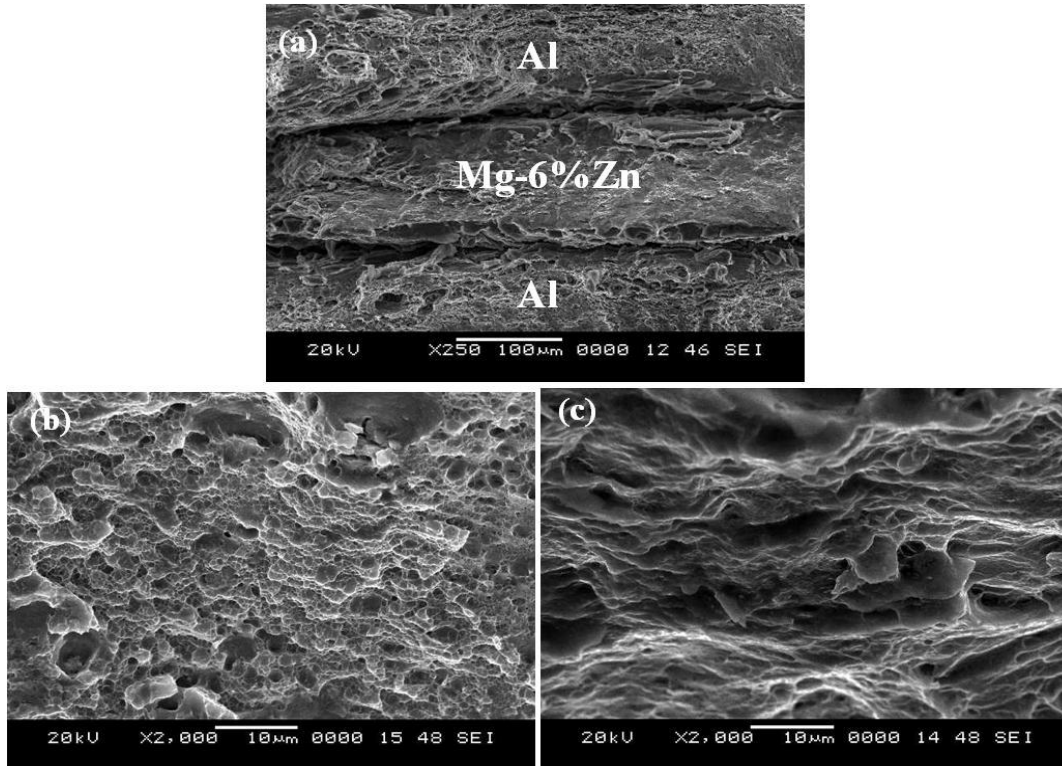


Figure 4.104. SEM micrographs of the fractured surface of the (a) 5-pass ARB processed Mg-6%Zn/Ce/Al hybrid composite (b) Al layer (c) Mg-6%Zn layer.

Magnified image of the Al layer (Figure 4.104 b) in the 5-pass ARB processed Mg-6%Zn/Ce/Al hybrid composite reveals dimples as a result of ductile fracture. Appearance of micro voids in the fracture surfaces are being affected by the state of shear stress. Therefore, the dimples are elongated which shows shear ductile failure. Mg-6%Zn layer (Figure 4.104 c) in composite was fractured in the shear mode and free from dimples which appear to be transgranular brittle fracture due to hexagonal closed packed (HCP) structure.

#### 4.4.3.9 Potentiodynamic polarization

Potentiodynamic polarization test results calculated from the polarization curves are summarized in Table 4.29. Corrosion current density ( $i_{\text{corr}}$ ) of the rolled Mg-4%Zn alloy and 5-pass ARB processed Mg-6%Zn/Ce/Al hybrid composite is  $16.1 \mu\text{A}/\text{cm}^2$  and  $9.1 \mu\text{A}/\text{cm}^2$  respectively, meanwhile shifts the corrosion potential ( $E_{\text{corr}}$ ) towards Noble direction as observed in figure 4.105.

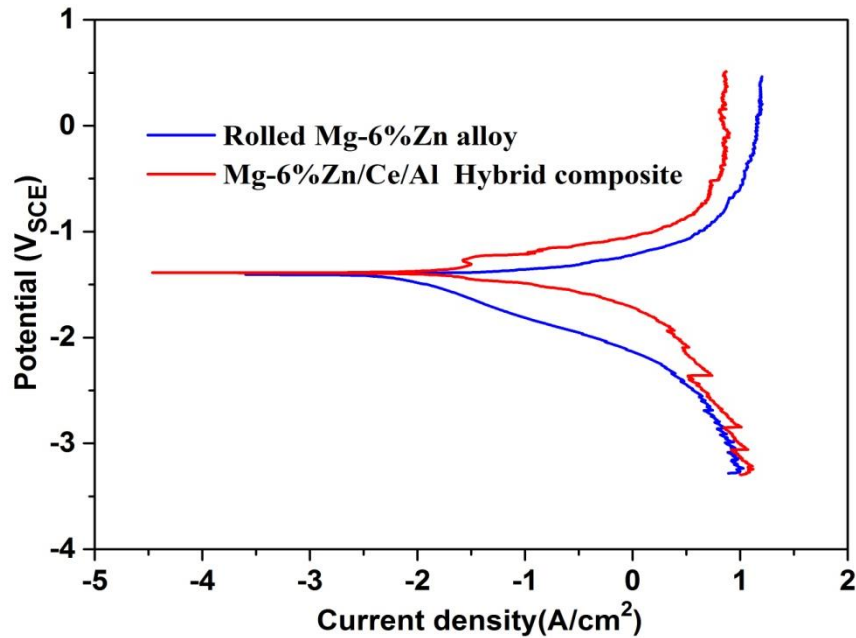


Figure 4.105. Potentiodynamic polarization curves of the Mg-6%Zn and 5-pass ARB processed Mg-6%Zn/Ce/Al hybrid composite.

Potentiodynamic polarization plot shows the corrosion potential in passive regions indicating a higher passivation exhibited in the ARB processed hybrid composites as compared to rolled Mg-6%Zn alloy.

Table 4.29. Potentiodynamic polarization test results.

Materials	$E_{\text{corr}}$ (V <sub>SCE</sub> )	$i_{\text{corr}}$ ( $\mu\text{A}/\text{cm}^2$ )	$\beta_a$ (mV/decade)	$\beta_c$ (mV/decade)	Corrosion rate (mm/y)
Mg-6%Zn	-1.53	16.19	175.8	302.7	0.49
Mg-6%Zn/Ce /Al composite	-1.33	9.1	123.5	-153.2	0.23

Corrosion rate was calculated from the EC-LAB software and tabulated in table 4.29. These small sized grains create more grain boundaries that act as a corrosion barrier (Hamu et al. 2009). During ARB process, intermetallics ( $\text{Al}_{12}\text{Mg}_{17}$ ,  $\text{AlMg}_4\text{Zn}_{11}$  and  $\text{Al}_{11}\text{Ce}_3$ ) formed due to bonding with Al are refined and uniformly distributed throughout the structure which acts as an anodic barrier to inhibit the overall corrosion. Mg-6%Zn/Ce/Al hybrid composite exhibited better corrosion resistance as compared to lower zinc alloying hybrid composites. It is due to presence of higher content of Zn in the hybrid composites results in the formation of large amount of ZnO (Ha et al. 2013), when can enhance the protectiveness of the passive film and kinetics of passivation there by inhibiting the corrosion.

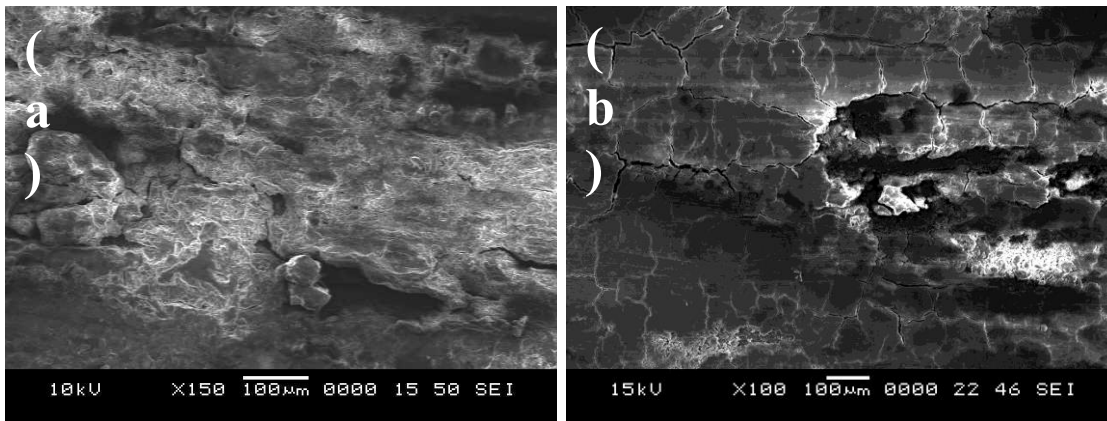


Figure 4.106. SEM micrographs of corroded (a) Mg-6%Zn (b) Mg-6%Zn/Ce/Al hybrid composite after electrochemical test in a 0.1 M NaCl solution.

Surface morphology after electrochemical polarization test in the solution of 0.1 M NaCl are shown in figure 4.106 for Mg-6%Zn and Mg-6%Zn/Ce/Al hybrid composite. A significant dissolution of Mg-2%Zn alloy (Figure 4.106 a) was observed as compared to Mg-2%Zn/Ce/Al hybrid composite. Mg-2%Zn/Ce/Al hybrid composite is exhibits layer-wise corrosion and bright region of Mg-2%Zn layer shown in Figure 4.106 (b) is covered with magnesium hydroxide (Huang et al. 2003). The addition of Ce particle during ARB process helps to form  $\text{Al}_{11}\text{Ce}_3$  phase (Figure 4.104), which increases the stability of passive films and thus attributes to improvement in the corrosion resistance of the Mg-2%Zn/Ce/Al hybrid composite (Yan et al. 2016).

#### 4.4.3.10 Immersion test

Table 4.30. Immersion test results.

Materials	Hydrogen evolution rate (ml/cm <sup>2</sup> /d)	Corrosion rate (mm/y)
Rolled Mg-6%Zn	0.28	0.62
Mg-6%Zn/Ce/Al hydrogen composite	0.14	0.26

Hydrogen evolution rate and corresponding corrosion rate of the wrought Mg-6%Zn alloy and ARB processed Mg-6%Zn/Ce/Al hybrid composite are illustrated in Table 4.30. Higher hydrogen evaluation was noticed for the Mg-6%Zn alloy as compared to hybrid composite due to refined microstructure as well as the presence of  $\beta$  phases ( $\text{Al}_{12}\text{Mg}_{17}$ ,  $\text{AlMg}_4\text{Zn}_{11}$  and  $\text{Al}_{11}\text{Ce}_3$ ). The potentiodynamic polarisation (Table 4.29) and immersion testing (Table 4.30) in 0.1 M NaCl solution showed similar trend in the corrosion rate.

#### 4.4.4 Summary

Mg-(2-6)%Zn/Ce/Al hybrid composite was fabricated by ARB at 300 °C up to five passes successfully. Microstructure, mechanical properties and corrosion behaviour of the multilayered composites was investigated. The following summaries have been derived from the obtained results.

Developed hybrid composite exhibits 1.2 times lighter weight as compared to Al.  $\text{Al}_{17}\text{Mg}_{12}$ ,  $\text{AlMg}_4\text{Zn}_{11}$  and  $\text{Al}_{11}\text{Ce}_3$  phases were identified through the XRD analysis of the ARB processed Mg-(2-6)%Zn/Ce/Al hybrid composite.

EBSD and TEM analysis showed the UFG with high angle misorientation in the microstructure. Average grain size was found to be (a) 1.8  $\mu\text{m}$  and 1  $\mu\text{m}$  and for Al and Mg-2%Zn layers in the Mg-2%Zn/Ce/Al hybrid composite. (b) 1.3  $\mu\text{m}$  and 1  $\mu\text{m}$  for Al and Mg-4%Zn layers in the Mg-4%Zn/Ce/Al hybrid composite (c) 0.73  $\mu\text{m}$  and 0.6  $\mu\text{m}$  for Al and Mg-6%Zn layers in the Mg-6%Zn/Ce/Al hybrid composite respectively.



As the number of ARB passes increases, microhardness of the different layers of the Mg-(2-6)%Zn/Ce/Al hybrid composite increases. After five pass of ARB process, Al and Mg-4%Zn layers of the Mg-4%Zn/Ce/Al hybrid composite exhibited 159.6 HV and 101.2 HV.

It is observed that, YS and UTS of the composites followed the same trend as that of microhardness with increase in ARB passes. Increase in strength was due to strain hardening, grain refinement, and cerium particle reinforcement. Mg-4%Zn/Ce/Al hybrid composite exhibited 192 MPa (YS) and 270 MPa (UTS). Percentage elongation decreases with increases in the number of ARB passes. Fractured surfaces of the Al layers of the hybrid composites are characterized by dimples and exhibited shear ductile fracture and Mg-Zn layers exhibited transgranular brittle fracture.

Potentiodynamic polarization and immersion study revealed that Mg-Zn/Ce/Al hybrid composites exhibited better corrosion resistance. It is mainly due to UFG structure and during ARB process, intermetallics ( $\text{Al}_{12}\text{Mg}_{17}$ ,  $\text{AlMg}_4\text{Zn}_{11}$  and  $\text{Al}_{11}\text{Ce}_3$ ) formed are refined and uniformly distributed throughout the structure which acts as an anodic barrier to inhibit the overall corrosion. Addition of Ce particle during ARB process helps to form  $\text{Al}_{11}\text{Ce}_3$  phase which increases the stability of passive films and thus attributes to improvement in corrosion resistance of the hybrid composites. Mg-6%Zn/Ce/Al hybrid composites exhibited better corrosion resistance as compared to lower Zn alloying composites of Mg-2%Zn/Ce/Al and Mg-4%Zn/Ce/Al. Presence of higher content of Zn in the composites results in the formation of large amount of ZnO, which can enhance the protectiveness of the passive film and kinetics of passivation there by inhibiting the corrosion.

## CHAPTER 5

### CONCLUSIONS

Objectives of the present work were to develop different Mg-Zn/Al and Mg-Zn/Ce/Al multilayered composites with improved mechanical and corrosion properties by developing ultra fine grained structures using accumulative roll bonding process. In the present work following composites systems are developed by ARB process.

- (i) Mg-(2-6)%Zn/Al and Mg-(2-6)%Zn/anodized Al multilayered composite
- (ii) Mg-(2-6)%Zn/Al-7075 and Mg-(2-6)%Zn/anodized Al-7075 multilayered composite
- (iii) Mg-(2-6)%Zn/Ce/Al multilayered hybrid composites

Mechanism of grain refinement, improvement of mechanical and corrosion properties were correlated with different passes of the ARB process. A thorough microstructural characterization was performed on the developed composites by SEM, EBSD, TEM and phase analysis by XRD. In addition, mechanical properties were evaluated by microhardness and tensile strength tests. Corrosion behavior was examined using electrochemical polarization and immersion test. From the overall observations, the following conclusions were categorized and derived as follows:

#### **Microstructure evolution**

Average grain size decreases with increase in ARB passes. Cumulative strain increases with increase in the number of ARB passes increases. Good bonding was observed in the layers of the multilayered composites and the microstructural homogeneity was improved as the number of ARB passes increases. After five pass of ARB process, multilayered composites exhibits ultra fine grains with high angle misorientation observed in the EBSD and TEM analysis.

Average grain size in the Mg-(2-6%)Zn/Al and Mg-(2-6%)Zn/anodized Al multilayered composites was found to be 1.9  $\mu\text{m}$ , 1.3  $\mu\text{m}$  and 1.04  $\mu\text{m}$  for Al, anodized Al and Mg-2%Zn layers respectively, 1.5  $\mu\text{m}$ , 1.3  $\mu\text{m}$  and 1  $\mu\text{m}$  for Al,

anodized Al and Mg-4%Zn layers and 1.8  $\mu\text{m}$ , 1.6  $\mu\text{m}$  and 0.6  $\mu\text{m}$  for Al, anodized Al and Mg-6%Zn respectively.

Average grain size in the Mg-(2-6%)Zn/Al-7075 and Mg-(2-6%)Zn/anodized Al-7075 multilayered composites was found to be 1.3  $\mu\text{m}$ , 1  $\mu\text{m}$  and 1  $\mu\text{m}$  for Al-7075 and anodized Al-7075 and Mg-2%Zn layers respectively, 1.3  $\mu\text{m}$ , 0.73  $\mu\text{m}$  and 1  $\mu\text{m}$  for Al-7075, anodized Al-7075 and Mg-4%Zn layers respectively and 1.3  $\mu\text{m}$ , 0.73  $\mu\text{m}$  and 0.6  $\mu\text{m}$  for Al-7075, anodized Al-7075 and Mg-6%Zn layers respectively.

Average grain size in the Mg-(2-6%)Zn/Ce/Al hybrid composites was found to be 1.8  $\mu\text{m}$  and 1  $\mu\text{m}$  and for Al and Mg-2%Zn layers respectively, 1.3  $\mu\text{m}$  and 1  $\mu\text{m}$  for Al and Mg-4%Zn layers and 0.73  $\mu\text{m}$  and 0.6  $\mu\text{m}$  for Al and Mg-6%Zn layers respectively. Grain refinement during ARB is due to (i) subdivision of the initial grains and formation of subgrain structure with low angle grain boundaries by multi-directional slip, (ii) misorientation increase and gradual transformation of low angle boundaries to high angle grain boundaries by dislocation accumulation, and (iii) migration of new high angle grain boundaries and formation of UFG structure.

### **Mechanical properties**

It is observed that, YS, UTS and microhardness of the composites increases with increases in ARB passes. Mg-(2-6%)Zn/Al composite gives better mechanical properties as compared to Mg-Zn rolled alloys, due to strain hardening and grain refinement during ARB process. Microhardness and strength of the multilayered composites is also affected by the presence of intermetallics ( $\text{Al}_{17}\text{Mg}_{12}$  and  $\text{AlMg}_4\text{Zn}_{11}$ ) which is formed during ARB process. Mg-(2-6%)Zn/anodized Al multilayered composite exhibited better properties as compared to Mg-(2-6%)Zn/Al composite which is due to reinforcement of harder alumina particles, (through anodization treatment) distributed uniformly in the microstructure during ARB process and act as a barrier to the dislocation movement.

Mg-4%Zn/Al and Mg-4%Zn/anodized Al composite exhibited better microhardness and strength as compared to other composite systems containing 2%Zn and 6%Zn. Zn acts as grain refiners up to 4% addition. Further addition of Zn, will react with Mg and form large amount of Mg-Zn phases in the matrix and grain boundary resulting in

residual defects and increase the number of crack sources, thus strength alloy of the alloy decreases.

Microhardness and strength of the Mg-(2-6%)Zn/Al-7075 and Mg-(2-6%)Zn/anodized Al-7075 multilayered composite followed identical trend with increase in ARB passes. Mg-(2-6%)Zn/Al-7075 composite gives better mechanical properties as compared to Mg-Zn alloys, due to strain hardening and grain refinement during ARB process. Microhardness and strength of the multilayered composites is also affected by the presence of intermetallic ( $Al_{17}Mg_{12}$  and  $AlMg_4Zn_{11}$ ) formed during ARB process. Mg-(2-6%)Zn/anodized Al-7075 multilayered composite exhibited better properties as compared to Mg-(2-6%)Zn/Al-7075 composite.

As the number of ARB passes increases, microhardness and strength of the Mg-(2-6)%Zn/Ce/Al hybrid composite increases. It is due to strain hardening, grain refinement and cerium particle reinforcement. Mg-4%Zn/Ce/Al hybrid composite exhibited higher strength as compared to Mg-2%Zn/Ce/Al and Mg-6%Zn/Ce/Al hybrid composite. Percentage elongation decreases with increases in the number of ARB passes. Fractured surfaces of the Al and anodized layers of the composites are characterized by dimples and exhibited shear ductile fracture and Mg-Zn layers exhibited transgranular brittle fracture.

### **Corrosion behavior**

Potentiodynamic polarization and immersion study revealed that the Mg-(2-6%)Zn/Al, Mg-(2-6%)Zn/Al-7075 and Mg-(2-6)%Zn/Ce/Al multilayered composite exhibited highest corrosion resistance as compared to rolled Mg-Zn alloy. ARB processed composites exhibited UFG structure and during ARB process, intermetallics ( $Al_{12}Mg_{17}$  and  $AlMg_4Zn_{11}$ ) formed during ARB process, are refined and uniformly distributed throughout the structure which acts as an anodic barrier to inhibit the overall corrosion. Good corrosion resistance of anodized multilayered composites are due to uniform distribution of alumina ( $Al_2O_3$ ) resulted from the anodization process. Mg-6%Zn/Al, Mg-6%Zn/Al-7075 and Mg-6%Zn/Ce/Al exhibited higher corrosion resistance as compared to lower Zn alloying composites which can be attributed to the formation of large amount of ZnO, which can enhance

the protectiveness of the passive film and kinetics of passivation there by inhibiting the corrosion.

### **Scope for future work**

Mg-(2-6%)Zn/Al and Al-7075 and Mg-(2-6%)Zn/Ce/Al developed by ARB process up to five passes at various processing temperatures. Microstructure studies and mechanical and corrosion tests were performed to know the behavior of the composites after ARB process. Apart from these characterization and observations, the following various studies can be consider to suite the requirement of the different applications.

- Effect of heat treatment on ARB processed composites to be evaluated.
- Fatigue life of the ARB processed composites to be evaluated.
- Tribocorrosion behavior and biocompatibility study is to be done on ARB processed composites for biomedical applications.
- Grain refinement and grain boundary analysis.
- Analytical study is to be done using 2D-Deform analysis.

## REFERENCES

- Aghion, E., Bronfin, B. and Eliezer, D. (2001). "The role of the magnesium industry in protecting the environment." *J. Mater. Process. Technol.*, 117(3), 381-385.
- Ahmadi, A., Toroghinejad, M. R. and Najafizadeh, A. (2014). "Evaluation of microstructure and mechanical properties of Al/Al<sub>2</sub>O<sub>3</sub>/SiC hybrid composite fabricated by accumulative roll bonding process." *Mater. Des.*, 53, 13-19.
- Alizadeh, M. (2011). "Strengthening mechanisms in particulate Al/B<sub>4</sub>C composites produced by repeated roll bonding process." *J. Alloys Compd.*, 509(5), 2243-2247.
- Ambat, R., Aung, N. N. and Zhou, W. (2000). "Evaluation of microstructural effects on corrosion behaviour of AZ91D magnesium alloy." *Corros. Sci.*, 42(8), 1433-1455.
- Amirkhanlou, S., Ketabchi, M., Parvin, N., Khorsand, S. and Bahrami, R. (2013). "Accumulative press bonding; a novel manufacturing process of nanostructured metal matrix composites." *Mater Des.*, 51, 367-374.
- Argade, G. R., Panigrahi, S. K. and Mishra, R. S. (2012). "Effects of grain size on the corrosion resistance of wrought magnesium alloys containing neodymium." *Corros. Sci.*, 58, 145-151.
- Atrens, A., Winzer, N. and Dietzel, W. (2011). "Stress corrosion cracking of magnesium alloys." *Adv. Eng. Mater.*, 13(1-2), 11-18.
- Aung, N. N. and Zhou, W. (2010). "Effect of grain size and twins on corrosion behaviour of AZ31B magnesium alloy." *Corros. Sci.*, 52(2), 589-594.
- Baazamat, S., Tajally, M. and Borhani, E. (2015). "Fabrication and characteristic of Al-based hybrid nanocomposite reinforced with WO<sub>3</sub> and SiC by accumulative roll bonding process." *J. Alloys Compd.*, 653, 39-46.
- Baker, H. (1999). *ASM specialty handbook: "Magnesium and magnesium alloys"* (Vol. 274). M. M. Avedesian (Ed.). Materials Park, OH: ASM international.
- Bhattacharya, R. and Wynne, B. P. (2011). "Hot working and crystallographic texture analysis of magnesium AZ alloys." *J. Mater. Sci. Technol.*, 27(2), 461-477.

Barsoum, I. and Faleskog, J. (2007). "Rupture mechanisms in combined tension and shear experiments." *Int J. Sol. and Struct.*, 44(6), 1768-1786.

Bhowmik, A., Biswas, S., Suwas, S., Ray, R. K. and Bhattacharjee, D. (2009). "Evolution of grain-boundary microstructure and texture in interstitial-free steel processed by equal-channel angular extrusion." *Metall. and Mater. Trans. A*, 40(11), 2729.

Bowden, F. P., Tabor, D., Bowden, F. P., and Tabor, D. (1950). "The Friction and Lubrication of Solids." Clarendon Press, Oxford.

Cai, S., Lei, T., Li, N. and Feng, F. (2012). "Effects of Zn on microstructure, mechanical properties and corrosion behavior of Mg–Zn alloys." *Mater. Sci. and Eng: C*, 32(8), 2570-2577.

Callister, W. D., and Rethwisch, D. G. (2008). *Fundamentals of Materials Science and Engineering*, second ed., John Wiley & Sons, USA.

Cao, F., Shi, Z., Song, G. L., Liu, M. and Atrens, A. (2013). "Corrosion behaviour in salt spray and in 3.5% NaCl solution saturated with Mg (OH) 2 of as-cast and solution heat-treated binary Mg–X alloys: X=Mn, Sn, Ca, Zn, Al, Zr, Si, Sr." *Corros. Sci.*, 76, 60-97.

Chang, H., Zheng, M. Y., Xu, C., Fan, G. D., Brokmeier, H. G. and Wu, K. (2012). "Microstructure and mechanical properties of the Mg/Al multilayer fabricated by accumulative roll bonding (ARB) at ambient temperature." *Mater. Sci. and Eng: A*, 543, 249-256.

Chang, H., Zheng, M., Gan, W., Xu, C. and Brokmeier, H. G. (2013). "Texture evolution of the Mg/Al laminated composite by accumulative roll bonding at ambient temperature." *Rare Metal Mater and Eng.*, 42(3), 441-446.

Chen, M. C., Hsieh, H. C. and Wu, W. (2006). "The evolution of microstructures and mechanical properties during accumulative roll bonding of Al/Mg composite." *J. Alloys Compd.*, 416(1), 169-172.

Chen, M. C., Kuo, C. W., Chang, C. M., Hsieh, C. C., Chang, Y. Y. and Wu, W. (2007). "Diffusion and formation of intermetallic compounds during accumulative roll-bonding of Al/Mg alloys." *Mater Trans.*, 48(10), 2595-2598.

Chino, Y., Kado, M. and Mabuchi, M. (2008). "Compressive deformation behavior at room temperature-773K in Mg–0.2 mass%(0.035 at.%) Ce alloy." *Acta Mater.*, 56(3), 387-394.

Christian, J. W. and Mahajan, S. (1995). "Deformation twinning." *Prog. Mater Sci.*, 39(1-2), 1-157.

Clark, J. B. (1968). "Age hardening in a Mg-9 wt.% Al alloy." *Acta Mater.*, 16(2), 141-152.

Cram, D. G., Zurob, H. S., Brechet, Y. J. M. and Hutchinson, C. R. (2009). "Modelling discontinuous dynamic recrystallization using a physically based model for nucleation." *Acta Mater.*, 57(17), 5218-5228.

Davis, J. R. (Ed.). (1999). *Corrosion of aluminum and aluminum alloys*. ASM International.

Doherty, R. D., Hughes, D. A., Humphreys, F. J., Jonas, J. J., Jensen, D. J., Kassner, M. E. and Rollett, A. D. (1997). "Current issues in recrystallization: a review." *Mater. Sci. and Eng: A*, 238(2), 219-274.

Dongsong, Y., Erlin, Z., and Songyan, Z. (2009). "Effect of Zn content on microstructure, mechanical properties and fracture behavior of Mg-Mn alloy." *Research & Development*.

Eckert, J., Holzer, J. C., Krill, C. E. and Johnson, W. L. (1992). "Reversible grain size changes in ball-milled nanocrystalline Fe-Cu alloys." *J of Mater Res.*, 7(8), 1980-1983.

Eizadjou, M., Talachi, A. K., Manesh, H. D., Shahabi, H. S. and Janghorban, K. (2008). "Investigation of structure and mechanical properties of multi-layered Al/Cu composite produced by accumulative roll bonding (ARB) process." *Compos. Sci. Technol.*, 68(9), 2003-2009.

Eliezer, D., Aghion, E. and Froes, F. S. (1998). "Magnesium science, technology and applications." *Adv Perform Mater.*, 5(3), 201-212.

Emley, E. F. (1966). "Principles of Magnesium Technologies." London.

Fattah-Alhosseini, A., Imantalab, O., Mazaheri, Y. and Keshavarz, M. K. (2016). "Microstructural evolution, mechanical properties, and strain hardening behavior of ultrafine grained commercial pure copper during the accumulative roll bonding process." *Mater. Sci. and Eng: A*, 650, 8-14.

Gao, Y., Wang, Q., Gu, J., Zhao, Y., Tong, Y. and Yin, D. (2009). "Comparison of microstructure in Mg-10Y-5Gd-0.5 Zr and Mg-10Y-5Gd-2Zn-0.5 Zr alloys by conventional casting." *J. Alloys Compd.*, 477(1), 374-378.

Gashti, S. O., Fattah-Alhosseini, A., Mazaheri, Y. and Keshavarz, M. K. (2016). "Effects of grain size and dislocation density on strain hardening behavior of ultrafine grained AA1050 processed by accumulative roll bonding." *J. Alloys Compd.*, 658, 854-861.



Ghali, E., Dietzel, W. and Kainer, K. U. (2004). "General and localized corrosion of magnesium alloys: a critical review." *J of Mater Eng and Perform.*, 13(1), 7-23.

Ha, H. Y., Kang, J. Y., Yang, J., Yim, C. D. and You, B. S. (2013). "Limitations in the use of the potentiodynamic polarisation curves to investigate the effect of Zn on the corrosion behaviour of as-extruded Mg-Zn binary alloy." *Corros Sci.*, 75, 426-433.

Hall, E. O. (1951). "The deformation and ageing of mild steel: III discussion of results." *Proc of the Phys Soc. Sec B*, 64(9), 747.

Hamu, G. B., Eliezer, D. and Wagner, L. (2009). "The relation between severe plastic deformation microstructure and corrosion behavior of AZ31 magnesium alloy." *J. Alloys Compd.*, 468(1), 222-229.

Hansen, N. and Juul Jensen, D. (2011). "Deformed metals—structure, recrystallisation and strength." *Mater Sci and Techn.*, 27(8), 1229-1240.

Hebert, R. J. and Perepezko, J. H. (2004). "Deformation-induced synthesis and structural transformations of metallic multilayers." *Scripta Mater.*, 50(6), 807-812.

Heintzenberg, J. (1989). "Fine particles in the global troposphere A review." *Tellus B*, 41(2), 149-160.

Hertzberg, R. W. (1996). *Deformation and fracture mechanics of engineering materials*. Wiley.

Hidalgo-Manrique, P., Cepeda-Jiménez, C. M., Ruano, O. A., and Carreño, F. (2012). "Effect of warm accumulative roll bonding on the evolution of microstructure, texture and creep properties in the 7075 aluminium alloy." *Mater. Sci. and Eng: A*, 556, 287-294.

Hidalgo-Manrique, P., Orozco-Caballero, A., Cepeda-Jiménez, C. M., Ruano, O. A. and Carreno, F. (2016). "Influence of the Accumulative Roll Bonding Process Severity on the Microstructure and Superplastic Behaviour of 7075 Al Alloy." *J of Mater Sci and Technol.*, 32(8), 774-782.

Honeycombe, R. W. K. (1984). "The plastic deformation of metals", Edward Arnold Ltd. London, UK.

Huang, J. Y., Zhu, Y. T., Jiang, H. and Lowe, T. C. (2001). "Microstructures and dislocation configurations in nanostructured Cu processed by repetitive corrugation and straightening." *Acta Mater.*, 49(9), 1497-1505.

- Huang, X., Kamikawa, N. and Hansen, N. (2008). "Strengthening mechanisms in nanostructured aluminum." *Mater. Sci. and Eng: A*, 483, 102-104.
- Huang, X., Tsuji, N., Hansen, N. and Minamino, Y. (2003). "Microstructural evolution during accumulative roll-bonding of commercial purity aluminum." *Mater. Sci. and Eng: A*, 340(1), 265-271.
- Hughes, D. A. and Hansen, N. (1997). "High angle boundaries formed by grain subdivision mechanisms." *Acta Mater.*, 45(9), 3871-3886.
- Humphreys, F. J. and Hatherly, M (2004). "Recrystallization and related annealing phenomena," Elsevier.
- Ion, S. E., Humphreys, F. J. and White, S. H. (1982). "Dynamic recrystallisation and the development of microstructure during the high temperature deformation of magnesium." *Acta Metallur.*, 30(10), 1909-1919.
- Iwahashi, Y., Horita, Z., Nemoto, M. and Langdon, T. G. (1997). "An investigation of microstructural evolution during equal-channel angular pressing." *Acta Mater.*, 45(11), 4733-4741.
- Jafarian, H., Habibi-Livar, J. and Razavi, S. H. (2015). "Microstructure evolution and mechanical properties in ultrafine grained Al/TiC composite fabricated by accumulative roll bonding." *Comp Part B: Eng.*, 77, 84-92.
- Jamaati, R. and Toroghinejad, M. R. (2014). "Effect of stacking fault energy on mechanical properties of nanostructured FCC materials processed by the ARB process." *Mater. Sci. and Eng: A*, 606, 443-450.
- Jamaati, R. and Toroghinejad, M. R. (2010). "High-strength and highly-uniform composite produced by anodizing and accumulative roll bonding processes." *Mater Des.*, 31(10), 4816-4822.
- Jamaati, R. Toroghinejad, M. R., Dutkiewicz, J., and Szpunar, J. A. (2012). "Investigation of nanostructured Al/Al<sub>2</sub>O<sub>3</sub> composite produced by accumulative roll bonding process." *Mater Des.*, 35, 37-42.
- Jonsson, M. and Persson, D. (2010). "The influence of the microstructure on the atmospheric corrosion behaviour of magnesium alloys AZ91D and AM50." *Corros. Sci.*, 52(3), 1077-1085.
- Kadkhodaei, M., Babaiee, M., Manesh, H. D., Pakshir, M. and Hashemi, B. (2013). "Evaluation of corrosion properties of Al/nanosilica nanocomposite sheets produced by accumulative roll bonding (ARB) process." *J. Alloys Compd.*, 576, 66-71.

Kamikawa, N., Sakai, T. and Tsuji, N. (2007). Effect of redundant shear strain on microstructure and texture evolution during accumulative roll-bonding in ultralow carbon IF steel. *Acta Mater.*, 55(17), 5873-5888.

Katgerman, L. and Eskin, D. (2003). "Hardening, Annealing, and Aging." *Handbook of Aluminum, Physical Metallurgy and Processes*, edited by GE Totten, DS MacKenzie, CRC Taylor and Francis, London, New York, 259-303.

Klosters, C.C. (2006). "Influence of surface conditioning on the mechanical properties of ultra-fine-grained plates produced by cumulative rolling". Department of General Materials, Friedrich-Alexander University Erlangen-Nuremberg.

Kojima, Y., Kamado, S. and Sato, T. (2000). Handbook Advanced Magnesium technology. *Kallos publishing co., ltd., Tokyo, 60.*

Krallics, G. and Lenard, J. G. (2004). "An examination of the accumulative roll-bonding process." *J. Mater. Process. Technol.*, 152(2), 154-161.

Koç, E., Kannan, M. B., Ünal, M. and Candan, E. (2015). "Influence of zinc on the microstructure, mechanical properties and in vitro corrosion behavior of magnesium–zinc binary alloys." *J. Alloys Compd.*, 648, 291-296.

Kulekci, M. K. (2008). "Magnesium and its alloys applications in automotive industry." *Int. J of Adv.Manuf. Technol.*, 39(9), 851-865.

Kuo, C. M. and Lin, C. S. (2007). "Static recovery activation energy of pure copper at room temperature." *Scripta Mater.*, 57, 667-70.

Kutniy, K. V., Papirova, I. I., Tikhonovsky, M. A., Pikalov, A. I., Sivtsov, S. V., Pirozhenko, L. A. and Shkuropatenko, V. A. (2009). "Influence of grain size on mechanical and corrosion properties of magnesium alloy for medical implants." *Materialwiss. Werkstofftech.*, 40(4), 242-246.

Laser, T., Hartig, C., Nürnberg, M. R., Letzig, D. and Bormann, R. (2008). "The influence of calcium and cerium mischmetal on the microstructural evolution of Mg-3Al-1Zn during extrusion and resulting mechanical properties." *Acta Mater.*, 56(12), 2791-2798.

Lee, D. W., and Kim, B. K. (2004). "Nanostructured Cu–Al<sub>2</sub>O<sub>3</sub> composite produced by thermochemical process for electrode application." *Mater. Lett.*, 58(3), 378-383.

Lee, S. H., Saito, Y., Tsuji, N., Utsunomiya, H. and Sakai, T. (2002). "Role of shear strain in ultragrain refinement by accumulative roll-bonding (ARB) process." *Scripta Mater.*, 46(4), 281-285.

- Li, B. L., Tsuji, N. and Kamikawa, N. (2006). "Microstructure homogeneity in various metallic materials heavily deformed by accumulative roll-bonding." *Mater. Sci. and Eng: A*, 423(1), 331-342.
- Liao, J., Hotta, M., and Yamamoto, N. (2012). "Corrosion behavior of fine-grained AZ31B magnesium alloy." *Corros. Sci.*, 61, 208-214.
- Liu, C. Y., Jiang, H. J., Wang, C. X., Li, Y. P. and Luo, K. (2016). "Fabrication and Strengthening Mechanisms of Al/WC Particles Composite Prepared by Accumulative Roll Bonding." *Materials Science Forum*, 849, 397-401.
- Liu, C. Y., Jing, R., Wang, Q., Zhang, B., Jia, Y. Z., Ma, M. Z. and Liu, R. P. (2012). "Fabrication of Al/Al<sub>3</sub>Mg<sub>2</sub> composite by vacuum annealing and accumulative roll-bonding process." *Mater. Sci. and Eng: A*, 558, 510-516.
- Liu, H. S., Zhang, B. and Zhang, G. P. (2011). "Microstructures and mechanical properties of Al/Mg alloy multilayered composites produced by accumulative roll bonding." *J of Mater Sci and Techno.*, 27(1), 15-21.
- Liu, P., Li, Y., Wang, J., Haijun, M. A., Guo, G. and Geng, H. (2006). "Microstructure and phase constituents in the interface zone of Mg/Al diffusion bonding." *Metallur. and Mater Trans. B*, 37(4), 649-654.
- Liu, X. B., Chen, R. S. and Han, E. H. (2008). "Effects of ageing treatment on microstructures and properties of Mg–Gd–Y–Zr alloys with and without Zn additions." *J. Alloys Compd.*, 465(1), 232-238.
- Lunder, O., Nisancioglu, K. and Hansen, R. S. (1993). "Corrosion of die cast magnesium-aluminum alloys." *SAE Technical Paper*, 930755.
- Luo, A. A. (2004). "Recent magnesium alloy development for elevated temperature applications." *Int. Mater. Rev.*, 49(1), 13-30.
- Ma, C., Liu, M., Wu, G., Ding, W. and Zhu, Y. (2003). "Tensile properties of extruded ZK60–RE alloys." *Mater. Sci. and Eng: C*, 349(1), 207-212.
- Mackenzie, L. W. F. and Pekguleryuz, M. O. (2008). "The recrystallization and texture of magnesium–zinc–cerium alloys." *Scripta Mater.*, 59(6), 665-668.
- Matsumoto, H., Watanabe, S. and Hanada, S. (2005). "Sheet cladding of Al–Mg/Mg–Li/Al–Mg at room temperature." *Mater Sci Forum*, 29, 446-451.
- Maurice, D. R. and Courtney, T. H. (1990). "The physics of mechanical alloying: a first report." *Metall Trans A.*, 21(1), 289-303.

- Mendis, C. L., Oh-Ishi, K., Kawamura, Y., Honma, T., Kamado, S. and Hono, K. (2009). "Precipitation-Hardenable Mg–2.4 Zn–0.1 Ag–0.1 Ca–0.16 Zr (at.%) Wrought Magnesium Alloy." *Acta Mater.*, 57(3), 749-760.
- Merino, M. C., Pardo, A., Arrabal, R., Merino, S., Casajus, P., and Mohedano, M. (2010). "Influence of chloride ion concentration and temperature on the corrosion of Mg–Al alloys in salt fog." *Corros Sci.*, 52(5), 1696-1704.
- Messler, R. W. (2004). "Joining of materials and structures: from pragmatic process to enabling technology." Butterworth-Heinemann.
- Min, G., Lee, J. M., Kang, S. B. and Kim, H. W. (2006). "Evolution of microstructure for multilayered Al/Ni composites by accumulative roll bonding process." *Mater Lett.*, 60(27), 3255-3259.
- Mishra, R. K., Gupta, A. K., Rao, P. R., Sachdev, A. K., Kumar, A. M. and Luo, A. A. (2008). "Influence of cerium on the texture and ductility of magnesium extrusions." *Scripta Mater.*, 59(5), 562-565.
- Mishra, R. S. and Ma, Z. Y. (2005). "Friction stir welding and processing." *Mater Sci and Eng. Rep.*, 50(1), 1-78.
- Mohammad, R. T., Roohollah, J., Ali, N. and Hossein, E. (2014). "Hybrid composites produced by anodizing and accumulative roll bonding (ARB) processes." *Ceram. Int.*, 40, 10027-10035.
- Mozaffari, A., Manesh, H. D. and Janghorban, K. (2010). Evaluation of mechanical properties and structure of multilayered Al/Ni composites produced by accumulative roll bonding (ARB) process. *J. Alloys Compd.*, 489(1), 103-109.
- Nam, N. D., Mathesh, M., Van Le, T. and Nguyen, H. T. (2014). "Corrosion behavior of Mg–5Al–xZn alloys in 3.5 wt.% NaCl solution." *J. Alloys Compd.*, 616, 662-668.
- Nordlien, J. H., NişancioĖu, K., Ono, S. and Masuko, N. (1996). "Morphology and structure of oxide films formed on MgAl alloys by exposure to air and water." *Electrochem. Soc.*, 143(8), 2564-2572.
- Orlov, D., Ralston, K. D., Birbilis, N. and Estrin, Y. (2011). "Enhanced corrosion resistance of Mg alloy ZK60 after processing by integrated extrusion and equal channel angular pressing." *Acta Mater.*, 59(15), 6176-6186.
- Pagounis, E. and Lindroos, V. K. (1998). "Processing and properties of particulate reinforced steel matrix composites." *Mater. Sci. and Eng: A*, 246(1), 221-224.

- Pardo, A., Merino, M. C., Coy, A. E., Viejo, F., Arrabal, R. and Feliu, S. (2008). Influence of microstructure and composition on the corrosion behaviour of Mg/Al alloys in chloride media. *Electroch. Acta.*, 53(27), 7890-7902.
- Parisa, D.M. and Beitallah, E. (2015). "Microstructure and mechanical properties of tri-metal Al/Ti/Mg laminated composite processed by accumulative roll bonding." *Mater. Sci. and Eng: A*, 628, 135-142.
- Pekguleryuz, M. O. and Kaya, A. A. (2003). "Creep resistant magnesium alloys for powertrain applications." *Adv. Eng. Mater.*, 5(12), 866-878.
- Perez-Prado, M. T. and Ruano, O. A. (2004). "Grain refinement of Mg–Al–Zn alloys via accumulative roll bonding." *Scripta Mater.*, 51(11), 1093-1097.
- Petch, N. J. (1953). "The cleavage strength of polycrystals." *J. Iron Steel Inst.*, 174, 25-28.
- Polmear, I. J. (2006). "Light metals: from traditional alloys to nanocrystals." *Elsevier, Oxford*.
- Quadir, M. Z., Wolz, A., Hoffman, M. and Ferry, M. (2008). "Influence of processing parameters on the bond toughness of roll-bonded aluminium strip." *Scripta Mater.*, 58(11), 959-962.
- Ralston, K. D. and Birbilis, N. (2010). "Effect of grain size on corrosion: a review." *Corrosion*, 66(7), 075005-075005.
- Rhodes, C. G., Mahoney, M. W., Bingel, W. H., Spurling, R. A., and Bampton, C. C. (1997). "Effects of friction stir welding on microstructure of 7075 aluminum." *Scripta Mater.*, 36(1), 69-75.
- Richert, J. and Richert, M. (1986). "A new method for unlimited deformation of metals and alloys." *Aluminium*, 62(8), 604-607.
- Richert, M., Liu, Q. and Hansen, N. (1999). "Microstructural evolution over a large strain range in aluminium deformed by cyclic-extrusion-compression." *Mater. Sci. and Eng: A*, 260(1), 275-283.
- Roy, S., Nataraj, B. R., Suwas, S., Kumar, S. and Chattopadhyay, K. (2012). Microstructure and texture evolution during accumulative roll bonding of aluminium alloys AA2219/AA5086 composite laminates. *J. Mater. Sci.*, 47(17), 6402-6419.
- Ryoo, K. (2005). "Metal oxide particle removal using electrolyzed anode water." *J. Electrochem. Soc.*, 152(11), G885-G888.

Saha, P., Roy, M., Datta, M. K., Lee, B. and Kumta, P. N. (2015). "Effects of grain refinement on the biocorrosion and in vitro bioactivity of magnesium." *Mater. Sci. and Eng: C*, 57, 294-303.

Saito, Y., Tsuji, N., Utsunomiya, H., Sakai, T. and Hong, R. G. (1998). "Ultra-fine grained bulk aluminum produced by accumulative roll-bonding (ARB) process." *Scripta mater.*, 39(9), 1221-1227.

Saito, Y., Utsunomiya, H., Tsuji, N. and Sakai, T. (1999). "Novel ultra-high straining process for bulk materials-development of the accumulative roll-bonding (ARB) process." *Acta Mater.*, 47(2), 579-583.

Salishchev, G. A., Valiakhmetov, O. R. and Galejev, R. M. (1993). "Formation of submicrocrystalline structure in the titanium alloy VT8 and its influence on mechanical properties." *J. of Mater Sci.*, 28(11), 2898-2902.

Sanders, P. G., Fougere, G. E., Thompson, L. J., Eastman, J. A. and Weertman, J. R. (1997). "Improvements in the synthesis and compaction of nanocrystalline materials." *Nanostruct. Mater.*, 8(3), 243-252.

Schmidt, C. W., Knieke, C., Maier, V., Hoppel, H. W., Peukert, W. and Goken, M. (2011). "Accelerated grain refinement during accumulative roll bonding by nanoparticle reinforcement." *Scripta Mater.*, 64(3), 245-248.

Segal, V. M., Reznikov, V. I., Drobyshvskii, A. E. and Kopylov, V. I. (1981). "Plastic working of metals by simple shear." *Russian J of Non-Ferrous Metals*, (1), 99-105.

Semiatin, S. L. and Piehler, H. R. (1979). "Formability of sandwich sheet materials in plane strain compression and rolling." *Metall. Mater. Trans. A*, 10(1), 97-107.

Shaarbaf, M. and Toroghinejad, M. R. (2008). "Nano-grained copper strip produced by accumulative roll bonding process." *Mater. Sci. and Eng: A*, 473(1), 28-33.

Shi, Z., Liu, M. and Atrens, A. (2010). "Measurement of the corrosion rate of magnesium alloys using Tafel extrapolation." *Corros Sci.*, 52(2), 579-588.

Sitdikov, O., Sakai, T., Goloborodko, A., Miura, H. and Kaibyshev, R. (2004). "Effect of pass strain on grain refinement in 7475 Al alloy during hot multidirectional forging." *Mater. Trans*, 45(7), 2232-2238.

Slamova, M., Homola, P. and Karlik, M. (2007). "Thermal stability of twin-roll cast Al-Fe-Mn-Si sheets accumulative roll bonded at different temperatures." *Mater. Sci. and Eng: A*, 462(1), 106-110.

- Smirnova, N. A., Levit, V. I., Pilyugin, V. I., Kuznetsov, R. I., Davydova, L. S. and Sazonova, V. A. (1986). "Evolution of structure of fcc single crystals during strong plastic deformation." *Phys Met. Metall*, 61(6), 127-134.
- Smirnova, N. A., Levit, V. I., Pilyugin, V. I., Kuznetsov, R. I., Davydova, L. S. and Sazonova, V. A. (1986). "Evolution of the fcc single-crystal structure during severe plastic-deformations." *Fiz. Met. Metalloved.*, 61(6), 1170-1177.
- Song, G. (2005). "Recent progress in corrosion and protection of magnesium alloys." *Adv. Eng Mater.*, 7(7), 563-586.
- Song, G. L. (Ed.). (2011). *Corrosion of magnesium alloys*. Elsevier. third ed., John Wiley & Sons Inc., Singapore, 1989, pp. 253–257.
- Song, G. L. and Atrens, A. (1999). "Corrosion mechanisms of magnesium alloys." *Adv Eng Mater.*, 1(1), 11-33.
- Song, G., Atrens, A. and Dargusch, M. (1998). "Influence of microstructure on the corrosion of diecast AZ91D." *Corros Sci.*, 41(2), 249-273.
- Stanford, N. and Barnett, M. R. (2008). "The origin of rare earth texture development in extruded Mg-based alloys and its effect on tensile ductility." *Mater. Sci. and Eng: A.*, 496(1), 399-408.
- Starke, E. A. and Staley, J. T. (1996). "Application of modern aluminum alloys to aircraft." *Prog in Aerospace Sci.*, 32(2-3), 131-172.
- Sverdlin, A. (2003). "Introduction to aluminum." *George E. Totten y D. Scott MacKenzie, Handbook of Aluminum*, 1, 1.
- Terada, D., Inoue, S. and Tsuji, N. (2007). "Microstructure and mechanical properties of commercial purity titanium severely deformed by ARB process." *J. of Mater Sci.*, 42(5), 1673-1681.
- Toroghinejad, M. R., Jamaati, R., Nooryan, A. and Edris, H. (2014 a). "The effect of alumina content on the mechanical properties of hybrid composites fabricated by ARB process." *Ceram. Int.*, 40(7), 10489-10498.
- Toroghinejad, M. R., Jamaati, R., Nooryan, A. and Edris, H. (2014 b). "Hybrid composites produced by anodizing and accumulative roll bonding (ARB) processes." *Ceram Int.*, 40(7), 10027-10035.
- Toth, L. S. and Gu, C. (2014). "Ultrafine-grain metals by severe plastic deformation." *Mater. Charact.*, 92, 1-14.
- Totten, G. E., and MacKenzie, D. S. (Eds.). (2003). "*Handbook of aluminum*": *Vol. 1: Phys Metall and Procresses* (Vol. 1). CRC Press.



Truszkowski, W., Krol, J. and Major, B. (1980). "Inhomogeneity of rolling texture in fcc metals." *Metallurgical Metall. Mater. Trans. A*, 11(5), 749-758.

Tsuji, N., Saito, Y., Lee, S. H. and Minamino, Y. (2003). "ARB (Accumulative Roll Bonding) and other new techniques to produce bulk ultrafine grained materials." *Adv Eng Mater.*, 5(5), 338-344.

Tsuji, N., Saito, Y., Utsunomiya, H. and Tanigawa, S. (1999). "Ultra-fine grained bulk steel produced by accumulative roll-bonding (ARB) process." *Scripta Mater.*, 40(7), 795-800.

Valiev, R. (1997). "Superplastic behaviour of nanocrystalline metallic materials." *Mater. Sci. Forum*, 243, 207-216.

Valiev, R. Z., Chmelik, F., Bordeaux, F., Kapelski, G. and Baudalet, B. (1992). "The Hall-Petch relation in submicro-grained Al-1.5% Mg alloy." *Scripta Mater.*, 27(7), 855-860.

Valiev, R. Z., Islamgaliev, R. K. and Alexandrov, I. V. (2000). "Bulk nanostructured materials from severe plastic deformation." *Prog. Mater Sci.*, 45(2), 103-189.

Valiev, R. Z., Krasilnikov, N. A. and Tsenev, N. K. (1991). "Plastic deformation of alloys with submicron-grained structure." *Mater. Sci. and Eng: A*, 137, 35-40.

Valiev, R. Z., Mulyukov, R. R. and Ovchinnikov, V. V. (1990). "Direction of a grain-boundary phase in submicrometre-grained iron." *Philos. Mag. Lett.* 62(4), 253-256.

Wang, T., Zheng, H., Wu, R., Yang, J., Ma, X. and Zhang, M. (2016). "Preparation of Fine- Grained and High Strength Mg-8Li-3Al-1Zn Alloy by Accumulative Roll Bonding." *Adv Eng Mater.*, 18(2), 304-311.

Wang, Y. M. and Ma, E. (2004). "Three strategies to achieve uniform tensile deformation in a nanostructured metal." *Acta Mater.*, 52(6), 1699-1709.

Wu, H. Y., Lee, S. and Wang, J. Y. (1998). "Solid-state bonding of iron-based alloys, steel-brass, and aluminum alloys." *J. of Mater Proc. Techno.*, 75(1), 173-179.

Wu, K., Chang, H., Maawad, E., Gan, W. M., Brokmeier, H. G. and Zheng, M. Y. (2010). "Microstructure and mechanical properties of the Mg/Al laminated composite fabricated by accumulative roll bonding (ARB)." *Mater. Sci. and Eng: A*, 527(13), 3073-3078.

Xin, Y., Hong, R., Feng, B., Yu, H., Wu, Y. and Liu, Q. (2015). "Fabrication of Mg/Al multilayer plates using an accumulative extrusion bonding process." *Mater. Sci. and Eng: A*, 640, 210-216.

Xing, Z. P., Kang, S. B. and Kim, H. W. (2002). "Microstructural evolution and mechanical properties of the AA8011 alloy during the accumulative roll-bonding process." *Metall. Mater. Trans. A*, 33(5), 1521-1530.

Yan, F. E. N. G., Li, L. I. U., Wang, R. C., Peng, C. Q. and Wang, N. G. (2016). "Microstructures and electrochemical corrosion properties of Mg-Al-Pb and Mg-Al-Pb-Ce anode materials." *Trans of Nonfer. Mets Soc of China*, 26(5), 1379-1387.

Yazar, O., Ediz, T. and Ozturk, T. (2005). "Control of macrostructure in deformation processing of metal/metal laminates." *Acta Mater*, 53(2), 375-381.

Yeh, J. W., Yuan, S. Y. and Peng, C. H. (1998). A reciprocating extrusion process for producing hypereutectic Al-20wt.% Si wrought alloys. *Mater. Sci. and Eng: A*, 252(2), 212-221.

Zeng, R., Kainer, K. U., Blawert, C. and Dietzel, W. (2011). "Corrosion of an extruded magnesium alloy ZK60 component—the role of microstructural features." *J. Alloys Compd.*, 509(13), 4462-4469.

Zhang, J. J., Liang, W. and Li, H. T. (2015). "Effect of thickness of interfacial intermetallic compound layers on the interfacial bond strength and the uniaxial tensile behaviour of 5052 Al/AZ31B Mg/5052 Al clad sheets." *RSC Advances*, 5(127), 104954-104959.

Zhang, X. P., Yang, T. H., Castagne, S. and Wang, J. T. (2011). "Microstructure; bonding strength and thickness ratio of Al/Mg/Al alloy laminated composites prepared by hot rolling." *Mater. Sci. and Eng: A*, 528(4), 1954-1960.

Zhang, R. and Acoff, V. L. (2007). "Processing sheet materials by accumulative roll bonding and reaction annealing from Ti/Al/Nb elemental foils." *Mater. Sci. and Eng: A*, 463(1), 67-73.

Zhilyaev, A. P., Nurislamova, G. V., Kim, B. K., Baro, M. D., Szpunar, J. A. and Langdon, T. G. (2003). "Experimental parameters influencing grain refinement and microstructural evolution during high-pressure torsion." *Acta Mater*, 51(3), 753-765.

Zhu, Y. T., Jiang, H., Huang, J. and Lowe, T. C. (2001). "A new route to bulk nanostructured metals." *Metall. Mater. Trans. A*, 32(6), 1559-1562.

Zhu, Y. T. and Liao, X. (2004). "Nanostructured metals: retaining ductility." *Nature Materials*, 3(6), 351-352.

## List of Publications based on PhD Research Work

Sl. No.	Title of the paper	Authors (in the same order as in the paper. Underline the Research Scholar's name)	Name of the Journal/ Conference, Vol., No., Pages	Month, Year of Publication	Category*
1.	Mg-Zn/Al multilayered composite developed by accumulative roll bonding; Investigation of microstructure and mechanical properties	<u>Gajanan Anne</u> , M R Ramesh, H Shivananda Nayaka, Shashi Bhushan Arya	International Conference on Recent Trends in Engineering and Material Sciences, Jaipur National University, Jaipur, India.	March 17-19, 2016	3
2.	Investigation of microstructure and mechanical properties of Mg-Zn/Al multilayered composite developed by accumulative roll bonding	<u>Gajanan Anne</u> , M R Ramesh, H Shivananda Nayaka, Shashi Bhushan Arya	Perspectives in Science (2016) 8, pp 104-106.	2016	1
3.	Microstructure evolution and mechanical and corrosion behavior of accumulative roll bonded Mg-2%Zn/Al-7075 multilayered composite	<u>Gajanan Anne</u> , M R Ramesh, H Shivananda Nayaka, Shashi Bhushan Arya, and Sandeep Sahu	Journal of Materials Engineering and Performance (2017), 6(4) pp 1726-1734.	2017	1
4.	Microstructure, mechanical and corrosion properties of accumulative roll bonded composite	<u>Gajanan Anne</u> , M R Ramesh, H Shivananda Nayaka, Shashi Bhushan Arya	6 <sup>th</sup> International Engineering Symposium, Kumamoto University, Japan.	March 1-3 2017	3
5.	Microstructure, mechanical and corrosion properties of accumulative roll bonded Mg-2%Zn/anodized Al-7075 composite	<u>Gajanan Anne</u> , M R Ramesh, H Shivananda Nayaka, Shashi Bhushan Arya	International Conference on Emerging Trends In Materials and Manufacturing Engineering, NIT Trichy, Tamilnadu, India. (Received best paper award)	March 10-12 2017	3
6.	Development and properties evaluation of Mg-6%Zn/Al multilayered composites processed by accumulative roll bonding	<u>Gajanan Anne</u> , M R Ramesh, H Shivananda Nayaka, Shashi Bhushan Arya, and Sandeep Sahu	Journal of Materials Research (2017), 32(12) pp 2249-2257.	May 2017	1

7.	Microstructure, mechanical and corrosion properties of accumulative roll bonded Mg-2%Zn/anodized Al-7075 composite	<b>Gajanan Anne</b> , M R Ramesh, H Shivananda Nayaka, Shashi Bhushan Arya	Materials Today; Proceedings (Accepted)	May 2017	1
8.	Investigation of mechanical and corrosion behavior of Mg-Zn/Ce/Al hybrid composite developed by accumulative roll bonding	<b>Gajanan Anne</b> , M R Ramesh, H Shivananda Nayaka, Shashi Bhushan Arya, Sandeep Sahu	Journal of Alloys and Compounds (2107), 724 pp 146-154.	July 2017	1
9.	Fabrication and characteristics of Mg-4%Zn/anodized Al-7075 multilayered composite by accumulative roll bonding	<b>Gajanan Anne</b> , M R Ramesh, H Shivananda Nayaka, Shashi Bhushan Arya, Sandeep Sahu	Material Science and Engineering Technology (Wiley Publication).		Under review
10.	Development of high strength, light weight and corrosion resistance multilayered composites by accumulative roll bonding	<b>Gajanan Anne</b> , M R Ramesh, H Shivananda Nayaka, Shashi Bhushan Arya, Sandeep Sahu	Materials Research Express (IOP Science)		Under review
11.	Investigation of corrosion behavior of Mg-Zn/Al multilayered composite developed by accumulative roll bonding	<b>Gajanan Anne</b> , M R Ramesh, H Shivananda Nayaka, Shashi Bhushan Arya	Materials and corrosion (Wiley Publication)		Under review
12.	Development of Mg-Zn/Al-1100 multi-layered composite by accumulative roll bonding process	<b>Gajanan Anne</b> , M R Ramesh, H Shivananda Nayaka, Shashi Bhushan Arya	International Conference on Advances in Materials & Processing: Challenges & Opportunities organizing by Dept of Metallurgical and Material Engineering, IIT Roorkee, India, during Nov 30-Dec 02, 2017	Nov 2017	3

\* Category: 1: Journal paper, full paper reviewed

4: Conference/Symposium paper, abstract reviewed

2: Journal paper, Abstract reviews

5: others (including papers in Workshops, NITK Research Bulletins, Short notes etc.)

3: Conference/Symposium paper, full paper reviewed

## BIO-DATA

**Name:** Gajanan Anne  
**Father's Name:** Dattatreya S Hegde  
**Date of Birth:** 08-01-1987  
**Nationality:** Indian  
**Marital Status:** Married

**Address:**

**Permanent Address**

S/o. **Dattatreya S Hegde**  
# 144, Anneraman keru,  
Post;Salkod, Honnavar (581334)  
Uttara Kannada, Karnataka  
India.

**Present Address**

Department of Mechanical Engineering  
National Institute of Technology Karnataka  
Surathkal-575025, Srinivasanagar,  
Mangalore, Karnataka, India.

**Mobile Number:** +919743506565

**E-mail id:** gajanan.anne25@gmail.com

**Educational Qualification:**

Qualification	College/school	University/Board	Year of Passing	Performance
<b>Ph.D.</b> Mechanical Engineering	National Institute of Technology Karnataka	NITK,Surathkal	Pursuing	8.25 (CGPA) (Course work)
<b>M. Tech</b> Manufacturing Engineering	M S Ramaiah Institute of Technology, Bangalore.	VTU	2013	9.45 (CGPA)
<b>B. Tech.</b> Mechanical Engineering	Siddaganga Institute of Technology Tumkur	VTU	2011	8.7 (CGPA)
<b>DIPLOMA</b> Automobile Engineering	R.N.S Rural Polytechnic Murdeshwar	TEB	2008	78.9%

**Publication Details**

Papers Published	Under Review	Conference	Workshops/Symposium	Awards and Recognitions
7	3	4	15	<ul style="list-style-type: none"><li>• MHRD Scholarship for perusing Ph.D.</li><li>• Best paper award at NIT Thrichy</li><li>• JASSO Scholarship at Kumamoto University, Japan</li></ul>

I declare that above information is true and correct to best of my knowledge.

**(GAJANAN ANNE)**